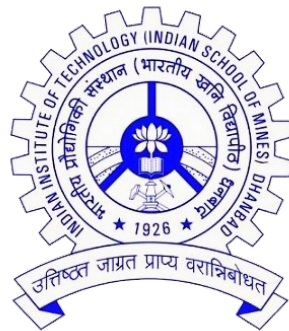


# **MECHANICAL STRENGTHENING OF CFRP COMPOSITE BY INTRODUCING METAL OXIDE NANOSTRUCTURES**

BY

**RAVI SHANKAR RAI**  
**Admission No. 17DR000647**



**THESIS**

**SUBMITTED TO**

**INDIAN INSTITUTE OF TECHNOLOGY  
(INDIAN SCHOOL OF MINES), DHANBAD**

For the award of the degree of  
**DOCTOR OF PHILOSOPHY**

**May 19, 2023**



Form No: PH13

**INDIAN INSTITUTE OF TECHNOLOGY (INDIAN SCHOOL OF MINES) DHANBAD**

**CERTIFICATE FROM THE SUPERVISOR(S)**  
**(To be submitted at the time of Thesis Submission)**

This is to certify that the thesis entitled “**Mechanical strengthening of CFRP composite by introducing metal oxide nanostructures**” being submitted to the Indian Institute of Technology (Indian School of Mines), Dhanbad by Mr. **Ravi Shankar Rai**, Admission No. **17DR000647**, for the award of Doctor of Philosophy (Ph.D.) Degree is a bonafide work carried out by him, in the Department of **Mechanical Engineering**, IIT (ISM), Dhanbad, under my supervision and guidance. The thesis has fulfilled all the requirements as per the regulations of this Institute and, in my/our opinion, has reached the standard needed for submission. The results embodied in this thesis have not been submitted to any other university or institute for the award of any degree or diploma.

*Vivek Bajpai*

Signature of Supervisor

Name: Prof. Vivek Bajpai

Date: 19/05/2023



**INDIAN INSTITUTE OF TECHNOLOGY (INDIAN SCHOOL OF MINES) DHANBAD**

Form No: PH12

**CERTIFICATE REGARDING ENGLISH CHECKING**  
(To be submitted at the time of Thesis Submission)

This is to certify that the thesis entitled “**Mechanical strengthening of CFRP composite by introducing metal oxide nanostructures**” being submitted to the Indian Institute of Technology (Indian School of Mines), Dhanbad by Mr. **Ravi Shankar Rai**, Admission No. **17DR000647**, for the award of Doctor of Philosophy (Ph.D.) Degree has been thoroughly checked for quality of English and logical sequencing of topics.

It is hereby certified that the standard of English is good and that grammar and typos have been thoroughly checked.

It is now worthy for evaluation by the panel of examiners.

Signature of Supervisor (s)

Name: Prof. Vivek Bajpai

Date: 19/05/2023

Signature of Scholar

Name: Ravi Shankar Rai

Date: 19/05/2023



Form No: PH11  
**INDIAN INSTITUTE OF TECHNOLOGY (INDIAN SCHOOL OF MINES) DHANBAD**

**CERTIFICATE FOR CLASSIFIED DATA**  
**(To be submitted at the time of Thesis Submission)**

This is to certify that the thesis entitled “**Mechanical strengthening of CFRP composite by introducing metal oxide nanostructures**” being submitted to the Indian Institute of Technology ( Indian School of Mines), Dhanbad by Mr. **Ravi Shankar Rai** for award of Doctor of Philosophy (Ph.D) Degree in **Mechanical Engineering** does not contains any classified information. This work is original and yet not been submitted to any institution or university for the award of any degree.

Handwritten signature of Nivetha Gupta in black ink.

Signature of Supervisor

Handwritten signature of Ravi Shankar Rai in blue ink.

Signature of Scholar



Form No: PH10

**INDIAN INSTITUTE OF TECHNOLOGY (INDIAN SCHOOL OF MINES) DHANBAD**

**COPYRIGHT AND CONSENT FORM**

(To be submitted at the time of Thesis Submission)

To ensure uniformity of treatment among all contributors, other forms may not be substituted for this form, nor may any wording of the form be changed. This form is intended for original material submitted to the IIT (ISM), Dhanbad and must accompany any such material in order to be published by the ISM. Please read the form carefully and keep a copy for your files.

**TITLE OF THESIS: “Mechanical strengthening of CFRP composite by introducing metal oxide nanostructures”**

**AUTHOR'S NAME & ADDRESS:** Ravi Shankar Rai & Kotwa narayanpur  
(Tulsi rai patti), Ballia, U.P- 277501

**COPYRIGHT TRANSFER**

1. The undersigned hereby assigns to Indian Institute of Technology (Indian School of Mines), Dhanbad all rights under copyright that may exist in and to:  
(a) the above Work, including any revised or expanded derivative works submitted to the ISM by the undersigned based on the work; and (b) any associated written or multimedia components or other enhancements accompanying the work.

**CONSENT AND RELEASE**

2. In the event the undersigned makes a presentation based upon the work at a conference hosted or sponsored in whole or in part by the IIT (ISM) Dhanbad, the undersigned, in consideration for his/her participation in the conference, hereby grants the ISM the unlimited, worldwide, irrevocable permission to use, distribute, publish, license, exhibit, record, digitize, broadcast, reproduce and archive; in any format or medium, whether now known or hereafter developed: (a) his/her presentation and comments at the conference; (b) any written materials or multimedia files used in connection with his/her presentation; and (c) any recorded interviews of him/her (collectively, the "Presentation"). The permission granted includes the transcription and reproduction of the Presentation for inclusion in products sold or distributed

by IIT(ISM) Dhanbad and live or recorded broadcast of the Presentation during or after the conference.

3. In connection with the permission granted in Section 2, the undersigned hereby grants IIT (ISM) Dhanbad the unlimited, worldwide, irrevocable right to use his/her name, picture, likeness, voice and biographical information as part of the advertisement, distribution and sale of products incorporating the Work or Presentation, and releases IIT (ISM) Dhanbad from any claim based on right of privacy or publicity.
4. The undersigned hereby warrants that the Work and Presentation (collectively, the "Materials") are original and that he/she is the author of the Materials. To the extent the Materials incorporate text passages, figures, data or other material from the works of others, the undersigned has obtained any necessary permissions. Where necessary, the undersigned has obtained all third party permissions and consents to grant the license above and has provided copies of such permissions and consents to IIT (ISM) Dhanbad.

#### **GENERAL TERMS**

- \* The undersigned represents that he/she has the power and authority to make and execute this assignment.
- \* The undersigned agrees to indemnify and hold harmless the IIT (ISM) Dhanbad from any damage or expense that may arise in the event of a breach of any of the warranties set forth above.
- \* In the event the above work is not accepted and published by the IIT (ISM) Dhanbad or is withdrawn by the author(s) before acceptance by the IIT(ISM) Dhanbad, the foregoing copyright transfer shall become null and void and all materials embodying the Work submitted to the IIT(ISM) Dhanbad will be destroyed.
- \* For jointly authored Works, all joint authors should sign, or one of the authors should sign as authorized agent for the others.



Signature of the Author

# Acknowledgments

I am very grateful to GOD ALMIGHTY without whose grace and blessings this study would not have been possible.

I extend my immeasurable appreciation and gratitude for the help and support I received from all the people who somehow contributed to making this study possible.

Foremost, I would like to express my sincere gratitude to my supervisor **Prof. Vivek Bajpai**, Associate professor, Department of Mechanical Engineering, for his valuable guidance, encouragement, immense support, and freedom throughout my Ph.D. His constant energy and immense enthusiasm for research always motivated me. Further, I would be thankful to him for providing excellent research facilities and resources throughout my work and for his willingness to spare time for clarifying my doubts and research discussion.

I wish to express my sincere thanks to **Prof. A. R. Dixit**, Chairperson of the Doctoral Scrutiny Committee (DSC), Associate Professor, Department of Mechanical Engineering, IIT (ISM), Dhanbad for his intimate inspiration and suggestions. I also wish to express my

sincere thanks to **Prof. N. K. Singh**, DSC Member, Associate Professor, Department of Mechanical Engineering, and **Prof. Chandan Guria**, Professor, Department of Petroleum Engineering, IIT (ISM) Dhanbad for their constant inspiration and thought-provoking suggestions. I also thank **Prof. Rajiv Shekhar**, Director, IIT (ISM) Dhanbad for providing all the necessary infrastructure and facilities for the research work during the period of study.

I would like to express my gratitude to **Prof. Nelson Muthu**, Assistant professor, Department of Mechanical Engineering, IIT Guwahati, India, for providing the facilities to perform drop-down impact testing of fabricated samples. Further, I would like to thank **Mr. Sanjib Sarma**, Sr. Technical Superintendent, Strength of materials lab, Department of Mechanical Engineering, IIT Guwahati, India, for support to perform the drop-down impact testing and analysis work. I also thank **Prof. Suresh Kumar Yatirajula**, Assistant professor, Department of Chemical Engineering, IIT (ISM) Dhanbad for providing their research facilities to conduct testing and analysis work.

I also thank all faculties and staff members in the Department of Mechanical Engineering, Central Workshop and Central Research Facility, IIT (ISM) who associated with me during this study, directly and indirectly, to support me during my Ph.D. work.

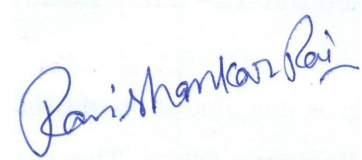
I individually thank all of my lab mates **Dr. Mohan Kumar, Dr. Rachit Ranjan, Dr. Shashank Shukla, Dr. Ankit Jain, Dr. Deepak Kumar, Arnab Das, Rajesh Sahoo, Abhipsa Kar** and **Prince Anand** for their continuous help and support during my research period.

I individually thank my seniors, dearest friends and juniors **Dr. Lukesh Kumar Mahato, Dr. Sawan Kumar, Dr. Vikash Kumar, Dr. Ramesh Kumar, Rohit Patel, Alok kumar, Ashutosh kumar, Sumit kumar, Abisoor, Deepti, Harsh Arora, Neeraj Lo-**



**hani, Dhruv, and Ankan Sarkar** who supported me and shared their knowledge with me on various aspects.

The dissertation would have been impossible without the support of my family. I express my deepest gratitude to my family- father **Shri. Jai Shankar Rai**, mother **Smt. Rupam Devi**, brothers **Girja Shankar Rai, Gouri Shankar Rai** and sister **Anupam Kumari** for their love and support throughout my life. Without their love, support, respect, and care, it is not possible to complete this journey. At last, I would like to thank everyone who directly or indirectly help me and associated with my thesis work.



Place: IIT ISM Dhanbad

Date: May 19, 2023

Ravi Shankar Rai

(17DR000647)



# Abstract

Modern high performance structures and systems must require the development of cutting edge low weight-to-strength materials. Considering that the constituents of composite materials can be altered to match the requirements of the advanced structural materials, they are an unquestionable choice in modern materials. To develop composites, which are exceptional materials, various elements are combined on a macro- to nano-scale. Therefore, in order to create composite materials, it is essential to comprehend distinct materials. There are two or more phases in this material out of which one serves the primary load-bearing component. The majority of the load applied to the material is carried by the stronger reinforcement, but the softer phase matrix has unique physical and mechanical characteristics. Fiber reinforced polymer composites (FRC) have a wide range of applications because of their exceptional strength and stiffness at low weight. Fiber and matrix are the two components that make up FRC and fibers can be artificially created or derived from natural resources like plants. Compared to natural fiber reinforced composites, synthetic fibers have excellent mechanical properties. One of the most significant reinforcement materials used in the creation of high performance FRC for crucial applications is carbon fiber. Due to their exceptional tensile strength, rigidity, low weight, and high heat resistance, carbon fiber reinforced composites (CFRP) have been gaining a lot of interest as

a new structural material. However, the interfacial bonding of untreated carbon fiber and resin matrix is poor, which impacts the promising performance of CFRP composite materials because to the substantial surface inertia of the carbon fiber, an inherent feature of the material. There are several potential processes for fiber/matrix adhesion include chemical bonding, adsorption, reaction bonding, wetting, electrostatic attraction, and exchange reaction bonding, however, promising performance characteristics for advance applications was not achieved by them. It is well known that, the shear stress is transferred between the carbon fiber and the polymer matrix through the interphase of CFRP composites. When the regional shear stress is greater than the CFRP composite's interfacial shear strength, debonding of the carbon fiber from the matrix will occur, which results in composite failure. Impact strength is a fascinating feature of CFRP composites which allows CFRP to be used in advanced applications where high stiffness and damage resistance is required. Regardless, plain carbon fiber strengthened polymer composites are exceptionally brittle; their low energy absorption capacity implies poor behavior under impact loading. Thus, woven carbon fibers are used for an elective reinforcement for polymer based composites because WCFs have cross-weaved design which gives good out-of-plane resistance, strength and durability. Further, the development of hybrid composites where more than one reinforcement media such as CNT, graphene and other nanostructures can be used for high performance CFRP composites. Dispersion of CNT, graphene and nanoparticles is the major concern of fabrication of hybrid composites. Therefore, developing nanostructures such as ZnO, CuO directly onto fiber surfaces is a successful strategy to improve fiber surface region, mechanical interlocking, and local softening at the interface, all of which may improve load exchange and interfacial properties of the CFRP composites. The performance of CFRP composites are majorly illustrated by the performance of their interphase. Despite of that, fiber cleavage in the interfacial region of the composites restrict the use of CFRP composites for high impact applications. The final performance of the

developed composites are majorly illustrated by the performance of their interphase. The interface between both the reinforcement primary and secondary with the polymeric matrix has been a subject of incredible interest. The idea of the interface has been seemed, by all accounts, to be a significant factor in an extensive part of the structure's mass properties. In like manner, various discernible masters have investigated procedures for improving the interface of present day composite materials. Different techniques for altering the surface of carbon fiber are attracting a lot of interest because they can increase the performance of composites. These techniques essentially consist of surface functionalization, surface roughening, surface whiskerization and creating secondary interphase. Thus, an exclusive approach required to be devised which can enhance the mechanical properties of CFRP composites for advanced applications. It is noted from the literature that fabricating a secondary interphase between the fiber and polymer matrix can be a successful way to raise the interfacial shear stress since the new interphase can boost adhesion, enhance load transmission, and expand the interfacial contact area. The sizing of fibers and fabrication of metal-oxide nanostructures (NSs) on fibers are the most suitable way to develop nanostructured interphase in the CFRP composites. It is estimated that this study will develop nanostructured CFRP composites for advanced applications such as structural, electronics and military with excellent mechanical performance.

The growth of metal oxide nanostructures on woven carbon fiber to minimize failure of CFRP composites under impact loading is not explored so far. The synthesis of well aligned ZnO nanorods on WCF strands using an economical seed-assisted hydrothermal strategy is not explored in an effective manner. The synthesis of metal-oxide nanostructures on different substrate using varied synthesis techniques is already present in literatures, however, this study is novel in terms as it introduced an easy practical approach to develop high performance metal-oxide nanostructured CFRP composites for advanced applications. The study of different factors affecting the performance of nanostructures and

their resulting composites are investigated using different physical and mechanical characterization techniques. Additionally, the effect of ZnO and CuO concentration on thermal stability and weight loss pattern on carbon fiber samples have been analyzed. The formation of secondary interphase between the fiber and polymer matrix can be achieved by synthesis of ZnO NSs on woven carbon fiber (WCF) by hydrothermal technique under varying conditions of the process parameters. The impact of process parameters such as pH and molar concentration of precursor solution, growth duration and growth temperature on morphology and dimensions of ZnO NSs has been investigated to propose favorable synthesis parameters for effective growth of NSs. Further, the rapid growth of ZnO NSs on WCF surface was achieved by combining microwave heating with an aqueous process known as the "microwave assisted chemical bath deposition approach." The study of different process parameters such as molar concentration, microwave duration, microwave power and growth solution were investigated to achieve optimum growth of ZnO NSs on WCF surface. In this study different morphologies of ZnO on WCF strands such as nanowires, hexagonal nanorods, nanoflakes, nanopallets, and nanoflowers were grown by tuning the hydrothermal and microwave process parameters. The findings of experimental outcomes are verified using different characterization techniques such as field emission gun-scanning electron microscope, energy dispersive spectroscopy, % weight change study, X-ray diffraction study, Fourier transform infrared spectroscopy, UV-VIS-NIR spectroscopy and others. The ZnO-modified WCF is used as reinforcement in the bisphenol-A epoxy resin and dimethyl aniline hardener as a polymer matrix for developing hybrid composites. The mechanical attributes of developed hybrid composites such as tensile strength, elastic modulus, in-plane shear, and impact resistance improved dramatically.

Further, other metal-oxide NSs such as copper-oxide NSs were grown on WCF using hydrothermal technique to produce a nanostructured interphase that increased the interfacial strength with an epoxy resin matrix. The outcomes demonstrate a considerable improve-

ment in impact energy absorption, elastic modulus, tensile strength and in-plane shear strength of the CuO-coated CFRP composites. In comparison to plain carbon fiber epoxy resin composites, the tensile strength, elastic modulus, and in-plane shear strength of ZnO-modified carbon fiber composites improved by up to 48.63 %, 46.44 %, and 20.79 %, respectively, while the impact energy absorption increased by 76 %. However, for the CuO nanostructured CFRP composite, 74.8 % increase in impact energy absorption, 42 % increase in tensile strength, 52 % increase in elastic modulus, and 32 % increase of in-plane shear strength were achieved. Thus, it can be concluded that the improved interfacial contact between the surface-functionalized WCF, metal-oxides, and BPA epoxy resin increased the mechanical and thermal properties of the composites, expanding their application range. The current research is important to the industries such as automobiles, electronics and aircraft industry because they used carbon fiber based advanced materials having strong interfacial strength and impact strength. In addition, incorporating metal-oxides such as ZnO and CuO in CFRP composites exhibit improved mechanical properties along with optoelectronic properties which is desirable for producing high strength electronic components. Furthermore, the developed hybrid composites samples are best suited for aircraft and automobile industries due to high impact strength and high modulus at light weight. Thus, the developed hybrid composites samples can be proposed as good replacement to the plain carbon fiber reinforced polymer composites for various applications due to high mechanical properties at low cost and less experimental setup. As synthesized metal-oxides NSs such as ZnO and CuO on WCF surface have its own superiority in terms of composite properties. The percentage increase in impact energy absorption, tensile strength and TGA thermal degradation pattern (weight loss) of ZnO nanostructured CFRP composites are better than the CuO nanostructured CFRP composites. Nevertheless, the elastic modulus and in-plane shear strength of CuO nanostructured CFRP composites are higher in comparison to ZnO nanostructured CFRP composites. Hence, both the metal-

oxide nanostructures can be used for the enhancement of mechanical and thermal properties of CFRP composites based on the requirement. However, the growth phenomenon and required process parameters for the CuO NSs have negative impacts in terms of large seeding cycles, high growth duration and high temperature. However, the occurrence of agglomeration in CuO NSs on WCF was higher, due to which the vertically aligned nanostructures were not grown. On analyzing each factors of both the nanostructured CFRP composites, the ZnO nanostructured CFRP composites are better in terms of ease of synthesis, less time consuming, high impact energy absorption capacity, high thermal stability, high tensile strength and moderate impact energy absorption. Thus, the developed metal-oxide nanostructured hybrid CFRP composites can be used as the promising composite material for various applications due to high impact strength and high modulus at light weight.



# List of Symbols and Abbreviations

$S_c$	Number of seed cycles
$C_g$	Concentration of growth solution
$T_g$	Total duration of growth treatment
$O_e$	Outcomes of the experiment
$N_g$	No growth
$A_g$	Agglomerated growth
$L_g$	Little growth
$M_g$	Moderate growth
$F_g$	Fine growth
$U_g$	Ultra-fine growth
mM	millimole
ZnO	Zinc-oxide
CuO	Copper-oxide
NPs	Nanoparticles
NSs	Nanostructures
NRs	Nanorods
CF	Carbon fiber
WCF	Woven carbon fiber

CNT	Carbon nanotube
CNF	Carbon nanofiber
CVD	Chemical vapour deposition
FRP	Fiber reinforced plastics
FRC	Fiber reinforced polymer composites
CFRP	Carbon fiber reinforced polymer composites
HMTA	Hexa-methyl-tetra-amine
BPA	Bisphenol-A
FESEM	Field emission scanning electron microscopy
EDS	Energy dispersive spectroscopy
XRD	X-ray diffraction
FWHM	Full-width at half-maximum
W-H	Williamson hall
FTIR	Fourier transform infrared spectroscopy
XPS	X-ray photoelectron spectroscopy
TGA	Thermo gravimetric analysis
TEM	Transmission electron spectroscopy
PL	Photo-luminescence spectroscopy
UTM	Universal testing machine
ILSS	Inter-laminar shear strength
IFSS	Interfacial shear stress

# Contents

<b>Acknowledgments</b>	<b>vii</b>
<b>Abstract</b>	<b>xi</b>
<b>Nomenclature</b>	<b>xvii</b>
<b>List of Figures</b>	<b>xxv</b>
<b>List of Tables</b>	<b>xxxii</b>
<b>1 Introduction</b>	<b>1</b>
1.1 Background . . . . .	1
1.2 Carbon fiber reinforced polymer composites . . . . .	4
1.3 Multiscale hybrid composites . . . . .	5
1.4 Nanostructured CFRP composites . . . . .	6
1.5 Need of interfacial treatments of CFRP . . . . .	8
1.6 Interfacial treatment by fiber modifications . . . . .	9
1.6.1 Surface functionalization and roughening . . . . .	9
1.6.2 Surface whiskerization . . . . .	10
1.6.3 Fabrication of secondary interphase . . . . .	10
1.7 Metal-oxide nanostructures . . . . .	11
1.7.1 Zinc-oxide . . . . .	12
1.7.2 Copper-oxide . . . . .	13
1.8 Need and scope of work . . . . .	13
1.9 Problem definition . . . . .	16
1.10 Aim and objectives . . . . .	17
1.11 Research novelty and originality . . . . .	17

---

1.12	Industrial importance . . . . .	18
1.13	Organization of presented report . . . . .	18
<b>2</b>	<b>Literature Review</b>	<b>21</b>
2.1	Introduction . . . . .	22
2.2	Recent advancements in carbon fiber reinforced polymer composites . . . . .	22
2.3	Recent advances in ZnO NSs . . . . .	24
2.4	Synthesis techniques of metal-oxide NSs . . . . .	25
2.4.1	Green synthesis . . . . .	25
2.4.2	Solution phase synthesis . . . . .	26
2.4.3	Gas phase synthesis . . . . .	27
2.5	Hydrothermal synthesis of ZnO NSs . . . . .	27
2.6	Morphological variations of ZnO NSs . . . . .	30
2.6.1	Nanoparticles . . . . .	30
2.6.2	Nanorods and Nanowires . . . . .	31
2.6.3	Blossoms and cabbage-like NSs . . . . .	35
2.6.4	Miscellaneous shapes . . . . .	38
2.7	Microwave assisted hydrothermal synthesis . . . . .	40
2.8	Doping in metal-oxide NSs . . . . .	42
2.9	Potential applications of metal-oxide NSs . . . . .	43
2.9.1	Photocatalysis . . . . .	43
2.9.2	Field emission . . . . .	45
2.9.3	Sensors . . . . .	45
2.9.4	Lithium ion batteries . . . . .	45
2.9.5	Antibacterial application . . . . .	46
2.9.6	Supercapacitors . . . . .	46
2.9.7	High performance composite materials . . . . .	47
2.10	Current research situation and challenges for ZnO nanostructured materials . . . . .	48
2.11	Modification strategies of ZnO nanomaterials . . . . .	50
2.12	Summary of Literature survey . . . . .	52
2.13	Research gap . . . . .	56
<b>3</b>	<b>Hydrothermal Growth of ZnO nanostructures on woven carbon fiber and effect of synthesis parameters on morphology</b>	<b>57</b>
3.1	Introduction . . . . .	58

---

3.2	Synthesis details . . . . .	60
3.2.1	Materials used . . . . .	60
3.2.2	Hydrothermal synthesis . . . . .	60
3.3	Results and Discussion . . . . .	63
3.3.1	Impact of seeding and growth phenomenon . . . . .	63
3.3.2	Impact of molar concentration . . . . .	64
3.3.3	Impact of pH on synthesis of ZnO NSs . . . . .	64
3.3.4	Impact of the Growth duration . . . . .	67
3.3.5	Impact of processing Temperature . . . . .	69
3.3.6	UV-VIS-NIR spectroscopy study . . . . .	71
3.4	Summary . . . . .	73
<b>4</b>	<b>One-step microwave-assisted hydrothermal synthesis of ZnO nanostructures on WCF and their characterization</b>	<b>75</b>
4.1	Introduction . . . . .	76
4.2	Materials and methodology . . . . .	78
4.2.1	Materials . . . . .	78
4.2.2	Preparation of growth solutions . . . . .	78
4.2.3	Surface functionalization of WCF . . . . .	79
4.2.4	Microwave synthesis of ZnO nanostructures on WCF . . . . .	79
4.2.5	Characterizations . . . . .	81
4.3	Result and discussion . . . . .	81
4.3.1	Morphological characterization of as grown ZnO NSs on WCF . . . . .	81
4.3.1.1	Influence of varying molar concentration . . . . .	81
4.3.1.2	Influence of microwave heating duration . . . . .	83
4.3.1.3	Influence of microwave power . . . . .	83
4.3.1.4	Influence of variety of growth solution . . . . .	86
4.3.2	Structural characterization of grown ZnO NSs . . . . .	88
4.3.3	Optical characterization of ZnO NSs grown on WCF . . . . .	91
4.3.3.1	Determination of the band gap value and Urbach energy . . . . .	93
4.3.3.2	Study of refractive index and dielectric constants of grown ZnO NSs on WCF . . . . .	95
4.3.3.3	Optical conductivity . . . . .	97
4.4	Summary . . . . .	99

---

<b>5</b>	<b>Development of ZnO-modified WCF reinforced epoxy resin composites and their mechanical characterizations</b>	<b>101</b>
5.1	Introduction . . . . .	102
5.2	Experimental . . . . .	104
5.2.1	Materials used . . . . .	104
5.2.2	Surface treatment of WCF . . . . .	104
5.2.3	Preparation of ZnO seed and growth solutions . . . . .	105
5.2.4	Preparation of ZnO/WCF/BPA epoxy resin composites . . . . .	106
5.2.5	Impact and tensile testing . . . . .	107
5.3	Results and discussion . . . . .	108
5.3.1	Morphological characterization of as grown ZnO NSs on WCF . . . . .	108
5.3.1.1	ZnO nanowire growth . . . . .	110
5.3.1.2	Effect of Seed treatment and growth treatment . . . . .	111
5.3.2	Compositional study of ZnO/WCF samples . . . . .	111
5.3.3	Structural characterization of grown ZnO NSs . . . . .	112
5.3.4	Optical characterization of ZnO NSs grown on WCF . . . . .	114
5.3.5	Fourier-transform infrared spectroscopy . . . . .	115
5.3.6	Study of thermal stability and weight change . . . . .	117
5.4	Volume fraction and void analysis of the composites . . . . .	118
5.5	Mechanical characterization of fabricated hybrid composites . . . . .	121
5.5.1	Drop weight impact test . . . . .	122
5.5.1.1	Energy–time response . . . . .	125
5.5.2	Tensile and In-plane shear strength . . . . .	126
5.6	Summary . . . . .	128
<b>6</b>	<b>Improvement of interfacial adhesion of CuO nanostructured carbon fiber reinforced polymer composites</b>	<b>131</b>
6.1	Introduction . . . . .	132
6.2	Materials and methods . . . . .	136
6.2.1	Materials . . . . .	136
6.2.2	Synthesis of reaction mixtures for hydrothermal treatment . . . . .	136
6.2.3	Preprocessing of carbon fiber fabric sample . . . . .	137
6.2.4	Formation of CuO nanostructures on WCF . . . . .	138
6.2.5	Fabrication of CuO/WCF/Epoxy hybrid composites . . . . .	139
6.2.6	Characterizations . . . . .	140

6.3	Results and discussion . . . . .	142
6.3.1	Morphological study and growth chemistry of CuO . . . . .	142
6.3.1.1	Structural and crystallographic analyses of CuO/WCF samples . . . . .	144
6.3.2	Compositional analysis of as fabricated CuO nanostructures on WCF	147
6.3.3	Impact of process parameters on dimensions of CuO nanostructures	149
6.3.4	Weight loss study of CuO by TGA thermograms . . . . .	150
6.3.5	Fourier-transform infrared spectroscopy . . . . .	151
6.3.6	X-ray photoelectron spectroscopy (XPS) analysis . . . . .	153
6.4	Volume fraction and void analysis of the composites . . . . .	156
6.5	Mechanical characterization of fabricated hybrid composites . . . . .	159
6.5.1	Drop weight impact test . . . . .	160
6.5.1.1	Impact energy absorption . . . . .	161
6.5.1.2	Energy Vs time response of impacted samples . . . . .	163
6.5.1.3	Fractured surface topography . . . . .	165
6.5.2	Tensile and In-plane shear strength . . . . .	166
6.6	Comparison on the effect of ZnO and CuO nanostructures . . . . .	170
6.7	Summary . . . . .	171
<b>7</b>	<b>Conclusion and Future Scope</b>	<b>173</b>
7.1	The key conclusion of the thesis . . . . .	174
7.1.1	Hydrothermal Growth of ZnO nanostructures on woven carbon fiber and effect of synthesis parameters on morphology . . . . .	174
7.1.2	One-step microwave-assisted hydrothermal synthesis of ZnO nanostructures on WCF and their characterization . . . . .	175
7.1.3	Development of ZnO-modified WCF reinforced epoxy resin composites and their mechanical characterizations . . . . .	176
7.1.4	Improvement of interfacial adhesion of CuO nanostructured carbon fiber reinforced polymer composites . . . . .	177
7.2	Contribution . . . . .	178
7.3	Future Work . . . . .	180
	<b>References</b>	<b>181</b>
	<b>List of Publications</b>	<b>227</b>





# List of Figures

1.1	Classes of composite materials . . . . .	2
1.2	Market shares of Fiber reinforced polymer composites . . . . .	3
1.3	Techniques for development of nanostructured fiber reinforced polymer composites . . . . .	8
1.4	(a) Wurtzite structure of ZnO showing lattice parameters and (b) tetrahedral coordination of ZnO [1] . . . . .	13
2.1	(a) SEM image of ZnO nanoparticles (Aqueous solution method), (b) SEM image of ZnO nanoparticles (sol-gel method), (c) SEM image of zinc oxide nanoparticles (hydrothermal method) [2] . . . . .	32
2.2	SEM image of ZnO nanowires (a) Growth of length (b) with no seeds (c) with seeds after polymer removal (d) without polymer removal and (e) with polymer removal after seed nanoparticle deposition [3] . . . . .	33
2.3	XRD results of (a) needle-like (b) plate-like ZnO NSs . . . . .	35
2.4	SEM images of the surface morphology of both (a–c) ZnO and (d–f) ZnO/CuO structures as a function of ZnO synthesis time . . . . .	37
2.5	SEM analysis of dumbbell-shaped ZnO at various magnifications: (a) and (b) low magnification; (c) and (d) high magnification [4] . . . . .	39
2.6	(a) SEM image of ZnO NSs; (b) twinned flower-like ZnO; (c) hexagonal nut structure . . . . .	40
2.7	Impact of $[Zn^{2+}]$ on grown ZnO NSs (a) 0.01, (b) 0.02, (c) 0.04 and (d) 0.06 M [5] . . . . .	41
2.8	Utilization range of ZnO nanostructured materials . . . . .	44
2.9	Major fields for utilization of ZnO photocatalyst . . . . .	44
2.10	Current research situation and challenges for ZnO materials . . . . .	49
2.11	Strategies to modify ZnO nanomaterials for better outcomes . . . . .	51

3.1	Schematic representation of growth mechanism of ZnO NSs . . . . .	62
3.2	FESEM images: (a) seeding; (b) growth phenomenon of ZnO NSs . . . . .	63
3.3	FESEM images of ZnO NSs on WCF at varied molar concentrations: (a) 10mM; (b) 30mM; (c) 50mM; (d) 70mM . . . . .	65
3.4	EDS spectra of ZnO NSs at different molar concentrations: (a) 10mM; (b) 30mM; (c) 50mM; (d) 70mM . . . . .	66
3.5	Effect of molar concentration on height and diameter of the ZnO NSs . . . . .	66
3.6	Variation in pH value of the solution in 4h growth duration . . . . .	67
3.7	The grown ZnO NSs under processing condition of 90°C, 4h, 6.5pH and 10mM . . . . .	68
3.8	ZnO NSs on WCF having pH of precursor solution (a) at 2.5, (b) at 4.5 (c) at 6.5 and (d) at 8.5 . . . . .	69
3.9	ZnO NSs on WCF at 90°C and at growth duration:(a) 2 h, (b) 4 h, (c) 6 h, (d) 8 h and (e) 10 h . . . . .	70
3.10	Effect of processing time on the dimensions (diameter and height) of ZnO NSs . . . . .	70
3.11	ZnO NSs on WCF for 4 h and 10 mM solution at temperatures: (a) 50°C, (b) 70°C, (c) 90°C and (d) 110°C . . . . .	71
3.12	Effect of growth temperature on the aspect ratio on ZnO NSs . . . . .	72
3.13	UV-VIS-NIR absorbance graph of ZnO NSs grafted on WCF samples . . . . .	73
4.1	Stepwise procedure to fabricate ZnO NSs on WCF using microwave-assisted chemical bath deposition . . . . .	81
4.2	FESEM results of as grown ZnO NSs on WCF by microwave heating under varying molar concentration (a) 10 mM (b) 30 mM (c) 50 mM and (d) 70 mM . . . . .	82
4.3	FESEM results of as grown ZnO NSs on WCF by microwave heating under different microwave duration (a) 5 minutes (b) 10 minutes (c) 15 minutes and (d) 20 minutes . . . . .	84
4.4	FESEM results of as grown ZnO NSs on WCF by microwave heating under different microwave power (a) 250 W (b) 500 W (c) 750 W and (d) 1000 W . . . . .	85
4.5	FESEM results of as grown ZnO NSs on WCF by microwave irradiation under different precursor solutions (a) nanopetals (b) twinned nanospheres (c) nanoflowers and (d) nanoflakes . . . . .	87

4.6	(i) EDS spectra and (ii) Size distribution of ZnO NSs under different precursor solutions . . . . .	87
4.7	(i) XRD spectra and (ii) Williamson Hall graph of as grown ZnO NSs on WCF sample . . . . .	89
4.8	Optical absorbance of ZnO NSs grown on WCF . . . . .	91
4.9	Optical transmittance of ZnO NSs grown on WCF . . . . .	92
4.10	Optical reflectance of ZnO NSs grown on WCF . . . . .	93
4.11	(i) Tauc's plot of grown ZnO NSs and (b) Band gap calculation by linear fitting of Tauc's plot . . . . .	94
4.12	Urbach energy of ZnO NSs grown on WCF . . . . .	95
4.13	Variation of (i) refractive index and (ii) extinction coefficient of grown ZnO NSs with wavelength . . . . .	96
4.14	Variation of (i) real part and (ii) imaginary part of dielectric function of ZnO NSs with wavelength . . . . .	98
4.15	Optical conductivity variation with wavelength for grown ZnO on WCF . . . . .	99
5.1	Hydrothermal development of ZnO-modified WCF polymer composites . . . . .	107
5.2	Hydrothermal development of ZnO-modified WCF polymer composites . . . . .	110
5.3	Growth of ZnO NSs on WCF (a) through 8 seeding cycle treatment only, (b) through 8h of growth treatment and (C) combined seeding followed by growth treatment . . . . .	112
5.4	EDS spectra of ZnO-modified WCF (a) 10 mM (b) 30 mM (c) 50 mM and (d) 70 mM . . . . .	113
5.5	(a) XRD peaks and (b) Williamson-Hall plot of as grown ZnO NSs on WCF . . . . .	113
5.6	(a) Optical transmittance spectra, (b) Tauc's plot and (c) linear fit ZnO band gap of as grown ZnO on WCF . . . . .	115
5.7	FT-IR spectroscopy spectra of ZnO-modified WCF samples . . . . .	116
5.8	(a) Thermogravimetric degradation and (b) weight loss pattern of ZnO-WCF samples . . . . .	117
5.9	(a) Set up for drop weight impact tester, (b) Impact data acquisition system and (c) Fabricated impact test samples . . . . .	123
5.10	(a) Impact energy absorption, (b) fracture surface topography and (c) energy-time response of composite samples . . . . .	124
5.11	EDS graph with compositional details at the fracture regime . . . . .	125

5.12 (a) Stress-strain characteristics and variation of (b) tensile strength, (c) elastic modulus and (d) in-plane shear strength of composite samples . . .	127
6.1 Surface modification of plain WCF by CuO nanowires . . . . .	132
6.2 Surface whiskerization of carbon fiber using CuO nanostructures . . . . .	134
6.3 Surface treatment of woven carbon fiber by CuO nanostructure deposition	138
6.4 Hydrothermal approach for development of CuO nanostructured-WCF and their hierarchical composites by vacuum bagging method . . . . .	140
6.5 Effect of hydrothermal treatment on WCF in (a) seed solution only, (b) growth solution only and (c) seed-assisted growth treatment . . . . .	144
6.6 Unsuccessful growth of CuO nanostructures on woven carbon fibers showing no-growth, agglomerated-growth, little-growth, moderate-growth and fine-growth . . . . .	145
6.7 Ultrafine growth of CuO nanostructures on WCF corresponding to 8 number of seeding cycles and 12 h of growth treatment having different molar concentration of (a) 10 mM, (b) 15 mM, (c) 25 mM, (d) 35 mM, (e) 45 mM and (f) 60 mM . . . . .	145
6.8 (a) XRD spectra and (b) Williamson Hall graph of as grown CuO nanostructures . . . . .	146
6.9 Elemental composition of CuO nanostructures . . . . .	148
6.10 Elemental mapping of the CuO nanostructures grown on WCF strands . .	149
6.11 Dimensional variation of as grown CuO nanostructures (a) under varied morphologies and (b) under varied molar concentrations . . . . .	150
6.12 (a) Thermogravimetric degradation pattern and (b) weight loss evaluation of WCF before and after CuO growth . . . . .	151
6.13 FT-IR spectroscopy spectra of plain WCF and CuO-modified WCF . . . .	152
6.14 (a) XPS survey scan for the grown CuO nanostructures on WCF, high resolution XPS spectrum of as synthesized CuO-modified WCFs for (b) Cu 2p and (c) O 1s regions . . . . .	154
6.15 Drop weight impact tester along with data collection system and fabricated samples . . . . .	161
6.16 Absorbed impact energy of impact test samples . . . . .	162
6.17 Variation of absorbed impact energy of samples as a function of time . . .	163
6.18 Investigation of load-deflection response of composites under impact loading	164

---

6.19	Fracture surface topography showing different fracture mechanism and interfacial interaction under impact loading . . . . .	166
6.20	(a) Micro-universal testing machine set up used for tensile testing, (b) enlarged view of gripped specimen and location of extensometer, (c) schematic representation of load direction and gauge length and (d) fractured specimen after tensile loading . . . . .	167
6.21	Variation of (a) Tensile strength, (b) Elastic modulus and (c) In-plane shear strength values of composite samples . . . . .	168
6.22	Stress-strain plot of the WCF/BPA and WCF/CuO/BPA epoxy resin composite . . . . .	169



# List of Tables

2.1	ZAH derived precursors groups with their Partial charge distribution $\delta_i$ in based on H-L model based estimations using Allred-Rochow electronegativity ( $\chi_0 = 3.5, \chi_c = 2.5, \chi_H = 2.1, \chi_{Zn} = 1.66$ ); where, $EtO = OC_2H_5$ ligands, $\chi_m$ = mean electronegativity . . . . .	30
2.2	Application area of Polymer based Nanocomposites . . . . .	48
2.3	Summary of findings of major research works done till date . . . . .	55
3.1	List of chemicals used in the process . . . . .	60
4.1	Process parameters used for synthesis on ZnO NSs . . . . .	80
4.2	Growth conditions and properties of as grown ZnO NSs on WCF . . . . .	90
4.3	Details of texture coefficient of ZnO/WCF samples . . . . .	90
5.1	Properties of Woven carbon fiber . . . . .	104
5.2	List of chemicals precursors . . . . .	105
5.3	Design of hydrothermal experiments and their findings . . . . .	109
5.4	Design of hydrothermal experiments and their findings . . . . .	118
5.5	Design of hydrothermal experiments and their findings . . . . .	120
5.6	Fabricated ZnO/WCF/BPA epoxy composite samples for mechanical characterizations . . . . .	121
6.1	Selected process parameters and their levels for full-factorial experimental design . . . . .	142
6.2	Findings of hydrothermal growth of CuO nanostructures on WCFs . . . . .	155
6.3	Study of CuO volume fraction and void content of fabricated composites . . . . .	159
6.4	Fabricated ZnO/WCF/BPA epoxy composite samples for mechanical characterizations . . . . .	160

- 6.5 Average, standard deviation, and coefficient of variance of each test results 170
- 6.6 Properties of as fabricated ZnO and CuO nanostructured CFRP composites 171



# 1

## Introduction

This chapter gives a brief introduction about the basics of carbon fiber reinforced polymer composites, research background and motivation of issues relevant to interfacial interaction of the composites with an emphasis to enhance it to a maximum extent for tailored properties. Further, it also covers the aims and objectives, scope, and organization of the thesis.

### **1.1 Background**

The future advancement of higher execution structures and frameworks depends intensely upon the work of more up to date, low weight-to-performance materials. In advanced materials, composite materials are an undeniable decision in light of the fact that the constituents can be modified to meet the structure's solicitations. Composites are created by combining several elements on a macro- to nano-scale to produce superior materials. Therefore, it is crucial to have an understanding of various materials in order to construct composite materials. Composites have two or more phases, one of which serves as the main load-bearing element. The stronger reinforcement carries the majority of the load placed on the material, but the softer phase matrix has particular mechanical and physical qualities.

According to the reinforcing and matrix materials employed, composites can be divided into several categories, as shown in Fig. 1.1. The performance of the composite is determined by the matrix and reinforcements combined, which is further influenced by the morphology, particle interface, bonding between the components, and distribution of the reinforcement.

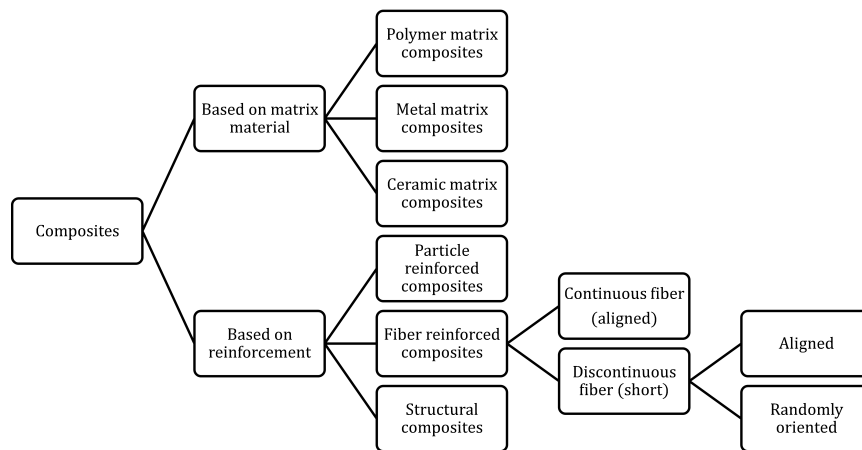


Figure 1.1: Classes of composite materials

High strength, light weight, and better mechanical or electronic capabilities are the benefits of composite materials, which can be micro, nano, polymer, or metal matrix composites. Other kinds of matrix materials, frequently metals, are necessary because final parts must be able to operate at temperatures high enough to melt or degrade a polymer matrix. In addition to high-temperature resistance, metal matrices also have strength and ductility, or "bendability," which boosts toughness. Even the lightest metals in metal-matrix composites are heavier than polymers, and processing these materials is extremely difficult. The skin of a hypersonic aircraft can be made of metal-matrix composites, although temperatures on the wing edges and in the engines frequently exceed the melting point of metals. Ceramic-matrix composites are being used more frequently for these latter applications, despite the fact that their technology is still in its infancy compared to polymer matrix composites. Alumina, silica, zirconia, and other elements purified from fine sand and soil or extracted compounds like silicon nitride or silicon carbide make up ceramics. Superior heat resistance and low abrasive and corrosive characteristics are two of ceramics'

attractive qualities. Brittleness is its main flaw, which can be remedied by adding fibers or whiskers. Metal or another type of ceramic might be used as the reinforcing material.

Specifically, a consistent fiber polymer matrix composite offers high quality to weight, high durability to weight, and design flexibility to coordinate the composites to the auxiliary requests. A fiber of business and scholarly interest is the aramid category of strands (Kevlar and Twaron) in grounds that the extremely crystalline structure overtures a stand-out amongst the most astounding specific strength extents and the specific nature of normal, economically accessible filaments [6]. Lately, strengthened plastics are likewise settled to be all around drafted for building and development, notwithstanding transport and electronic applications. A portion of the real application territories of Fiber Reinforced Plastics (FRP) in transportation are automobile, flight, delivery and other related segments. In the vitality/electronic division, FRP are utilized for the creation of high voltage switches, cryostats, dry transformers and many more. Of late, carbon fiber reinforced polymers are additionally utilized for cutting edge specialized applications, for example, in rocket spouts. The pie outline shown in Fig. 1.2 gives a brief picture of market shares of FRPs in different application territories [7]. In the present market, there has been a snappy im-

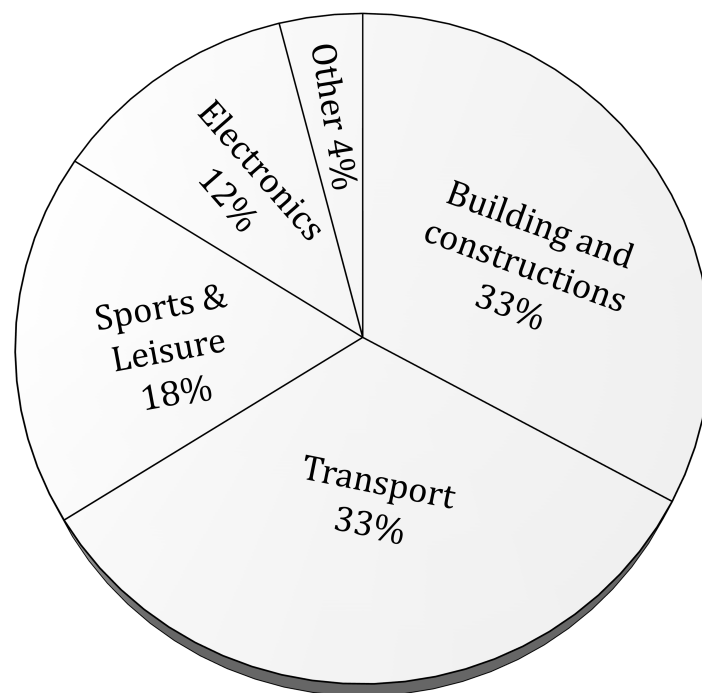


Figure 1.2: Market shares of Fiber reinforced polymer composites [7]

provement in research and headway in the field of Natural fiber composite (NFC). On account of the advantages of these materials appeared differently in relation to others, for instance, engineered fiber composites, including low environmental impact and simplicity and support their power over a broad assortment of utilization [8]. Fiber reinforced polymer composites are utilized as a part of numerous modern applications in light of their extreme specific strength and firmness. Carbon fibers (CFs) are extensively used as a piece of polymer composites to upgrade the quality and strength-to-weight extents and along these lines give enhanced mechanical properties at low densities [9]. Carbon fiber (CF) is an extraordinary material to the extent that the material properties navigate a broad assortment of thermo-physical properties that can be handcrafted to the coveted application, considering a massive extent of material properties. Carbon fiber composites are as of now utilized as a part of the avionics, amusements, automobiles, sports, musical instruments, marine, and wind energy zones. The overall carbon fiber feature accomplished 1.98B dollars in 2014, while the carbon fiber composite market (counting all system materials) accomplished 16.6B dollars in 2014. Figures predict the carbon fiber and carbon fiber composite markets will expand to 4.3B dollars and 33.6B dollars in 2021, separately. Such a significant increase can be credited to the expansion in aeronautics and other markets. Overall carbon fiber ask is to increase from 58,000 tonnes in 2015 to more than 100,000 tonnes by 2020 [10].

## **1.2 Carbon fiber reinforced polymer composites**

Fiber reinforced polymer composites (FRC) have a wide range of applications because of their exceptional strength and stiffness and low weight [11]. Fiber and matrix are the two components that make up FRC. Fibers can be artificially created or derived from natural resources like plants. Compared to natural fiber reinforced composites, synthetic fibers have excellent mechanical properties. However constraints of synthetic fibers stem from their inability to degrade raises issues for the government and researchers regarding disposal, recycling, and environmental impact. One of the most significant reinforcement materials used in the creation of high performance FRC for crucial applications is carbon fiber [11, 12]. Due to their exceptional tensile strength, rigidity, low weight, and high heat resistance, carbon fiber reinforced composites (CFRP) have been gaining a lot of interest as a new structural material [13, 14]. However, the interfacial bonding of untreated carbon fiber and resin matrix is poor, which impacts the promising performance of carbon fiber reinforced composite materials because to the substantial surface inertia of the carbon fiber,

an inherent feature of the material [15, 16, 17]. The out of plane properties of the composite laminates are primarily controlled by the matrix and matrix-fiber interface/interphase [18, 19]. The many potential processes for fiber/matrix adhesion include chemical bonding, adsorption, reaction bonding, wetting, electrostatic attraction, and exchange reaction bonding [20].

The weaker out of plane response of CFRP composites prevents them from being used to their full potential in many crucial engineering applications such as aircraft wings, air-frame structures, bulletproof armors and automobiles front panels [19, 21, 22].

Woven carbon fiber (WCF) composite materials are getting more enthusiasm for some territories of building because of simplicity of make (notwithstanding for parts with intricate designs) and simplicity of orientation enabling researchers to fix optimum level of strength and stiffness. Thus, woven fiber composites are frequently less expensive than different kinds of composites. Be that as it may, the fiber structure can prompt "unexpected" delaminations, interlaminar stresses and cracks [23]. A few works have been directed on woven composite materials. Vieille et al. [24] strengthened polyether ether ketone, polyphenylene sulfide and epoxy independently with WCF to examine the impacts of the polymer lattice on the fracture mechanism under low speed affect. The outcome of the investigation is that the lattice greatly influences the intra-ply harm and delamination with a harder framework giving high impact execution. The 3D WCF composite is a spatial net-shape surface, framed by interweaving confining strings in the thickness going to join layers of twist and weft together, and cured with system under certain condition. The obtained material have tailored properties such as high resilience, low manufacturing cost and high impact resistance than plain WCF composites [25]. In this way, 3D WCF composites have been extensively utilized as a part of aviation, vehicle, marine, and defense. Most researches create the quality of woven composite materials with impact and interlaminar stresses. However, a couple of numerical investigations utilizing representative volume elements have been performed to decide the elastic modulus.

### **1.3 Multiscale hybrid composites**

Polymer composites fortified with nanomaterial are picking up an exceptional consideration because of their remarkable enhancements in properties, like strength, elastic modulus, impact, out-of-plane stiffness, and toughness [26, 27]. Various authors have officially utilized carbon filaments, glass strands, cellulose filaments, and whiskers for enhancement in the field of composites [28, 29]. Albeit distinctive sorts of CNT, graphene oxides, and

distinctive filling elements are also extensively used to overhaul the quality of a polymer network, for every circumstance, the qualities have not upgraded to the coveted level. To be a productive reinforcement, the filler materials must have a huge aspect ratio, great arrangement, and sufficient dispersion in the polymer network [30]. Without the closeness of these parameters, the composite may not fulfill the needs of end applications [31]. More strikingly, interface of the fiber network is moreover also basic in choosing the general execution of the composite [32]. Strong fiber interfaces result in capable load transmission and, in this manner, the capabilities of the composites enhances [33]. Sometimes the connection between the phases between the layers of the composites is not adequate to get the desired properties. Everything considered, reinforcement approaches to go must be gotten to upgrade the interfacial quality and furthermore the stress transfer. This enables the headway of multiscale hybrid composites where more than one bracing media is used [34], considering the advancement of microscale whiskers, nanostructures like tubes, rods, and wires around the strands. These topographies connect into the lattice, augment the surface domain for holding, and improve the load across the fiber and interfaces. For example, Mathur et al. [35] developed a hybrid composite by creating CNTs on the surface of carbon strands and investigated critical upgrades in the flexural quality and elastic modulus. Hybrid composites based on copper have numerous usages in light of the broad load bearing limit, notwithstanding, there are good interfacial cooperation between the CuO nanowires and carbon fibers [36]. They likewise react with polar practical gatherings, including carboxyl, hydroxyl, and carbonyl, which may be accessible on the layers of the carbon strands. These strong affinities, close by the reaction with polymer linkages of sap, result in strong interlocking inside the composite that stunningly improves the desired properties.

## 1.4 Nanostructured CFRP composites

Impact strength is a fascinating feature of CFRP composites which allows CFRP to be used in advanced applications where high stiffness and damage resistance is required. Regardless, plain carbon fiber strengthened polymer composites are exceptionally brittle; their low energy absorption capacity implies poor behavior under impact loading. Thus, woven carbon fibers are used for an elective reinforcement for polymer based composites because WCFs have cross-weaved design which gives good out-of-plane resistance, strength and durability [37]. Materials consist of carbon strands are confined by a weaving methodology did in two ordinarily symmetrical courses, and matrix material is added by impregna-

tion. The particular composites have better out-of-plane firmness, quality, and durability properties in comparison to the composites of laminated kind [38]. At a time although a composite is exposed to a sudden load (impact loading), it fails like a brittle material without appreciable energy absorption and damage resistance [39]. The persistent cracks spread up to inter molecular bonding of the interphase, up to the point that the highest level of impact energy absorption has been come to. Plain composite fails during an impact testing is begun by structure splits, trailed by delineation at the interface territory between the interphase and the fortifications. In this way, the development of hybrid composites where more than one reinforcement media such as CNT, graphene and other nanostructures are used with customary miniaturized scale has been studied. Hybrid structures are broadly seen in nature, such as plant cell, creature shells and skeletons, demonstrating that high mechanical properties can be gotten, even from genuinely frail constituents, by organizing matter over a scope of length scales [40]. While on a fundamental level we are not restricted by the necessities of physiological conditions and can utilize characteristically more grounded constituents, we presently cannot seem to misuse the chances of multiscale gathering of composite materials, methodically.

The fundamental reason for adding CNTs to traditional fiber composites is to mitigate the current impediments related with the matrix ruled properties. For instance, CNTs could offer both intralaminar and interlaminar fortification, subsequently enhancing delamination resistance and through-thickness properties, without compromising in-plane properties. The CNTs should be better than different methods for improving through-thickness execution like z-pinning, sewing, twisting and so forth, which will in general lessen the in-plane overlay execution, by exasperating and harming the primary filaments [41, 42]. The mix of nanostructures with regular fiber-fortifications in polymer composites has been accomplished predominantly through two distinct methods: scattering CNTs altogether all through the polymer matrix and growing nanostructures legitimately onto essential fortifying fibers as portrayed in Fig. 1.3 [43, 37]. First strategy has the simplicity of creation and compatibility with standard mechanical strategies however it has restriction of low loading values. However in the second strategy the fiber-ruled in-plane features are not altogether influenced but rather grid-dominated properties such as ILSS (inter-laminar shear strength) are enhanced by about 8-30%. Developing nanostructures onto fiber surfaces is a successful strategy to improve fiber surface region, making mechanical interlocking, and local softening at the fiber/grid interface, all of which may improve load exchange and interfacial properties explicit nanoscale impacts on the mass polymer properties are likewise conceivable [37, 44].

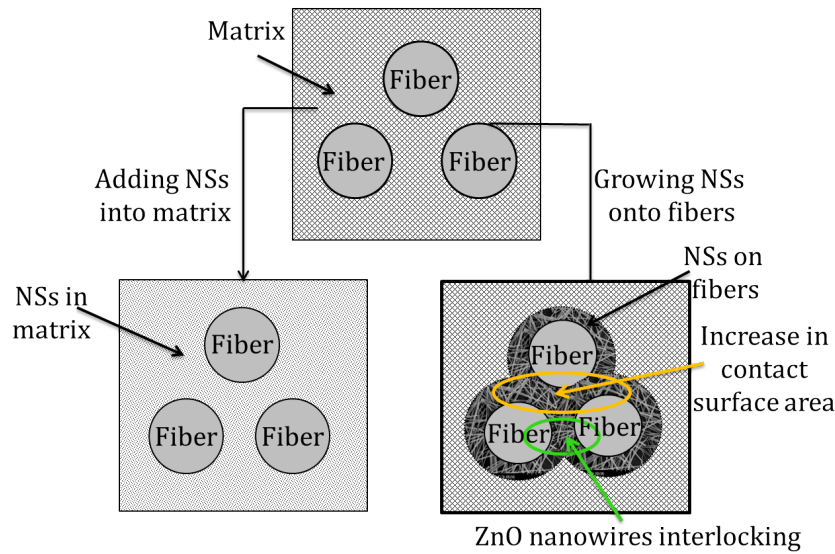


Figure 1.3: Techniques for development of nanostructured fiber reinforced polymer composites

## 1.5 Need of interfacial treatments of CFRP

Delamination is a major damage mechanism behind deployment of mechanical property of laminated composites. Despite of that, fiber cleavage in the interfacial region of the composites restrict the use of CFRP composites for high impact applications such as ballistic applications. The final performance of the developed composites are majorly illustrated by the performance of their interphase. Despite of the fact that the interphase assumes a prominent part in choosing the development of composites, nanostructures of wire shapes assist in the protection from sudden loading. As the data of composites has built up, the interface between the both the reinforcement primary and secondary with the polymeric matrix has been a subject of incredible interest. The idea of the interface has been seemed, by all accounts, to be a significant factor in an extensive part of the structure's mass properties [45]. Additionally, a solid fiber and solid network may not by any stretch of the imagination achieve a solid composite in light of the fact that the interface is also basic in developing the general nature of the consequent material. In like manner, various discernible masters have investigated procedures for improving the interface of present day composite materials. Whiskerization, chemical treatment, and plasma treatment have all indicated favorable outcomes for interface upgrades; regardless, the properties of fibers are partially utilized, realizing a final material with diminished in-plane properties [46, 47, 48, 49].



## 1.6 Interfacial treatment by fiber modifications

Shear stress is transferred between the carbon fiber and the polymer matrix through the interphase of carbon fiber composites. When the regional shear stress is greater than the carbon fiber composite's interfacial shear strength, debonding of the carbon fiber from the matrix, takes place which results in composite failure. Different techniques for altering the surface of carbon fiber are attracting a lot of interest because they can increase the performance of composites. These techniques essentially consist of surface functionalization, surface roughening, surface whiskerization and creating secondary interphase.

### 1.6.1 Surface functionalization and roughening

The surface of the carbon fiber can be functionalized and roughened to increase the interaction between the carbon fiber and polymer matrix. When the smooth outer layers of carbon fiber are removed, the rough surface of the carbon fiber can mechanically interlock with the polymer matrix, increasing the wetting and adherence of the carbon fiber to the polymer matrix. However, due to the damage caused by these methods, the in-plane mechanical characteristics of carbon fiber, such as its tensile strength, would decline. These treatments can increase the adhesion between carbon fiber and polymer matrix. Common techniques used in these techniques include plasma oxidation, acidic and basic oxidation, electrochemical oxidation, and high energy irradiation.

Li et al. [50] successfully developed chemical treatment of carbon fiber using aqueous ammonia etching, nitric acid oxidation, and their combination. Nitric acid generated oxygen-containing functional groups on the surface of the carbon fiber, and aqueous ammonia increased the roughness. The carbon fiber's tensile strength was somewhat reduced while its wettability improved. The largest improvement of interfacial shear stress (IFSS) over bare carbon fiber was 43.36%. Continuous atmospheric plasma oxidation was utilized by Erden et al. [51] to treat carbon fiber. The wettability of carbon fiber was enhanced by the introduction of polar oxygen-containing groups. The single fiber fragmentation test revealed that after 4 minutes of exposure to the plasma, the IFSS of carbon fiber increased from 40 to 83 MPa. The effect of electrochemical oxidation on carbon fiber was studied by Kim et al. [52]. The fiber roughness was enhanced along with formation of oxygen functional groups on fiber surface. The interfacial shear strength was assessed using the micro-bond method. The IFSS improved by 144% compared to bare carbon fiber, and it was discovered that the adhesion between the fiber and resin was substantially improved.

High energy irradiation has the potential to significantly increase the IFSS between aramid fiber and resin as demonstrated by Xing et al. [53]. The amount of polar groups formed on fiber increased along with the roughness and wettability of the carbon fiber. The IFSS was improved by 45.17% compared to untreated fiber composites.

### **1.6.2 Surface whiskerization**

The surface whiskerization of fibers has been analyzed comprehensively. This strategy can enhance load exchange and bonding between the fiber and the resin of the composite. Single crystal SiC or Si<sub>3</sub>N<sub>4</sub> bristles are created on the surface of a fiber with incredible accomplishment in growing the interfacial shear strength [54]. Surface whiskerization of fibers is commonly performed by creating nanowires, nanotubes or smaller scale bristles over standard fundamental strands, for instance, fiberglass, aramid, carbon, SiC filaments [55]. Such type of fill in as an auxiliary support and upgraded the quality of interphase and increase complete execution of the composites. It was furthermore noted, regardless, that the high temperatures and catalysts required for improvement of the whiskers ordinarily harmed the primary fiber and diminished the in-plane quality of the composite. These examinations were tested on carbon strands, which can sustain high heat in comparison to fibers of aramid or other polymers.

### **1.6.3 Fabrication of secondary interphase**

Fabricating a secondary interphase between the fiber and polymer matrix is also a successful way to raise the IFSS since the new interphase can boost adhesion, enhance load transmission, and expand the interfacial contact area. The sizing of fibers [56] and fabrication of carbon nanotubes [57] or metal-oxide nanostructures [9] on fibers are the most suitable way to develop nanostructured interphase in the CFRP composites. When compared to direct fiber-to-matrix connections, the sizing layer will adhere to the polymer matrix more effectively. Both fiber and polymer were suitable with the sizing. Aligned carbon nanotubes and metal-oxide nanostructures are two examples of nanostructured interfaces with much greater surface contact areas. Nanostructures introduced into the polymer matrix will operate as mechanical interlocking and improve their load bearing capacity.

The interfacial adhesion of sized and desized T300 and T700 carbon fibers was investigated by Dai et al. [56] to assess the impact of sizing. Comparing desized carbon fiber to the two commercial carbon fibers, the polar surface energy and concentration of active carbon atoms were lower. The IFSS of carbon fiber composites is dependent on both chemical

bonding and physical adhesion. Excellent mechanical characteristics of carbon nanotubes allow them to strengthen the in-plane and out-of-plane characteristics of composite materials. Because aligned carbon nanotubes can improve load transfer, their use can result in a considerable rise in the IFSS. One of the common method for producing carbon nanotubes is through chemical vapour deposition (CVD). However, the high temperature and catalyst use in the CVD process causes carbon fiber to deteriorate and flaws are developed in composites.

Sager et al. [57] used CVD to generate carbon nanotubes on carbon fiber. The developed nanotubes were randomly oriented and radially aligned. For each morphology of carbon nanotubes, the tensile strength of carbon fiber decreased by 37% and 30%, respectively. It was thought that the surface oxidation and thermal deterioration that occurred during the CVD process added to the surface flaws, reducing the mechanical characteristics of carbon fiber but enhances the interfacial characteristics of composites as investigated through single fiber fragmentation test. The findings of the single fiber fragmentation test exhibits improvement in the IFSS for both randomly oriented and aligned carbon nanotubes by 71% and 11%, respectively. The interphase shear yield strength and matrix adherence to the fiber were both strengthened by the presence of nanotubes. Lin et al. [9] proposed a hydrothermal strategy to overcome the drawbacks of generating carbon nanotubes by CVD on carbon fibers and boost the IFSS. Due to the low temperature during growth, the tensile characteristics of carbon fiber were preserved. Song et al. [58] employed electrochemical deposition technique to deposit seed layers of nanoparticles in the first stage of hydrothermal development. In the second stage, microwave radiation was used to accelerate the growth of nanorods. The use of microwave drastically shortened the development period of nanowires by 95.8%.

## 1.7 Metal-oxide nanostructures

Metal oxide nanostructures have undoubtedly received the most attention in contemporary nanoscience over a decade [59]. The fundamental cause of this is that when their size is altered down to the nanoscale range, metal oxides frequently exhibit completely different properties for example gold nanostructures are known to be active catalysts for oxidation reactions while bulk gold is passive [60]. The last ten years have seen extensive research on and discovery of a variety of properties of metal oxide nanostructures, including catalytic activity, mechanical properties, electrical and thermal conductivities, antibacterial activities and optical attributes [61, 62, 63]. In catalysis, electronics, photonics, energy storage,

sensors, optoelectronics, biomedical and healthcare sectors, metal oxide nanostructures are widely employed [64, 65]. By customizing the shape, size, crystallinity, and architecture of nanostructured materials, diverse properties of resulting materials can be developed.

### 1.7.1 Zinc-oxide

In the present scenario of materials, Zinc-oxide (ZnO) is a prime and innovative material. Their nonappearance of a state of merging of symmetry in wurtzite, joined with huge electro-mechanical coupling, accomplishes favorable piezoelectric and pyro-electric qualities and the accompanying utilization of ZnO in piezoelectric sensors and mechanical actuators. Additionally, ZnO is a wide band gap (3.37 eV) compound semiconductor that is appropriate for short wavelength optoelectronic usage. The high exciton confining criticalness in ZnO crystal can guarantee gainful excitonic transmission at room temperature and ultraviolet shimmer has been represented in scattered nanoparticles and thin films [1]. ZnO is direct to visible range of light and can be ultra-conductive by doping. ZnO is a versatile utilitarian material that is available in the form like nanorings, nanobelts, nanocombs, nanocages and nanowires [66].

#### Crystal and surface structure of ZnO

Wurtzite ZnO consist of a hexagonal shape with cross-sectional indices  $a = 0.3296$  and  $c = 0.52065$  nm. ZnO structure can be essentially portrayed as various substituting planes made out of tetrahedrally organized  $O^{2-}$  and  $Zn^{2+}$  atoms, stacked on the other hand along the  $c$  pivot as delineated in Fig.1.4. The tetrahedral coordination in ZnO realizes non-central symmetric structure and in this manner display piezoelectricity and pyroelectricity. Another basic trademark for ZnO is their polar surfaces [67]. Basal plane is the most primarily recognized polar surface. The opposite charge particles deliver emphatically charged  $Zn^+(0001)$  and adversely charged  $O^-(000\bar{1})$  surfaces, bringing about a typical dipole minute and unconstrained polarization charged  $O^-(000\bar{1})$  along the  $c$ -axis and additionally a divergence in surface vitality. The polar surfaces have to features or display enormous surface reproductions, yet  $ZnO^-(0001)$  are exceptional to develop a stable structure without recreation [68].

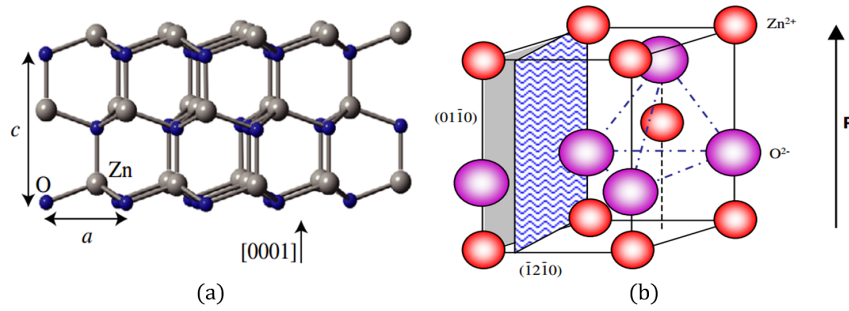


Figure 1.4: (a) Wurtzite structure of ZnO showing lattice parameters and (b) tetrahedral coordination of ZnO [1]

### 1.7.2 Copper-oxide

Copper oxide (CuO) is a direct band gap p-type semiconducting material that has been identified as a practical substance enabling a range of technologies, including catalytic systems, electrodes, magnetic storage devices, renewable energy integration, biosensors, and biomedical applications [69, 70]. As a result, development of CuO nanostructures and their research is considered valuable for both functional and basic uses. CuO is a photo-diode and photonic semiconductor substance consists of narrow energy band [71]. Due to its significant electrical and optical properties, that are fundamentally essential in building nanosized electronic and optoelectronic devices, there has been constantly significant focus in the creation of nanostructured semiconducting materials in past few years. Because of its unique features, such as high surface-to-volume proportion, excitability, specific electrical characteristics, and interesting optical attributes relative to conventional materials, nano-crystalline semiconductors have attracted a lot of attention over the few years [72]. Transition metal oxides nanostructures are a kind of optoelectronic material that has implications in magnetic recording, renewable energy integration, electronic parts, and catalytic systems [73, 74].

## 1.8 Need and scope of work

The excellent strength-to-weight ratio, corrosion resistance, and design flexibility of light-weight structural composite materials have recently received a lot of interest. A promising strategy to enhance the characteristics of composites is to incorporate nanomaterials and nanostructures into traditional fiber reinforced composites. Due to their high specific strength and stiffness, as well as flexible tailoring, carbon fiber composites have been play-

ing a crucial role in industry. The interfacial phase between the fiber and polymer matrix, which dictates in-plane properties like interfacial shear stress, as well as out-of-plane properties like interlaminar shear strength, affect composites' performance.

Impact strength is a fascinating feature of CFRP composites which allows CFRP to be used with full potential in advanced applications where high stiffness and damage resistance is required. Regardless, plain carbon fiber strengthened polymer composites are exceptionally brittle; their low energy absorption capacity implies poor behavior under impact loading. Thus, woven carbon fibers are used for an elective reinforcement for polymer based composites because WCFs have cross-weaved design which gives good out-of-plane resistance, strength and durability. Further, the development of hybrid composites where more than one reinforcement media such as CNT, graphene and other nanostructures can be used for high performance CFRP composites. Dispersion of CNT, graphene and nanoparticles is the major concern of fabrication of hybrid composites. Therefore, developing nanostructures such as ZnO, CuO directly onto fiber surfaces is a successful strategy to improve fiber surface region, mechanical interlocking, and local softening at the interface, all of which may improve load exchange and interfacial properties of the CFRP composites. The performance of CFRP composites are majorly illustrated by the performance of their interphase. Despite of that, fiber cleavage in the interfacial region of the composites restrict the use of CFRP composites for high impact applications. The final performance of the developed composites are majorly illustrated by the performance of their interphase. The interface between both the reinforcement primary and secondary with the polymeric matrix has been a subject of incredible interest. The idea of the interface has been seemed, by all accounts, to be a significant factor in an extensive part of the structure's mass properties. In like manner, various discernible masters have investigated procedures for improving the interface of present day composite materials.

High performance composites are always desired, however because carbon fiber's surface is flat and inert, applications of such composites are constrained. Several studies avoided putting nanomaterial directly into polymeric hosts due to cost and processing challenges. Hybrid fibers, on the other hand, are a new concept. Standard structural fibers (e.g., carbon, fiberglass, aramid, or SiC) are combined with nanofibers or nanotubes formed on the surface (e.g., carbon nanotubes or ZnO nanorods).

Different techniques for altering the surface of carbon fiber are attracting a lot of interest because they can increase the performance of composites. These techniques essentially consist of surface functionalization, surface roughening, surface whiskerization and creating secondary interphase. Thus, an exclusive approach required to be devised which

can enhance the mechanical properties of CFRP composites for advanced applications. It is noted from the literature that fabricating a secondary interphase between the fiber and polymer matrix can be a successful way to raise the interfacial shear stress since the new interphase can boost adhesion, enhance load transmission, and expand the interfacial contact area. The sizing of fibers and fabrication of metal-oxide nanostructures (NSs) on fibers are the most suitable way to develop nanostructured interphase in the CFRP composites. It is estimated that this study will develop nanostructured CFRP composites for advanced applications such as structural, electronics and military with excellent mechanical performance.

Growing nanostructures on fiber surfaces is a good way to increase fiber surface area, mechanical interlocking, and/or local stiffening at the fiber/matrix interface, all of which can help with stress transfer and interfacial characteristics. Extensive studies on WCF grafted with metal-oxide nanostructures primarily rely upon micro fiber tows or woven preforms. The nanostructure synthesis technique requires to be scaled up to manufacture continuous nanostructured WCF, so that these grafted WCF will allow fabrication of hybrid composites tapes/pre-pregs and composites with enhanced mechanical properties such as compression, shear, impact and reduced delamination. Tailored properties variation due to nanostructures of resulting composites need to be assessed by open hole compression and compression after impact. In the long run, the fabrication and characterization of hybrid composites structures simultaneously grown on the fibers and spreading in the matrix may be possible, permitting even better service conditions. The development in the field of metal-oxide nanostructured hybrid composites reveals that, in coming years metal-oxide assisted advanced material must be pioneer material for aviation and industrial usage. Various studies and researches on hybrid composites are still going on but reflect huge promise for large scale production of nanostructured composites.

The growth of metal oxide nanostructures on woven carbon fiber to minimize failure of CFRP composites under impact loading is not explored so far. The synthesis of well aligned ZnO nanorods on WCF strands using an economical seed-assisted hydrothermal strategy is not explored in an effective manner. The synthesis of metal-oxide nanostructures on different substrate using varied synthesis techniques is already present in literatures; however, this study is novel in terms as it introduced an easy practical approach to develop high performance metal-oxide nanostructured CFRP composites for advanced applications. The study of different factors affecting the performance of nanostructures and their resulting composites are investigated using different physical and mechanical characterization techniques. Additionally, the effects of ZnO and CuO concentration on thermal

stability and weight loss pattern on carbon fiber samples have been analysed.

## 1.9 Problem definition

Enhancement in the nanostructured materials allow researchers to implement these materials into the diverse applications due to their enhancement in absorption range, stability, sensitivity, crystallinity, mechanical properties and many more. The extensive literature survey has been done to extract the following existing problems in the development of high performance metal-oxide nanostructured carbon fiber composites:

- Improved synthesis techniques for controlled growth of metal-oxide nanostructures on fabrics are required for the development of 3D hierarchical composites.
- Enhancement in the quantification of scale and size of nanostructures and their reproducibility are still unsolved issue.
- Quality and non-uniformity in the growth of metal-oxide nanostructures using hydrothermal technique.
- Effect of alignment, volume fraction, aspect ratio and morphology of metal-oxide nanostructures on WCF.
- Non-wettability leads to improper interfacial bonding and weak inherent properties.
- Effect of synthesis parameters for well-aligned metal-oxide nanostructures on WCF fabrics and its hierarchical polymer composites.
- Enhancement of impact energy absorption and load bearing capacity of carbon fiber reinforced polymer composites.

Most of the work reported on synthesis and characterization of metal-oxide nanostructures is on optoelectronics, photonics, sensors, energy storage and environmental applications. However, few literatures are available on the utilization of metal-oxide nanostructures for FRP composites.

Furthermore the synthesis and development of metal-oxide nanostructures on carbon fiber and their mechanical characterizations need to be addressed for advanced applications such as opto-electronics and aviation industry. This study demonstrated that growing metal-oxide nanostructures such as ZnO, CuO on the surface of WCF is a novel approach to



improve multifunctionality that could be exploited in diverse applications such as electric cars, unmanned aerial vehicles, and portable electronic devices. Furthermore, the current research findings can help in the development of structural supercapacitors for automotive industries, electronic components for energy storage in electric vehicles, unmanned aerial vehicles, and in the aerospace industry.

## **1.10 Aim and objectives**

The present research focuses on synthesizing metal-oxide nanostructures on woven carbon fiber using solution phase synthesis such as hydrothermal method, microwave-assisted hydrothermal method and further investigating its effect on polymer matrix to achieve high-performance CFRP composite material. To accomplish aim of the work, following objectives have been established:

- Surface functionalization of woven carbon fiber fabrics by growth of metal-oxide nanostructures using solution phase synthesis.
- Hydrothermal growth of ZnO nanostructures on WCF and effect of synthesis parameters on morphology.
- One-step microwave-assisted hydrothermal synthesis of ZnO nanostructures on carbon fiber fabric and their characterizations.
- Fabrication of ZnO-modified WCF reinforced polymer composites for enhanced mechanical properties and investigation of their damage response.
- Development of carbon fiber fabrics functionalized with monoclinic CuO nanostructures using seed-assisted hydrothermal growth treatment and their characterization.
- Improvement of interfacial adhesion of CuO nanostructured carbon fiber reinforced polymer composites and their impact damage response.

## **1.11 Research novelty and originality**

The research carried out is significantly novel, since the growth of metal oxide nanostructures on woven carbon fiber to minimize failure of CFRP composites under impact loading is not explored so far. The synthesis of well aligned ZnO nanorods on WCF strands using

an economical seed-assisted hydrothermal strategy is not explored in an effective manner. The synthesis of metal-oxide nanostructures on different substrate using varied synthesis techniques is already present in literatures, however, this study is novel in terms as it introduced an easy practical approach to develop high performance metal-oxide nanostructured CFRP composites for advanced applications. The study of different factors affecting the performance of nanostructures and their resulting composites are investigated using different physical and mechanical characterization techniques. Additionally, the effect of ZnO and CuO concentration on thermal stability and weight loss pattern on carbon fiber samples have been analyzed. Application of growing metal-oxide nanostructures on carbon fiber fabrics with hydro-thermal method for high performance structural material is a novel task performed in the present work. Further, the introduction of a large interfacial area and load transfer capacity of nanostructured interphase in CFRP is the successful outcome of the thesis.

## **1.12 Industrial importance**

This project is important to the industry using advanced materials especially to the electronics and aircraft industry as it proposes strong interfacial strength and impact strength of the CFRP composites which helps in production of high performance FRP composites. In addition, incorporating metal-oxides such as ZnO and CuO in CFRP composites exhibit improved mechanical properties along with optoelectronic properties which is desirable for producing high strength electronic components. Furthermore, the developed hybrid composites samples are best suited for aircraft and automobile industries due to high impact strength and high modulus at light weight. Thus, the developed hybrid composites samples can be proposed as good replacement to the plain carbon fiber reinforced polymer composites for various applications due to high mechanical properties at very low cost and less experimental setup.

## **1.13 Organization of presented report**

The thesis comprises of seven chapters and brief description of each chapter is given below:

*Chapter 1* deals with the brief introduction about background of FRP and CFRP along with the need and motivation for development of high performance CFRP composites. In this chapter the need and scope of surface functionalization of WCF using metal-oxide

nanostructures is defined to resolve the existing problem of CFRP. In addition, this chapter includes problem definition, aim and objectives of the work, research novelty and industrial importance of the current research.

**Chapter 2** focuses on detailed literature survey on synthesis of metal-oxide nanostructures such as ZnO and CuO on WCF fabrics along with their merit and limitations. In addition, the chapter includes morphological variation of nanostructures, strategies for effective growth of nanostructures, research gap and research methodologies adopted in previous works.

**Chapter 3** includes synthesis of ZnO nanostructures on WCF surface using hydrothermal technique and effect of hydrothermal process parameters on growth rate and morphologies of ZnO nanostructures.

**Chapter 4** deals with an attempt of synthesis of ZnO nanostructures on WCF surface in shortest possible duration using one-step microwave-assisted hydrothermal technique. It shows structural, morphological and optical characterization of the ZnO-modified WCF samples. Effect of microwave parameters and effect of different growth solutions are also illustrated in this chapter.

**Chapter 5** includes development of ZnO-functionalized carbon fiber reinforced epoxy resin composites by vacuum bagging method. The mechanical attributes of developed hybrid composites such as tensile strength, elastic modulus, in-plane shear, and impact resistance improved dramatically in comparison to plain carbon fiber epoxy resin composites. Further, the impacts of cross-linked networks of ZnO-WCF-epoxy in hybrid composite on mechanical properties are illustrated in this section.

**Chapter 6** focuses on fabrication of monoclinic CuO nanostructures on carbon fiber fabrics using seed-assisted hydrothermal method and their characterization. Evaluations of the optimum process parameter used in hydrothermal synthesis are identified to achieve ultra-fine growth. Further, this chapter describes study of improvement in interfacial adhesion of CuO-modified WCF reinforced polymer composites and their impact damage response. Furthermore, the impacts of varying molar concentration of CuO nanostructures on mechanical attributes of the fabricated hybrid composite samples are explored in this section.

**Chapter 7** summarizes key findings of each chapter for the development of high performance carbon fiber reinforced polymer composites and proposes suggestions for the potential future work.



# 2

## Literature Review

The brief introduction about background of FRP and CFRP along with the need and motivation for development of high performance CFRP composites is discussed in chapter-1 along with the need and scope of surface functionalization of WCF using metal-oxide NSs. The different techniques for synthesis of metal-oxide NSs (ZnO, CuO), effect of morphological variations, desired process parameters and limitations have been discussed in this chapter. In addition, the chapter includes detailed study about hydrothermal synthesis of nanostructures, morphology of ZnO NSs such as nanoparticles, nanorods, nanowires, nanoflowers, nanopetals, nanopallets, nanoneedle and others. The literature review presents the prior work done in the relevant areas such as challenges of existing surface functionalization techniques, nanostructured CFRP composites, mechanical characterizations of CFRP composites, hydrothermal synthesis using microwaves, doping of ZnO NSs and techniques for the fabrication of CFRP laminates. In addition, the recent work done in the field of carbon fiber surface functionalization, improvement in interfacial interaction, and enhancement of mechanical properties for advanced applications are discussed. Further, the chapter summarizes concluding remarks of the literature surveyed and concluded with the formation of research gap, research problem and the objectives for the present research work.

## 2.1 Introduction

This chapter addresses the recent developments of the processing of ZnO NSs and characterizations of the developed NSs by various techniques, mainly hydrothermal technique. Various kinds of ZnO NSs such as wires, rods, flowers, dumbbells, spheres, particles and combs created by hydrothermal process on different substrate are explained in brief. Metal-oxides likely have the wealthiest group of NSs among all materials, both in structures and properties. The NSs could have novel applications in sensors, transducers, optoelectronics, and biomedical sciences. The ZnO NSs processed on any substrate makes a hierarchical structure and can altogether enhance the specific properties in the final nanocomposites. The potential of ZnO NSs for fiber reinforced nanocomposites, focusing on the most used techniques used for the creation of ZnO NSs reinforced hierarchical composites are used for development of high performance CFRP composites. Recently few innovative concepts are used for improving or synthesizing other distinctive NSs that can be implemented for the development of hybrid composites for specific applications.

## 2.2 Recent advancements in carbon fiber reinforced polymer composites

Researchers are required to create sophisticated materials with improved qualities as a result of the emergence of the cutting-edge engineering period. Due to their low specific gravity, higher strength, higher stiffness, simple fabrication process, higher corrosion resistance, improved fatigue resistance, extended life cycle property, and most importantly convenient-lightweight structure, composite materials—especially carbon fiber-reinforced polymer composites (CFRPs)—have recently been displacing various orthodox metal and metallic alloys [75, 76, 21, 77]. Additional benefits that should not be disregarded include multi-functionality, part integration favorability, and design flexibility [78]. Because of this, CFRPs have been resonating with a seismic effect in structural applications ranging from sports equipment to aerospace since their first commercial use in 1960. By 2025, the CFRP market is anticipated to be worth 32 billion dollars worldwide [21]. Carbon fiber (CF) serves as reinforcement in a thermoplastic or thermoset polymer matrix that makes up CFRP [79]. There is a three-dimensional interphase zone with distinct properties located between the two elements. Additionally, a two-dimensional construction known as an interface marks the boundary between these components. A CFRP's main objective is to

produce a lightweight material with superior mechanical properties that cannot be obtained from its component parts alone. These enhanced properties are influenced by the morphological structure and the interaction between the reinforcing material and the matrix at the interface, which takes the form of hydrogen bonds and Vander Waals forces [80]. When the binding energy between the CF and the polymer replaces the cohesion energy produced by all of the individual constituents, this interaction may change the mechanical properties of the composite. Physical dovetailing, chemical inertness, and thermal parallelism are required for this [48]. These are partly accomplished by the polymer matrix, which secures the fiber and shifts the load towards it, and the filler CF, which carries the load in addition to it. Delamination, weak interfaces, low impact damage resistance, poor wettability and fatigue resistance, inferior strain, mismatched surface energies between matrix and reinforcement, and therefore uncompetitive traversal properties are challenges faced by CFRP [79, 81]. Vapour phase-grown carbon nanofiber (VGCNF), which has a diameter of less than 200 nm and appears to have better mechanical properties than CFRP, has been tried as reinforcement to address these problems [82]. The curved structure of VGCNF, however, limited the quantity of fiber volume fraction (FVF) and homogenous resin distribution in composite, which was a drawback [83]. As a result, it was unavoidably quickly eclipsed by the forceful application of various carbonaceous nanofillers. The most popular carbonaceous nanofillers for changing the mechanical properties of neat composites are one-dimensional (1D) CNT, two-dimensional (2D) graphene, and zero-dimensional (0D) nanodiamond [84, 85]. The term "hybrid composite" will also be limited to "CF-based fiber hybrid composite," which is a polymeric composite that combines two distinct reinforcing fibers.

The implementation of CNT, graphene and other nanofillers in CFRP composites has limited improvement in the mechanical and thermal characteristics which provide basis for further advancement in the nanofillers [86, 87, 21]. Further, the dispersion of CNT, graphene and nanoparticles in the polymer matrix is the major concern of fabrication of hybrid composites. Therefore, developing metal-oxide nanostructures such as ZnO, CuO directly onto fiber surfaces is a successful strategy to improve fiber surface region, mechanical interlocking, and local softening at the interface, all of which may improve load exchange and interfacial properties of the CFRP composites [33, 36, 37]. The performance of CFRP composites are majorly illustrated by the performance of their interphase. The fabrication of secondary interphase between the fiber and polymer matrix can be a successful way to raise the interfacial shear stress since the new interphase can boost adhesion,

enhance load transmission, and expand the interfacial contact area. The sizing of fibers and fabrication of metal-oxide nanostructures (NSs) on fibers are the most suitable way to develop nanostructured interphase in the CFRP composites [88, 89, 90]. It is estimated that this study will develop nanostructured CFRP composites for advanced applications such as structural, electronics and military with excellent mechanical performance [91, 92, 89].

### 2.3 Recent advances in ZnO NSs

In the present scenario of materials, ZnO is a prime and innovative material. Their non-appearance of symmetry in wurtzite structure, high electro-mechanical coupling, accomplishes favorable piezoelectric and pyro-electric attributes and the accompanying utilization of ZnO in piezoelectric sensors and mechanical actuators [93]. Additionally, ZnO is a wide band gap (3.37 eV) compound semiconductor that is appropriate for short wavelength optoelectronic usage. The high exciton confining criticalness in ZnO crystal can guarantee gainful excitonic transmission at room temperature and ultraviolet shimmer has been represented in scattered nanoparticles and thin films [94, 95]. ZnO is direct to visible range of light and can be made ultra-conductive by doping [96]. ZnO is a versatile utilitarian material that can come in different morphologies like nanorings, nanobelts, nanocombs, nanocages and nanowires [97, 98]. Since 2000 and particularly lately, the ZnO based nanocomposites have gained more consideration as ZnO displays piezoelectric and semi-conducting dual properties [99]. Specialists discovered inspiration to build up a material which has elite and the novel applications in the field of innovative upgrade, for example, optoelectronics, sensors, transducers and biomedical sciences [100, 101]. ZnO based groups of NSs such as nanowires are frequently utilized for an extensive variety of utilities from power devices to solar products to semiconductor devices [102]. Morphologies of the nanowires with the surface of carbon fibers are the prime factor to enhance the structural properties of the nanocomposites [103]. All together for the interphase of nanowire to develop interactions between the interfaces of composites, which must offer upgraded bonding between the polymer lattice and base fiber. While bonding with the base fiber, the extended surface domain and mechanical interlocking of the nanowire covering ensured and upgraded collaboration with the polymer matrix. This reaction was guessed to be an eventual outcome of the collaboration of ZnO with oxide groups like carboxylic acid. But the correct interactions have not been estimated, it is striking that ZnO combines unequivocally with COOH groupings. There have been a couple of findings of how ZnO associates with the COOH groupings, however, concrete conclusions on exact strength of such bond-



ing was not yet explored [104]. Distinctive methods for synthesizing ZnO nanowires have been outlined, including the aqueous method, template based development, thermal dissipation, plasma beam epitaxy, CVD, and MOCVD [105, 106, 107, 108]. The aqueous procedure is frequently used to produce ZnO NSs with generally negligible cost at very low temperatures. In this system, NSs are developed by varying the precursor chemicals, fixation, reaction time and development temperature [88]. Regardless of the way that it was extremely difficult to manage the development of ZnO NSs, a restraint way of development of NSs of zinc oxides has been accomplished by Liang et al. [109].

## **2.4 Synthesis techniques of metal-oxide NSs**

Different preparation and synthesis techniques for nanomaterials have been developed over the last few decades. Identifying the purpose for which nanomaterials are being produced is one of the key goals of the process. In order to properly synthesize the nanomaterials, the researchers must be aware of their uses. It will be different from the approach used to produce nanomaterials for biological or medical applications to employ them in industrial applications for the creation of numerous items. Better functioning and cheaper cost are two further goals of the researchers who are synthesizing nanomaterials. Several physical and chemical techniques have been employed in recent years to enhance the functionality of nanomaterials that already exhibit improved characteristics [110]. The amalgamation techniques of various metal-oxide NSs can comprehensively be classified into three major categories such as green synthesis, solution phase synthesis and gas phase synthesis.

### **2.4.1 Green synthesis**

Green synthesis of nanomaterial includes synthesis of metals, metal oxide, bimetallic and their functional NSs [111, 112, 113, 114]. Fundamental properties of ZnO remain undisturbed as compared to synthesis using non-green process. Green synthesis of ZnO nanoparticles (NPs) have been done by employing plants, algae, fungus and bacteria [115]. The production of zinc oxide without causing any damage to the environment is also a major concern. Green synthesis focuses on biological approach that is less toxic, environment-friendly, safe and biocompatible. This process enhances properties of zinc oxide apart from its basic properties. Reducing and limiting the degree of agglomeration of zinc oxide has led to the introduction of green synthesizing using different organic substances. According to observations, basic properties of ZnO NPs are undisturbed but it is found that

ZnO NPs have obtained additional properties by following Green synthesis procedures like antioxidant, antibacterial, antifungal properties and many more [116]. It is also observed that different morphological structures like nanorods, nanospheres, nanoflowers and many more can be Green synthesized [117]. The implementations of green technology based ZnO nanomaterial may have few limitations. The heterogeneity of ZnO nanomaterial, for instance, is innate to the manufactured conventions, where the crude materials may lack homogeneity in composition and chemical circulation, while the possible connection of harmful parts from bacterial or parasites cells to the produced nanomaterial could be another wellspring of constraint for their bio-engineering applications. Thus, and in spite of the way that there is few researches on the utilization of green technology incorporated ZnO nanomaterial as biological specialists, there presently need a deficiency of descriptive comprehension of their specific cytotoxic system and biocompatible strategies as well.

#### **2.4.2 Solution phase synthesis**

In comparison to traditional ceramic routes, soft chemical routes, which are primarily represented in the solution phase by hydrolytic or non-hydrolytic sol-gel processing, as well as photo- or thermal metal organic decomposition (MOD), have many advantages, including access to desired forms of inorganic nanomaterials at much lower temperature [118, 119]. The precursor molecules employed in these processes, however, have a significant impact. These precursors need to possess a number of desired properties in order to be used in solution phase synthesis, including solubility, control of hydrolysis/condensation, surface properties or texture (homogeneity, porosity, and specific surface area), formation of gels for coatings or embedding, access to organic-inorganic systems with a covalent bond, low temperature decomposition pathways, and for multi-metallic materials, a proper stoichiometry of the constituent parts [120]. In the solution phase synthesis, the development procedure is performed under liquid phase. The procedure is known as hydrothermal process or solvothermal process because of utilization of typical aqueous solution. Following are involved in the solution phase synthesis processes:

- i. Zinc acetate hydrate (ZAH) in alcoholic solutions with NaOH or Tetra Methyl Ammonium Hydroxide
- ii. Spray pyrolysis for growth of thin films
- iii. Electrophoresis

- iv. ZAH derived nano-colloidal sol-gel route
- v. Template assisted growth

### 2.4.3 Gas phase synthesis

This process utilizes gaseous atmosphere in enclosed containers. Generally, this process involves high temperatures in the range of (500-1500)°C. Through further inert-gas cooling and gas-phase condensation of the sputtered atomic vapour, magnetron-sputtering has been extensively employed to synthesis of single- and multi-component nanomaterials. Following the work of Haberland et al. [121], there has been a rapid advancement in the synthesis of nanomaterials using magnetron-sputtering; in-depth theoretical studies have clarified the fundamentals of particle formation [122]. There are many technologically sophisticated variations of nanomaterials fabrication systems, such as those with improved geometries, pulsed plasma or multiple-target usage, enabled high cluster yields, post-deposition thermal treatment, oxidation control, etc [123, 124]. Some of the prominent work on gas phase synthesis of nanomaterials concluded that, the nanomaterial synthesis procedure may provide good control over nanoparticles size, crystallinity, and, most crucially, functionality [125, 126]. Following are the usually available methods of gas phase:

- i. CVD (Chemical vapour deposition)
- ii. Metal oxide CVD
- iii. Thermal oxidation of pure Zn and condensation
- iv. Vapour phase transport, which consist of vapour solid (VS) and vapour liquid solid (VLS) growth
- v. Physical vapour deposition
- vi. Microwave assisted thermal decomposition

## 2.5 Hydrothermal synthesis of ZnO NSs

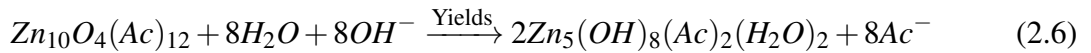
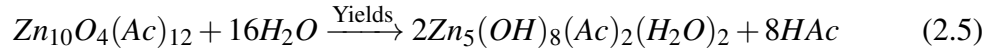
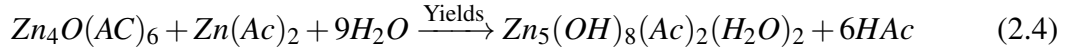
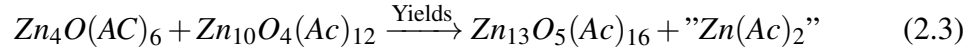
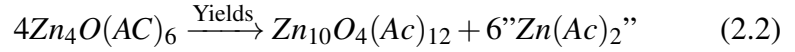
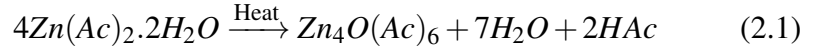
The “Zinc acetate hydrate based nanocolloidal sol-gel course”, when this approach was proposed, claimed "size quantized Q-ZnO" nano-colloids were successfully clarified and their key optical features especially revealed. The genuine disadvantages of such solutions

having low concentration as  $\sim 1\text{mM}$  were their robustness and utility potential, fundamentally kept to vital spectroscopic examinations [105]. This issue could be overpowered by displaying the sol-gel idea that allowed raising the volume segment of non-accelerated ZnO colloids by small rate of variation, down to between molecule partitions pushing toward one atom separate over. This new approach yielding straightforward completions opened us new possible results of making thin films and nanocomposites [127]. It also enabled a controlled association, shape adjustment and outlining on the nano and micro scale. Sol-gel technique has picked up prominence as it allows restrained combination, shape regulation and designing of the NSs [128]. A transparent solution will form when concentrated ethanolic ZAH suspension was refluxed and distilled. Under high fixation conditions small ZnO nanoparticles of measurement of 5nm (approx.) can be developed by the aid of hydroxides such as LiOH, NaOH. For the development of ZnO NSs there are several literatures of changes of the ZAH dehydration or disintegration and further condensation [129, 130]. The scan for essential bunches to fill in as building hinders for different NSs has been continuing for a long while. The detachment and recognizable proof of essential bunches is a region of dynamic research. The blend of essential structures relies upon different situations like the amalgamation temperature, initial concentration of the salt, nature of the solvent and warming time. The ZnO groups can be individuals from any of the three unique families mentioned beneath:

- i. The  $Zn_4O(Ac)_6$  named as “basic zinc acetate” and their greater itself similar homologue  $Zn_{10}O_4(Ac)_{12}$ ,
- ii. The ethoxy-acetate  $(EtOZnAc)_n$  for creating wire-shape Nano-features and
- iii. The hydroxy-acetate  $Zn_5(OH)_8(Ac)_2(H_2O)_2$  monomer of lamellar sheet compounds, also named as “hydroxy double salt” (Zn-HDS).

The  $Zn_4O(Ac)_6$  amass is encircled in ethanol and 1-propanol at temperatures more than  $50^\circ\text{C}$  as observed by researchers in XRD and Raman spectroscopy estimations [131]. All the more as of late, Tokumoto et al. [132] successfully proposed a depth study time settled EX-AFS examine joined with UV-VIS optical analysis and FTIR-spectroscopic outcomes. Researchers unreservedly and unambiguously exhibited the appearance and expanding groupings of these tetrahedral bunches by deferred refluxing of ethanolic ZAH arrangements [133, 134]. The entire test perceptions exhibit that underlying heating ad-

vance can be depicted by the going with complete reactions:



### Stability of ZAH-derived NSs

To analyze the stability of the ZAH-inferred clusters, partial charge estimations utilizing the model of Henry-Livage [135] have been studied. The estimated trend is illustrated in Table 2.1 exhibiting consistency with the above stated experimental findings [135, 136]. The chemical clusters are recorded by the expanding thermodynamic stability. This might be watched that bunches of tetrahedral oxy-acetate have fairly more stability than the highest responsive ZAH. Additionally, the dependability of the auxiliary  $Zn_{10}O_4(Ac)_{12}$  antecedent is positively extended inside seeing  $1 - H_2O$  and  $7 - EtOH$ , continually found in synthetic examination. The more noteworthy solidness of monomer ( $Zn - HDS$ ) concerning the exposed oxy-acetic acid derivation clusters anticipates that once a specific measure of water is accessible, an unconstrained and specific course of action of Zn-HDS can be normal that also agrees with produced literature. Authors have figured charge course in the advance state contrasting with the response between oxy-acetic acid derivation and water and saw an unconstrained improvement of  $Zn - OH$  under  $HAc$  release. The zinc ethoxy acetate is most stable precursor bunch and without a doubt, this is experimentally affirmed. In spite of the fact that, in a moderate response constrained process, these groups develop to huge single crystal in ethoxy-acetic acid derivation solutions [137].

Table 2.1: ZAH derived precursors groups with their Partial charge distribution  $\delta_i$  in based on H-L model based estimations using Allred-Rochow electronegativity ( $\chi_0 = 3.5, \chi_c = 2.5, \chi_H = 2.1, \chi_{Zn} = 1.66$ ); where,  $EtO = OC_2H_5$  ligands,  $\chi_m$  = mean electronegativity

Precursor clusters	$\delta_{Zn}$	$\delta_{Ac}$	$\delta_{H_2O}$	$\delta_{OEt}$	$\delta_{OH}$	$\chi_m$
$Zn(CH_3COO)_2 \cdot 2H_2O$	0.471	-0.227	-0.011			2.485
$Zn(CH_3COO)_2$	0.469	-0.235				2.482
$Zn_4O(CH_3COO)_6$	0.467	-0.245				2.479
$Zn_{10}O_4(CH_3COO)_{12}$	0.465	-0.254				2.476
$Zn_5(OH)_8(CH_3COO)_2 \cdot 2H_2O$	0.463	-0.269	-0.027		-0.22	2.471
$Zn_{10}O_4(CH_3COO)_{12} \cdot H_2O \cdot 7EtOH$	0.429	-0.462	-0.111			2.412
$EtOZn \cdot CH_3COO$	0.411	-0.567		0.16		2.379

## 2.6 Morphological variations of ZnO NSs

Various morphologies of ZnO NSs can be developed by altering the different process parameters such as precursor chemicals and growth solutions of hydrothermal synthesis. The morphological variation of the nanomaterial have great impact on the desirable properties of resulting materials. Some of the major morphology types and details of their synthesis or properties are discussed in this section.

### 2.6.1 Nanoparticles

Despite the fact that the organo-metallic blend of nanoparticles of ZnO in atmosphere of alcohol has gotten more extensive acknowledgment for reasons of speedier nucleation and development when contrasted with water. In this survey the distinguished reports of aqueous amalgamation in fluid medium are presented. Baruwati et al. [138] revealed the liquid amalgamation of nanoparticles of zinc oxide utilizing  $Zn(NO_3)_2 \cdot 6H_2O$ . Blend was done in autoclave at 120°C in the wake of changing the pH to 7.5 utilizing  $NH_4OH$ . In the wake of cleaning, the particles were kept at 80°C medium-term for procuring into the powdered form by drying. Bhattacharyya et al. [139] first uncovered that nanoparticles of ZnO can be used for potential antimicrobial applications, they investigated the antimicrobial and characteristics of ZnO nanoparticles to bacterium *Streptococcus pneumoniae*. ZnO nanoparticles demonstrated solid antimicrobial properties against *S. pneumoniae*, with a minimum inhibitory concentration (MIC) estimation of 40 *lg/ml*. The literature shows that sub-MIC dosages of ZnO nanoparticles show antagonistic behavior towards biofilm activity of *S. pneumoniae*. Along these lines, ZnO nanoparticles may fill in as a major aspect

of a blend treatment contrary to medicate resistant *S. pneumoniae* contaminations, where biofilm arrangements accept an essential part in disease progression. Das et al. [140] arranged organic-inorganic heterogeneous hybrid anion leading films utilizing 1,4-diglycidyl butane ether with the aid of synthetic nanoparticles of  $SiO_2$  onto polyvinyl alcohol (PVA). They showed that PVA cross-connected with at room temperature added to the DGBE and  $SiO_2$  upgrade of rigidity and conductivity in comparison to their uncross-connected portion. Deka et al. [28] effectively created Wood polymer nanocomposite by utilizing HDPE, LDPE, PP, PVC, wood powder, polyethylene-co-glycidyl methacrylate, and diverse nano-sized particles of ZnO, clay, and  $SiO_2$ . By the joining of such nanoparticles the UV protection properties get enhanced. Bacterial deployment of composite was also enhanced by the aid of clay and nanoparticles. Brintha et al. [2] effectively synthesized nanoparticles of ZnO by various strategies such as hydrothermal techniques, sol-gel method and aqueous emulsion and the arranged nanoparticles were analyzed by SEM, EDX, XRD and UV. Figure 2.1(a) outlines the SEM results of zinc oxide nanoparticles produced by aqueous solution technique. The image indicates spherical and flower like structure. Figure 2.1(b) demonstrates SEM pictures of the ZnO nanopowders arranged by sol-gel technique. The ZnO nanoparticles have blossom like shape. Similar outcomes were observed in structural and optical portrayal of nanopowders of Ni and Ni-Al co-doped with ZnO orchestrated by means of the sol-gel process [141]. Figure 2.1(c) demonstrates the SEM image of ZnO nanoparticles arranged by hydrothermal strategy. The zinc oxide particles arranged are round shape. It likewise demonstrates that a network formation of the zinc oxide nanoparticle has occurred which clearly shows that agglomeration has occurred. Ramimoghadam et al. [142] produces NSs of ZnO by means of hydrothermal technique utilizing uncooked rice (UR) form as a bio-resource that can be used as bio-template for directing the morphology of nanoparticles. The influences of the rice on ZnO properties were investigated. Mechanics of the development of the ZnO crystal is conceivable coordinated by conjugated and contending amalgamation of Zn and starches.

### 2.6.2 Nanorods and Nanowires

Nanorods and nanowires of metal oxides have been developed by various researchers to achieve tailored properties for high performance material applications. Some of the prominent work is discussed in this section. Most of the researchers use hydrothermal technique for enhanced morphologies of ZnO NSs. Deka et al. [36] adequately made CuO nanowires encapsulated in WCF polyester resin composites utilizing vacuum assisted resin transfer

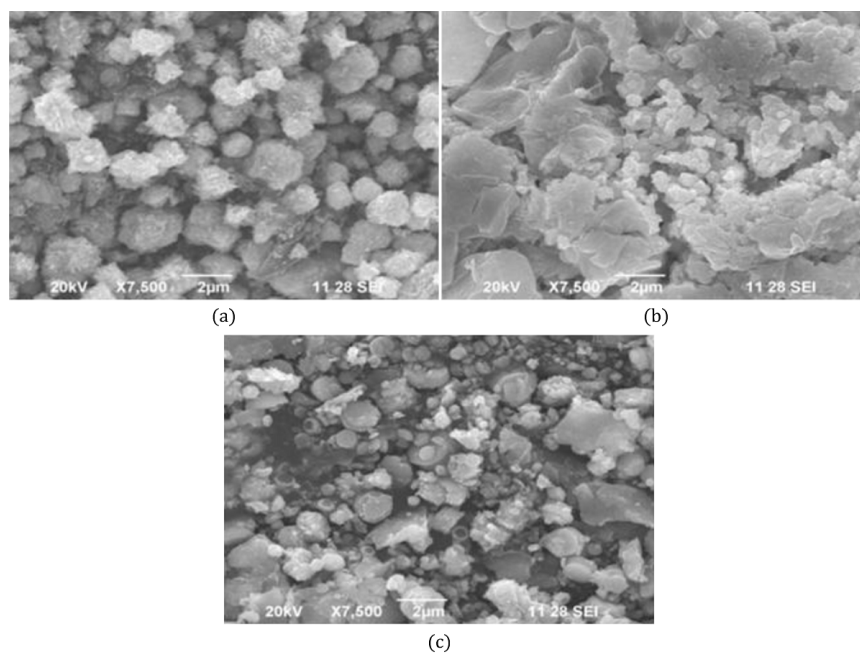


Figure 2.1: (a) SEM image of ZnO nanoparticles (Aqueous solution method), (b) SEM image of ZnO nanoparticles (sol-gel method), (c) SEM image of zinc oxide nanoparticles (hydrothermal method) [2]

molding (VARTM) procedure. Initially, seeding of CuO on WCF was done then nanowires on that portion were allowed to grow via hydrothermal synthesis. The development of nanowires completely depends upon the seeding cycles and there are no influences of concentration of development solution and development time on the growth of nanowires. Due to the development of nanowires on WCF, properties like strength and tensile modulus increased by 42.8% and 33.1%, respectively. Ko et al. [3] demonstrated nanoforest by means of a simple selective hierarchical development that would fundamentally enhance the efficiency of DSSC power converter. Developed nanoforest consist of high density long branched tree-like various leveled crystalline ZnO photoanodes. The effectiveness of overall light transformation and short circuit current density of the stretched nanowires DSSCs were appropriate around 5 times greater than the productivity of upstanding ZnO nanowires. The productivity augmentation is because of significantly enlarged surface territory enabling greater dye stacking and light collecting, and in addition diminished charge recombination through direct conduction along ZnO nanotree branches. The foundation of leveled ZnO nanoforest is basically a cluster of vertically adjusted long ZnO nanowires as shown in Fig. 2.2. Furthermore, Fig. 2.2b, 2.2c portray the "seed effect" and Fig.



2.2d, 2.2e exhibit the "polymer removal effect". Hazarika et al. [143] effectively created

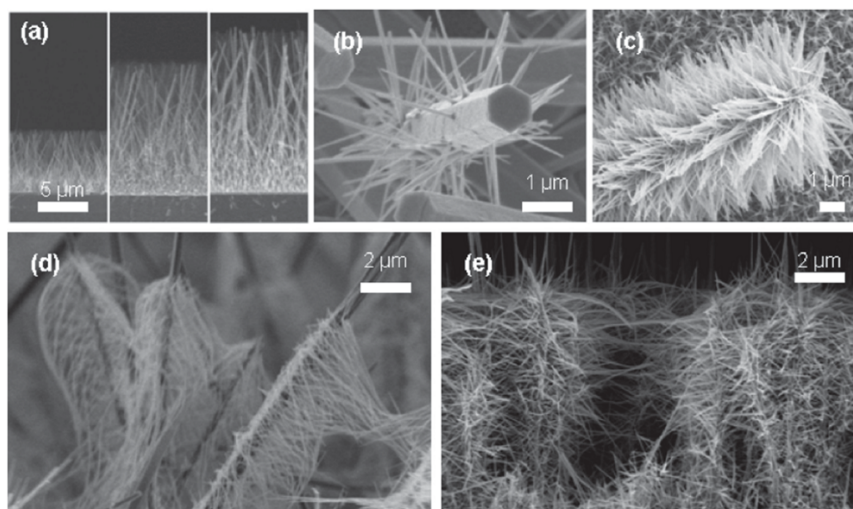


Figure 2.2: SEM image of ZnO nanowires (a) Growth of length (b) with no seeds (c) with seeds after polymer removal (d) without polymer removal and (e) with polymer removal after seed nanoparticle deposition [3]

ZnO nanorods on woven kevlar fiber (WKF) via hydrothermal strategy as a way to upgrade the interfacial stronghold of aramid composites. Initially the WKF was treated by surface hydrolysis and an ion-exchange procedure to consolidate  $\sim\text{COOH}$  group on the filaments of WKF to upgrade the attachment of ZnO to main strands. Dependency of development of ZnO nanorods was examined by SEM results and it was found that the development of nanorods completely relied upon quantity of seeding, time for treatment and the convergence of ZnO utilized. The impact of time, pH, molar concentration, and temperature on the morphology of ZnO NSs was considered by Amin et al. who detailed consistent and enduring development of ZnO nanorods up to 10h of synthesis [144]. Kong et al. [37] created ZnO nanorods on WCF utilizing hydrothermal strategy. The VARTM technique was utilized to totally mix the ZnO/WCFs with polyester resin. The test results demonstrate that the developed ZnO will enhance the energy absorption because cross connected network transfers energy through interfaces and also enhances the load exchange and interfacial strength. Ruqeshi et al. [145] successfully developed a piezoelectric nanogenerator by producing ZnO nanorods on inner side of horizontal quartz tube. Nanorods were successfully made and used as an alternating electric current producer. Tube-in-tube chemical vapor deposition (CVD) technique was used to grow 3-5g of ZnO nanorods in every cycle which is sufficient to respond to mechanical stress by producing current. Salahuddin et al.

[146] effectively created ZnO nanotube with mean external diameter and span of 200nm and 2.4 $\mu$ m separately by hydrothermal strategy. The FTIR demonstrated the characteristic absorption groups at 508 and 404 $cm^{-1}$ . These two retention peaks connect with the mass To-phonon frequency and the Lo-phonon frequency. The XRD investigation affirmed that the ZnO nanotubes have the hexagonal wurtzite structure. The optical properties were estimated by UV spectroscopy. Ghasaban et al. [147] experimentally accomplished needle-like and plate-like morphologies of ZnO in a higher scale (60g) of creation by means of a hydrothermal response performing in low temperature of 115°C and low response time of 2 or 6h. They suggested that the hydrothermal response can be a reasonable technique to orchestrate ZnO NSs with the particular size and morphology and it is able to do simple scaling up. When ammonia (pH = 9) is utilized as an anionic antecedent, a needle-like morphology with a mean diameter 240nm is shaped. As the anionic antecedent was supplanted by sodium hydroxide (pH = 13), the morphology is changed to plate-like NSs with mean diameter under 50nm. XRD investigations of ZnO nanoparticles appeared as in Fig. 2.3. Both ZnO NSs have comparative XRD designs, aside from relative pinnacle intensities, because of their irregular orientation. XRD designs were recorded by hexagonal wurtzite shape of ZnO ( $a=3.249\text{\AA}$ ,  $c=5.206\text{\AA}$ ; JCPDS card no. 36-1451). XRD results displayed sharp and solid signals supporting that the item is an exceedingly crystalline material. Utilizing Scherrer condition, the crystallite size (L) of the particles can be resolved as follows [148]

$$L = \frac{K\lambda}{\beta_s} \cos\theta \rightarrow \cos\theta = \left(\frac{K\lambda}{L}\right) \cdot \left(\frac{1}{\beta_s}\right) \quad (2.7)$$

Where, L is crystallite size in nm,  $\lambda$  is the radiation wavelength 1.540 for  $CuK\alpha$  in  $\text{A}^0$ ,  $\beta_s$  is the full width (at half-maximum) of ZnO diffraction crest profile in radian,  $\theta$  is the diffraction angle (top position) and K is the shape factor ( $0.89 < K < 1$ ) which is viewed as 0.94 here. It is important to decide the instrumental expanding and correct the deliberate  $\beta$  as following:

$$(\beta_s)^2 = (\beta_{measured})^2 - (\beta_{instrumental})^2 \quad (2.8)$$

As indicated by Scherrer condition, the crystallite size can be acquired by plotting  $\cos\theta$  versus  $\frac{1}{\beta_s}$  and figuring L parameter from the slant of regression line going through the origin facilitates. The other technique is directed by making logarithm on both sides of equation (2.7) as follows [149]

$$\beta_s = \left(\frac{K\lambda}{L}\right) \left(\frac{1}{\cos\theta}\right) \rightarrow \ln(\beta_s) = \ln\left(\frac{K\lambda}{L}\right) + \ln\left(\frac{1}{\cos\theta}\right) \quad (2.9)$$

By drawing  $\ln(\beta_s)$  versus  $\ln(\frac{1}{\cos\theta})$ , a straight line with a slant of around one and an intercept ca.  $\ln(\frac{K}{L})$  must be found. Yilmaz et al. [150] viably applied hydrothermal technique and chemical spray pyrolysis to successfully create nanocubes and nanorods. Amount of  $Zn^{2+}$  ion assumes a critical part for different shapes of the nanoparticles. Presence of nanoparticles of ZnO indicates great photo-iridescence so that synthesized product can have optoelectronic utilities. Grain size (D) and dislocation density ( $\delta$ ) have been estimated with the help of mathematical relations given by Scherer as mentioned below [151].

$$D = \frac{0.9\lambda}{\beta \cos\phi} \quad (2.10)$$

$$\delta = \frac{1}{D^2} \quad (2.11)$$

In above relations,  $\lambda$  represents incident X-beam's wavelength,  $\beta$  represents FWHM and  $\phi$  represents Bragg's angle.

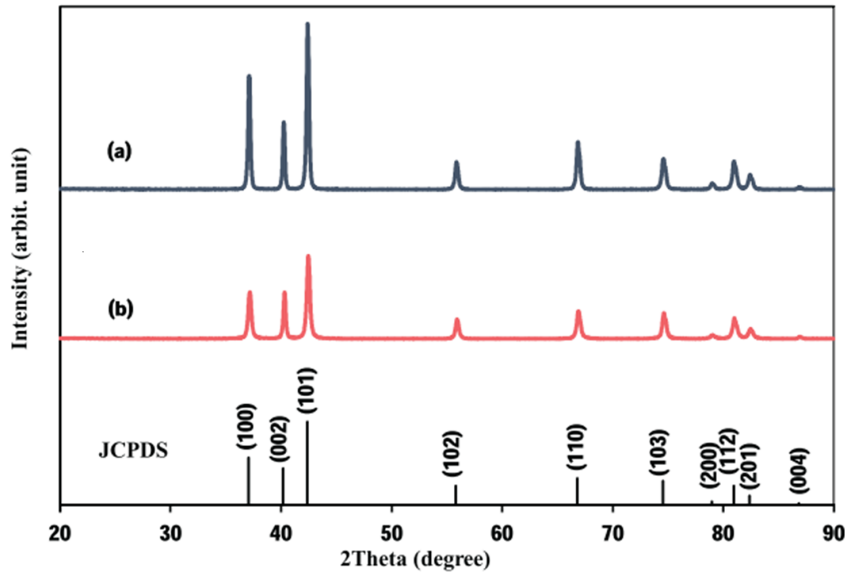


Figure 2.3: XRD results of (a) needle-like (b) plate-like ZnO NSs [147]

### 2.6.3 Blossoms and cabbage-like NSs

The NSs like as blossoms are extremely rare of zinc oxide and can be created utilizing hydrothermal techniques. The development of blossoms like ZnO utilizing hydrothermal

technique was revealed by Yoo et al. [152]. They demonstrated amalgamation of nanopowders of CuO on high surface region of ZnO blossoms via hydrothermal technique. Resulting materials had exceptionally sensitive dimethyl methyl phosphate (DMMP) gas detecting qualities. Affirmation of the arrangement of CuO/ZnO heterojunction was assessed by PXRD and TEM examinations. Figure 2.4 indicates the results of SEM examination of both ZnO and CuO/ZnO morphologies in the function of time. Blossom molded ZnO structures were framed and by expanding ZnO production time, the span of the bloom expanded from around  $\sim 3-3-10\mu\text{m}$  in diameter. In the wake of blending of CuO in ZnO blooms, CuO nanoparticles were consistently kept of the top of the blossoms as depicted in the Fig. 2.4(d-f). Xu et al. [153] successfully grown hierarchical ZnO crystals on polyimide (PI) film without any additional seeds under hydrothermal condition. The morphologies of ZnO crystals can be tuned just by changing the concentration of zinc ion solution. Stearic acid (SA) can self-assemble into nanoflowers when ZnO modified PI film was immersed into SA solution. The surface wettability of the films was tuned by the self-assembly of SA. On the contrary, concentration of Zn exhibits a significant role in determining the morphologies of ZnO on PI film. For better understanding the surface wettability transition of PI(ZnO-SA) films, they further investigated their surface morphologies. Compared with PI(ZnO) films, newly belt or sheet-like morphologies were found. Original morphologies of ZnO flowers on PI film show slight change after stearic acid (SA) solution immersing procedure, which is attributed to the wet chemical fabrication process in the presence of SA [154]. Guo et al. [155] proposed a novel method for the selective growth of 3D ZnO flower-like NSs. The flower-like structure could be varied by adjusting hydrothermal reaction conditions and laser irradiated parameters. This approach offers synthetic flexibility in controlling film architecture, coating texture and crystallite size. The control of flower density is another important aspect in spatial organization. It is also worth to mention that no NSs are observed in the un-irradiated area. Abdelfatah et al. [156] detailed the creation of ZnO clusters using hydrothermal technique which developed vertically on FTO substrates. Molarity of KOH guided the strategy of development procedure. The outcomes demonstrated that ZnO exhibits along [0 0 2] plane. These ZnO rod clusters next to lowest diameter will create the favorable optoelectronic systems. ZnO nanorods and nanoflowers gives high extent of volume to surface with respectably high sensitivity both are required to great extent of practical and redesign sensor execution in characteristic appliances [157]. Fan et al. [158] viably made enormous measure of nanoflowers of ZnO on *graphene/SiO<sub>2</sub>/Si* substrate by aqueous technique. Findings of the XRD examination conforms the presence of pure wurtzite stage in nanoflowers. Star-like morphology were

seen in the prepared nanoflowers of ZnO. ZnO nanoflowers were displayed in narrow band gap in comparison to powders of ZnO because of the presence of O-vacancy.

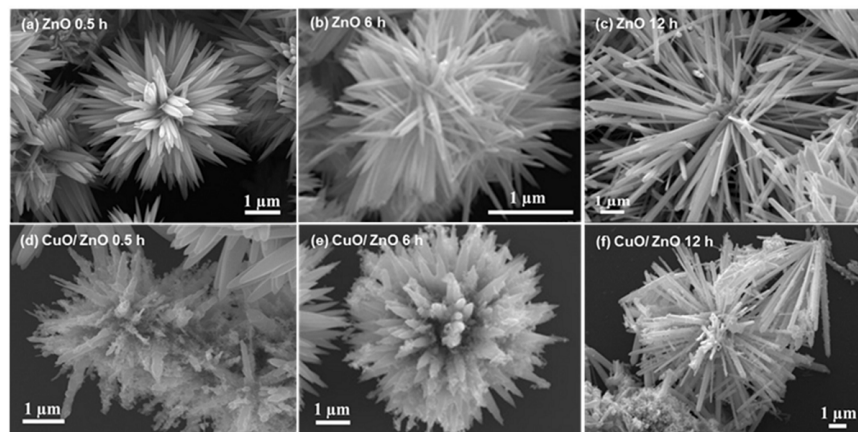


Figure 2.4: SEM images of the surface morphology of both (a–c) ZnO and (d–f) ZnO/CuO structures as a function of ZnO synthesis time [152]

Venkatesha et al. [159] utilizes electrochemical strategy to orchestrated bloom molded zinc oxide microstructures. Controlled development of these structures was conceivable at bring down current densities and electrolyte focuses. Notwithstanding, sporadic development occurred at higher current density with a little abatement in the band gap of this semiconductor. Sun et al. [160] mentioned an easy aqueous strategy to specifically create bloom-like microstructures of ZnO via high photocatalytic movement. By changing the molar extents of  $Zn^{2+}$  to caustic soda, morphologies of the acquired samples can be controlled. At a point, when the free  $[Zn(OH_4)]^{2-}$  contents were satisfactory, the hexagonal biprism-like and bar-like shapes were developed. Be that as it may, the conditions of ZnO center would change into oblate-like, nut-like, hexagonal circle-like and blossom-like when the free  $[Zn(OH_4)]^{2-}$  contents were for the most part phenomenal. Additionally, bloom-like examples display great photocatalytic movement for decoloration of methylene blue (MB). Pant et al. [161] successfully utilizes the facile one-pot hydrothermal process for blending blossom shaped ZnO particles progressively collected with Ti and Ag nanoparticles. The developed composite demonstrated brilliant photocatalytic execution which is credited to a moderate electron acceptor supporting the trading of photogenerated electrons from the conduction band. The size of the produced structures diminished by adding  $TiO_2$  and  $AgNO_3$  blend in hydrothermal framework. The conceivable reason for reduction in bloom size may be because of the reduction in per unit volume of ZnO concentration in aqueous

course of action. Liu et al. [162] prepared diverse blossom-like ZnO hierarchical designs by  $C_4H_6O_6$  (Tartaric acid, TA) aided hydrothermal technique particularly four bloom shape NSs were gotten all the while under a similar response condition. When spherical shaped nanoparticles get amassed then the resulting structure looks like a cauliflower shaped ZnO. Similarly by gathering of hexagonal rods and prism, other blossoms-like structure can be developed. TA goes about as a topping operator and structure-coordinating agent in the midst of combination. Affirmation of the oxygen opening for the most part originates from the ZnO surface as explained in XRD, PL and Raman spectra. The blossoms-shaped specimens of 1 : 4.5 and 1 : 3 with the higher aspect proportions have most astounding photocatalytic execution. The upgraded photocatalytic execution is predominantly incited by oxygen opportunity of ZnO.

#### 2.6.4 Miscellaneous shapes

Several other shapes of the NSs such as nanodumbbell, nanoflakes, nanodisk, twinned dumbbells and double disk have been developed by prominent researchers. Guo et al. [163] effectively produced the twinned ZnO disks using Cetyltrimethyl Ammonium Bromide (CTAB) assisted aqueous technique at lower temperature. Literatures recommended that, by the expansion of duration of development, the size and intensity of UV NBE peak diminishes. For the imperfection associated visible outflows, it increment with the time taken for development. In light of the preliminary outcomes, CTAB and improvement temperature are proposed as main segments for the formation of twinned plates molded ZnO. Wang et al. [4] incorporated dumbbell-formed ZnO microstructures by utilizing an effortless aqueous technique. The obtained shape of ZnO was around 5-20 $\mu$ m in length and diameter of two closures and center part was around 1-5 $\mu$ m and 0.5-3 $\mu$ m, separately. Figure 2.5 represents different magnified pictures of SEM examination of produced dumbbell-like ZnO. Sun et al. [164] effectively developed twinned blossom like ZnO structure by CTAB helped low temperature aqueous technique. The principle emanation peaks is identified with the bound exciton recombination of the acceptor as demonstrated by the temperature dependent PL spectra. It also demonstrated a decent crystal nature of specimens. In perspective of the preliminary outcomes, the self-etching and regrowth are proposed as the reason behind the improvement of stream-like structures. The trailing effect of as-developed twinned bloom like ZnO structures are outlined in Fig. 2.6(a). The magnified twinned bloom-like ZnO structures is portrayed in Fig. 2.6(b). The outside forms of the twinned bloom-like ZnO particles exhibited the hexagonal profile, as differentiated from

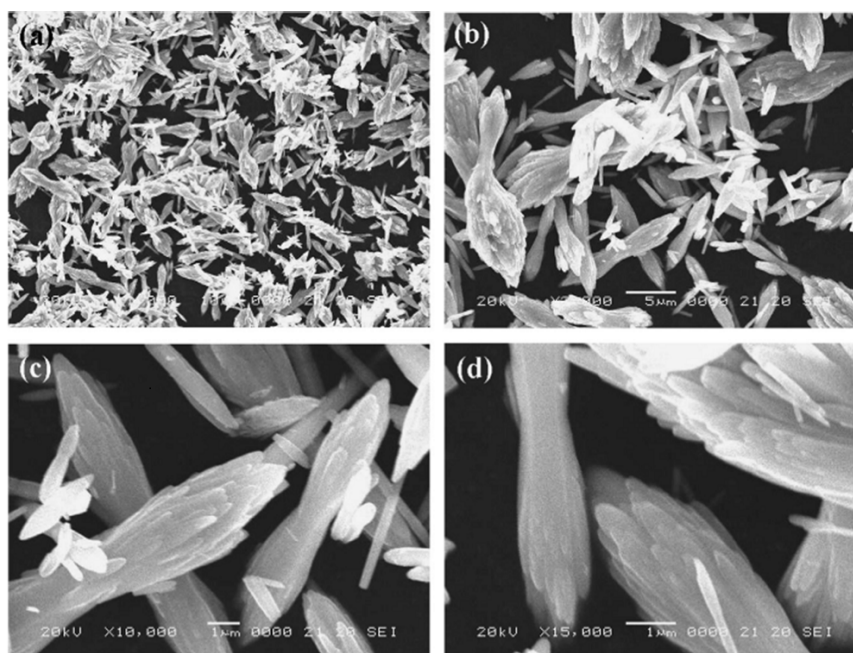


Figure 2.5: SEM analysis of dumbbell-shaped ZnO at various magnifications: (a) and (b) low magnification; (c) and (d) high magnification [4]

the double-disk molded ZnO in Fig. 2.6(a). The bloom shape is made of little wafers that are enclosed by an empty hexagonal ZnO. A hexagonal nut structure delineated in Fig. 2.6(c) is the base to shape bloom-like structures. Kumar et al. [165] developed an innovative idea to grow ultrathin ZnO nanoflakes to prepare a tip based tool by hydrothermal assisted electrochemical discharge deposition process. In the same way researchers are developing hybrid process in corporation with hydrothermal process for better morphologies of ZnO NSs.

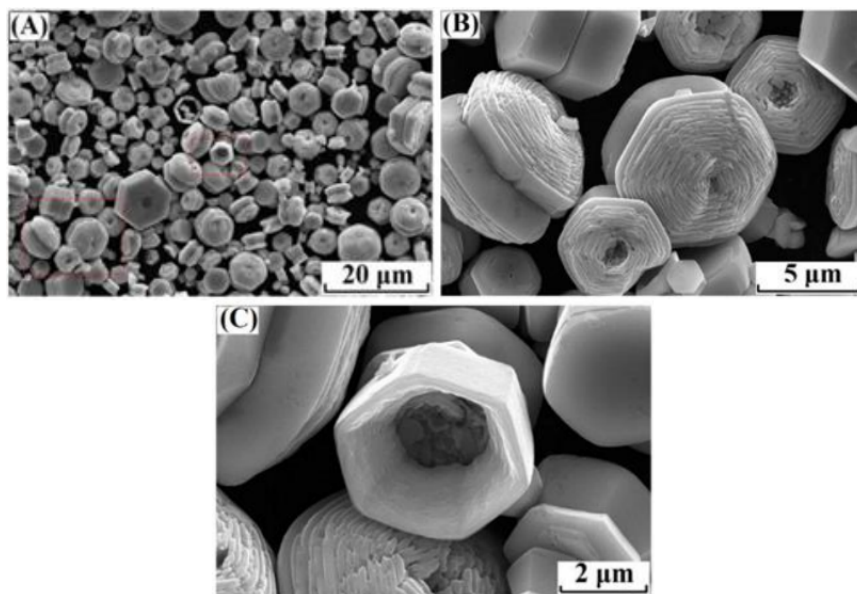


Figure 2.6: (a) SEM image of ZnO NSs; (b) twinned flower-like ZnO; (c) hexagonal nut structure [164]

## 2.7 Microwave assisted hydrothermal synthesis

Another technique for creation of NSs which is accepting a considerable measure of intrigue of late is the utilization of microwave warming instead of regular warming. Utilization of microwaves based heating for amalgamation provides basis for synthesizing ZnO NSs in field of high performance nanostructured materials for varied applications [166, 167, 168, 169]. Zhu et al. [170] effectively incorporated ZnO rod-amassed microspheres by means of a basic microwave-helped aqueous strategy. The as-arranged ZnO structures have astounding optical features and high photocatalytic action than conventional ZnO for deployment of MB under UV illumination, which can be ascribed to basic contrast, considering morphology, surface features and surface imperfections. The utilization of microwave aqueous amalgamation in modern situations may constitute an imperative commitment to the improvement of a green chemistry idea in industrial blend technology [171]. Witkowski et al. [172] integrated all around adjusted ZnO nano/microrods with indistinguishable crystallographic introduction on a c-plane GaN template, utilizing a microwave-assisted aqueous technique at 50°C for term of 2 minutes. In the meantime, this technique empowers a more prominent level of control over the diameter and thickness of the nanorods. Two-dimensional ZnO nanosheets and one-dimensional drib-



ble pipe-like, baseball bat-like, gear-like, bud-like, grenade-like, prism-like, bamboo-like, brush-like, arrow-like, pencil-like, strolling stick-like, taper-like, shuttle-like, and hollow pinnacle-like ZnO nanorods with different tips were combined by a basic hydrothermal course from the system of  $CO(NH_2)_2^{2-}N_2H_4$  [173]. Liang et al. [5] detailed a clear, single-step, microwave-aided hydrothermal technique to create ZnO NSs with inconsistent morphologies. Balancing of  $[Zn^{2+}]$  in solution precursors with no auxiliaries will allow to create urchin-shaped, blossom-shape, seven-spine and rod-like ZnO. Samples of ZnO were furthermore organized with contrasting  $[Zn^{2+}]$  under a similar microwave illumination situation as represented in Fig. 2.7. The great command of the MAH amalgamation parameters similar to time, temperature and solvent of amalgamation response kept the primary ZnO hexagonal wurtzite stage. In any case, the concentration of Zn precursor as well as solvent time and amalgamation temperature influence the morphological structure creating rounded plates, producing plates, brush-like and 3D blossoms [174]. Caglar et al. [175] explored that in the microwave-helped hydrothermal strategy illumination time influenced the diameter of nanorods and orientation degree while, pH value totally changed the molecule size and shape. The nanorods at first glance vanished after a little measure of decreasing in pH value. The adjustments in stoichiometry connection amongst  $Zn^{2+}$  and  $OH^-$  directly influence the morphology of the final structures [176].

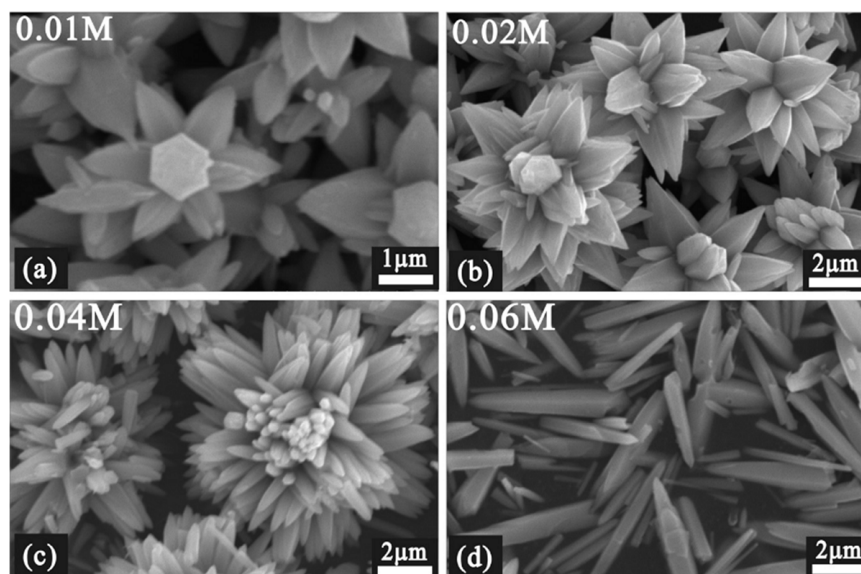


Figure 2.7: Impact of  $[Zn^{2+}]$  on grown ZnO NSs (a) 0.01, (b) 0.02, (c) 0.04 and (d) 0.06 M [5]

## 2.8 Doping in metal-oxide NSs

For controlling properties like band gap, ferromagnetism and electrical conductivity, some essential steps have to be taken in the form of doping of semiconducting nanostructured materials [177]. A great deal of enthusiasm from analysts for conceivable applications in optics, electronics and visible light photocatalysis are produced by doping of transition metal of II-VI and III-V categories [178]. Remarkable works have been done by the researchers in the field of doping of ZnO single crystal and thin films by transition metal [179, 180, 181]. To enhance photocatalytic movement, ZnO nanowires were altered by Co doping and CuS was coupling by means of a progression of advantageous hydrochemical reactions. In any case, a couple of reports on the blend and portrayal of doped ZnO NSs with various dopants like Co, Al, Mn, Ga, Cu, Sb, and so forth are accessible in the literature [182, 183, 184, 185]. The measure of doping is a conspicuous factor for fitting the properties of the NSs, there must be a conceivable method to control the morphology and doping fixation [186]. Hwang et al. [187] controlled the morphology and doping centralization of P-doped ZnO NSs sequentially framed on the top sides of undoped ZnO nanorods by means of aqueous technique. Ajala et al. [188] reasoned that, to the extent the optoelectronic highlights are concerned, Al doping initiated a blue move of the band gap and a cathodic move of the quasi Fermi level. Notwithstanding, as the degree of these adjustments was too low, it was inferred that the optoelectronic highlights did not assume a huge part in the upgraded photocatalytic action of the powders. Then again, the nearness of surface defectivity initiates high water fondness of the Al adjusted samples. Mendez et al. [189] arranged the C-doped photoactive circular  $TiO_2$  and ZnO semiconductors by microwave-helped solvothermal amalgamation. They prepared two C-doped  $TiO_2$  and ZnO tests with an unmistakable red-move in the vitality band gap of the semiconductors, essentially in  $TiO_2$  based materials. Literature inferred that fitting of the crystalline stage, morphology, and porosity qualities can be accomplished by microwave-helped blend and consequently, this system is a promising outline device for the planning of C-doped mesopore photoactive semiconductors with a blend of anatase and rutile stages. An easy citric acid-mediated aqueous course has been utilized for blend of Eu-doped bloom-like ZnO progressive structures by Sin et al. [190]. Sathya et al. [191] effectively arranged Pb doped ZnO semiconductor NPs by the straightforward chemical precipitation technique. XRD examination affirmed that the crystallite size expands persistently to 10 (wt%). SEM outcomes affirmed the microstructural change from nanoparticle to rod-like microstructure on 10 (wt.%) Pb dopant. The aqueous synthesis of undecorated and Ag improved ZnO

nanorods were accounted for by Wei et al. [192]. Byun et al. [193] revealed that titanate NSs doped with Nb having upgraded photocatalytic movement under visible light illumination were effectively integrated by an aqueous procedure utilizing  $TiO_2$  and  $Nb_2O_5$  powders. Blended Nb-doped titanate NSs were made out of nanotubes, nanosheets, and  $TiO_2$  NPs. They had organized a structure, with  $TiO_2$  NPs at the center site, and titanate NSs went head to head with bordering titanate NSs. The fluorescence discharge is likewise adjusted upon gallium doping prompting an adjustment in the relative power, which persists for higher measures of dopant [194]. The room temperature ferromagnetism (RTFM) with upgraded polarization and coercivity in the Tb and co-doped ZnO nanoparticles were accounted for by Das et al. [195]. Chen et al. [196] detailed that the gas detecting features of silver-doped sensors were great astounding than unadulterated, and the sensor of 1.0 wt% silver-doped ZnO ocean urchin-like NSs demonstrated the most raised response to ethanol with bring down fixation of 10 ppm at 260°C. The reasons were that ocean urchin-like structure could give broad specific surface locale and the doping extended flaws at first glance; both of them could assemble the consumed oxygen species.

## 2.9 Potential applications of metal-oxide NSs

Different applications based on the ZnO hierarchical architectures are photocatalysis, field emission, electrochemical sensors, supercapacitors, antibacterial agent and electrodes for lithium ion batteries [197, 198, 199, 200]. Various morphologies of ZnO NSs possess novel benefits of large surface area, permeable designs, and interdependent associations of the comprised nano-sized parts. Subsequently, ZnO NSs have tailored chemical and physical features, which are profoundly required for diverse applications [201, 202, 64]. Following are the most prominent regions where ZnO NSs are exceptionally consolidated as portrayed in Fig. 2.8. The detailed description of significant application fields with examples are discussed in this section.

### 2.9.1 Photocatalysis

Catalysis are considered as a significant tool in reducing harmful products arises from industries like refinery, food, petrochemical, and environment pollution [203, 204]. Photo-irradiation under UV visible source is the prime solution to expand the pace of photocatalysis process along with specific semiconductor photocatalyst under specific circumstances. Different application fields such as green organic synthesis, air and water treatment, renew-

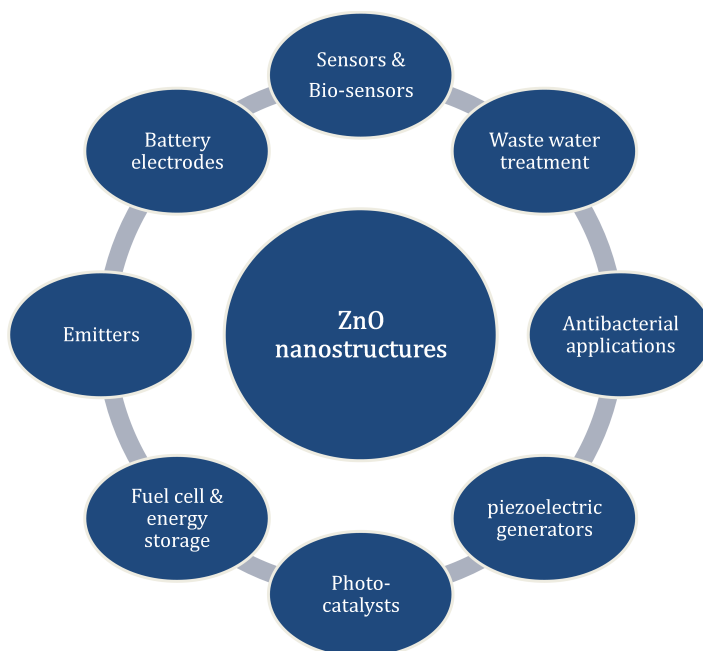


Figure 2.8: Utilization range of ZnO nanostructured materials

able energy,  $CO_2$  reduction and self-cleansing phenomenon are using ZnO photocatalyst for better outcome [205]. A pictorial representation of potential application of ZnO photocatalysts are outlined in Fig. 2.9.

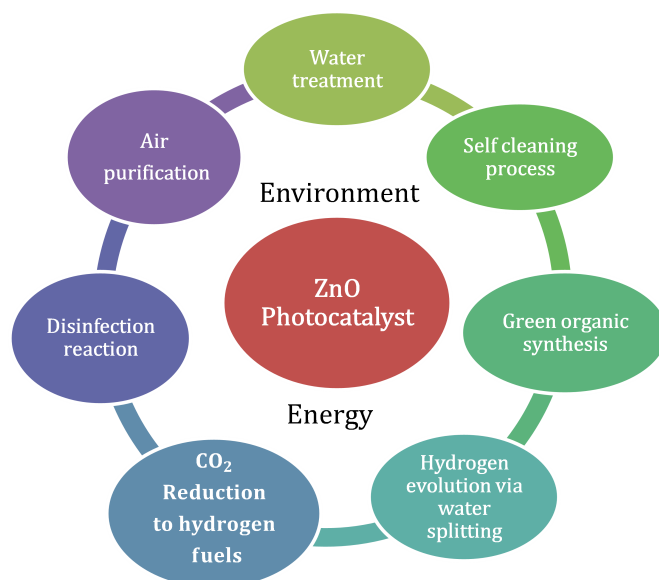


Figure 2.9: Major fields for utilization of ZnO photocatalyst

### 2.9.2 Field emission

These devices exhibit various benefits, like low power utilization, protection from fluctuation of temperature and radiation, less thermionic emission, less dissipation of energy, micro-sized and nonlinearity, and remarkable characteristic of current and voltage behavior which shows significant variation of emission current at low voltage changes [206, 207]. ZnO NSs incorporated in field emission were studied by Umar et al. [208] and they reported the growth of ZnO nanoflowers by thermal evaporation on Si-substrate and concluded that incorporation of ZnO NSs shows efficient field emission properties for device applications. Several researches were performed to assess the feasibility of different morphology of ZnO NSs on field emission devices and it was revealed that the development of ZnO NSs causing the great emission properties and promoting connection with integrated circuits as well as vacuum device applications [64, 209, 210].

### 2.9.3 Sensors

Industries like biotechnology, food processing and pharmaceutical sciences require non-stop observation of biological phenomenon occurring during biological reactions. In such manner, the growth of different sensors such as electrochemical sensors exhibit novel benefits such as large detection span, quick response, continuous observation, controlled manufacturing at less capital and reproducibility [211]. In these devices, concepts of electro-analytical processes are used which provide quality investigation and sensing under the variation of potential and their resulting current. There are various techniques such as linear scan voltammograms and electrochemical impedance spectroscopic techniques which are used for efficient application of ZnO based sensors in biological applications [212]. Doped-ZnO hybrid sensors have high sensitivity and reproducibility which are used for gas sensing applications and also applied in biomedical industries [213, 214, 215].

### 2.9.4 Lithium ion batteries

In the present scenario of increasing population and industries, demand of high energy and climate balance for sustainable environment is becoming a big challenge for researchers. Thus they are investigating the development of renewable energy source and their conversion and storage systems also [216]. ZnO NSs materials are now a days very promising materials for energy storage application such as batteries [217]. Li-ion batteries are perhaps the main energy storage system which overcome the problems of electronic industries

and furthermore have application in hybrid vehicles. Materials for high performance electrodes are prominent active material which influence the overall response of the batteries thus the development of electrode materials are again a challenging task for researchers [218, 219]. ZnO NSs and doped ZnO NSs electrode materials are promising materials for high performance electrodes because of great optoelectronic properties, low cost, nontoxic and abundance. On a basic level, the response among lithium and ZnO anodes happens under the purported system of "conversion phenomenon" [220]. In the process of lithiation, the ZnO anode produces  $Li_2O$  by conversion reaction implanted with nanosized metallic zinc groups [221].

### 2.9.5 Antibacterial application

The high biocompatibility and magnificent antimicrobial features of ZnO makes it as a prominent antibacterial agent [222]. Especially, ZnO NSs exhibits better results from the antibacterial application on Gram-negative and positive bacteria [223]. Nonetheless, the exact study of antibacterial phenomenon of ZnO is still under process, in this way confining the complete utilization of ZnO as an antibacterial material [224]. Recent and upcoming examinations on ZnO NSs based antibacterial system can provide the basis for specific application on antibacterial work but in future ZnO can be a promising agent for clinical usage after upgrading the investigations and overcoming the challenges.

### 2.9.6 Supercapacitors

Another class of energy storage device is "supercapacitors" which possesses high importance in view of its rate of quick charging and discharging, high service span and high capacity of power. Due to these features supercapacitors are mostly used for backup source of energy, emergency source of energy and hybrid transport systems [225]. Nano-sized particles available in the nanocomposite materials are responsible for low ionic dissemination and less transfer of energy which is very much required to produce supercapacitors [226]. Nanocomposite materials having high specific capacitance value and service span are broadly utilized for developing supercapacitors. Yun et al. [227] reported electrospinning technique to develop  $ZnMn_2O_4$  electrode having one dimensional hollow NSs which produces high crystallinity. The developed electrode shows 100.8% of capacitance retention which is a remarkable cycle performance for different electronic systems. Guerra et al. [228] fabricated ZnO coated carbon nanomaterial to develop an electrode for supercapacitor using laser technique. The finding of their experiments reveals that the electrodes are

independent of thickness of deposited ZnO but ZnO film improves the specific capacitance and retention values which provides basis to use ZnO as a low cost potential material for supercapacitors.

### **2.9.7 High performance composite materials**

Researches are going on to implement such distinguished properties of ZnO NSs into the field of high performance composite materials. Some of the prominent applications of such composites are in aviation industries due to improved mechanical properties especially impact strength [27]. Continuous improvements of such materials will take the materials applications into different level such as in robotics and artificial intelligence, sensors and biomaterials, micro-electronics and photonics and defense and artillery [229]. Recent advancements in the fabrication of ZnO NSs on the WCF lead towards the numerous applications in comparison to the natural carbon fibers [230, 231] and more advanced development status compared to metal and ceramic counterparts, in addition to their unique properties [232, 233]. Application ranges of polymer nanocomposites are represented in Table 2.2. As it can be clearly discovered, the prominent usages of nanocomposites are huge, consisting of evolution of advanced materials and the quality advancement of components like sensors, cells and super-capacitors. Still there is least application of nanocomposites in industries but advancements of these material from research to industry is growing and in coming few years it is expected to be extensive.

Table 2.2: Application area of Polymer based Nanocomposites

<b>Nanocomposites</b>	<b>Applications</b>
Polyimide/ $SiO_2$	Microelectronics
Polycaprolactone/ $SiO_2$	Bone-bioerodible for skeletal tissue repair
Polyethylacrylate/ $SiO_2$	Catalysis support, stationary phase for chromatography
PMMA/ $SiO_2$	Dental application, optical devices
Poly(amide-imide)/ $TiO_2$	Composite membranes for gas separation applications
Polycarbonate/ $SiO_2$	Abrasion resistant coating
Shape memory polymers/SiC	Medical devices for gripping or releasing therapeutics within blood vessels
Poly(p-phenylene vinylene)/ $SiO_2$	Non-linear optical material for optical waveguides
poly(3,4-ethylene-dioxythiophene)/ $V_2O_5$	Cathode materials for rechargeable lithium batteries
PEO/LS	Airplane interiors, fuel tanks, components in electrical and electronic parts, brakes and tires
Nylon-6/LS	Automotive timing-belt – TOYOTA
PET/clay	Food packaging applications
PLA/LS	Lithium battery development
Polyimide/clay	Automotive step assists - GM Safari and Astra Vans
SPEEK/laponite	Direct methanol fuel cells
Epoxy/MMT	Materials for electronics
Thermoplastic olefin/clay	Beverage container applications

## 2.10 Current research situation and challenges for ZnO nanostructured materials

The blend of ZnO NSs and their potential usage are checked on as far as development strategy, qualities, and utilities. The zinc oxide has an incredible variety in underlying morphology, most likely the most extravagant group of NSs among all materials, which subsequently lead the distribution of thousands of literatures and patents. The utilizations of ZnO NSs incorporate field-effect semiconductors, field-emission devices, piezoelectric nanogenerators, biosensors, p-n heterojunction diodes and photovoltaic cells. A minimal cost and simple method should be created by which a uniquely needed shape of NSs can be incorporated. Particularly, the designing and specific developments of ZnO NSs on wanted destinations are needed for the nanodevices creations and incorporations. The most promising quality of 3D ZnO nanostructured material is large surface area with porous structure, and enables more than one chemical and physical process. Additionally,



nanostructured materials allow tailored properties of each NSs and also create advance features because of in-between relation of each NSs. Hence 3D nanostructured materials allow a wide variety of utility. ZnO NSs grown on WCF also have potential to use as hybrid nano-composites incorporation with the suitable matrix medium. ZnO NSs-WCF-epoxy hybrid composites have great potential to replace existing non-reinforced materials in industries like aerospace, petrochemical and automobiles. Tailored properties like high impact strength, wear resistant, corrosion resistant and low friction coefficient allow these materials to become prominent choice in various technological utilities. ZnO keeps on being seriously concentrated because of its special and complex properties, just as incredible potential for an assortment of pragmatic applications. Despite various investigations in the literature, few significant issues stay uncertain which need to be studied, as summarized in Fig. 2.10.

There has been loads of progress in development of ZnO NSs and their utilization for

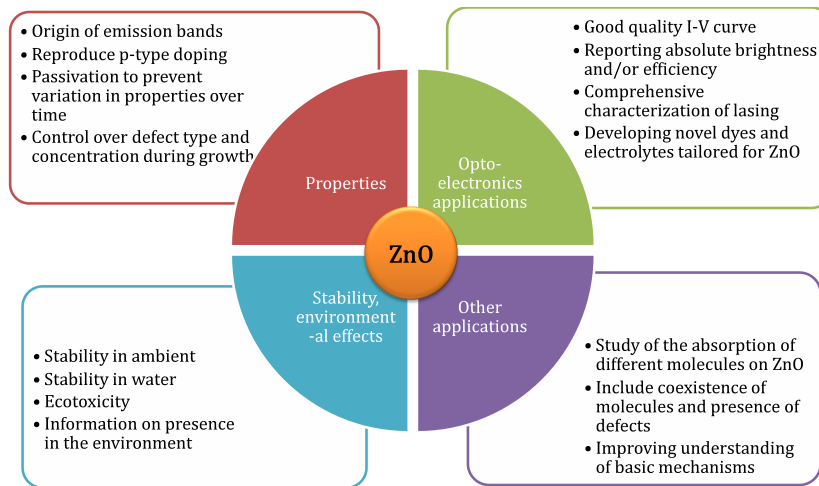


Figure 2.10: Current research situation and challenges for ZnO materials

an assortment of useful applications. Eventually, the reproducibility and dependability of the acquired outcomes (particularly on account of doping of ZnO) is a huge concern. A significant issue which should be defeated to tackle this issue is the explanation of the connection between development conditions, types and groupings of imperfection framed, and properties estimated. Additionally, there is significant interest in the advancement of surface change or passivation agents which could bring about the decrease of imperfection emission, solid and stable electronic features, improved charge transport, and device execution. Because of huge surface-to-volume proportions of the n NSs, surface nature of the

material assumes an essential part in deciding its general conduct and a huge change in the material properties can be accomplished with appropriately planned surface adjustments. It is additionally important to examine significant issues of harmfulness and ecotoxicity of ZnO NSs. For instance, in reports worried about the optical or electronic properties of ZnO and its applications in electronic or optoelectronic appliances, ZnO is much of the time depicted as a non-harmful or even biocompatible material. However, various investigations show that ZnO displays huge ecotoxicity to a wide range of organic entities. This should be considered in the uses of this material, with the goal that guidelines concerning its removal to forestall uncontrolled delivery into the climate could be set up. Besides, most of ecotoxicity considers have been performed on uncovered nanomaterials. In existing applications, for example, sunscreens, nanoparticles as a rule have altered surfaces. Surface alterations as examined above will likewise be alluring for optoelectronic and electronic gadget applications. Hence, there is a conspicuous and pressing requirement for considering the impact of surface alterations on the harmfulness of ZnO NSs.

## 2.11 Modification strategies of ZnO nanomaterials

For the treatment of waste water, ZnO NSs are reasonable photocatalyst to remove azo dyes dissolved in waste water. ZnO based photocatalysts are very popular because of its high UV-photoactive, economical, stability and chemically and naturally inertness. Notwithstanding, the response of ZnO catalyst is restricted due to variable like insensitivity in visible region due to wide band gap, less photonic efficiency due to quick recombination of holes and electrons, and corrosive disintegration. To overcome these issues, doping of the nanomaterial and hybrid material formation is required. Thus altered ZnO nanomaterials based photocatalysts are the required solution for successful treatment of azo dye in waste water treatment and removal of harmful substance from any surface. Scientists have utilized different techniques to enhance the properties of ZnO NSs photocatalyst for effective removal of organic toxins as portrayed in Fig. 2.11. Doping of ZnO exhibits morphological variation, crystal imperfections such as dislocation and deformation. With the aid of required doping agent in adequate amount these defects of ZnO crystals can significantly upgrade the photocatalytic phenomenon. It was noted that, the amount of doping agent is a vital parameter to enhance the visible range photocatalytic action that relies upon synthesis technique and size of the doping agent [234]. Metallic dopants produces another energy band level but do not alter location of CB and VB of ZnO and this intra energy band is required for certain uses like creation of large oxidant holes. But, nonmetallic dopant

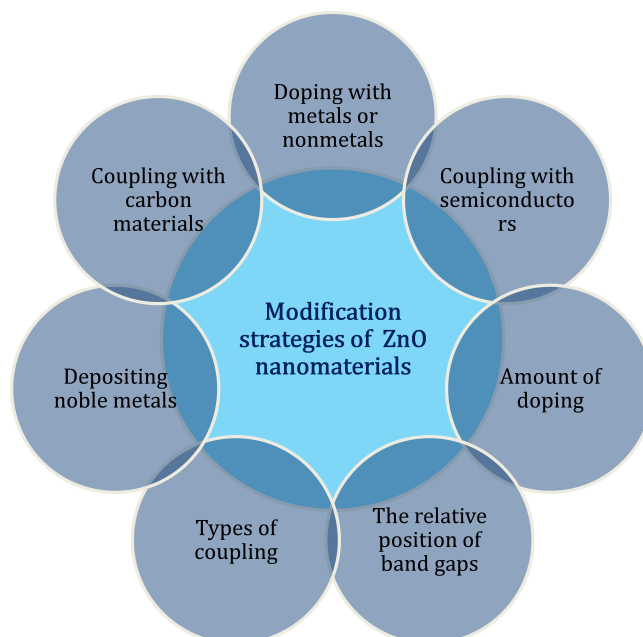


Figure 2.11: Strategies to modify ZnO nanomaterials for better outcomes

increases VB level of ZnO and exhibits decrement in band gap. Corrosion of ZnO under photon energy is a significant problem which can be resolved by the metallic dopant. Metal dopant also causes reduction in ZnO growth thus the small crystals having large surface area is produced. On the basis of exploratory and hypothetical outcomes, doped ZnO photocatalyst is perceived as a fitting technique to upgrade photocatalytic action [235]. But still there are some prominent concerns which are affecting the photocatalytic utilizations. Following are some major issues:

- Survey of literatures exhibits that mostly doped ZnO were used for removal of harmful substances such as dye, thus detailed analysis of fragmentation and photo degradation of pollutants.
- Detailed study of antibacterial phenomenon of pollutants and their detoxification ought to be also performing on ZnO photocatalysts.
- Limited study is available for oxidization of volatile matter by photocatalysis and lack of study on purification of indoor and outside air by ZnO photocatalysts.

## 2.12 Summary of Literature survey

Development in the available metal-oxide nanostructured materials allow researchers to implement those materials into the diverse electronic applications due to their enhancement in absorption range, stability, sensitivity, crystallinity of ZnO and many more. Notwithstanding these noteworthy improvements, still few difficulties remain unsolved.

- i. Irrespective of the improved synthesis techniques for controlled growth of ZnO NSs and their 3D hierarchical composites, enhancement in the quantification of scale and size of NSs and their reproducibility are still unsolved issues. There are lots of ongoing researches showing the impact of varied morphologies and synthesis mechanism which shows further scope to investigate the novel features of ZnO based on their synthesis, applications, shape, size and structure.
- ii. Apart from ZnO hierarchical structure, the execution of electronic systems also relies upon concentration, dimensions and imperfections in NSs. Incorporating 3D ZnO NSs having controlled geometry and chemical stability will further quantify the properties of resulting materials.
- iii. Study of real time application of ZnO NSs and their variations due to dynamic factors will also provide basis to improve the overall performance by understanding and resolving the real-time issues.
- iv. Due to limited availability on high performance ZnO NSs/heterojunction development strategies, devices are not economical and efficient. Thus further investigations are needed to implement current development in the nanoscience to develop novel devices.
- v. To resolve the issue of low effectiveness and durability of ZnO based devices, further study of ZnO catalysts are needed. Also practical difficulty in terms of sensitivity and effectiveness provides basis for the researchers to develop advanced hybrid materials based on ZnO NSs using novel strategies of doping and synthesis.
- vi. Different analytical tools and software should be used to assess the real time situation of the fabricated ZnO NSs electronic devices.
- vii. Development of optimum designs of electronic devices by mathematical and logical computations is needed for economically feasible large scale heterojunction semiconductors.

- viii. It is profoundly imperative to develop beneficial and reformist nanomaterials to set up the ZnO NSs heterojunction for sensible usage and their commercialization.

Extensive studies on WCF grafted with metal-oxide NSs primarily relies upon micro fiber tows or woven preforms, the NSs synthesis technique requires to be scaled up to manufacture continuous nanostructured WCF, so that these grafter WCF will allow fabrication of hybrid composites tapes/pre-pregs and composite to assess mechanical properties via compression, shear, impact and delamination testing. Tailored properties variation due to NSs of resulting composites need to be assessed by open hole compression and compression after impact. In the long run, the fabrication and characterization of hybrid composites structures simultaneously grown on the fibers and spreading in the matrix may be possible, permitting even better service conditions. The development in the field of ZnO nanostructured hybrid composites reveals that, in coming years ZnO assisted advanced material must be pioneer material for aviation and industrial usage. Various studies and researches on hybrid composites are still going on but reflect huge promise for large scale production of nanostructured composites. The accompanying comments were extracted in the view of thorough study of literatures based on ZnO/polymer nanocomposite which exhibit the current difficulties in nanocomposite.

- i. Overall features of the nanocomposite greatly rely on the interface parameter between the polymeric matrix and ZnO NSs. Surface modification is one of the best suited technique for enhancing the interfacial strength and modulus of the nanocomposites. Current situation of interaction between matrix and reinforcement is only based on ZnO NSs containing polar groups which can be further improved by aiding more surface modification techniques.
- ii. The dispersion of NSs into the matrix is one of the deciding factors for properties of the resulting composites. Thus appropriate method of fabrication must be used for optimum dispersion of ZnO NSs into the polymer matrix with uniform material properties and light weight. Current fabrication techniques also require further modification so that final composite can contain desirable outcomes.
- iii. Dielectric properties of the composite materials can be tuned by adding ZnO NSs into matrix even at low concentration because polar group present in the ZnO surface cause reduction of surface charge of the composites.
- iv. Detailed study of interfacial interaction of ZnO NSs and polymer matrix by different

analysis software or simulation technique is much needed to assess the real time application behavior of resulting nanocomposite.

- v. High performance ZnO nanostructured composite materials which are compatible with the sensors to measure the failure mechanism are expected. ZnO nanomaterial composites are favorable for device applications and biomedical area but least possible weight and toxicity are also deciding parameters for commercialization of material for mankind.

Numerous categories of NSs improvised matrix products are now conventionally used including nanostructured epoxy resins, prepregs and sizings, which will propagate the production of large scale nanostructured composites. Additionally the excellent thermal and electrical conductivity of ZnO NSs should enable nanostructured hybrid composites to become new era of multifunctional materials. Currently preparation of functional and structural hierarchical composites having distinguished performance characteristics is under development. This can be concluded that more application range of nanostructured hybrid composites will come in knowledge in few years. The Summary of findings of major research works done till date has been illustrated in the Table 2.3 for better understanding of the current work.

Table 2.3: Summary of findings of major research works done till date

S.no.	Author/Year	Research findings	References
1	Mathur et al. (2008)	Developed a hybrid composite by growing CNTs on the surface of CFs, and observed significant improvements in the flexural strength and flexural modulus	[35]
2	Amin et al. (2011)	Discussed the behavior of conceivable parameters like pH, time, concentration and development temperature on the control of morphologies of ZnO nanostructures	[144]
3	Deka et al. (2012)	Fabricated wood polymer nanocomposite by utilizing HDPE, LDPE, PP, PVC, wood powder, polyethylene-co-glycidyl methacrylate, ZnO NPs, clay, and SiO <sub>2</sub> . UV protection and Bacterial deployment of composite has been enhanced	[28]
4	Kong et al. (2013)	Created ZnO NRs on WCF utilizing hydrothermal strategy and fabricated the composite in polyester matrix. Developed ZnO enhances the energy absorption, load exchange and interfacial strength	[37]
5	Brintha and Ajitha (2015)	Synthesized nanoparticles of ZnO by various strategies such as hydrothermal techniques, sol-gel method and aqueous emulsion	[2]
6	Hazarika et al. (2015)	Developed ZnO nanorods on woven Kevlar fiber via solvothermal strategy as a way to deal with upgrade the interfacial stronghold of aramid composites	[143]
7	Deka et al. (2015)	Developed CuO nanowires encapsulated in WCF-polyester resin composites which results significant improvement in properties like strength and tensile modulus	[36]
8	Ghasaban et al. (2017)	Developed needle-like and plate-like morphologies of ZnO in a large scale and suggested that the hydrothermal response can be a reasonable technique to graft ZnO NSs with the particular size and morphology	[147]
9	Das et al. (2018)	Utilizes the concept of doping in ZnO nanostructures and achieved the Room temperature ferromagnetism (RTFM) with upgraded polarization and coercivity in the Tb (terbium) and co-doped ZnO nanoparticle	[195]
10	Yoozbashizadeh et al. (2019)	Investigated the impacts of plasma treatment process parameters at ambient pressure in the enhancement of bonding characteristics of CFRP composites and proposes optimum parameter settings using regression analysis	[49]
11	Upadhaya et al. (2020)	Successfully synthesized seed layer assisted one dimensional ZnO nanorods having super-hydrophobic wettability and photocatalytic characteristics using hydrothermal synthesis on borosilicate glass substrate	[246]
12	Preda et al. (2021)	Functionalized basalt fibers by ZnO electroless deposition for obtaining a nanostructured interphase and enhanced wettability for upgrading the interfacial strength of Basalt fiber reinforced polymer composites	[315]
13	Li et al. (2022)	Developed ZnO nanosheet on WCF using a simple electroplating and oxidation method and studied interfacial modification and tribological properties of ZnO-carbon fiber reinforced poly(hexahydrotriazine) composites	[89]

## 2.13 Research gap

Upon a thorough review of the literature, the following research gaps are discovered.

- Researchers have already used different types of fibers and fillers but the properties have not improved to the desired level.
- Development of effective reinforcement materials and the secondary reinforcement techniques have to be explored by researchers.
- Synthesis of metal-oxide NSs on WCF fabrics as a secondary reinforcement and their optimum synthesis conditions need to be examined for effective growth of nanorods for high performance CFRP composites.
- To improve the interfacial strength as well as the stress transfer, multiscale hybrid composites with more than one reinforcing filler need to be developed.
- Recently researchers studied metal-oxide hybrid structures and its applications in different heterogeneous fields. However, there has been less research on the mechanical properties of ZnO nanowires embedded in composites, such as impact behavior and elastic modulus.
- Limited research has been found on metal-oxide nanostructured CFRP composites and its effect on mechanical strengthening of FRP composites.



# 3

## Hydrothermal Growth of ZnO nanostructures on woven carbon fiber and effect of synthesis parameters on morphology

This chapter introduces synthesis of ZnO NSs on woven carbon fiber by hydrothermal technique under varying process parameters. The impact of process parameters such as pH and molar concentration of precursor solution, growth duration and growth temperature on morphology and dimensions of ZnO NSs has been investigated in this section. The findings of experimental outcomes are verified using different characterization techniques such as FESEM, EDS and UV-VIS-NIR spectroscopy. Further, this chapter illustrates formation of different ZnO NSs such as nanopallets-like, nanoflowers-like and nanoflakes-like which were achieved at pH >7 but nanorods-like and nanowires-like morphology were achieved at low pH. In addition, the impact of the chemical reactions, seeding and the growth phenomenon on formation of ZnO nanostructures on woven carbon fibers has been discussed in this chapter.

### 3.1 Introduction

The ZnO NSs have gained extensive research potential because of its inherent physical properties and demand for various electronics and photonics industries [104]. ZnO is a very promising semiconductor material due to presence of its symmetry of focal point, wurtzite structure and excellent thermal and chemical stability. ZnO has wide energy band of 3.37eV and 60meV of binding energy [236]. Zinc oxide nanomaterials have high possible utility range in technological devices such as LEDs, optical modulator waveguides, solar cells, acoustic filters, gas sensors and varistors [237, 238, 156, 239]. Over the few years ago, different techniques have emerged for the development of 1-D nanomaterials such as vapour-liquid-solid technique, sol-gel technique, template-assisted solvothermal and electrochemical processes [127]. ZnO NSs with oriented arrays were successfully prepared via hydrothermal decay of  $Zn^{2+}$  amine, metal-oxide chemical vapour deposition, physical vapour deposition, vapour-liquid-solid epitaxial, laser pulsed deposition, ultrasonic synthesis and epitaxial electro deposition [240, 241, 242]. The above techniques require extensive experimental setup with controlled environment such as fixed gas concentration, high temperature and rate of flow or complex procedures are required to achieve growth of metal oxides. This has motivated to develop simple method which can operate at low temperature for grafting metal-oxide NSs. In comparison with the above methods, the modified solvothermal process (Hydrothermal technique) is found to be simple, low cost and can be done at low temperature. The Hydrothermal technique can deposit wide range of eco-friendly metal oxide [4, 147, 95]. Density and orientation of the grafted ZnO NSs via hydrothermal technique depends upon various factors such as seeding treatment of the sample [243, 244], in the spin coating process, the concentration of seed layer highly depends on the speed of spinning and on the amount of impurity present in the seeded layer which affect the amount of growth and crystallinity of NSs [245, 246]. Several other factors such as orientation of sample, time, temperature and pH affect the development of NSs [247]. The size of the NSs increases with increment in growth temperature based on the selection of chemical agents [248, 164]. In the same way size of NSs can be modified by varying the growth duration [249] and concentration of  $Zn^{2+}$  [163]. Hydroxyl ions are responsible for the chemical reactions to develop ZnO NSs and the amount of hydroxyl ion can vary by varying the pH, thus pH of the solution has great impact on the growth of NSs [250, 251]. First-ever production of ZnO rods with the help of new hydrothermal process was discussed by Vayssieres et al. [252]. The process involves use of equivalent molar emulsion of Hexamethylenetetramine (HMTA,  $C_6H_{12}N_4$ ) and zinc nitrate hexahy-

drate ( $Zn(NO_3)_2 \cdot 6H_2O$ ) on different substrate by planting seeds of resynthesized nanoparticles on the epitaxial layers which grows into ZnO rods. Hazarika et al. [143] applied hydrothermal technique on woven Kevlar fabric to successfully grow ZnO nanorod at low temperature and the grafted nanorod enhanced interfacial strength of hybrid composites. Kong et al. [37] successfully grew ZnO NSs on WCF and achieved improved energy absorption property on fabricated composites due to cross linking of nanorods which transfer the energy over the interface area. Amin et al. [144] investigated impact of factors such as time, temperature, pH and precursor concentration on morphologies of ZnO NSs grown on silicon (100) substrates. The effect of surface chemistry and growth mechanism of ZnO nanowires upon carbon fiber at the interphase was investigated by Ehlert et al. [231]. Single fiber fragmentation testing technique were used to check the adhesion of the grown ZnO nanowires and it was found that concentration of ketone groups is the prime reason for the interface strength. Caglar et al. [175] investigated the impact of variation of irradiation time and pH of precursor solution during synthesis of ZnO nanopowder using microwave-assisted hydrothermal technique. Findings of experiments showed that largest crystal size and crystallinity were achieved at 20 min of synthesis time, also damage in crystal structure of ZnO was found while diminishing the pH value of growth solution.

Extensive research on the control of shape of different NSs has been investigated by several researchers. It was found that dimensions, shapes, compositions and orientation of NSs have great impact on physical and chemical features of the resulting materials [253, 254]. It is evident that star like morphology of CuO NSs has high percentage of photo-degradation rate of methylene blue [255]. Nevertheless, most of the researcher demonstrated impact of one or two parameters on growth of NSs grafted on different types of metallic substrate but limited work has been done on WCF. In the present scenario of advance materials, different morphologies of ZnO NSs can be used to improve the interface parameter of hybrid materials such as nanostructured fiber reinforced polymer composites. Very few literatures are available demonstrating impact of process parameters on development of metal-oxide NSs on WCF. Morphologies of NSs grafted on the carbon fiber are major parameter to improve the structural properties of hybrid composites. To achieve varied range of morphologies, it is required to regulate the process parameters such as pH, synthesis time, temperature and molar concentration. Different conditions of seeding and growth reactions also have to examine to understand their impact on growth.

Therefore, this chapter presents a brief discussion on the development of varied NSs of ZnO on WCF using hydrothermal technique. A brief investigation of impact of hydrothermal factors such as pH of solution, growth time, temperature and molar concentration of

chemicals on growth of varied morphologies of ZnO NSs has been performed. Confirmation of varied morphologies of ZnO was examined by FESEM, EDS and UV-VIS-NIR spectroscopy. Series of experiments were systematically conducted to study morphology and structure of ZnO grafted samples. The findings reveal that synthesis and control of varied NSs can be done by varying the process parameters.

## 3.2 Synthesis details

### 3.2.1 Materials used

Unmodified WCF of grade T-300 consisting of 3000 wires, 200 GSM size, 7µm diameter and 0.25mm thickness designed as plain woven and bi-directional structure and chemicals precursor of analytical grade applicable for experiments were procured and used in the process. A list of chemicals used and its purpose have been listed in Table 3.1.

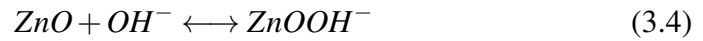
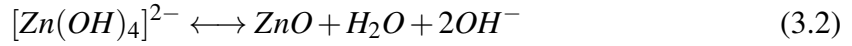
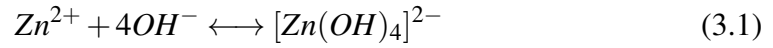
Table 3.1: List of chemicals used in the process

Sr.no.	Name of the chemical	Chemical formula	Purpose
1	Zinc Acetate dihydrate (ZAD)	$Zn(CH_3COO)_2 \cdot 2H_2O$	To prepare seed solution
2	Ethanol/Acetone	$C_2H_5OH$	Cleaning of samples/substrates
3	Sodium hydroxide	$NaOH$	To prepare seed solution
4	Zinc nitrate hexahydrate (ZNH)	$Zn(NO_3)_2 \cdot 6H_2O$	To prepare growth solution
5	Hexamethylene tetramine (HMTA)	$C_6H_{12}N_4$	To prepare growth solution
6	Water (deionized)(DIW)	$H_2O$	Solvent to prepare growth solution and to rinse the sample to halt the growth of NSs

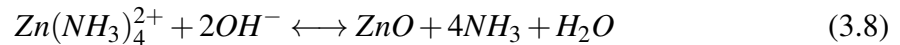
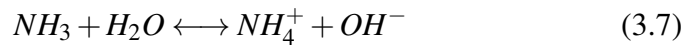
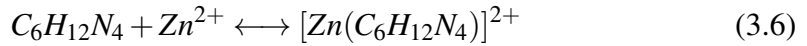
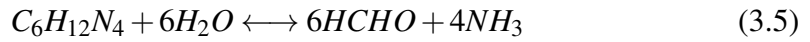
### 3.2.2 Hydrothermal synthesis

Seed solution and growth solutions have been prepared as the first step of the hydrothermal technique. In the preparation of the seed solution, first solution is made up of 0.30g of Zinc acetate dihydrate and 420ml of ethanol mixed together in magnetic stirrer at 75°C for 45 min. Similarly second solution is made by mixing 2mM NaOH with 80ml of ethanol and continuously stirred at 70°C for 15 min, this second solution was then transferred slowly into first solution and extra 300ml of ethanol was also poured to make 800ml of

seed solution. This solution was mixed vigorously using a magnetic stirrer without heat source for 45 min and left for cooling at atmospheric condition with maintained pH of 5-6 [256]. This is the final seed solution used for seeding treatment of the samples; chemical reactions in making of seed solution are described as:



The growth solution is a mixture of HMTA and zinc nitrate hexahydrate. It was an equimolar solution prepared by stirring for 20 min to the mixture of 10mM HMTA in 650ml distilled water, further 10mM of zinc nitrate hexahydrate was mixed with HMTA solution and continuously mixed by magnetic stirrer for 45 min under room temperature while maintaining its pH at 6-8. With the same process, ZnO growth solution with different concentration were prepared (30mM, 50mM and 70mM). Following chemical reactions occurred in preparation of the growth solution:



After preparing the seed and growth solutions now the WCF was cut into pieces of size 120mm X 100mm and then cleaned by a solution of ethanol-acetone to extract foreign impurities. Then the rinsed pieces were put in an oven and let them desiccated at 90°C for 20 min. This treatment helped in the removal of any foreign elements contamination and oxide layers and made the samples suitable for synthesis of ZnO NSs. The treated pieces were then dipped in the firstly prepared seed solution for 15min followed by removal of solvent via thermal annealing at 120°C for 15min. This process is called as seeding process which forms a ZnO seed layer on the WCF surface which will further act as growth site of ZnO NSs. The seeding treatment of samples was performed in four repetitive cycles. Seed treatment of WCF with ZnO particles present in the seed solution was formed to bring down the thermodynamic obstruction by giving nucleation locales. It is a significant

factor to accomplish uniform development of ZnO NSs through aqueous procedure. Now the seeded samples were then kept in hot air oven for 4h at constant temperature of 90°C. Now the samples were withdrawn from oven and then rinsed by DI-water for 30min to stop further development of ZnO NSs. On a final approach, the WCF samples with grown NSs were dried for 24h under ambient condition. In the same way different morphologies of ZnO NSs can be grown on WCF by tuning the hydrothermal parameters. Schematic representation of synthesis technique used for growing the ZnO NSs is depicted in Fig. 3.1. Growth of ZnO NSs also relies on pH of the precursor solution. To study the impact of pH,

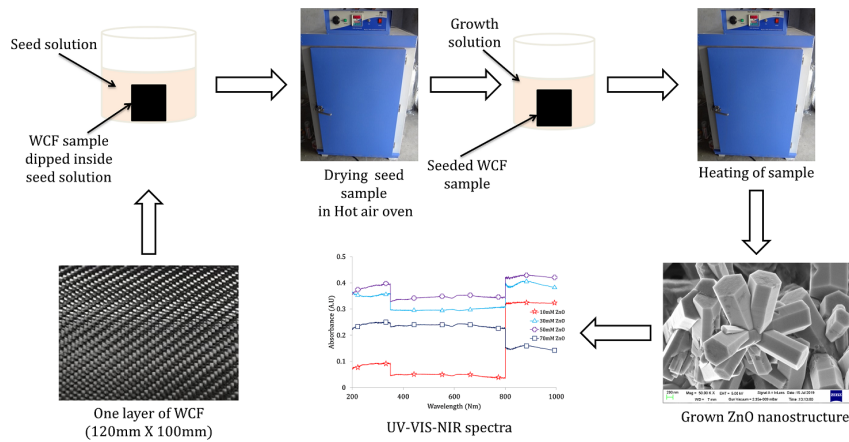


Figure 3.1: Schematic representation of growth mechanism of ZnO NSs

growth solutions were prepared by varying the pH in the range of 2.5–8.5, and each solution was used for the growth of NSs on pre-seeded samples at 90°C for 4h in hot air oven. To change the pH value of solution, *NaOH* pallets were added to the growth solutions. Other chemicals such as *HCl*, *HNO<sub>3</sub>* and *NH<sub>3</sub>* can also be used to vary pH. The intrinsic pH of the growth solution was 6.5. In the final step, the grown samples were washed many times by DI-water and then desiccated at atmospheric condition. The pH of solution was measured after growth phenomenon by pH meter. Impact of growth duration and temperature on NSs was also studied by using constant molar concentration and varying growth duration. In the same way, impact of varying molar concentration of growth solution was studied. The NSs characterization was done using FESEM at different magnification size and confirmation of presence of ZnO was examined by EDS and UV-VIS-NIR spectroscopy analysis.

### 3.3 Results and Discussion

Impact of process parameters viz. molar concentration of precursor solution, pH of growth solution, growth duration and processing temperature has been studied on shape, dimensions and aspect ratio of the grown ZnO NSs. Separate effect of seeding and growth on morphology of ZnO NSs has been also studied.

#### 3.3.1 Impact of seeding and growth phenomenon

To understand the separate behavior of seeding treatment and growth treatment a sample has been prepared in a seed solution and another sample has been prepared in 10mM of growth solution. Effect of seed solution treatment and growth solution treatment for processing of ZnO NSs on WCF is illustrated in Fig. 3.2. It is clearly seen that ZnO nanorods

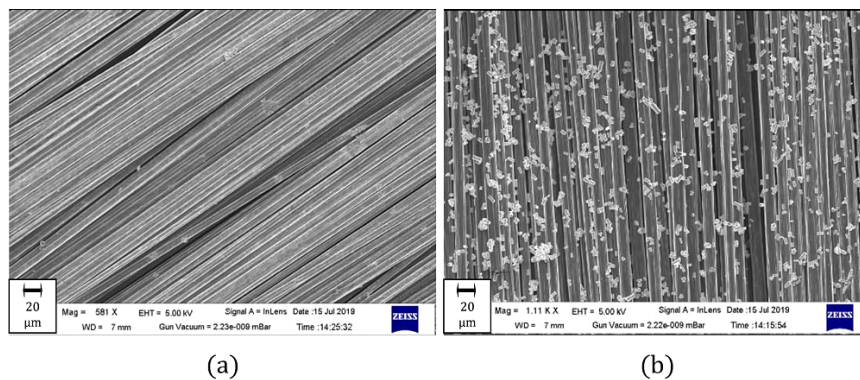


Figure 3.2: FESEM images: (a) seeding; (b) growth phenomenon of ZnO NSs

are nucleated at some portion on the WCF surface only by seeding. The growth solution treatment produces low quality nanorods on WCF which provides a basis that nanorods can be grown by growth solution treatment only. But successive treatment of seeding followed by growth treatment produces high quality nanorods on WCF samples. The concentration of  $OH^-$  ion in the solutions has a vital role in development of the different shaped ZnO NSs along the c-direction which is verified in the literatures [147, 257]. Crystalline ZnO nanorods grown on WCF crucially depend on the amount of impurities in the solution. The morphology achieved lies upon the seeding solution for desired usage.

### 3.3.2 Impact of molar concentration

The change in molar concentration of the precursor solution using inherent pH of 6.5 is illustrated in this section. It is evident that, the variation in molar concentration of the precursor solution causes modification in the final outputs. The growth of ZnO NSs using aqueous method is available in the literature in which researchers synthesized scale-like ZnO while using the high molar concentration of the solution and they also synthesized spindle-like ZnO while using lower molar concentration [258]. Thus it can be said that the required size of the NSs can be grafted by controlling the molar concentration of the precursor solution. Based on the above mentioned fact, authors studied the impact of molar concentration on ZnO NSs grafted upon WCF using hydrothermal technique. ZnO NSs have been grafted on WCF at different molar concentration with constant pH of 6.5, 4h duration and 90°C temperature (see Fig. 3.3(a)-(d)). The dimensions of the NSs are different for different molar concentrations such as nanoflakes were grown at higher concentration as depicted in Fig. 3.3(d). Rather than nanowires of diameter <100nm and 1.2µm height were grafted at lower concentration as depicted in Fig. 3.3(a) and (b). Figure 3.4 demonstrated the EDS spectra of ZnO grown samples conforming the deposition of Zn and O on WCF strands.

Zhu et al. [259] grafted different size of ZnO spheres for semiconductor core/shell structures at 5mM molar concentration in shorter time upon glass/Si substrates using a general chemical conversion route. A plot of impact of concentration of precursor solution on dimension of ZnO NSs is clearly depicted in Fig. 3.5. The chart obviously shows that a straight connection can be seen among the expansion of the molar concentration and NSs measurements; strikingly diameter increments progressively, but height gets consistent over 50mM. This suggests there is a critical height for the ZnO NSs at which further increment of the molar value did not affect axial development heading though the radial course develops ceaselessly and at sufficiently high fixation the nanorods converge to shape ultrathin nanoflakes. As per the experimental ZnO NSs, the ZnO morphologies have bigger diameter and smaller height as molar fixation raised. It was clearly seen that lower zinc forerunner molar value produces more slender and longer NSs.

### 3.3.3 Impact of pH on synthesis of ZnO NSs

Huge impact of pH value was seen while synthesizing the ZnO NSs on WCF using solvothermal process. To examine the impact of pH on development of ZnO NSs on WCF, the initial and final value of pH during synthesis of NSs was recorded. Different chemicals such as



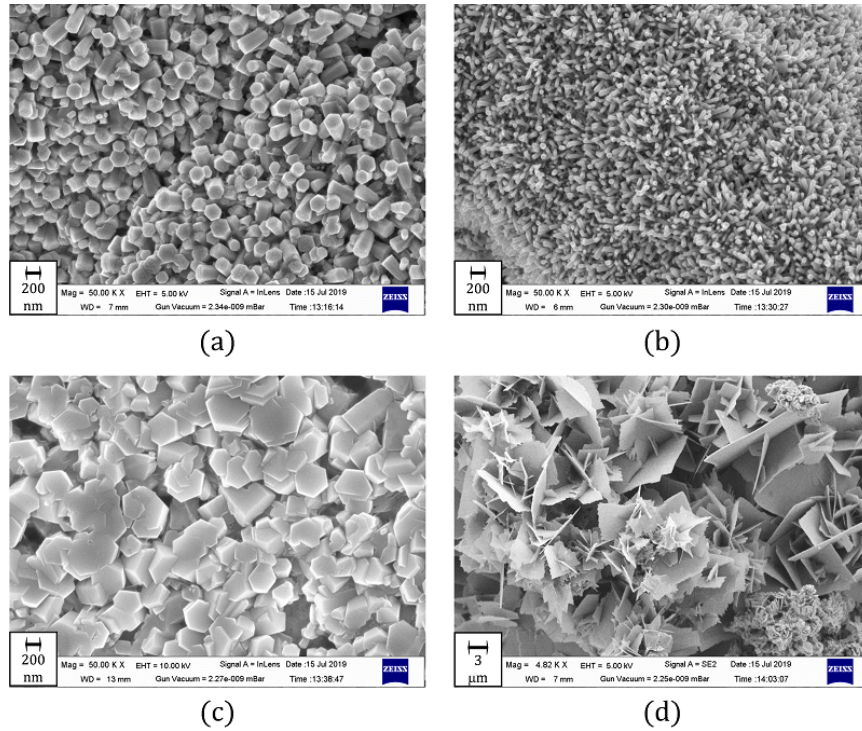


Figure 3.3: FESEM images of ZnO NSs on WCF at varied molar concentrations: (a) 10mM; (b) 30mM; (c) 50mM; (d) 70mM

$NaOH$  and  $NH_3$  can be used to modify pH value of the solutions. Initial pH values of solutions were varied to 2.5, 4.5, 6.5 and 8.5 respectively. The variation of initial versus final pH value of solution calculated over 4h of processing using 10mM molar concentration was plotted in Fig. 3.6. Four cycles of experiments were performed to check the reproducibility of the procedure. It was found that alkaline pH was comparatively diminished at identical rate instead of acidic pH which approaches to inherent pH of 6.5. A series of samples were used to graft ZnO NSs on preseeded WCF pieces at  $90^\circ C$  and 4h of processing in prepared  $pH_{initial}$  growth solutions. Appearance of the solution was transparent and consists of white precipitates at inherent pH value. The ZnO NSs having height  $1.2\mu m$  and diameter 60nm were grafted on WCF from prepared solution. Cross-sectional FESEM image was used for measurement of average height (Fig. 3.7) and top view of image was used to calculate diameter as depicted in Fig. 3.8(c) and (d). When ammonia was added for increment in pH of the solution,  $NH_3$  started hydrolyzing into  $NH_4^+$  and hydroxide thus increases  $OH^-$  ion in the solution. FESEM images of different ZnO NSs grafted under varied  $pH_{initial}$  values are depicted in Fig. 3.8 in which Fig. 3.8(c) demonstrated high

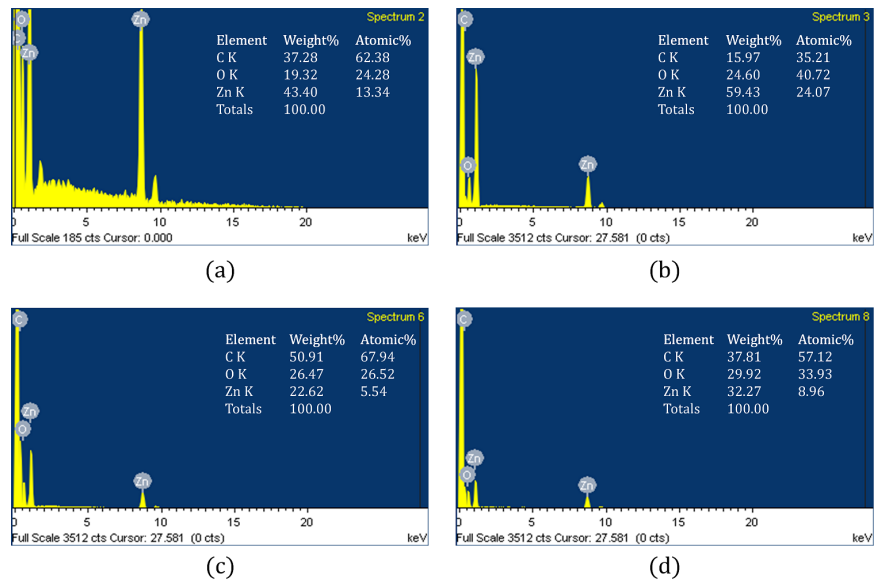


Figure 3.4: EDS spectra of ZnO NSs at different molar concentrations: (a) 10mM; (b) 30mM; (c) 50mM; (d) 70mM

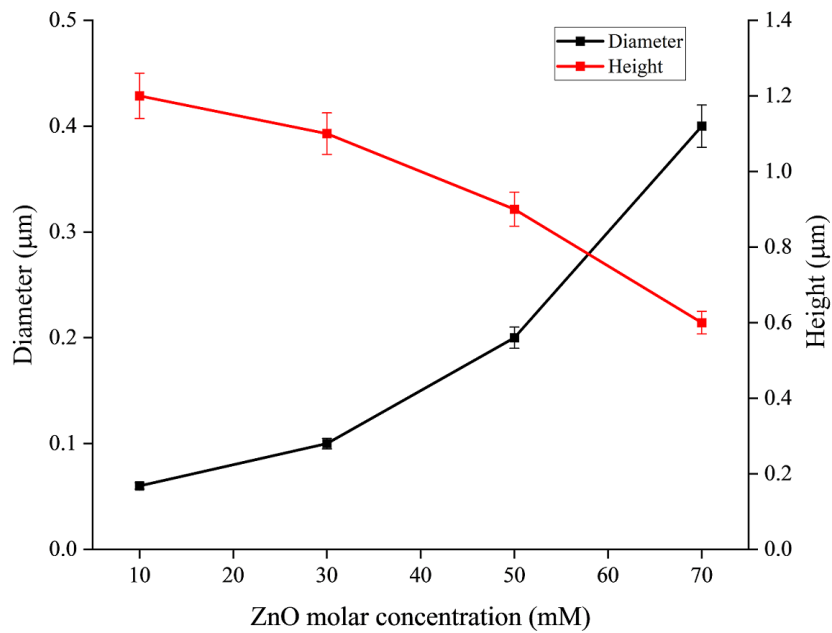


Figure 3.5: Effect of molar concentration on height and diameter of the ZnO Nss

density NSs grafted at pH value of 6.5 of precursor solution. When pH value was raised to 8.5, ultrathin nanoflakes of ZnO were produced as depicted in Fig. 3.8(d). Thus, finding

of variation of pH above inherent value shows anisotropic development headings because of increment in concentration of  $OH^-$  ions [144].

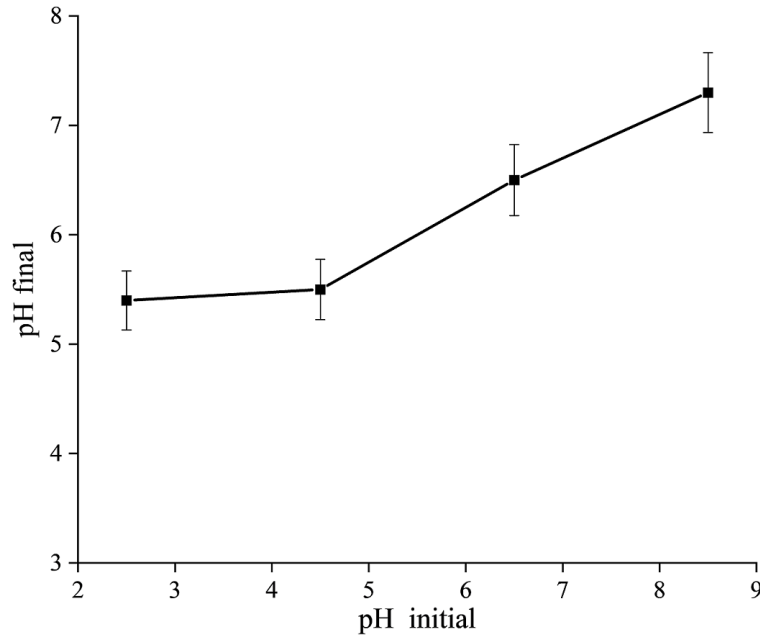


Figure 3.6: Variation in pH value of the solution in 4h growth duration

This can be concluded as, for the high pH value solution NSs were grafted in self-assembly manner. For the case of  $pH < 7$  due to addition of  $HNO_3$  or  $HCl$  varied ZnO NSs were achieved as depicted in Fig. 3.8(a) and (b). The grafted shapes of ZnO were hexagonal nanorods or nanowires of increased height and diameter with less density due to inclusion of acids such as  $HNO_3$  or  $HCl$  which reduces the pH value and increase the formation of  $Zn^{2+}$  as depicted in Fig. 3.8(a) and (b).

### 3.3.4 Impact of the Growth duration

Growth duration has huge impact on the processing of different morphologies of ZnO NSs on WCF. The investigation of impact of growth duration on grafted morphologies of ZnO NSs was performed for equimolar precursor concentration of 10mM and varied growth duration of 2, 4, 6, 8 and 10 h with inherent pH value of 6.5 at 90°C temperature. The grafted morphologies of ZnO NSs on WCF at specified growth duration were analyzed by FESEM examination as illustrated in Fig. 3.9. FESEM images reveal that growth duration is a prime factor to modify dimension and morphology of resulting ZnO NSs. Figure



Figure 3.7: The grown ZnO NSs under processing condition of 90°C, 4h, 6.5pH and 10mM

3.9(a) illustrates FESEM result of ZnO NSs grafted on WCF for growth duration of 2h. The grown structure is hexagonal nanorods with average height of 400nm and diameter 80nm, but the nanorods were not vertically aligned because of lack of growth duration. The grafted NSs were started modifying their size when the growth duration rose to 4h. The average height of the NSs is 1.1 $\mu$ m with diameter of 100nm with increase in density of the nanostructure as depicted in Fig. 3.9(b). The FESEM results clearly shows that for 4h of processing time grafted NSs are properly grown and vertically align. Thus, for grafting the ZnO NSs on WCF via hydrothermal synthesis at 10mM precursor concentration, 90°C growth temperature and pH value of 6.5; 4h of growth duration is sufficient. There is boost in average height of ZnO NSs for further increase in growth duration upto 8h of processing time, while decrements in size, density and morphology was observed above 8h. Other NSs such as nanoflowers, nanoflakes and nanopallets were grown on WCF above 4h of growth duration as depicted in Fig. 3.9(c), (d) and (e). The variation of dimensions of ZnO NSs with growth duration is illustrated in Fig. 3.10.

It was found that ZnO NSs were continuously grown till 8h of processing time and then the growth phenomenon reached to equilibrium, thus growth was started diminishing and precursor precipitation was happened as shown in Fig. 3.10. All the seeded ZnO nanopar-

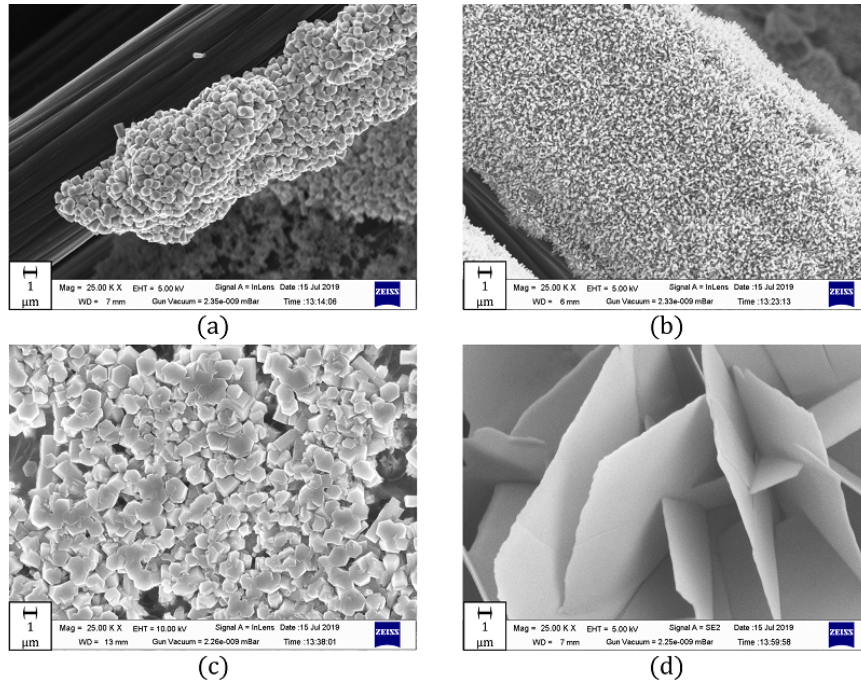


Figure 3.8: ZnO NSs on WCF having pH of precursor solution (a) at 2.5, (b) at 4.5 (c) at 6.5 and (d) at 8.5

ticles on WCF surface started growing after 2h of growth duration and it increases on increasing the growth duration. However, after 8h of growth duration no seeded particles are left to grow because the system has been reached in equilibrium and on further increase in the growth duration, the chemical precursors are started precipitating on the WCF surface which cause reduction in the size of nanostructures or development of agglomerated nanoparticles. The results also defined that growth duration also affects the density of NSs. The limiting growth duration for grafting ZnO NSs on WCF was observed to be 2h, below which agglomerated ZnO was collected on the WCF surfaces causing no growth, these results are found in accordance with the previous work [37, 260].

### 3.3.5 Impact of processing Temperature

The temperature at which seeded WCF samples were kept for growth of different NSs of ZnO also play major role to achieve varied morphologies and dimensions. To examine the impact of growth temperature, a series of experiments were performed on seeded WCF samples using 10mM molar concentration, 4h of processing time and inherent pH of 6.5. Four set of processing temperature such as 50°C, 70°C, 90°C and 110°C was used for

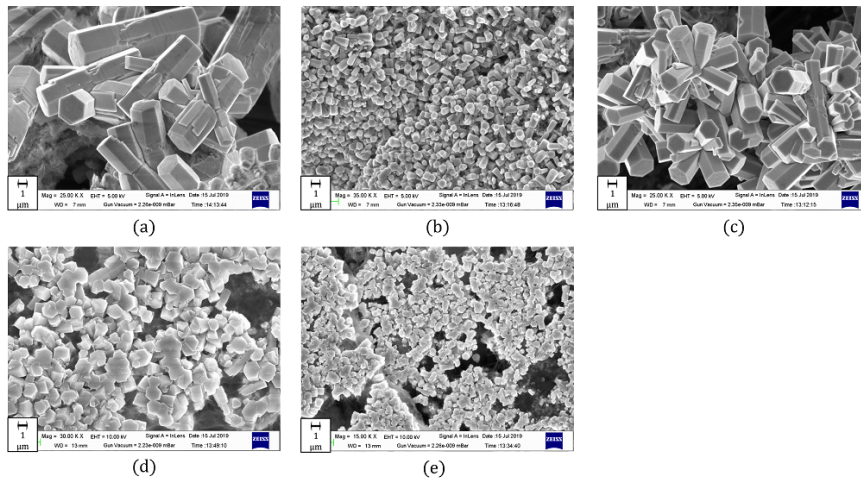


Figure 3.9: ZnO NSs on WCF at 90°C and at growth duration:(a) 2 h, (b) 4 h, (c) 6 h, (d) 8 h and (e) 10 h

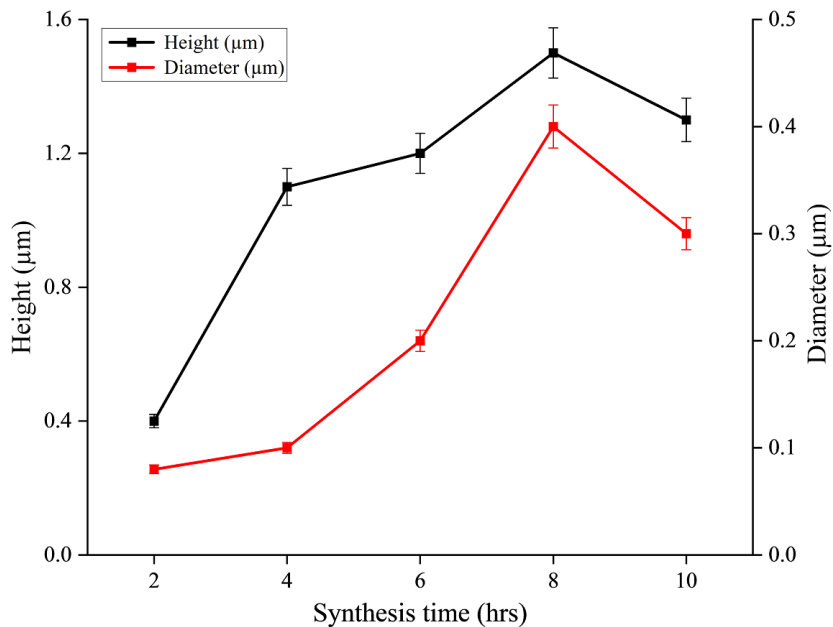


Figure 3.10: Effect of processing time on the dimensions (diameter and height) of ZnO NSs

experimentation by using hot air oven. ZnO NSs morphologies grafted on WCF at each set of growth temperature is demonstrated by FESEM image shown in Fig. 3.11. It can be seen that NSs were not properly grown at low temperature such as at 50°C and 70°C

(see Fig. 3.11(a) and (b)). FESEM image also shows that, the size and density of grafted NSs also depends upon temperature. Graph for variation of aspect ratio on ZnO NSs with processing temperature at fixed remaining parameters is illustrated in Fig. 3.12. From graph, it is found that aspect ratio increases gradually on increasing the temperature till 90°C. However, on further increment in temperature, the aspect ratio becomes constant till 95°C and then started decreasing in irregular manner. From complete experimentation of impact of growth temperature it reveals that dimensions and shapes of ZnO NSs can be modified by varying the growth temperature and the limiting growth temperature must be  $< 100^{\circ}\text{C}$  because the process used is hydrothermal (aqueous-based solution) technique [261].

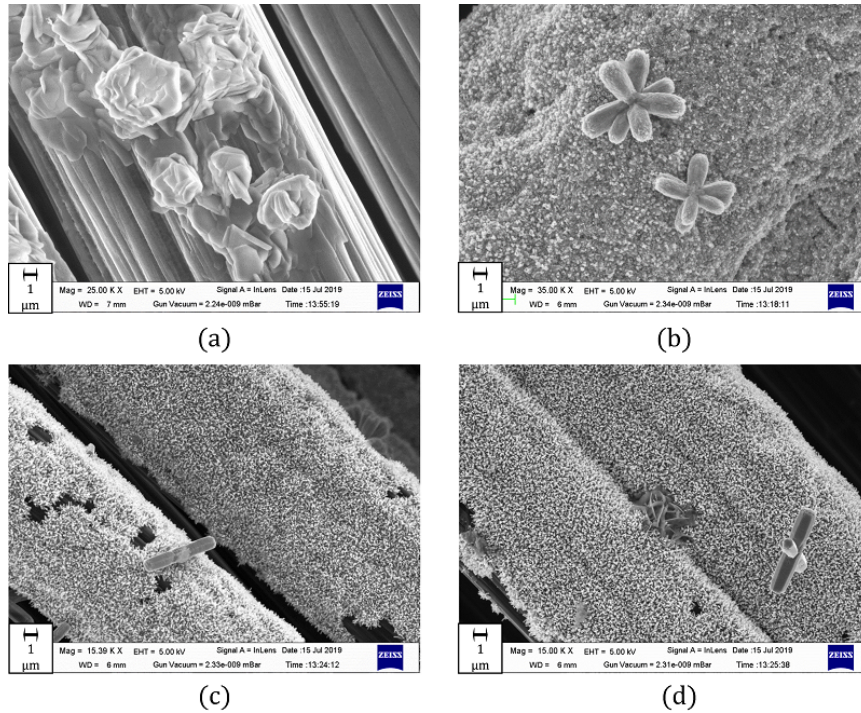


Figure 3.11: ZnO NSs on WCF for 4 h and 10 mM solution at temperatures: (a) 50°C, (b) 70°C, (c) 90°C and (d) 110°C

### 3.3.6 UV-VIS-NIR spectroscopy study

Spectroscopy technique is an analysis process to understand the optical nature of grown NSs. The absorption graph from UV range to NIR range wavelength of ZnO NSs at 90°C, 4h, pH value of 6.5 and different molar concentration is depicted in Fig. 3.13.

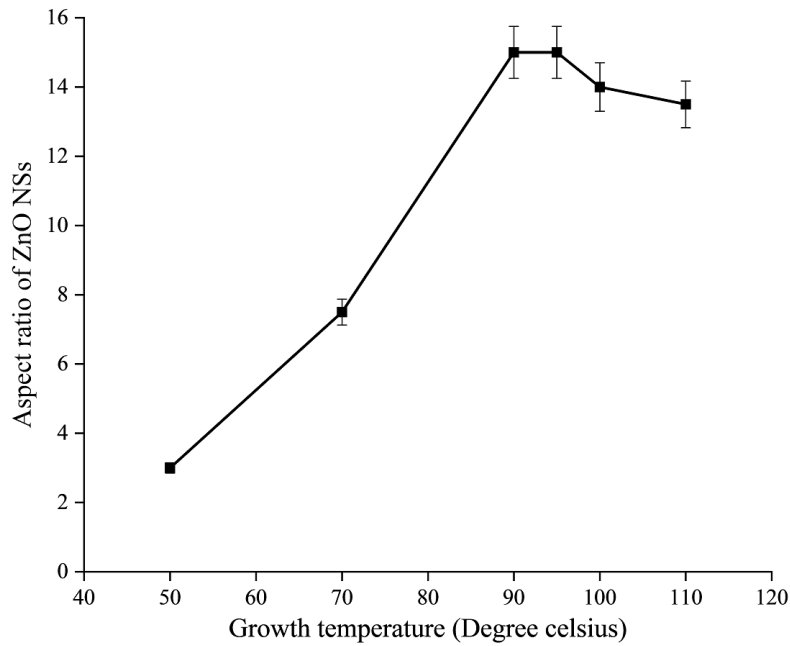


Figure 3.12: Effect of growth temperature on the aspect ratio on ZnO NSs

If a particular wavelength is utilized to illuminate a sample, then there may be absorption of that radiation. But no absorption will occur at remaining wavelength. This absorption behaviour is used for material characterization such as colour, filtering and metamerism. ZnO has a direct wide band gap at room temperature with a large exciton binding energy (60meV). Absorption graph reveals that the first strong absorption band occurs at wavelength of 355nm in UV region which lies to ZnO band gap excitonic emission range of 360-380 nm ( $E_g = 3.37eV$ ). This obvious absorption corresponds to band gap of ZnO (360 – 380nm;  $E_g = 3.37eV$ ) is greater than the as grown ZnO NSs (355nm). It is likewise obvious that critical sharp retention of ZnO shows the monodispersed nature of grafted NSs as discussed in the literature [262, 263]. The next sharp absorption peak exists at 800nm which attributes the traces of ionized oxygen vacancies. The radiative recombination of a photo-generated hole with an electron taking the oxygen vacancy is the main reason for such emission. Thus UV-VIS-NIR spectra reveal that morphologies of the ZnO NSs have great impact on the optical properties of the material.



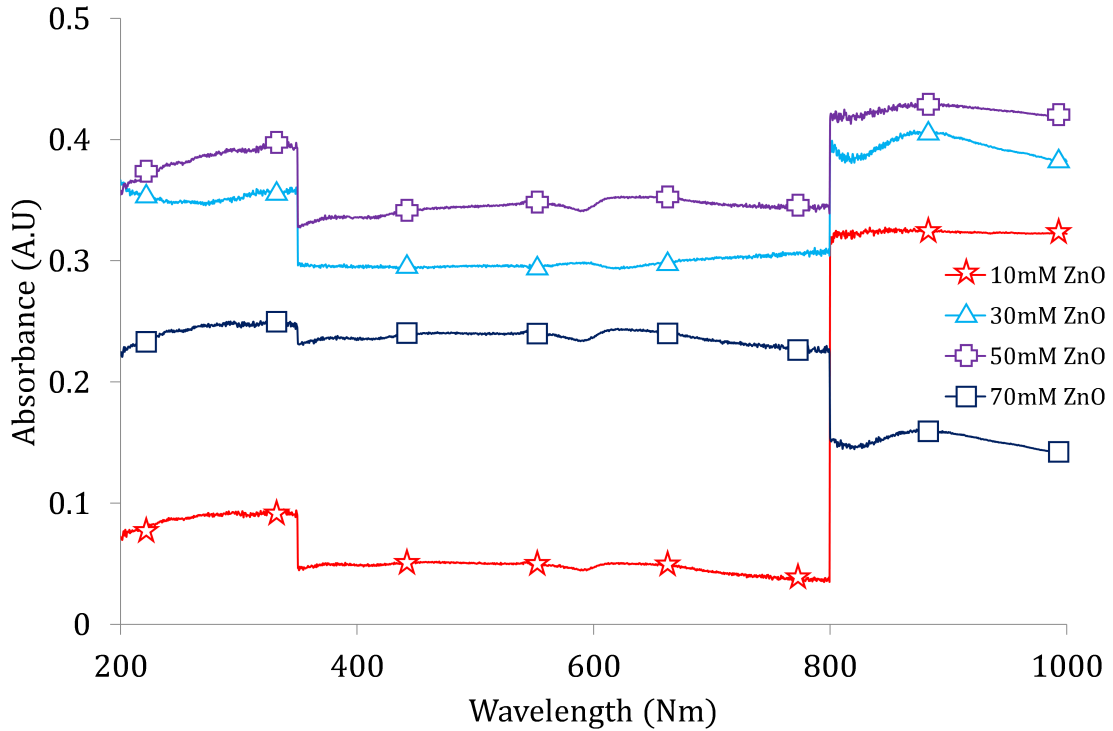


Figure 3.13: UV-VIS-NIR absorbance graph of ZnO NSs grafted on WCF samples

### 3.4 Summary

In conclusion, this chapter deals with grafting of ZnO NSs on WCF samples using hydrothermal synthesis technique and analysis of impact of synthesis conditions on ZnO NSs. Variation and control in size and shapes of the ZnO NSs can be done by varying synthesis conditions such as pH, molar concentration, time and temperature. Different NSs such as nanorods, nanowires, nanoflakes, nanoflowers and nanopallets were developed by varying the pH of precursor solution, molar concentration, growth duration and growth temperature. It can be concluded that the pH commands the morphological structure of NSs and the nucleation density of NSs was directed by molar concentration of precursor solution. Aspect ratio of the grafted ZnO NSs can be adjusted by varying the synthesis time and growth temperature but growth temperature also influences the morphology. Thus the varied shapes and size of ZnO NSs can be grafted on woven carbon fibers by hydrothermal technique and their structure and morphology can be directed simply by adjusting the above discussed parameters to achieve desire NSs as per the potential usage.



# 4

## One-step microwave-assisted hydrothermal synthesis of ZnO nanostructures on WCF and their characterization

This chapter investigates the rapid growth of ZnO NSs on WCF surface by combining microwave heating with an aqueous process known as the "microwave assisted chemical bath deposition approach." This method allows the generation of ZnO NSs with varied morphologies such as nanowires, hexagonal nanorods, nanoflakes, nanopallets, and nanoflowers by heating WCF samples in different precursor solutions in a household microwave. A probable development phenomenon of various morphologies of ZnO NSs on WCF has been described based on microwave compatibility with materials. Furthermore, study of different process parameters such as molar concentration, microwave duration, microwave power and growth solution were investigated to achieve optimum growth of ZnO NSs on WCF surface. In this study different morphologies of ZnO on WCF strands were grafted by tuning the microwave power, microwave duration and type of precursor solution. The developed ZnO on WCF was characterized to understand their morphologies, size variation, crystallinity and optical behavior. These analyses will provide the basis to implement ZnO

embedded WCF to developed advanced nanocomposite materials for optoelectronics and photonics applications. The development of ZnO NSs on WCF surface develops functional groups which may react with the other bracing media and polymer matrix during fabrication of hybrid composites. The current work can be used to develop high performance nanocomposites for industrial applications.

## **4.1 Introduction**

In the developing era of advanced materials, combination of different metal oxide nanostructures along with different base materials having specific properties are combined together to fabricate hybrid/composite materials. The developed hybrid materials possess tailored properties for diverse applications [264]. Woven carbon fibers are one of the prominent fibrous material which possesses high strength and light weight required for extensive applications in the field of fiber reinforced polymer composites [25]. Woven carbon fibers are a primary bracing media for polymer composites to enhance the properties of the final composites but single bracing media is not sufficient, thus the concept of secondary reinforcement such as metal oxide nanostructures arises as green field of research [265]. Since very limited work has been done on the growth of nanostructures on woven carbon fiber surface therefore it is required to investigate the advancement of ZnO nanostructured woven carbon fiber materials for varied applications. Out of several metal oxides, zinc oxide (ZnO) is the prominent metal-oxide because of its significant and varied features such as wide energy band of approx.  $\sim 3.3$  eV at atmospheric condition, piezoelectric nature, optical nature, chemically stable and is biocompatible [266]. The unique properties of ZnO NSs created from synthetic morphology would create undiscovered probabilities for ZnO NSs to be used in a wide range of semiconducting and functional devices. ZnO nanostructures can be orchestrated by considerably acknowledged amalgamation techniques such as solvothermal, chemical bath deposition, pyrolysis, sol-gel technique, vapour deposition, microwave assisted technique and others [95, 165]. They reveals that due to high amalgamation temperature in most cases, agglomerated NSs formed on the surface which had to be unnecessarily granulated, resulting in little control over molecular shape and size dispersal. Out of all the strategy for synthesis of ZnO NSs, the aqueous strategy has several points of interest over other engineered techniques that make chemical bath deposition synthesis as one of the prominent routes for NSs development [267]. The chemical bath deposition route enables superior purity and phenomenal control over the morphology and size of NSs [268]. Recently, another method for formation of NSs which is gaining inter-

est of late is the use of microwave warming rather than standard warming which improves the development phenomena. Microwave-assisted warming is used for the synthesis of metal-oxide NSs on diverse substrates [269]. In this case, the benefits of microwave warming can be used in chemical bath deposition synthesis for annealing sample and precursor solutions [270]. Because of its various advantages, such as reaction at atmospheric pressure, low response duration, fast warming, low response temperature, uniform heating, and phase immaculateness with better yield, microwave assisted chemical bath deposition amalgamation has gained widespread attention as a new heating route in the development of NSs [271]. A rapid combination process called as microwave-aided aqueous course is now being developed for nanostructure production. This is a fast warming method based on microwave dielectric warming of the precursor arrangement, which results in volumetric warming of chemical precursors and solutions. As a result, it is faster, easier, and more energy efficient than traditional conduction heating [272].

Several studies have been published on the microwave-assisted wet-chemical development of ZnO nanostructures. However, only a few comprehensive studies on the effects of growth variables on the characteristics of microwave-generated ZnO nanostructures have been conducted. But in case of woven carbon fiber as a substrate, there are very few authors who worked on growth of ZnO on woven carbon fiber however but there is no work related with growth of ZnO nanostructures using microwave assisted chemical bath deposition method on woven carbon fiber surfaces and their optical characterization. Ahmed et al. [273] describe the effect of precursor molar ratio and reaction duration on the shape and aspect ratio of ZnO nanostructures created by microwave aided wet-chemical technique. Radhakrishnan et al. [274] found that changing the microwave power per growth run can vary the morphology of individual ZnO nanostructures from hexagonal cones to faceted hexagonal nanorods to hollow hexagonal nanorods. El-Nahas et al. [275] effectively synthesized ZnO NS with diverse morphologies using a household microwave treatment at 200 Watt power for 15 minutes as well as a minimal amount of capping and complexing agents. Fabrication and characterization of ZnO nanorods upon woven Kevlar fibers by applying low temperature chemical bath deposition process has been achieved by Hazarika et al. [143]. Enhancement of energy absorption properties of ZnO embedded WCF composite and their energy transmission under impact loading were discussed by Kong et al. [37]. It was found that the grown ZnO nanorods combined with matrix in a crosslinking manner causing high interface properties of final composite. Rai et al. [88] concluded that, the nucleation, growth and morphology of ZnO nanostructures on woven carbon fiber by chemical bath deposition route mainly depends on synthesis parameters such as solvent,

growth time, precursor concentration, external agitation, seed layer, and pH. Caglar et al. [175] used a microwave-assisted chemical bath deposition approach to study the effects of varying the irradiation period and pH of the precursor solution during the production of ZnO nanopowder. Experiments revealed that the maximum crystal size and crystallinity were attained after 20 minutes of synthesis, and that damage to the crystal structure of ZnO was discovered when the pH value of the growth solution was decreased.

## **4.2 Materials and methodology**

### **4.2.1 Materials**

As a substrate material for the synthesis of ZnO NSs, T-300 grade unmodified WCF with 3000 wires, 0.2 mm fabric thickness and 200 GSM size with filament diameter of 7  $\mu\text{m}$  was used. Some precursors of analytical-grade were employed in the production of growth solutions and fiber modifications as presented in Table 3.1. Without any refining, all of the raw ingredients and chemicals were used. Synthesis was carried out on a household microwave with nine power levels and a power output of 1000 W at a frequency of 2.45 GHz.

### **4.2.2 Preparation of growth solutions**

Microwave aided chemical bath deposition methods were used to produce various morphologies of ZnO NSs. Growth solutions of different molar concentrations were prepared using equimolar (1:1 ratio) solution of ZNH and HMTA in DIW. To prepare 10 mM of growth solution, 2.97 g of ZNH is mixed in 650 ml of DIW using magnetic stirrer operated at 400 rpm and ambient temperature for 45 minutes. Then 1.4 g of HMTA was added in the prepared solution and stirred for 45 minutes. The resulting solution was allowed to cool at room temperature and maintained at pH of 10-12. Similarly, the other concentrations of growth solutions such as 30 mM, 50 mM and 70 mM were prepared. These prepared growth solutions were used for synthesis of ZnO NSs on WCF surface and to study the effect of molar concentrations, microwave duration and microwave power. Furthermore to study the effect of different type of growth solutions on the synthesis of ZnO NSs on WCF, four separate kinds of growth solutions having 30 mM concentration were synthesized and named as A, B, C, and D. To prepare these solutions different set of chemical precursors were mixed in de-ionized water. Solution A was prepared using 2.5 g of ZAD mixed with

500 ml of DIW in a beaker. A magnetic stirrer was used to mix the solution for 45 minutes at 400 rpm at a constant temperature of 50 °C. Similarly, another solution was prepared using 8 gram of sodium hydroxide into 100 ml of DIW. The NaOH solution was gently poured into the first beaker and vigorously mixed for 30 minutes at 400 rpm. Growth solution 'A' is the resultant solution. At a regulated pH of 10-12, the resulting growth solution was allowed to cool to ambient temperature. The precursor mixture (Solution-B) consisted of an equimolar mixture of ZNH and HMTA. Mix 30 mM HMTA in 600 ml DIW for 30 minutes at 300 rpm to make the ZnO precursor mixture (30 mM). The ZNH arrangement was added to the HMTA arrangement, and the resulting mixture was mixed for 30 minutes at atmospheric condition with a pH of 6–8. Similarly, 600 ml of solution-C was made by combining 4.5 gram ZNH, 1.35 gram NaOH, and 13.3 gram HMTA. 2.5 gram of ZAD, 1.35 gram of NaOH, and 13.3 gram of HMTA were mixed in 600 ml of DIW to make solution D. For optimal growth of ZnO NSs onto WCF, all of the resultant solutions should be cooled to room temperature and kept at a pH of 10-13.

### **4.2.3 Surface functionalization of WCF**

Surface functionalization is a type of fiber modification that comes before the creation of nanostructures on any substrate and is a crucial step. An unaltered form of woven carbon fabric was cut into a square-section of 100 mm X 100 mm dimension to create the sample, and then all of the pieces were cleaned with an acetone-ethanol solution to eliminate dust, dirt, and other impurities that may cling to fiber during manufacture. After dipping the samples in an ethanol-acetone solution for 10 minutes, they were dried in a hot air oven at 90 °C for 20 minutes. DIW cleaned the treated WCF many times before drying it in the oven at 90 °C for 30 minutes. This phase of surface modification improves the quality of substrate by eliminating foreign impurities and oxides that may be present on the surface and inhibit nanostructure formation [88]. Microwave assisted chemical bath deposition growth technique was employed to produce ZnO NSs from functionalized WCF samples.

### **4.2.4 Microwave synthesis of ZnO nanostructures on WCF**

The prepared growth solution was poured into a glass flask in which the dried surface treated WCF samples were dipped then the glass flask was placed into a domestic microwave (Samsung-QW71X, 1000 W, 2.45 GHz) for 10 minutes to irradiate the precursor solution and WCF sample. Microwaves travel at the speed of light and consist of two mutually perpendicular electric and magnetic fields which cause linear temperature variation of

WCF samples dipped in precursor solution. Since microwave photon energy is moderately low (0.03-0.00003 kcal/mol) and only influences kinetic molecular excitation therefore tetra ammonium zinc complex  $[Zn(NH_3)_4]^{2+}$  and  $OH^-$  present in the precursor solution started generating ZnO NSs on WCF samples dipped into growth solution, microwave irradiation causes the growth of NSs. After microwave irradiation, the WCF samples were left in the growth solution for 10-15 minutes before being withdrawn and allowed to cool naturally to ambient temperatures. Then DIW is used to rinse the treated WCF and samples were dried in a 70 °C oven for 6 hours before storing them at room temperature for 24 hours. The characterization was carried out on the ZnO nanostructured WCF samples that resulted for further study of grown nanostructures. Similarly, ZnO NSs were synthesized under the varying set of experiments to study the effect of different process parameters such as varying molar concentration (10 mM, 30 mM, 50 mM and 70 mM); microwave duration (5 minutes, 10 minutes, 15 minutes and 20 minutes) and microwave power (250 W, 500 W, 750 W and 1000 W).

The details of process parameters used for synthesis of ZnO nanostructures on WCF surface using microwave-assisted chemical bath deposition are illustrated in the Table 4.1. The outcomes of these experiments were analyzed and it was found that the optimum

Table 4.1: Process parameters used for synthesis on ZnO NSs

Sample	Molar Concentration (mM)	Microwave power (Watt)	Microwave duration (minutes)
A	10	250	5
B	30	500	10
C	50	750	15
D	70	1000	20

growth condition can be developed by varying the type of growth solutions such as solution-A, solution-B, solution-C and solution-D). Furthermore, another set of experiments were performed on varying growth solutions of 30 mM concentration such as A, B, C, and D for the production of ZnO NSs on WCF under microwave irradiation for 10 minutes operated at 1000 W microwave power. The flow chart of synthesis of ZnO NSs on WCF using microwave-aided chemical bath deposition is illustrated in the Fig. 4.1. Microwave irradiation of the WCF surface produced various distinct morphologies of ZnO under different set of process parameters. According to FESEM data, the sizes of generated ZnO NSs were around 300-2300 nm in longitudinal direction and 200-1100 nm in lateral direction.



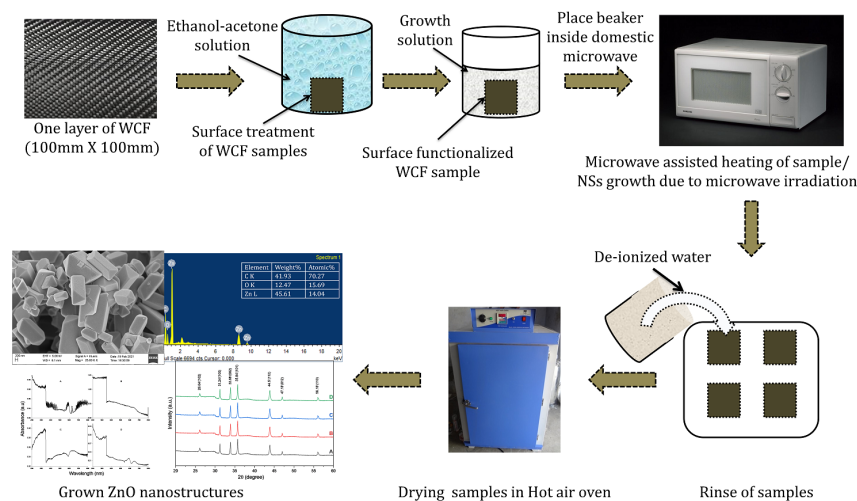


Figure 4.1: Stepwise procedure to fabricate ZnO NSs on WCF using microwave-assisted chemical bath deposition

## 4.2.5 Characterizations

FESEM model-Supra 55 (make-Carl Zeiss, Germany) was used to characterize the generated morphologies and growth structure of ZnO NSs on WCF at various magnifications. FESEM results were also used to examine the size and morphology of the growing NSs. The presence of ZnO on WCF strands was investigated using EDS technique combined with FESEM. The absorption graphs of as generated ZnO NSs on WCF were investigated using UV-vis spectroscopy (model-Agilent Cary 5000) with attachments of an integrating sphere, and study of their optical nature at room temperature were assessed using tauc's plot method. Using wide-angle XRD automated with guidance software (SmartLab Studio II) of Rigaku Smartlab using  $Cu - K\alpha$  radiation imaging, the crystalline structure of the grown morphologies of ZnO on WCF was examined.

## 4.3 Result and discussion

### 4.3.1 Morphological characterization of as grown ZnO NSs on WCF

#### 4.3.1.1 Influence of varying molar concentration

The surface morphology of all of the ZnO nanostructures grown on the woven carbon fiber fabrics was directly observed by FESEM. To investigate the influence of the molar con-

concentrations of precursor chemical such as ZNH and HMTA on the growth and morphology of the ZnO nanostructures, a set of experiments was performed. The attachment of ZnO nanostructures may be seen on the surface of the woven carbon fibers as shown in Fig. 4.2. It was found that the concentrations of zinc nitrate hexahydrate and HMTA had a great influence on the size and structure of the grown nanostructures. At low zinc nitrate hexahydrate and HMTA concentration of 10 mM (Fig. 4.2a), small ZnO nanorods were found on the surface of the carbon fiber, but the quantity of nanorods coated on the carbon fiber surface is very less. Furthermore, some tiny ZnO crystals were sparsely coated upon large nanorods and fiber surface. A non-uniform and discontinuous layer of grown ZnO nanorods can be seen on all of the samples synthesized at different molar concentrations using the microwave-aided chemical bath deposition except for the sample with a concentration of 50 mM (Fig. 4.2c). It is clear that the molar concentration of the growth

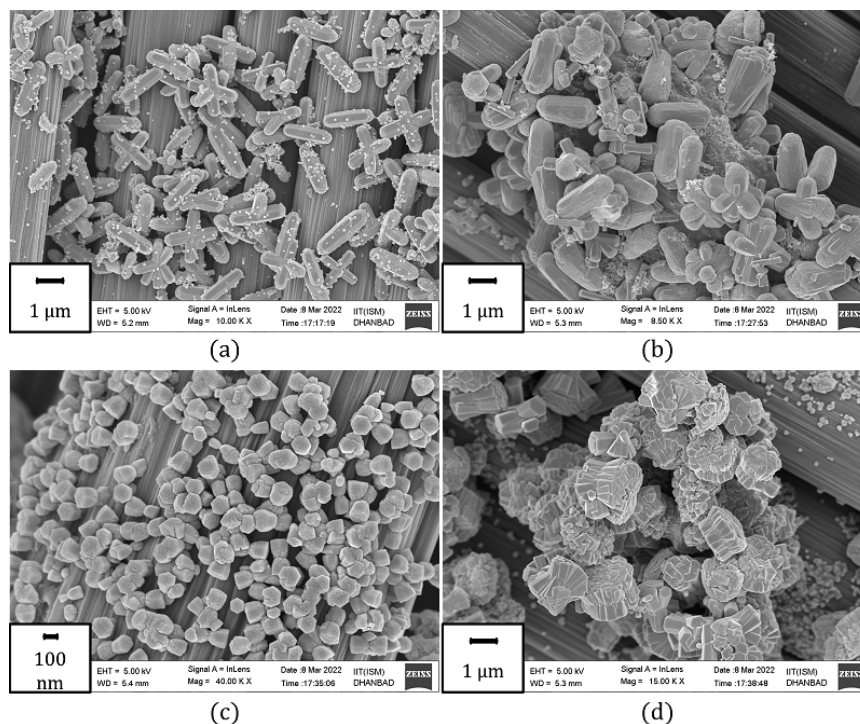


Figure 4.2: FESEM results of as grown ZnO NSs on WCF by microwave heating under varying molar concentration (a) 10 mM (b) 30 mM (c) 50 mM and (d) 70 mM

solution plays a vital role in developing different shape and size of the ZnO nanostructures. However, the variations of molar concentration for growth of ZnO nanostructures on WCF using microwave heating did not develop well distributed nanostructures bonded

with carbon fiber surface. Although the ZnO nanorods were grown at a higher concentration (i.e. 30 mM, 50 mM, 70 mM), thicker nanorods were obtained compared to the lower concentrations. The higher concentration led to the supersaturation and formation of many small nuclei, which results in fast nucleation and a slow growth rate. Consequently, this will retard the growth rate of the (0001) plane and will make the ZnO nanorods thicker and twinned (Fig. 4.2d).

#### 4.3.1.2 Influence of microwave heating duration

Figure 4.3 illustrates the FESEM micrographs of the as-prepared nanorods grown on the ZnO seeded woven carbon fibers after solution based microwave irradiation reaction at different reaction times. It can be clearly seen that the carbon fibers are partially covered with non-uniform ZnO nanorods at lower microwave duration. However, the uniformity and density of grown ZnO nanorods increases as the microwave duration increases and carbon fiber fabric was completely covered with a uniform and dense film of ZnO nanorods. The as-prepared ZnO nanostructures were non-uniform hexagonal nanorods with an axial length of 1000-1500 nm and a diameter of 300-500 nm under varying microwave duration (Fig. 4.3). As the microwave treatment time varies, the shape of nanorods started changing due to twinning of nanorods into flower shape structure. However, the well distributed nanoflower structures were developed at 10 minutes of treatment due to twinning of nanorods into a bunch a flower (Fig. 4.3b). The length and diameter of developed nanostructures increased with an increase in the reaction time. For instance, the length and diameter increased from 1000 to 1500 nm and 300 nm to 500 nm, respectively, when the reaction time increased from 5 to 20 minutes. Therefore, the reaction time is also an important factor for controlling the size of the nanorods.

#### 4.3.1.3 Influence of microwave power

The effects of microwave power on the growth rate of the ZnO nanostructures were also studied. The microwave power was found to have a great influence on both the axial and lateral growth rates of the nanorods. The microwave power level was found to be proportional to the growth rate of the nanorods, mainly due to the rapid heating of the precursors to its crystallization temperature and quick dissolution of the precipitated hydroxides. It was observed that longer and thicker nanorods may be obtained at higher microwave power levels. Figure 4.4 shows the FESEM images of as-grown nanorods at different microwave power levels (250 W, 500 W, 750W and 1000 W) for 10 min. A homogenous and continu-

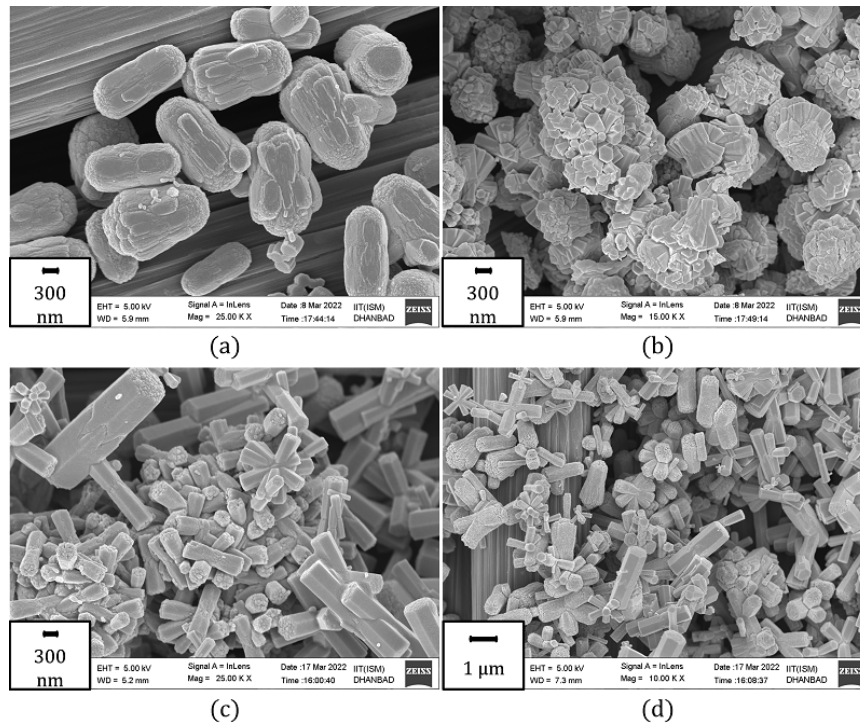


Figure 4.3: FESEM results of as grown ZnO NSs on WCF by microwave heating under different microwave duration (a) 5 minutes (b) 10 minutes (c) 15 minutes and (d) 20 minutes

ous film of ZnO nanorods may be seen on the WCF. The hexagonal ZnO nanorods grown at a high microwave power (1000 W) had a greater diameter (300 nm) and length (600 nm) than nanorods grown at 250 W, 500 W and 750 W (Fig. 4.4a to c). An increase in the microwave power causes the rapid heating of the solution, which enhances the nucleation and growth of the ZnO crystals. The well distributed nanorods of hexagonal cross-section were developed at microwave power of 1000 W for 10 minutes of treatment in 30 mM of reaction mixture as illustrated in Fig. 4.4d. Therefore, rapid growth of longer and thicker nanorods may be achieved by increasing the microwave power. It may be concluded that the microwave power has a great influence on enhancing the dimensions of the nanorods. The above discussion indicated that a ZnO nanorod film may be successfully prepared on the WCFs. The findings of FESEM images illustrated in the Figure 4.4 clearly exhibited that, the alteration of microwave power influences the variation of radiation heat in the system causing growth of ZnO NSs in varied shape and size. It has been noticed that the average thickness of the produced nanorods increases with increasing microwave power and the calculated thickness of the nanorods are 150 nm at low power (250 W) and 320 nm at high

power (1000 W). It was found that when microwave power increases, aggregation formation is preferred. The temperature of the mixture's aqueous solution rises with microwave power, increasing the tendency of the ZnO nuclei to congregate [278]. As the microwave power rises, the system becomes less homogeneous and poorly dispersed due to the formation of agglomerates. However, due to the precursor solution being heated quickly for 10 minutes of irradiation time, agglomerated but well-aligned hexagonal nanorods are produced at 1000 W of microwave power.

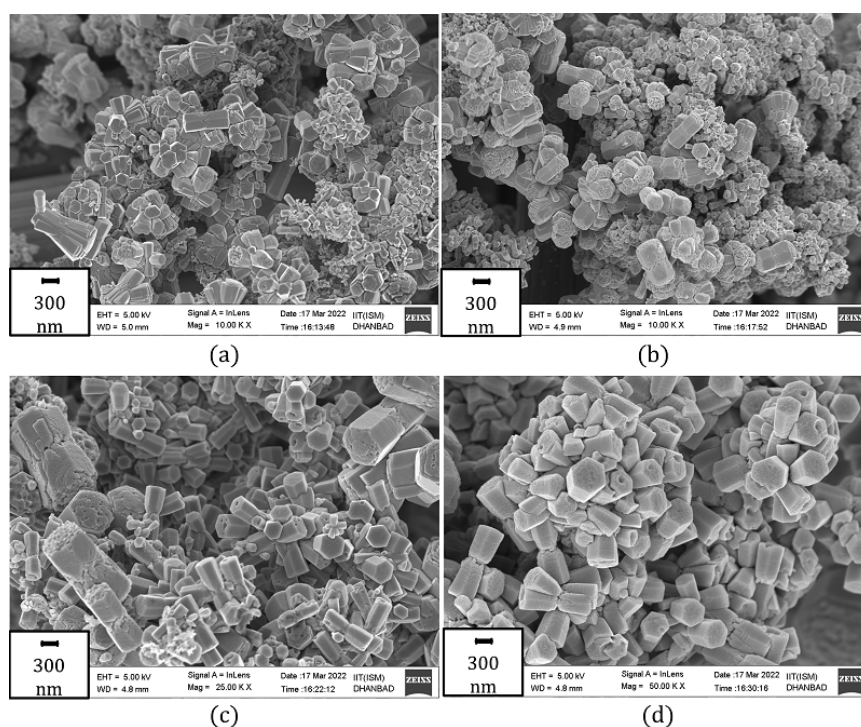


Figure 4.4: FESEM results of as grown ZnO NSs on WCF by microwave heating under different microwave power (a) 250 W (b) 500 W (c) 750 W and (d) 1000 W

The size and morphology of the as-prepared nanorods may be controlled by changing the salt concentrations, reaction time and microwave power levels. Therefore, we may conclude that an increase in the concentration of zinc nitrate hexahydrate/HMTA induces changes in the kinetics of nucleation and growth, which may result in a change in the size and density of the ZnO nanorods on the fiber surfaces. Similarly, the reaction time and microwave power also had a great effect on the size and density of the ZnO nanorods. In particular, these parameters influenced the growth rate of the nanorods along different planes resulting in varying sizes of ZnO nanorods. Finally, a controlled and uniform film

of ZnO nanorods of the desired shape and size may be developed under optimized parameters. The developed nanostructures under varying experimental conditions such as solution concentration, microwave duration and microwave power are discussed in this work. The development of ZnO nanostructures on the carbon fiber fabric in one-step solution based synthesis is a challenging task because it requires seeding of WCF in a seed solution which produces ZnO nucleation [143]. Since some of the developed nanostructures are not well distributed and non-uniform in shape and size, therefore an attempt has been taken to study the effect of different type of growth solution for the development of well distributed ZnO nanostructures on woven carbon fiber fabric. Four different kind of growth solution named as A, B, C and D having 30 mM concentration were prepared using different precursor chemicals in deionized water. These solutions were used to synthesize ZnO nanostructures on carbon fiber fabric.

#### 4.3.1.4 Influence of variety of growth solution

In the current work the effects of different process parameters such as molar concentration, microwave duration and microwave power on the growth rate of the ZnO nanostructures on carbon fiber fabric were studied. These process parameters were found to have a great influence on morphologies and growth rates of the ZnO nanorods. Furthermore, it is required to study the impact of different kind of growth solutions on morphologies and growth rates of the ZnO nanorods. Four different kind of growth solutions such as A, B, C and D having 30 mM concentration were prepared using precursor chemicals such as ZAD, ZNH, HMTA and NaOH in deionized water. The prepared growth solutions of 30 mM concentration were used to synthesize ZnO nanorods on carbon fiber fabric using solution based microwave irradiation reaction at microwave power of 1000 W for 10 minutes. The grown morphologies and growth structure of ZnO NSs on WCF by microwave aided chemical bath deposition method under four distinct growth solutions prepared with different set of precursor chemicals are represented by FESEM micrographs. As shown in Fig. 4.5, different solutions exhibit varied morphologies of ZnO NSs on the strands of carbon fibers, such as nanopetals, nanospheres, nanoflowers, and nanoflakes. The grown nanostructures have an uneven shape, which could be due to post heating at 70 °C for 6 hours in a hot air oven.

The impact of microwave treatment on the precursor chemicals and polar groups present on the WCF surface is the growth mechanism of ZnO NSs on WCF via microwave based chemical bath deposition process. Due to exposure of WCF samples to the electric field

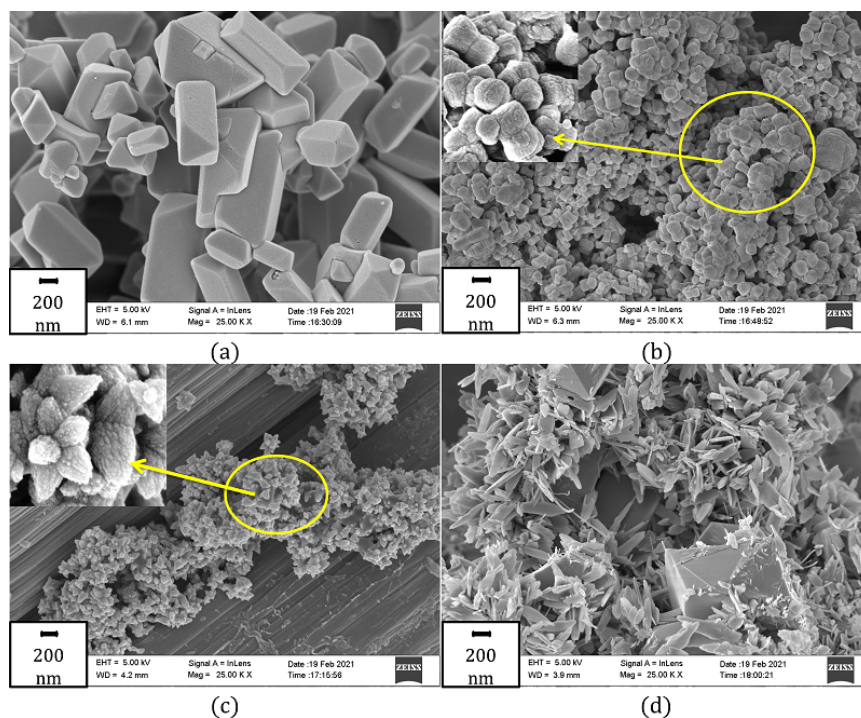


Figure 4.5: FESEM results of as grown ZnO NSs on WCF by microwave irradiation under different precursor solutions (a) nanopetals (b) twinned nanospheres (c) nanoflowers and (d) nanoflakes

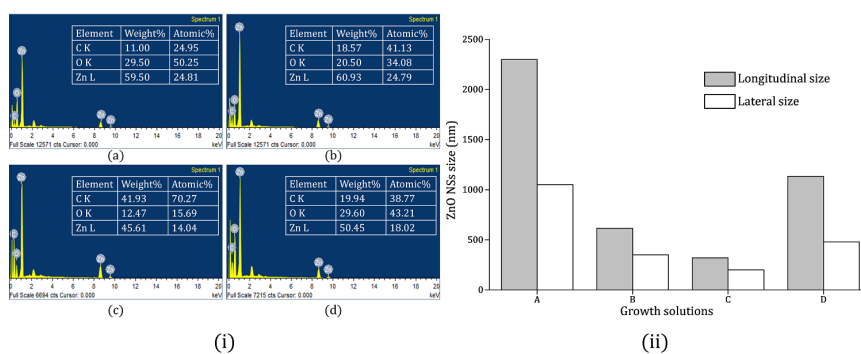


Figure 4.6: (i) EDS spectra and (ii) Size distribution of ZnO NSs under different precursor solutions

during microwave irradiation, precursor chemicals such as ZAD and ZNH in the solution began breaking down into ZnO nuclei, which started acting like dipoles in the precursor solution. After that, under the influence of microwave power of 1000 W, the generated nuclei began polarizing and aggregating to produce ZnO nanostructures on the WCF sur-

face for the duration determined for each sample. ZnO NSs with different morphologies and different dimensions with smooth surfaces were produced because of post heating of samples at 70 °C for 6 hours in a hot air oven. The blossom shaped ZnO NSs were developed on WCF when the microwave power is exposed to the samples for 10 minutes in solution C. The amalgamation of ZNH and HMTA with NaOH caused the flower shape to grow with nine petals as depicted in the inset of Fig. 4.5c. While processing WCF in solution D, where the presence of ZAD generates ZnO nuclei, ZnO nanoflakes were generated. Some of the nanoflakes were destroyed due to 10 minutes of microwave irradiation and subsequent heating during post-annealing process. FESEM micrographs were used to calculate the dimensions of the produced ZnO NSs. Different morphologies have different sizes of the NSs mainly in longitudinal and lateral direction as shown in Fig. 4.6(ii). Nanopetals and nanoflakes have large longitudinal and lateral sizes, but the overall surface area of nanoflowers and twinned nanospheres is substantial, which will improve the surface properties of the final ZnO/WCF samples. The FESEM images confirmed that the ZnO grown on WCF has a variety of morphologies and emerges from the distinct cross-sections of the NSs. EDS spectra indicated the growth of ZnO NSs on WCF surface with weight percentages of Zn and O as shown in Fig. 4.6(i). It was found that the growth of NSs on WCF is in good quantity with a weight percentage range of 45-62 % of Zn and 12-30 % of O. XRD and UV-VIS spectra analysis were used to further investigate the produced ZnO. The EDS spectra analysis demonstrated that the produced ZnO NSs have excellent purity and contain no impurities.

### 4.3.2 Structural characterization of grown ZnO NSs

Figure 4.7(i) shows the XRD spectra of as-grown ZnO NSs on WCF fibers, such as nanopetals, twinned nanospheres, nanoflowers, and nanoflakes. The results of XRD peak analysis confirmed that the developed ZnO NSs have a high purity wurtzite phase of ZnO and possess hexagonal crystal system having space group “P 63 m c”; space group number- 186;  $a=b=3.2530 \text{ \AA}$ ;  $\alpha = \beta = 90^\circ$ ;  $\gamma = 120^\circ$ ; cell volume-  $47.72 \times 10^6 \text{ pm}^3$  and density =  $5.66 \text{ g/cm}^3$ ; JCPDS card no. 96-900-4180). Crystallite sizes of the ZnO NSs were deduced from the XRD peaks using the full-width at half maximum (FWHM) of high intensity peak using the Debye Scherrer relation. In this method, the effects of peak broadening of the XRD spectra due to instrumental errors and inhomogeneous strain were not considered. In order to calculate crystallite size (D) and strain ( $\epsilon$ ) of the synthesized ZnO NSs on WCF, Williamson-Hall (W-H plot) technique was applied by calculating FWHM. The overall



broadening of XRD peaks is the sum of broadening due to crystallite size and broadening due to strain [276]. That is;

$$\beta_t = \beta_D + \beta_\epsilon \quad (4.1)$$

And the Scherrer formula is;

$$D = \frac{K\lambda}{\beta_D \cos\theta} \quad (4.2)$$

Where, K is the shape factor which is equal to 0.9,  $\lambda$  is the wavelength of X-ray source which is equal to 0.15406 nm,  $\theta$  (in radian) is the location of peaks and D is the size of grown crystals. The overall broadening of XRD peak may be written as:

$$\beta_t = \frac{K\lambda}{\beta_D \cos\theta} + 4\epsilon \tan\theta \quad (4.3)$$

The above equation can be written as,

$$\beta_t \cos\theta = \epsilon(4 \sin\theta) + \frac{K\lambda}{D} \quad (4.4)$$

This statement is equivalent to a straight line equation, therefore the W-H graph is essen-

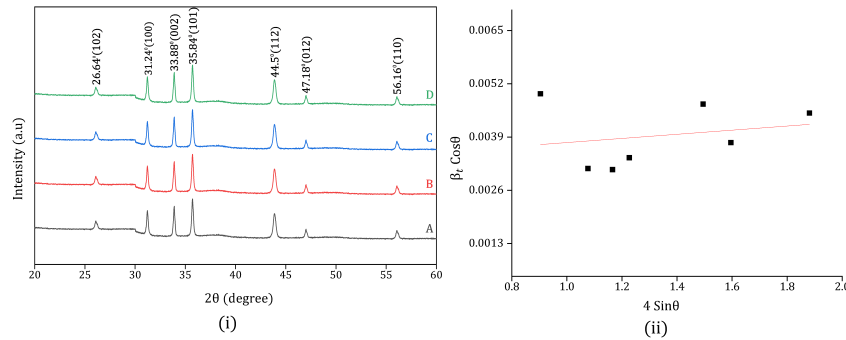


Figure 4.7: (i) XRD spectra and (ii) Williamson Hall graph of as grown ZnO NSs on WCF sample

tially a straight line drawn with  $(4 \sin\theta)$  on the x-axis and  $(\beta_t \cos\theta)$  on the y-axis, as seen in Fig. 4.7(ii). The slope of the line will give the amount of strain “ $\epsilon$ ” and the y-intercept will give the value of crystal size. The computed value of the strain is  $5.03698 \times 10^{-4}$  and the crystallite size is 42.53 nm. The observed value of the crystallite size using Scherrer formula for all XRD peaks of ZnO NSs is found to be in the range of 30-40 nm and the analogous value of D corresponding to the high intensity peak (101) of all the samples was observed to be in the range of 32-43 nm as illustrated in the Table 4.2. The expression to

Table 4.2: Growth conditions and properties of as grown ZnO NSs on WCF

ZnO/WCF sample	Growth solution	Developed morphology	mor-	Microwave duration (minutes)	Crystallite size, $D_{101}$ (nm)	Energy level ( $E_g \sim$ eV)
A	A	Nanopetals		10	$\sim 38$	$\sim 3.358$
B	B	Twinned-nanospheres		10	$\sim 40$	$\sim 3.29$
C	C	Nanoflowers		10	$\sim 43$	$\sim 3.18$
D	D	Nanoflakes		10	$\sim 32$	$\sim 3.32$

calculate the texture coefficient  $T_{c(hkl)}$  which will provide the basis to deduce the preferred orientation of crystal growth and their orientation in the (h k l) plane is defined as [277]:

$$T_{c(hkl)} = \frac{\frac{I_{(hkl)}}{I_{0(hkl)}}}{\left[\frac{1}{n} \sum \frac{I_{hkl}}{I_{0(hkl)}}\right]} \quad (4.5)$$

Where,  $I_{(hkl)}$  is the calculated XRD intensity corresponding to (h k l) plane derived from the XRD data,  $I_{0(hkl)}$  is reference data of XRD peak intensities from (JCPDS card no. 96-900-4180) and n is the total number of XRD peaks. The texture coefficients ( $T_{c(hkl)}$ ) of the as grown ZnO NSs on WCF are tabulated in the Table 4.3. If the value of  $T_{c(hkl)}$  is more than one then there is affluence of grain in the corresponding plane but if the value equal to one then it shows random orientation of crystals. It can be observed that the largest value of  $T_{c(hkl)}$  lies in the plane (101) for each sample but sample C (nanoflowers morphology) has the highest value of texture coefficient because of the larger surface area of nanoflowers as mentioned in Table 4.3. Finally it can be concluded that the preferred orientation for the crystal growth of ZnO NSs is along the (1 0 1) plane which is largest for sample-C.

Table 4.3: Details of texture coefficient of ZnO/WCF samples

Sample	$T_{c(102)}$	$T_{c(100)}$	$T_{c(002)}$	$T_{c(101)}$	$T_{c(112)}$	$T_{c(012)}$	$T_{c(110)}$
A	1.21	1.06	1.054	2.35	0.78	1.02	1.24
B	1.14	0.97	1.18	2.42	0.92	0.91	0.97
C	1.2	1.18	1.23	2.78	0.98	1.06	1.13
D	1.01	0.96	1.04	2.26	0.88	0.91	0.96

### 4.3.3 Optical characterization of ZnO NSs grown on WCF

The optical properties of produced ZnO NSs on WCF were investigated using a UV-vis spectrophotometer with a wavelength range of 200-800 nm (visible range). UV-vis analysis of samples was analyzed by optical absorbance, optical transmittance and optical reflectance spectrum in the visible range as illustrated in Fig. 4.8, Fig. 4.9 and Fig. 4.10 respectively. At a particular wavelength sample illuminates due to the absorption of that radiation and at the remaining wavelength no absorption will occur. In the same way transmittance and reflectance will be seen while transmitting and reflecting that radiation at a particular wavelength. ZnO include a large direct energy band and large exciton energy at atmospheric conditions (60 meV). From Fig. 4.8, the strong absorption occurred near  $\sim 353$  nm wavelength for all the samples that exhibit presence of ZnO because pure ZnO has band gap ( $E_g=3.37$ eV) in the wavelength range of  $\sim 360$  nm. In Fig. 4.8(a), the graph shows that the absorbance varies nonlinearly, however there is a sharp decline in absorbance at wavelengths near  $\sim 350$ - $355$  nm, which is due to optical conversions occurring at the energy level of the ZnO nanopetal morphology. In Fig. 4.8(b and d) there is a decrement in the absorption value just after the wavelength of  $\sim 350$ - $355$  nm and small variation near the wavelength of 650 nm which may be due to oxygen vacancies. However in the

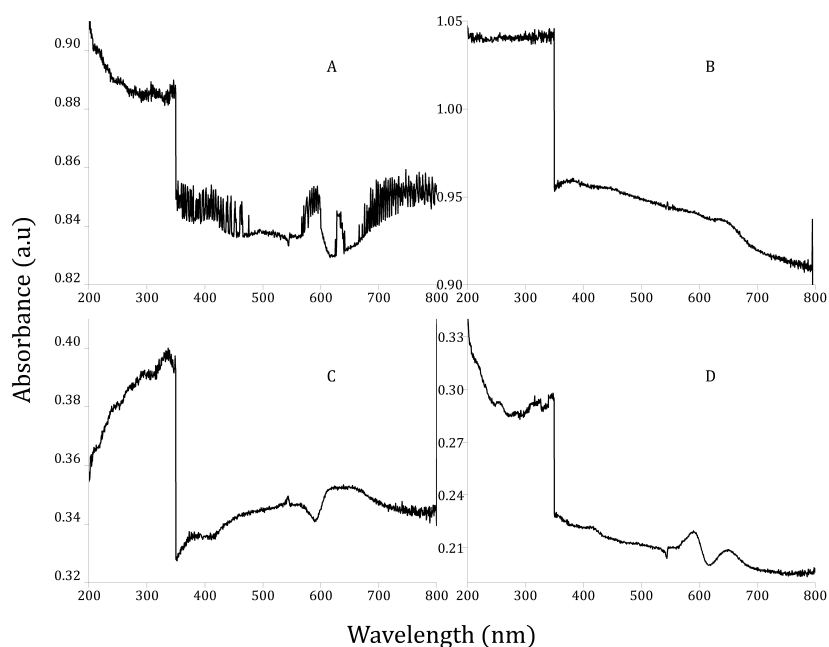


Figure 4.8: Optical absorbance of ZnO NSs grown on WCF

case of Fig. 4.8(c), the graph indicates a dramatic drop in absorption value, followed by an increase, shortly after the 353 nm, which could be owing to the nanoflower shaped ZnO formed on WCF. As shown in Fig. 4.9 and Fig. 4.10, the transmittance and reflectance graphs of the grown ZnO NSs on WCF show irregular change of transmitted and reflected radiation near 350 nm. Due to morphological diversity of produced ZnO NSs on WCF, it can be assumed that the developed ZnO NSs have optical absorbance, optical transmittance, and optical reflectance up to a certain level in the visible range. The reflectance values of sample A, B, D are a combination of positive and negative value but sample C has positive values. The reflectance values of sample A and B are showing negative value because nanopetals and nanosphere morphologies of ZnO might act like a mirror, causing glossy peaks in the spectra when the angle of observation corresponds to the angle of incidence. The negative reflectance is not desirable. Thus it can be concluded that only nanoflower shaped ZnO NSs have positive value of all three spectrum of UV-VIS spectroscopy which shows nanoflower shaped ZnO NSs are most suited for optics applications.

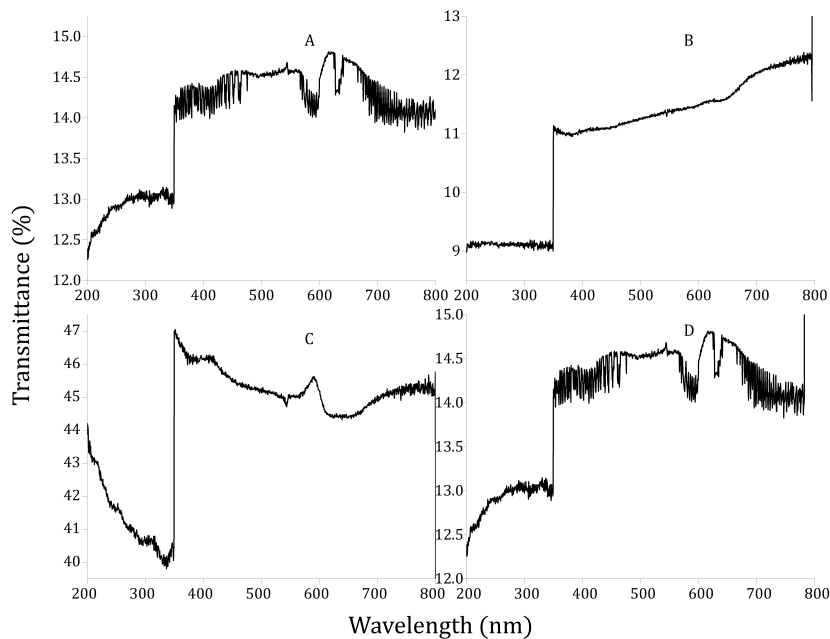


Figure 4.9: Optical transmittance of ZnO NSs grown on WCF

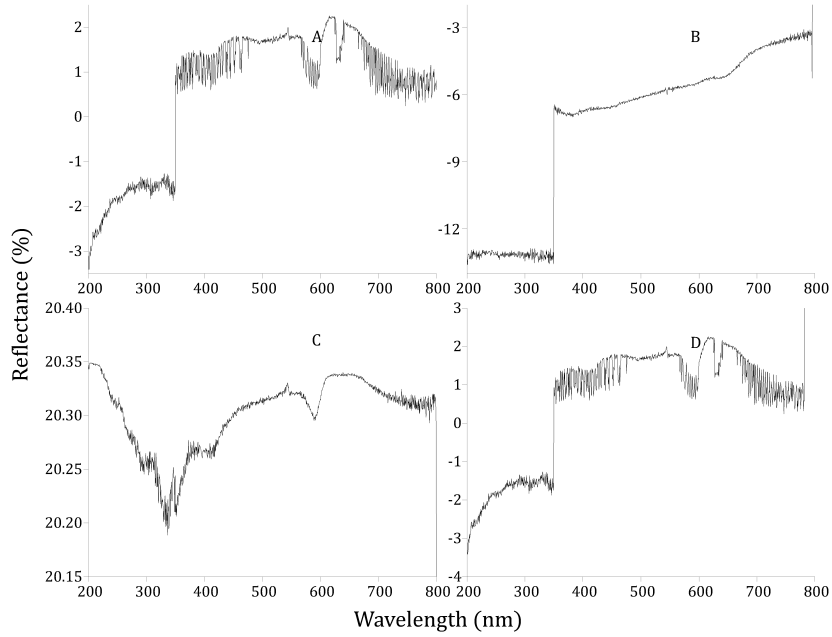


Figure 4.10: Optical reflectance of ZnO NSs grown on WCF

#### 4.3.3.1 Determination of the band gap value and Urbach energy

The energy band values ( $E_g$ ) of the fabricated ZnO NSs on WCF samples were determined using following equation and Tauc's plot method [278]:

$$(\alpha h\nu)^n = B(h\nu - E_g) \quad (4.6)$$

Where,  $\alpha$  represents coefficient of absorption  $h\nu$  represents photon energy,  $n$  represents the exponent of the band gap which is  $\frac{1}{2}$  for indirect band and 2 for direct band.  $B$  is the constant depending upon material used. The value of  $\alpha$  can be calculated by subsequent relation:

$$\alpha \approx \frac{2.303xA}{l} \quad (4.7)$$

Where,  $A$  is absorbance value from UV-VIS spectra and  $L$  is the thickness of the film (in this case it is  $4 \mu\text{m}$ ). Tauc's plot is a plot between  $(\alpha h\nu)^2$  and photon energy ( $h\nu$ ) as illustrated in the Fig. 4.11(i). As shown in Fig. 4.11(ii), the value of energy band gap for each sample can be determined by linear fitting analysis of their Tauc's plot. Table 4.2 displays the band gap values of various morphologies of ZnO on WCF. The computed energy gap is concordance with the energy gap of bulk ZnO ( $E_g=3.37 \text{ eV}$ ). Differing ZnO NSs mor-

phologies exhibit different computed optical band gap values, in which ZnO nanopetals (sample-A) have higher value of band gap while ZnO nanoflowers (sample-C) possesses low band gap. At the principal absorption line, the coefficient of absorption depends in

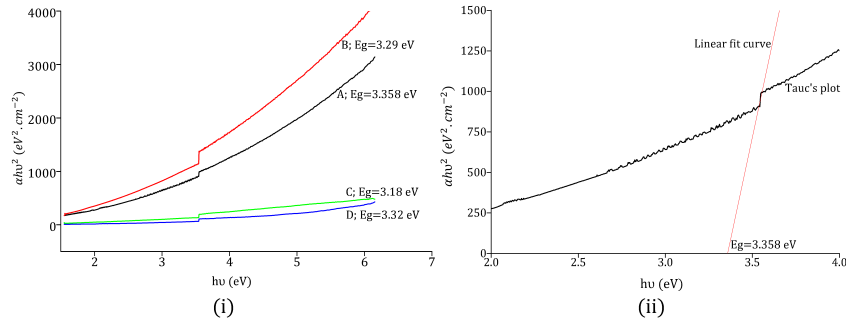


Figure 4.11: (i) Tauc's plot of grown ZnO NSs and (b) Band gap calculation by linear fitting of Tauc's plot

exponential manner with the incident photon energy and compiles an empirical formula which is called Urbach's expression. Thus expression to calculate Urbach energy may be defined as [276]:

$$\alpha = \alpha_0 \exp\left[\frac{h\nu - E_1}{E_u}\right] \quad (4.8)$$

Where,  $E_1$  and  $\alpha_0$  represent constants and  $E_u$  represent Urbach energy which is equal to the width of the exponential absorption edge. The Urbach energy  $E_u$  is a vital boundary to portray the problem of a material. It has to do with transitions between enlarged valence band circumstances and constrained conduction band ones. The width of the band's restricted states in the band gap is defined as the urbach energy, ' $E_u$ '. It is possible to deduce the problem in the compound from the variation of the retention coefficient. The urbach energy ' $E_u$ ' represents the concept of material disorderliness and has been proven to be a crucial aspect in understanding material irregularity [279]. It relates between expanded conditions of the valence band and confined condition of the conduction band. The urbach energy, ' $E_u$ ' is defined as the width of the confined state of the band gap. The change in the coefficient of absorption can be used to express disorder in a material. The plot against  $\ln(\alpha)$  and  $h\nu$  of grown ZnO NSs on WCF reveals the amount of the urbach energy as illustrated in the Fig. 4.12. Samples A and D have growing urbach energies, whereas sample B has a stable value after  $\sim 3.6$  eV photon energy, but sample C (nanoflowers) has started to decrease. This variation demonstrates the material's disorderliness, namely microstructural lattice disorder. The dependence of the optical coefficient of absorption with ' $h\nu$ '

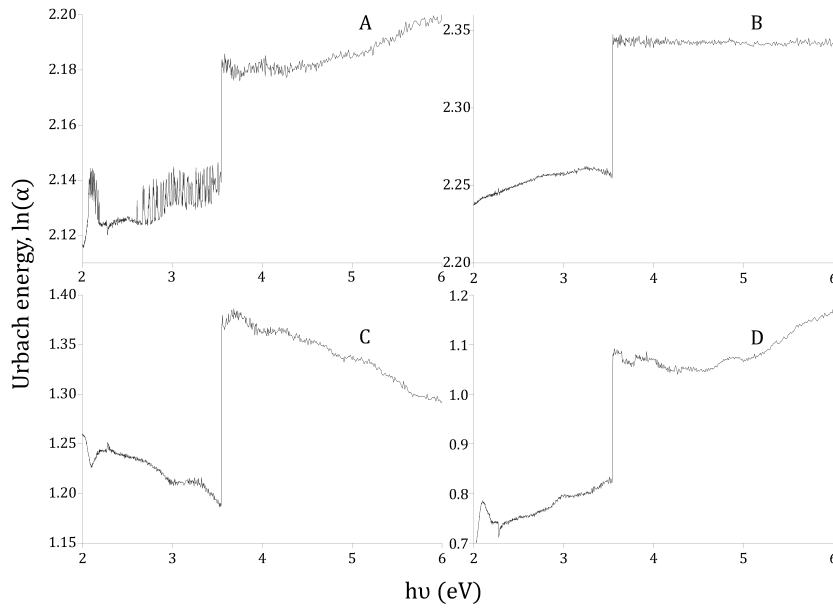


Figure 4.12: Urbach energy of ZnO NSs grown on WCF

may appear from ambush levels at grain borders.

#### 4.3.3.2 Study of refractive index and dielectric constants of grown ZnO NSs on WCF

The complicated behavior of refractive index and dielectric constants can also be used to define the optical properties of solid materials. Because dispersion is a vital parameter in optical communication and producing spectra dispersion appliances, dispersion plays an important role in the analysis of optical materials. The optical performance of developed ZnO NSs in the UV-visible region was studied using absorbance, transmittance, and reflectance spectra. The refractive index is a function of wavelength  $n(\lambda)$  and can be derived from Fresnel's expression of reflectance as [280]:

$$R = \frac{(n-1)^2 + k^2}{(n+1)^2 + k^2} \quad (4.9)$$

Where,  $n$  and  $k$  represent factor of real and the imaginary portion of complex refractive index  $n^*$ ; and the factor  $k = \frac{\alpha\lambda}{4\pi}$  is named as extinction coefficient. The expression of

refractive index can be written as [280]:

$$n = \left( \frac{1 + R}{1 - R} \right) + \sqrt{\frac{4R}{(1 - R)^2} - k^2} \tag{4.10}$$

The behavior of the observed refractive index with the function of wavelength is illustrated

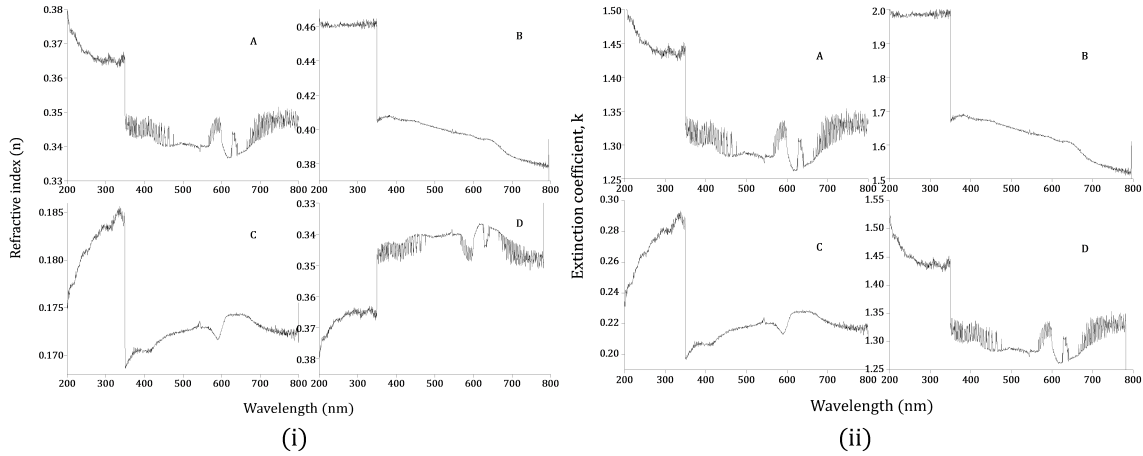


Figure 4.13: Variation of (i) refractive index and (ii) extinction coefficient of grown ZnO NSs with wavelength

in Fig. 4.13(i). The graph reveals the non-monotonic variation of refractive index with respect to wavelength in the region of (200-360 nm) which is called “anomalous dispersion”. The fluctuation then follows a normal dispersion pattern for the wavelength range (360-800 nm). The anomalous dispersion could be caused by a resonance between electromagnetic radiation and electron polarization, which causes electrons in ZnO NSs to pair with the oscillating electric field. Because of the growth of diverse morphologies of ZnO NSs on WCF surface, the refractive index of as grown ZnO NSs exhibit nonlinear and irregular variations for each sample, however there is a sudden change in the value of refractive index near the wavelength range of 350-360 nm. The variation of parameter  $k = \frac{\alpha\lambda}{4\pi}$  (extinction coefficient) with the prescribed wavelength range in the visible region is illustrated in Fig. 4.13(ii). Because of the nanoflowers shape of the ZnO, the values of ‘k’ for developed ZnO NSs decrease up to a particular wavelength range and subsequently increase for all samples except sample-C. The variation of ‘k’ for all samples is nonlinear and irregular and there is dramatic variation in the value near  $\sim 350-360$  nm wavelengths due to different morphology of ZnO NSs. The frequency dependability of the complex dielectric function



is used to characterize the principal electron excitation peak of ZnO NSs. It should also be mentioned that polarizability of solid is determined by their dielectric function, which is linked to the density of states in the forbidden band. As a result, understanding the nature of the real and imaginary parts of the dielectric function in terms of photon energy is critical. The complex dielectric function is expressed as [281]:

$$\varepsilon^* = \varepsilon_r + i\varepsilon_i \quad (4.11)$$

Where,  $\varepsilon_r$  and  $\varepsilon_i$  represents the real part and imaginary part of the dielectric function respectively. Also,  $\varepsilon_r$  and  $\varepsilon_i$  are depending on the n and k value in the subsequent manner;

$$\varepsilon_r = n^2 - k^2 \quad (4.12)$$

$$\varepsilon_i = 2nk \quad (4.13)$$

The variation of  $\varepsilon_r$  and  $\varepsilon_i$  as a function of photon energy for the grown ZnO NSs on WCF is illustrated in Fig. 4.14(i) and Fig. 4.14(ii), respectively. The variation of dielectric constant of fabricated ZnO on WCF is nonlinear in the whole range of wavelengths but there is dramatic change in value near  $\sim 350\text{-}360$  nm. It is caused because of the low estimation of the coefficient of extinction which is credited to the profound coefficient of absorption. Furthermore, the plot reveals that both  $\varepsilon_r$  and  $\varepsilon_i$  have non-monotonic changes, with  $\varepsilon_r$  being more articulated than  $\varepsilon_i$ . This pattern can be explained by the fact that in this energy range, specific collaborations between photons and electrons within the sample occur. The  $\varepsilon_r$  and  $\varepsilon_i$  of the dielectric function demonstrate almost similar model.

#### 4.3.3.3 Optical conductivity

This is an important material feature that connects the current density to the electric field at normal frequencies. Optical conductivity is a modified kind of high-frequency electrical transfer. It is a contactless, quantitative test that's prone to charged outputs. The optical conductivity of the material is computed from the following expression [276]:

$$\sigma_{opt.} = \frac{\alpha nc}{4\pi} \quad (4.14)$$

Where,  $\alpha$ , n and c represents absorption coefficient, refractive index and speed of light (in vacuum), respectively. Figure 4.15 illustrates the variation of optical conductivity of the synthesized ZnO NSs on WCF having different precursor solution treatment under

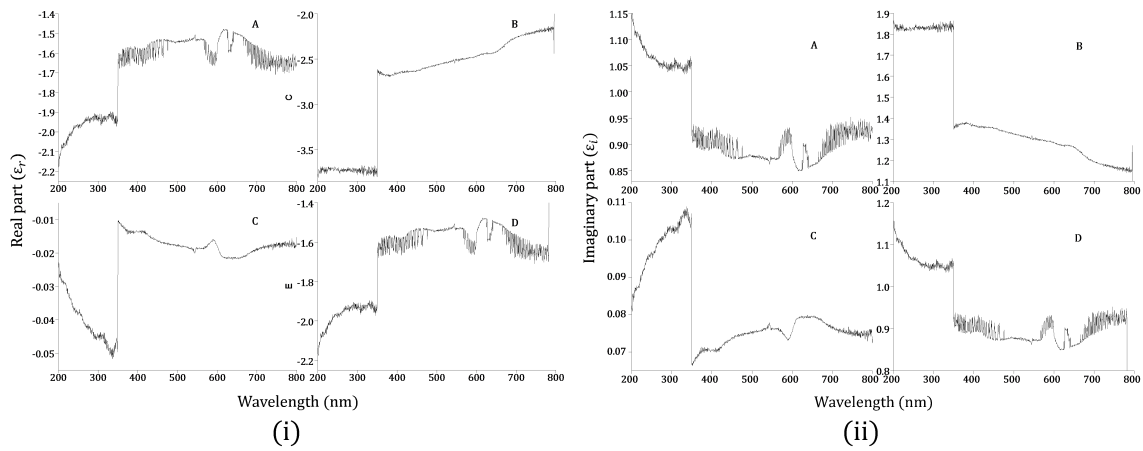


Figure 4.14: Variation of (i) real part and (ii) imaginary part of dielectric function of ZnO NSs with wavelength

microwave with in visible range. The plots of four different morphologies of ZnO reveal their particular conductivity nature. Because of the activation of electrons in interactions with photons, the behavior of optical conductivity ( $\sigma$ ) with photon energy is nonlinear, as shown in the graph. The optical conductivity of nanoflowers (sample-C) displays a positive variation in conductivity value before  $\sim 353$  nm wavelength, but then drops abruptly under the band gap region before increasing nonlinearly.

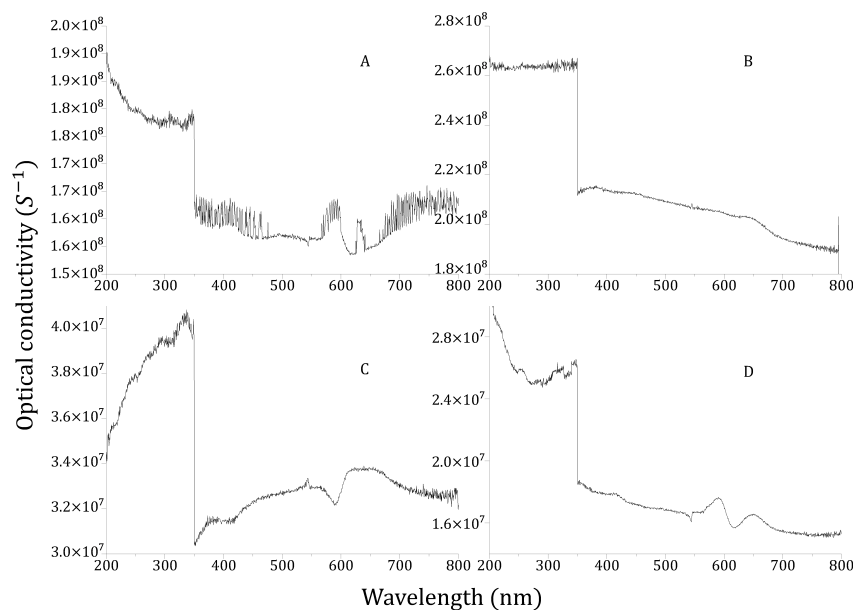


Figure 4.15: Optical conductivity variation with wavelength for grown ZnO on WCF

## 4.4 Summary

One step rapid growth of ZnO nanostructures on carbon fiber fabric using microwave-assisted chemical bath deposition technique has been advanced which is quicker than the chemical bath deposition process. Rapid heating of growth solution of  $[Zn(NH_3)_4]^{2+}$  under microwave irradiation causes production of ZnO nanostructures by forced hydrolysis. The impact of different microwave synthesis parameters such as salt concentration, microwave duration and microwave power have great influence on morphologies and growth rates of the ZnO nanorods. The distributions and orientations of nanostructures can be optimized by tuning these process parameters and their reaction with growth solution. The FESEM analysis of developed ZnO NSs on WCF at different microwave synthesis parameters such as salt concentration, microwave duration and microwave power revealed that the nanostructures are not uniform and well aligned. However it gives basis to set the best conditions of process parameters for effective growth of ZnO NSs on WCF. Further, different growth solutions were prepared to analyze the effects of precursor chemicals used for making growth solution. It was found that, the well distributed and uniform growth of ZnO NSs on WCF can be developed using different growth solutions. The best conditions for development of ZnO NSs on WCF using microwave-assisted solution phase synthesis are

30 mM of molar concentration, 1000 watt of microwave power, 10 minutes of microwave duration and type 'C' growth solution. Thus, The impact of different kind of growth solution for the well distributed and uniform growth of ZnO nanostructures on carbon fiber fabric provides a basis to effective functionalization of fabrics. The FESEM result shows that nanostructures are irregular in shape and size but have smooth surface. The sizes of generated ZnO NSs were around 300-2300 nm in longitudinal direction and 200-1100 nm in lateral direction based on FESEM findings. The preferred orientation of ZnO growth is in the [1 0 1] direction, which is highest for nanoflowers, according to XRD and texture coefficient results. The optical characteristics of the samples reveal that nanopetals have a big band gap and nanoflowers have a small band gap which indicates greater size crystals possess smaller band gaps. The refractive index, extinction coefficient, dielectric constant, Urbach energy, and optical conductivity of growing morphologies of ZnO on WCF surface are also investigated and depicted in graphs. The findings of all the analyses of grown ZnO NSs on WCF are in convergence with the already published experimental results and other available literatures. As formed ZnO NSs on WCF have these features, indicating that they have the potential to be employed in high performance nanocomposites for optoelectronics and photonics applications such as sensors, emitters, catalysts, active medium, and electrodes. Its potential may be expanded in energy harvesting devices, bio-sensing, medicinal implementations, and environmental pollution sectors due to its outstanding morphological structure and enhanced surface to volume ratio.

# 5

## Development of ZnO-modified WCF reinforced epoxy resin composites and their mechanical characterizations

The aim of the chapter is to investigate the impact of surface functionalization of carbon fibers by the growth of ZnO nanostructures via hydrothermal route on the mechanical characteristics of a carbon fiber reinforced polymer composites. The ZnO-modified carbon fiber fabric is used as a reinforcement in the bisphenol-A epoxy resin polymer matrix for developing hybrid composites. The formations of ZnO on the surface of the carbon fibers are analyzed through field emission scanning electron microscopy, % weight change study, X-ray diffraction study, Fourier transform infrared spectroscopy, UV-VIS spectroscopy and energy dispersive spectroscopy technique. In comparison to plain carbon fiber epoxy resin composites, the tensile strength, elastic modulus, and in-plane shear strength of ZnO-modified carbon fiber composites improved by up to 48.63 %, 46.44 %, and 20.79 %, respectively, while the impact energy absorption increased by 76 %.

## **5.1 Introduction**

Carbon fiber reinforced polymers (CFRPs) have attracted a lot of attention in high-performance applications because they are 70 % lighter than steel and have extremely high specific mechanical characteristics [282, 283]. However, because to the high rigidity of carbon fibers, which are about two to five times more rigid than aluminium and steel for a given weight, CFRPs are vulnerable to impact damage. Low-impact energy absorption makes CFRP composites vulnerable to impact damage. When a composite is impacted, it absorbs the impact energy and deforms as a result. When enough impact energy is absorbed, cracks in the matrix begin to form. The cracks continue to spread up to the interphase until they reach the maximum amount of impact energy absorption. Matrix cracks commence the overall composite damage process during an impact test, which is then followed by delamination at the matrix-reinforcement contact, and lastly fiber breakage [284]. Delamination is a common cause of laminate composite mechanical property degradation. In ductile or brittle fiber composites, however, fiber breaking in the areas surrounding the impact loading point plays a significant effect. The interfacial performance is ultimately what determines the composite's effectiveness [285]. The type of composite reinforcement utilized in the textile industry is woven carbon materials. Carbon fiber textile composites are created using a weaving process in two mutually orthogonal directions, and then impregnated with a resin substance. In comparison to laminate composites, these composite materials exhibit better out-of-plane stiffness, strength, and toughness qualities [286]. Delamination and fiber pull-out, which are hardly apparent due to inadequate adhesive bonding in composites, can dramatically degrade the mechanical strength of composites and even cause catastrophic structural failures. Due to their thermal stability, electrical conductivity, and improved mechanical properties, nanoscale carbon-based fillers such as carbon nanotubes (CNTs), graphene/graphite nanoplatelets, carbon nanofiber (CNF), and carbon black have recently gained a lot of attention [287, 288]. However, due to the strong intermolecular vanderwall interactions between CNTs and graphene, as well as the tendency for CNFs and carbon black to form bundles and branches, it is difficult to prepare uniform dispersions of these nanoscale carbon-based fillers; as a result, these materials may aggregate in the composites [289, 290]. To overcome these issues, whiskerization has been utilized to grow a secondary reinforcement directly onto the surface of the fiber to get the appropriate interfacial reinforcement, which is the most important aspect in composite performance. The benefits of growing 1-D metal oxide NSs in general and ZnO nanorods in particular over structural and conductive fibers include smart materials for energy scavenging,

improved mechanical behavior through better matrix-to-fiber adhesion, gas sensors, field emission, photo-electrochemical cells, surface polarity shielding, and improved damage resistance [291, 61]. Because of their superior piezoelectric, optical, electrical, mechanical, dielectric, and microwave absorption properties, ZnO NSs have been selected as one of the most promising whiskerization materials [292]. ZnO NSs arrays improve load transfer capacity from fiber to matrix without compromising fiber mechanical qualities; they reduce stress concentration and increase surface area for interfacing with the polymer matrix [143]. While other nanowires can improve interfacial mechanical properties, ZnO nanowires are projected to be less susceptible to impact damage. Increased surface area between ZnO nanowires and a polymer matrix is thought to improve these qualities via improving chemical reactivity and mechanical load-transfer efficiency. It is due to the presence of functional groups (hydroxyl, carbonyl, and carboxyl) on the surface of carbon fibers. ZnO nanowires have a great affinity for these functional groups. The polar groups on the carboxylic acid of the carbon fiber surface react with the  $Zn^{2+}$  of the ZnO nanowires to generate a strong ionic connection. In addition, the existence of two lone electron pairs in the carbonyl group has a great affinity for ZnO nanowires. Furthermore, these functional groups react quickly with the ester linkages in polyester resin, generating a strong bond. Overall, all of these interactions between the functional groups of carbon fiber, ZnO nanowires, and resin boost the composite's impact strength [37].

The hydrothermal approach, template-based growth, thermal evaporation, plasma-molecular beam epitaxy, and metal organic chemical vapour deposition have all been established as ways for producing ZnO nanowires [108, 165, 293]. The hydrothermal approach is extensively used to create ZnO nanowires at low temperatures and at a low cost. ZnO nanowires are made using this process by varying the precursor chemicals, concentration, growth temperature, and time. Although controlling the growth of ZnO NSs was difficult, Liang et al. [109] succeeded in controlling the formation of ZnO structures. Researchers have recently looked at ZnO nanowires/graphene hybrid structures and their applicability in a variety of diverse sectors. However, mechanical properties of ZnO nanowires incorporated in composites, such as impact behaviour and elastic modulus, have received less attention. Impact strength is a fascinating composite feature that is crucial for understanding the damage mechanism in terms of stiffness [294].

In the present work, the energy absorption of ZnO-modified woven carbon fibers reinforced bisphenol-A epoxy resin (ZnO/WCF/BPA epoxy resin) hybrid composites is examined in terms of ZnO concentration, which controls the microstructure of the ZnO NSs. An energy balance equation is used to describe produced hybrid composites after they have been dis-

torted by an impact test in order to better understand the damage mechanism. The growth morphology of ZnO NSs on the surface of woven carbon fibers is studied using field emission scanning electron microscopy (FESEM). The vacuum bagging procedure is used to explore the energy absorption and tensile modulus of ZnO/WCF/BPA epoxy resin hybrid composite specimens, which saves time and money while ensuring uniform mechanical properties [295, 296].

## 5.2 Experimental

### 5.2.1 Materials used

The substrate material for the formation of ZnO NSs was unmodified WCF of grade T-300 consisting of 3000 wires and 200 GSM size with attributes (as listed in Table 5.1). For the studies, analytical grade chemical precursors (as listed in Table 5.2) were utilized to prepare seed and growth solution. All of the materials were used in their natural state.

Table 5.1: Properties of Woven carbon fiber

S.no.	Characteristics	Specifications
1	Woven type	Bidirectional plain woven
2	Fabric thickness	0.20 mm
3	Filament diameter	7 $\mu\text{m}$
4	Tensile strength	4000 MPa
5	Tensile modulus	240 GPa
6	% Elongation	1.7
7	Density	1.8 $\text{g}/\text{cm}^3$

### 5.2.2 Surface treatment of WCF

To eliminate any organic impurities, samples of unaltered WCF were cut into 120 x 100  $\text{mm}^2$  (length x width) pieces and rinsed in an acetone–ethanol solution. After that, the samples were oven dried for 20 minutes at 90 °C. After that, the samples were immersed in a 10 % NaOH solution for 30 minutes at room temperature. The WCF samples were rinsed multiple times with deionized water before being oven dried for 1 hour at 90 °C. The functionalized WCF pieces were immersed in aqueous HCl (10 N) for 10 seconds before being rinsed and oven-dried for 1 hour at 90 °C. Excess metal ions that would contaminate the growth solution were eliminated by immersing the specimens in aqueous HCl. Through



Table 5.2: List of chemicals precursors

S.no.	Name of the chemical	Chemical formula	Purpose
1	Zinc Acetate dihydrate	$Zn(CH_3COO)_2 \cdot 2H_2O$	To prepare seed solution
2	Ethanol/Acetone	$C_2H_5OH$	Cleaning of samples/substrates
3	Sodium hydroxide	$NaOH$	To prepare seed solution
4	Zinc nitrate hexahydrate	$Zn(NO_3)_2 \cdot 6H_2O$	To prepare growth solution
5	Hexamethylene tetramine	$C_6H_{12}N_4$	To prepare growth solution
6	Water (distilled/dionized)	$H_2O$	Solvent to prepare growth solution and to rinse the sample to halt the growth of NSs
7	Bisphenol A (BPA) epoxy resin	$(CH_3)_2C(C_6H_4OH)_2$	Used a matrix material for WCF/ZnO polymer composites

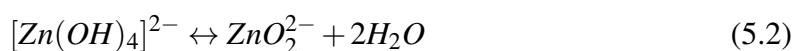
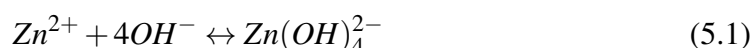
an ion-exchange reaction, the hydrogen ions in the HCl solution induced carboxylic acid groups to develop on the fiber surfaces [297]. Surface treatment causes the production of active groups on the WCF surfaces, such as ( $-O-C-$ ,  $-C=O$ ,  $-O-C=O$ ), which increased the sample's overall surface energy and polarity, as well as its wettability to interact with other components and the polymer matrix [88]. The process parameters for hydrothermal synthesis of ZnO NSs on WCF surface have been defined after detailed literature survey. However, the variations of selected process parameters have been defined after performing several some preliminary experiments. The variations of different factors affecting the growth of ZnO NSs on WCF have been studied and illustrated in the Chapter 3. Thus, the selection of process parameters for this work has been decided upon literature outcomes and our preliminary experimental findings.

### 5.2.3 Preparation of ZnO seed and growth solutions

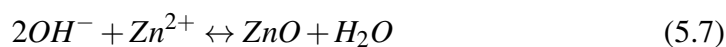
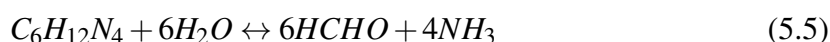
At 65 °C, 0.25 g zinc acetate dihydrate was dissolved in 400 ml ethanol to make the seed solution. For 30 minutes, the solution was vigorously swirled. In a separate beaker, 2 mM NaOH was dissolved in 80 ml ethanol and agitated for 15 minutes at 65 °C. The resulting solution was slowly poured into the zinc acetate dihydrate solution, followed by the addition of 320 ml of ethanol to form a total volume of 800 ml. Without using heat, the mixed solution was agitated for 30 minutes. The pH of this homogeneous seed solution was kept in 5-6 range while it was cooled to ambient condition. An equimolar solution of zinc nitrate hexahydrate and HMTA was used as the growth solution. The ZnO growth solution (10 mM) was made by stirring 10 mM HMTA for 20 minutes in 650 ml distilled water. The

zinc nitrate hexahydrate solution was put into the HMTA solution, which was then agitated for 30 minutes at room temperature while maintaining a pH of 6-8. The remaining growth solutions (30, 50, and 70 mM) were made in the same manner. For the growth of diverse morphologies of ZnO NSs on the surface modified WCF strands, the prepared seed and growth solutions were introduced. During the hydrothermal synthesis of ZnO on WCF in the prepared seed and growth solution, the following chemical reactions occurred:

During the seed treatment process:



During the growth treatment process:



#### 5.2.4 Preparation of ZnO/WCF/BPA epoxy resin composites

The surface altered WCF samples were soaked in seed solution for 15 minutes before being annealed at 120 °C to eliminate the solvents and aid in seed layer adherence for ZnO NSs development. The technique was repeated four times, for a total of two, four, six, and eight cycles. In a stainless steel autoclave, the samples were placed in the growth solution and sealed. The samples were hydrothermally treated by placing the autoclave in a hot air oven set to 90 °C for 8 hours. After growth treatment, the samples were removed and properly cleaned with distilled water to stop the ZnO NSs from growing further. After drying the decorated WCF samples for one day in ambient settings, a vacuum bagging technique was employed to make the composite by layering ZnO NSs decorated WCF with BPA epoxy resin. Using a vacuum bagging method on a glass plate, WCFs adorned with ZnO NSs were integrated into composites using BPA epoxy resin. The plate was 600 x 600 x 8 mm in size. To remove contaminants, the plate was extensively cleaned with a mixture of acetone and ethanol. The glass plate was covered with a release fabric, and a single sheet of WCFs containing ZnO NSs was placed on top. A silk cloth that served as a peel ply was used to

cover the samples. A distribution media was laid on top of this to ensure that the resin was distributed evenly. The system was entirely sealed after a rubber gasket was connected to the edge of the releasing cloth. To prevent resin or air leakage, a vacuum was established inside the sealed system by forcefully pressing a plastic film onto the rubber gasket. All of the samples were made with unsaturated BPA epoxy resin. Dimethyl aniline, which served as a catalyst, was carefully incorporated into the resin. After completely combining the catalyst with the resin, methyl ethyl ketone peroxide, a curing agent, was applied. The resin was introduced into the system via an inlet, which was connected to a vacuum pump via an output. At a vacuum pressure of 60 kPa, the resin was put into the chamber. After the chamber had been filled with enough resin, the entrance and outflow were shut. To guarantee a complete cure of the resin, the chamber was kept at room temperature for 48 hours. The growth of ZnO NSs on WCFs and the vacuum bagging technique utilized to make the composites are depicted in Fig. 5.1.

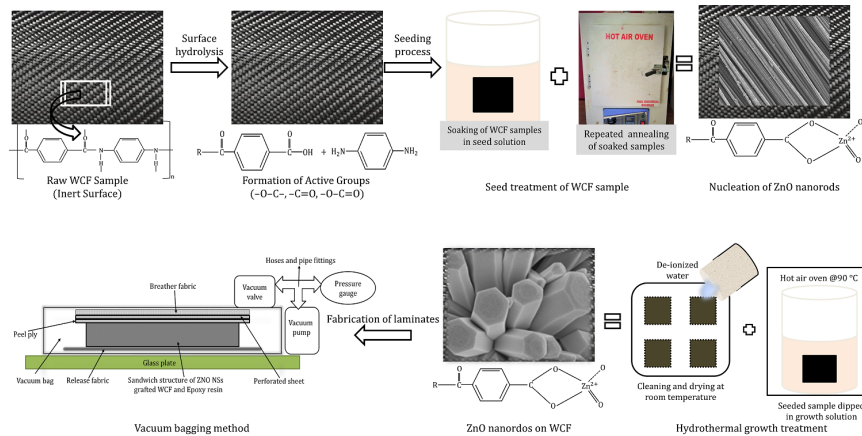


Figure 5.1: Hydrothermal development of ZnO-modified WCF polymer composites

### 5.2.5 Impact and tensile testing

With an instrumented drop-weight impact tester fully computer controlled with data gathering system, the energy absorption and impact force due to vertically dropped weights on the ZnO/WCF/BPA epoxy resin composites were investigated. The range of impact energy is (0-120) J, while the range of impact height is (0.1-1.0) m. The photoelectric sensor recorded data from the initial impact contact point until penetration happened or the tub maximum weight capacity was achieved, and the circular clamping size was 40 mm in diameter to fix the specimens. The tensile test was carried out on fifteen samples (3 samples

from each of the five categories) on an Instron 5982 universal testing machine with a 100 kN load cell, with the load increased till fracture. The findings of the experiment were calculated using the average of three samples, excluding the greatest and lowest replies. In accordance with ASTM D3039, a constant strain rate of 1 mm/min was used to pull the sample. The end tabs were employed to prevent joint failure and slippage during testing.

## 5.3 Results and discussion

### 5.3.1 Morphological characterization of as grown ZnO NSs on WCF

The experimental settings for the reaction sequences used to generate the ZnO nanorods on the WCF surface were developed from extensive literature survey. The experimental process took into account three separate parameters: the number of seeding cycles, the concentration of the growth solution, and the duration of the hydrothermal treatment. The designed set of experiments under the defined process parameters with their outcomes are illustrated in the Table 5.3. Field-emission scanning electron microscopy (FESEM; Supra 55, Zeiss-Germany) with an Air Lock chamber at a 15 kV operating voltage was used to conduct preliminary research on the formation of ZnO nanowires on WCF. Researchers have previously achieved well-grown ZnO nanofibers on polycarbonate substrates by seeding the growing process with zinc nuclei [143]. However, regardless of the growth solution concentration or growth period, no development of ZnO nanowires was seen after two seeding cycles. The nanowires did not grow due to the small number of seeding cycles, despite the fact that the growth solution concentration and growth time were both appropriate. The seeding process was recognized as an important element in the growth process as a result of these findings. Even when the growth solution concentrations were 50 and 70 mM, WCF samples with four seeding cycles and four hours of growth period showed agglomerated or minimal development of ZnO NSs. Although the concentration of the growth fluid was relatively high, the seed nuclei did not have enough time to grow, therefore the nanowires' short growth period played a major role [88]. Table 5.3 exhibits that, nearly all seeding cycles  $\geq 4$  resulted in considerable NSs development. The concentration of the growing solution was not a critical parameter, although it may be exploited to alter the ZnO morphologies. For ultra-fine development of ZnO NSs, the length of the hydrothermal treatment was critical. Zhang et al. [298] used an ethylene glycol-assisted hydrothermal technique to establish regulated development of a CuO nanostructure. CuO nanowires were successfully produced at all growth solution concentrations from 10 mM

Table 5.3: Design of hydrothermal experiments and their findings

S.no.	Seed cycles (10+10 min)	Concentration (mM)	Time (hrs)	Results
1	2	10	4	No growth
2	2	10	8	No growth
3	2	30	4	No growth
4	2	30	8	No growth
5	2	50	4	No growth
6	2	50	8	No growth
7	2	70	4	No growth
8	2	70	8	No growth
9	4	10	4	Agglomerated growth
10	4	10	8	Agglomerated growth
11	4	30	4	Agglomerated growth
12	4	30	8	Little growth
13	4	50	4	Agglomerated growth
14	4	50	8	Little growth
15	4	70	4	Little growth
16	4	70	8	Little growth
17	6	10	4	Agglomerated growth
18	6	10	8	Little growth
19	6	30	4	Agglomerated growth
20	6	30	8	Little growth
21	6	50	4	Little growth
22	6	50	8	Little growth
23	6	70	4	Little growth
24	6	70	8	Fine growth
25	8	10	4	Fine growth
26	8	10	8	Fine growth
27	8	30	4	Fine growth
28	8	30	8	Ultra-fine growth
29	8	50	4	Fine growth
30	8	50	8	Ultra-fine growth
31	8	70	4	Fine growth
32	8	70	8	Ultra-fine growth

to 60 mM for all growth times longer than 1 h. For 8 seeding cycles and 8 hours of growing period, the highest concentration of nanowires was achieved. As a result, the seeding cycles and growth duration were the most important factors in the growth process. Nanowires grew in practically every concentration of growth solution. The findings of the tests that induce the most effective development of ZnO NSs on WCF, corresponding to 8 seeding cycles, 8 hours growth treatment at molar concentrations of growth solution 10 mM, 30 mM, 50 mM, and 70 mM, will be utilized for further analysis and their behaviour.

### 5.3.1.1 ZnO nanowire growth

The hydrothermal approach was used to investigate the ZnO crystalline formation process. The prevailing zinc/OH<sup>-</sup> concentration ratio initially aided ZnO development during hydrothermal treatment. Many ZnO nanowires' morphologies will begin to transition from hexagonal rods to "syringe"-like structures if the ZnO growth time exceeds 3 h [299]. In the research of Amin et al. [144], average sized ZnO NSs were classified by ZnO nanorods when development was completed for 3 h. The ZnO growth time was chosen at 4 h and 8 h in this work, with the pH of the ZnO growth solution varying from 6 to 8, to evaluate the morphologies in terms of the ZnO molar concentration. Hu et al. [300] and Greene et al. [301] described a method for synthesizing and organizing ZnO nanoparticles. The growth rate in the axial direction (c-axis direction) was affected by increasing the molar concentration of zinc nitrate hydrate and HMTA, but it also enabled the nucleation of unwanted micron-sized rods and non-uniformity. Growth time is a significant component in determining the lengths and diameters of the NSs in the hydrothermal process of developing ZnO structures [88, 144]. Seed layer treatment of woven carbon fibers was carried out in a

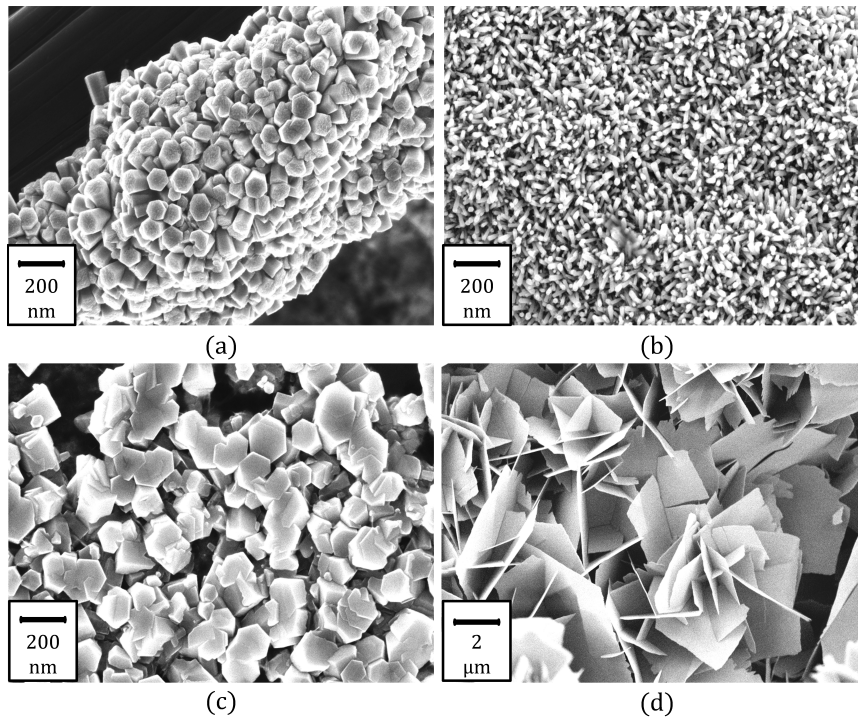


Figure 5.2: Hydrothermal development of ZnO-modified WCF polymer composites

stainless-steel autoclave at an external temperature of 90 °C for 4 and 8 hours in this work.

As the molar concentration of ZNH and HMTA increased from 10 mM to 70 mM, the surface density of the ZnO NSs increased. Figure 5.2 shows FESEM images of successfully produced ZnO NSs on WCF which shows homogeneous and well-distributed morphology of ZnO. The ultra-fine ZnO NSs were produced on WCF after 8 seeding cycles and 8 hours of growth treatment. For the ZnO molar concentrations of 10 mM, 30 mM, 50 mM, and 70 mM, four distinct morphologies such as hexagonal nanorods, vertically aligned nanowires, nanopellets, and nanoflakes were produced. To create the ZnO/WCF/BPA epoxy hybrid composite for future study, five layers of each ZnO concentration sample were stacked together, and a BPA epoxy resin and hardener mixture was added to the stacked fiber using the vacuum bagging technique.

### 5.3.1.2 Effect of Seed treatment and growth treatment

WCFs were decorated with the zinc compound  $ZnOOH^-$ , as well as ZnO nanoparticle seeds, following pyrolysis treatment with the ZnO seed solution only, as shown in Fig. 5.3(a). As a result, the ZnO seeds chemically interacted with the woven carbon fibers. ZnO crystalline development, on the other hand, happened during hydrothermal treatment with only the growth solution. When there was no chemical pretreatment with the ZnO seed solution, the ZnO morphology took the form of clusters laying on the woven carbon fibers, as shown in Fig. 5.3(b). Pretreatment, on the other hand, caused ZnO NSs to stick to the WCFs, and the growth direction was aligned with the c-axis, as illustrated in Fig. 5.3(c). As a result, ZnO seed layer treatment is critical for the growth of ZnO NSs on WCFs.

### 5.3.2 Compositional study of ZnO/WCF samples

The compositional assessment of the as grown ZnO/WCF samples was carried out using the EDS equipment connected to the FESEM setup. The results of the Energy Dispersive Spectroscopy (EDS) investigation are reported in Fig. 5.4. The EDS spectra clearly show the presence of Zn, O, and C components, and statistical analysis indicates that Zn and O are in a 1:1 stoichiometric ratio. It reveals the presence of zinc and oxygen elements on WCF, confirming the nano-growth of ZnO in the provided growth solution by hydrothermal deposition. The EDS spectra were also used to calculate the atomic % and weight % of each element, as shown in Fig. 5.4. After the presence of ZnO NSs on the WCFs has been confirmed, the samples can be used to manufacture hybrid composites using BPA epoxy resin as a matrix for a variety of applications.

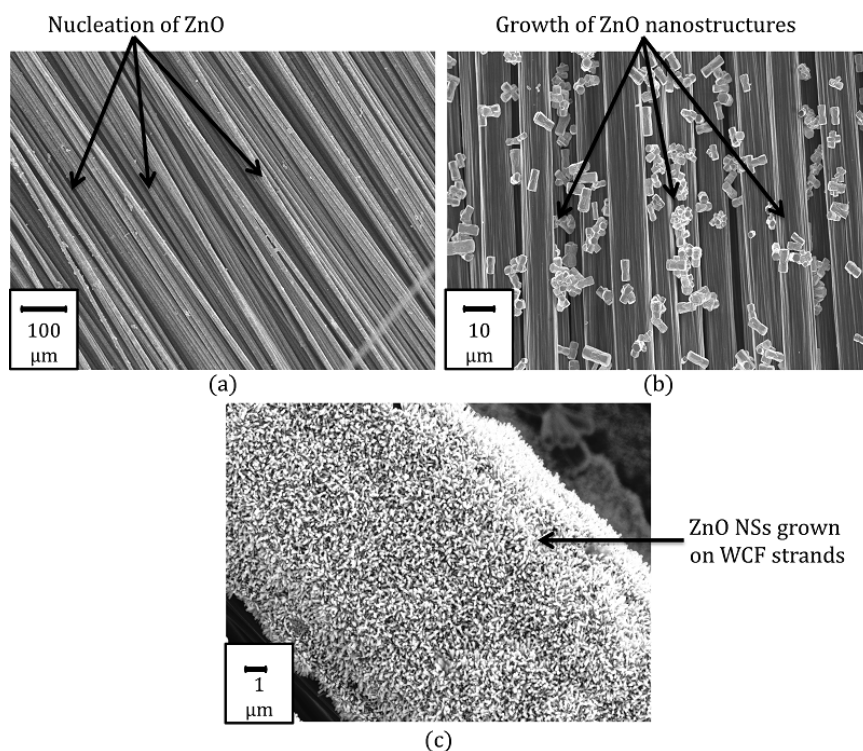


Figure 5.3: Growth of ZnO NSs on WCF (a) through 8 seeding cycle treatment only, (b) through 8h of growth treatment and (C) combined seeding followed by growth treatment

### 5.3.3 Structural characterization of grown ZnO NSs

The X-ray diffraction (XRD) study of WCF embedded by ZnO NSs is shown in Fig. 5.5(a). The sample's braided carbon fiber exhibits the large diffraction peak of the (002) crystal plane at  $26.2^\circ$ . The formation of ZnO NSs on the surface of WCFs produces a new series of crystal planes at  $31.26^\circ$ ,  $33.88^\circ$ ,  $36.2^\circ$ ,  $43.92^\circ$ ,  $47.04^\circ$ , and  $56.2^\circ$ , which closely resembles the hexagonal structure described in JCPDS No. 36-1451. The created ZnO NSs have a high purity wurtzite phase of ZnO and a hexagonal crystal system with space group "P 63 m c"; space group number-186;  $a=b=3.2530 \text{ \AA}$ ;  $\alpha = \beta = 90^\circ$ ;  $\gamma = 120^\circ$ ; cell volume-  $47.72 \times 10^6 \text{ pm}^3$  and density =  $5.66 \text{ g/cm}^3$ . In addition, the ZnO NSs were formed along the c-axis, as evidenced by the (002) diffraction peak at  $33.88^\circ$  ( $2\theta$  angle) [302]. According to the ZnO molar concentration, the XRD patterns had a different intensity. As the molar concentration of ZnO growth rose, the intensity of the diffraction peaks increased as well. The molar concentrations of zinc nitrate hexahydrate and HMTA influenced the rate of ZnO development in the axial direction (i.e., the c-axis direction). ZnO NSs with



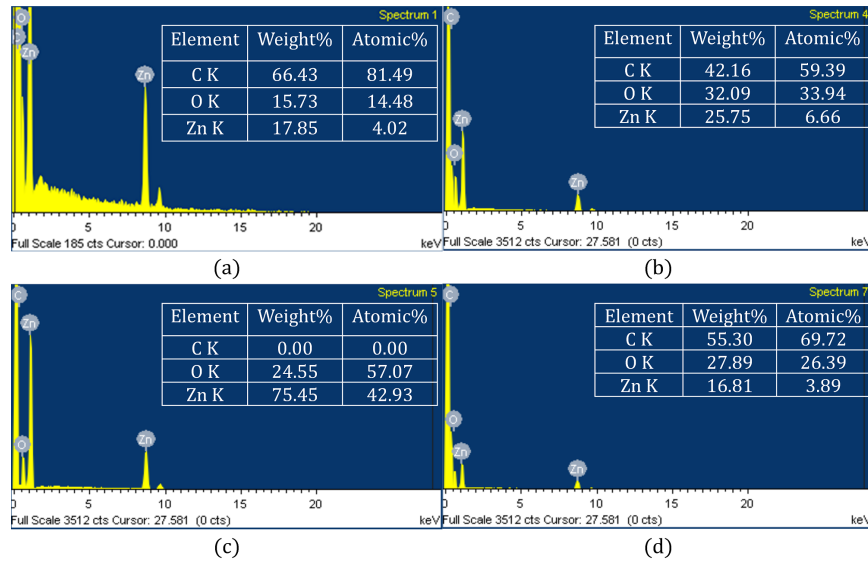


Figure 5.4: EDS spectra of ZnO-modified WCF (a) 10 mM (b) 30 mM (c) 50 mM and (d) 70 mM

a significant surface density were produced with a uniform and well-distributed morphology [303]. The Debye Scherrer relation was used to calculate the crystallite sizes of the

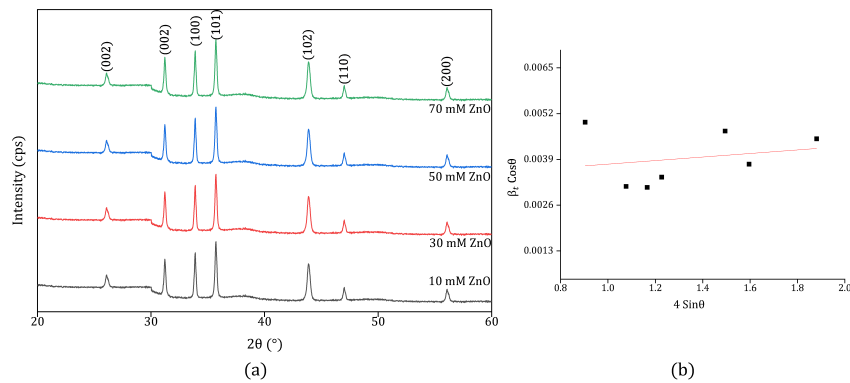


Figure 5.5: (a) XRD peaks and (b) Williamson-Hall plot of as grown ZnO NSs on WCF

ZnO NSs from the XRD peaks using the FWHM of the high intensity peak. Peak broadening of the XRD spectra owing to experimental errors and inhomogeneous strain were not taken into account in this procedure. The Williamson-Hall (W-H plot) approach was used to measure crystallite size ( $D$ ) and strain ( $\epsilon$ ) of the produced ZnO NSs on WCF by

determining FWHM. The Scherrer's expression is defined as [304];

$$D = \frac{K\lambda}{\beta_D \cos\theta} \quad (5.8)$$

And the overall broadening of XRD peak may be written as [304]:

$$\beta_t = \frac{K\lambda}{D \cos\theta} + 4\varepsilon \tan\theta \quad (5.9)$$

The W-H graph, which is essentially a straight line drawn with  $(4 \sin\theta)$  on the x-axis and  $(\beta_t \cos\theta)$  on the y-axis, was plotted using these two equations, as shown in Fig. 5.5(b). The amount of strain "ε" will be determined by the slope of the line, and the value of crystal size will be determined by the y-intercept. The calculated strain value is  $46.98 \times 10^5$ , and the crystallite size is 41.96 nm. For all XRD peaks of ZnO NSs, the crystallite size was found to be in the range of 32-42 nm using Scherrer's formula, and the comparable value of D corresponding to the high intensity peak (101) of all the samples was reported to be ~43 nm.

### 5.3.4 Optical characterization of ZnO NSs grown on WCF

A UV-vis spectrophotometer with a wavelength range of 200-800 nm was used to study the optical characteristics of the generated ZnO NSs on WCF (visible range). The optical transmittance spectrum in the visible region was used to assess UV-vis examination of materials, as shown in Fig. 5.6(a). The transmittance of the radiation illuminates the sample at a certain wavelength, whereas no transmittance occurs at the remaining wavelengths. At atmospheric circumstances, ZnO has a huge direct energy band and high exciton energy (60 meV). Because pure ZnO exhibits a band gap ( $E_g=3.37\text{eV}$ ) in the wavelength range of 360 nm, the strong transmittance for all the samples that show presence of ZnO occurred about 350 nm wavelength. The transmittance fluctuates nonlinearly, although there is a strong variation near ~350-355 nm, which is related to optical conversions at the energy level of the ZnO NSs shape. There is a decrease in transmittance near the wavelength of ~350-360 nm, as well as a slight change near the wavelength of 800 nm, which could be due to oxygen vacancies. Because of the low concentration and high concentration of ZnO in the 10 mM and 70 mM ZnO/WCF samples, there is no appreciable transmittance. Using the following equation and Tauc's plot approach, the energy band values ( $E_g$ ) of the

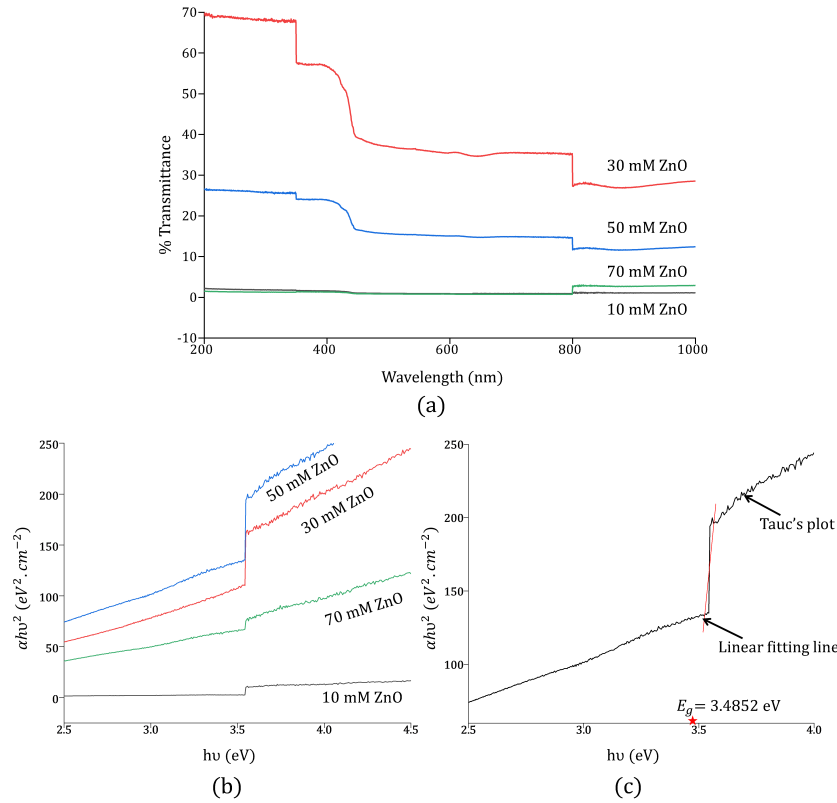


Figure 5.6: (a) Optical transmittance spectra, (b) Tauc's plot and (c) linear fit ZnO band gap of as grown ZnO on WCF

fabricated ZnO NSs on WCF samples were calculated [305]:

$$(\alpha h\nu)^n = B(h\nu - E_g) \quad (5.10)$$

Tauc's plot is a plot between  $(\alpha h\nu)^2$  and photon energy ( $h\nu$ ) as illustrated in the Fig. 5.6(b). These plots are used to calculate band gap values for ZnO/WCF samples using linear fitting technique as illustrated in Fig. 5.6(c). For all samples, the computed band gap values for the evolved morphologies of ZnO NSs on WCF are 3.4852 eV. The calculated energy gap agrees with the bulk ZnO energy gap ( $E_g=3.37 \text{ eV}$ ).

### 5.3.5 Fourier-transform infrared spectroscopy

The functional groups and metal-oxide interactions contained in the compounds were identified using FT-IR spectroscopy, which is a qualitative technique. In the wavenumber range

of 500 to 4000 ( $\text{cm}^{-1}$ ), the FT-IR spectrum of plain WCF and as manufactured ZnO NSs on WCF surfaces is shown in Fig. 5.7. The distinctive stretching mode of the Zn-O bond

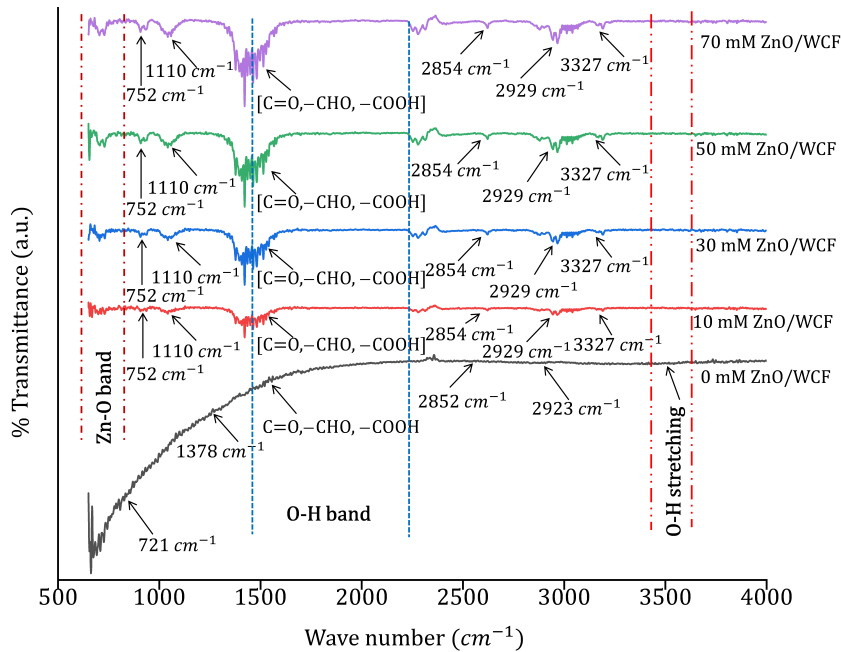


Figure 5.7: FT-IR spectroscopy spectra of ZnO-modified WCF samples

is ascribed to a prominent vibration band in the FTIR spectra ranging from 600 ( $\text{cm}^{-1}$ ) to 800( $\text{cm}^{-1}$ ). At 721, 1110, 1378, 1459, 1626, 2852, 2854, 2923, 2929, 3327, 3428, and 3578 ( $\text{cm}^{-1}$ ), there are multiple distinct absorption peaks. The bending vibrations of methylene ( $\text{cm}^{-1}$ ) were attributed to the peak at 721 ( $\text{cm}^{-1}$ ), the bending vibrations of the  $-\text{CH}_3$  groups and  $-\text{CH}$  bonds were attributed to the peaks at 1378 and 1459 ( $\text{cm}^{-1}$ ), and the stretching vibrations of the  $-\text{CH}$  bonds were attributed to the peaks at 2852 and 2923 ( $\text{cm}^{-1}$ ). The peaks at 1626 ( $\text{cm}^{-1}$ ) were attributed to  $\text{C}=\text{C}$  or  $\text{C}=\text{N}$  stretching vibrations, whereas the peaks at 3327 ( $\text{cm}^{-1}$ ) and 3428 ( $\text{cm}^{-1}$ ) were assigned to  $-\text{OH}$  stretching vibrations. These findings suggested that some polar groups were present on WCF surfaces. The  $\text{H}-\text{O}-\text{H}$  vibration of a cluster of crystallization water molecules peaks at 2370 ( $\text{cm}^{-1}$ ). The  $\text{C}=\text{C}$  stretching of an alkane group,  $\text{C}=\text{C}$  stretching in an aromatic ring and stretching in polyphenol ( $\text{C}=\text{O}$ ),  $\text{C}-\text{H}$  bending vibration of an alkane group, stretching of  $\text{C}-\text{N}$ , and bending vibration of  $\text{C}-\text{H}$ , respectively, correspond to the peaks at 1652, 1520, 1110, and 885 ( $\text{cm}^{-1}$ ) [306]. The existence of  $\text{C}$ -alkyl chloride and  $\text{ZnO}$  hexagonal phase is revealed by the tiny peak at 664 ( $\text{cm}^{-1}$ ). The intensity of the peak at 3327 ( $\text{cm}^{-1}$ ) was reduced for the  $\text{ZnO}$ -decorated WCF, indicating that the carboxylic acid was involved in the creation of

the ZnO bond. A new peak for a Zn/WCF/O stretching vibration emerged at  $752\text{ (cm}^{-1}\text{)}$ .

### 5.3.6 Study of thermal stability and weight change

A Thermo Gravimetric Analyzer (TGA) was used to evaluate the yield of the ZnO synthesis and its impact on the thermal stability of modified WCF (DTG-60, Shimadzu Co., Japan). The ZnO/WCF sample was heated from ambient temperature to  $1000\text{ }^{\circ}\text{C}$  in a platinum crucible on the microbalance pan. The experiment was carried out using nitrogen flow and a heating rate of  $10\text{ }^{\circ}\text{C}/\text{min}^{-1}$ . Figure 5.8(a) shows the TGA degradation trend of WCFs before and after surface modification by ZnO NSs. With the development of NSs on the surface of the WCFs, the thermal stability enhanced. When compared to the unmodified WCF samples, the initial degradation temperature ( $T_i$ ), maximum pyrolysis temperature ( $T_m$ ), and residual weight of the samples all improved. The improved thermal stability was due to a significant interfacial contact between the carbon fiber and the ZnO. The  $\text{Zn}^{2+}$  ions made strong ionic interactions with the carboxylic acid groups on the surface of the WCF in particular. This interaction resulted in the construction of a densely networked

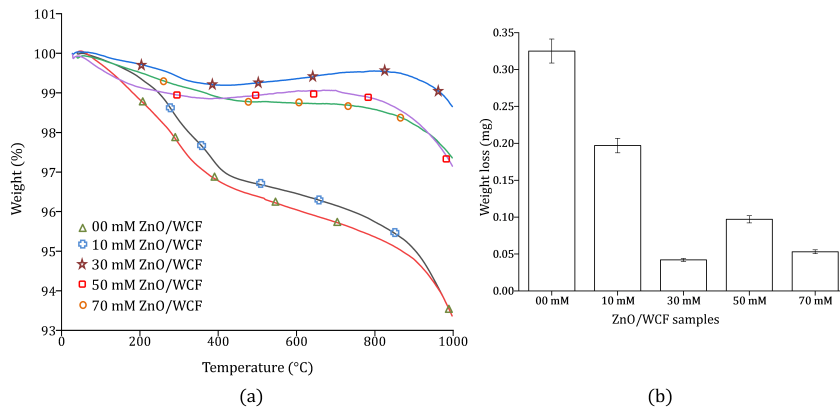


Figure 5.8: (a) Thermogravimetric degradation and (b) weight loss pattern of ZnO-WCF samples

structure that served as a barrier to the transport of volatile breakdown products, improving the thermal stability of the WCF samples [307]. The difference in mass loss between the ZnO-embedded WCF and the pure WCF was used to estimate the amount of ZnO formed on the surface of the WCF. The amount of CuO generated on the surface of WCFs was previously estimated using this method [308]. The weight loss of the untreated WCF and ZnO implanted WCF samples are displayed in Fig. 5.8(b) as a bar chart. Table 5.4 shows

Table 5.4: Design of hydrothermal experiments and their findings

S.no.	Sample	Weight change (%)
1	10 mM ZnO/WCF	12.8
2	30 mM ZnO/WCF	28.4
3	50 mM ZnO/WCF	23.2
4	70 mM ZnO/WCF	27.3

the percent variations in weight of the ZnO/WCF samples. In comparison to the plain WCF sample, all of the ZnO-embedded WCF samples created by hydrothermal synthesis showed a significant weight shift. The weight loss of the sample reduces as the ZnO concentration rises. When compared to the other samples, the samples with 30 mM ZnO concentration and eight seeding cycles and eight hours of treatment duration lost much more weight. For the samples treated with eight seed cycles, 30 mM, 8 h, the residual weight rose by 28.4 %; these conditions resulted in the maximum development of ZnO on the WCF. This sample shows the most regulated development of ZnO on vertically aligned WCF pieces and can be used to determine the best growth conditions for future studies.

## 5.4 Volume fraction and void analysis of the composites

Numerous studies have established that the fiber content is one of the most significant variables in improving the mechanical attributes of fiber reinforced composites [309, 310, 311], therefore its correct proportion should be identified. Fiber volume proportion is commonly computed as per ASTM D2584 standard [312];

$$V_f = \left\{ \frac{\rho_m \cdot w_f}{\rho_m \cdot w_f + \rho_f \cdot w_m} \right\} \quad (5.11)$$

Where,  $V_f$  represents volume fraction of the fiber,  $\rho_f$  represents density of the fiber,  $\rho_m$  represents density of the matrix,  $w_f$  represents weight of the fiber and  $w_m$  represents the weight of the matrix. When it comes to textiles, the yarns with fiber volume proportions are designed and implemented in a particular framework, and the overall fiber volume proportion is established by the spacing between the yarns of textile pattern. As a result, estimating the fiber content depending on the area between yarns in the textile is inadequate because the yarns would be occupied by the polymeric matrix. As a result, the volume

fraction of fiber can be calculated using rationalized mathematical expression [312]:

$$V_f = \left\{ \frac{\rho_m \cdot w_y}{\rho_m \cdot w_y + \rho_y \cdot w_m} \right\} \quad (5.12)$$

Where,  $V_f$  represents fiber volume fraction,  $\rho_y$  represents yarn density of the fabric,  $\rho_m$  represents density of the matrix,  $w_y$  represents weight of the yarns and  $w_m$  represents weight of the matrix. Applying the aforementioned mathematical formulas, the fiber volume proportion of the fabricated composites was calculated utilizing ratio of mixing for density, with the composite density measured and the fiber and matrix densities known. Table 5.5 illustrates the computed fiber volume proportion estimates for the fabricated composites. Similarly, the volume proportions of ZnO nanostructures implanted in ZnO/WCF/BPA epoxy resin hybrid composites were calculated employing the accompanying equation:

$$V_{ZnO} = \left\{ \frac{\left( \frac{W_{ZnO}}{\rho_{ZnO}} \right)}{\left( \frac{W_{ZnO}}{\rho_{ZnO}} \right) + \left( \frac{W_f}{\rho_f} \right) + \left( \frac{W_m}{\rho_m} \right)} \right\} \quad (5.13)$$

Where,  $\rho_{ZnO}$  represents density of ZnO NSs,  $w_{ZnO}$  represents weight of ZnO NSs,  $V_{ZnO}$  represents volume fraction of ZnO NSs,  $w_f$  and  $w_m$  represent weight of fiber and matrix respectively. Table 5.5 demonstrates the measured values of volume fraction characterization of ZnO NSs in the synthesized nanocomposite. Specimens containing four seeding cycles, the volume proportion of ZnO NSs improves, and this trend persists as the amount of seeding cycles and development duration rise. Based on the most effective growth of ZnO NS, the samples corresponding to 8 no. of seeding cycles and 8 hours of growth treatments with different molar concentrations were examined for volume fraction evaluation. As the molar concentration of the growth solution increases, the volume proportion of ZnO in the composite samples developed with the most successful growth of ZnO on WCF and BPA epoxy resin also increases, i.e., 10 mM > 30 mM > 50 mM > 70 mM. With the synthesis of ZnO NSs, the % volume fraction and density of WCF increased. The quality of the manufactured hybrid composites is likewise improved as the volume fraction and density rise. The specimens obtained with 70 mM solution seemed to have the largest volume fraction of ZnO, signifying the highest growth of ZnO NSs among the specimens, using 8 seeding cycles and 8 h growth time. As the ZnO NSs growth improves, the interfacial contact among the ZnO NSs, WCF, and BPA epoxy resin becomes stronger. The net load transmission rate from matrix material to the fibers gets improved as a result of such

interactions. As a result, composites with greater volume fractions of ZnO perform more effectively [103]. Void content assessments are used to measure the characteristics of a

Table 5.5: Design of hydrothermal experiments and their findings

S.no.	Sample category	Fiber volume fraction (%)	ZnO volume fraction (%)	Void content (%)	Tensile strength (MPa)	Elastic Modulus (GPa)	In-plane shear strength (MPa)
1	00 mM ZnO/WCF/BPA Epoxy resin hybrid composite	≈ 53.8 ± 0.60	0.0	≈ 11.64	257.78	14.75	163.94
2	10 mM ZnO/WCF/BPA Epoxy resin hybrid composite	≈ 58.7 ± 0.75	≈ 1.62	≈ 7.86	299.82	16.23	167.16
3	30 mM ZnO/WCF/BPA Epoxy resin hybrid composite	≈ 61.3 ± 0.40	≈ 2.26	≈ 6.42	337.9	18.18	168.37
4	50 mM ZnO/WCF/BPA Epoxy resin hybrid composite	≈ 62.4 ± 0.38	≈ 2.84	≈ 5.37	354.72	19.47	159.25
5	70 mM ZnO/WCF/BPA Epoxy resin hybrid composite	≈ 64.3 ± 0.24	≈ 3.56	≈ 5.14	383.16	21.6	192.36

composite and its potential for different operations. The void fraction affects the majority of a composite's material characteristics. ASTM D792 was used to estimate the densities of composites. The weights of the specimens were examined after they were dipped in distilled water at ambient level. The % void proportions of the specimens were computed with the help of standard mathematical formulas derived from experimental and theoretical density as per ASTM D2734 standard:

$$Voidcontent = \frac{(\rho_{theoretical} - \rho_{experimental})}{\rho_{theoretical}} \quad (5.14)$$

$$\rho_{theoretical} = \frac{1}{\left(\frac{W_{ZnO}}{\rho_{ZnO}}\right) + \left(\frac{W_f}{\rho_f}\right) + \left(\frac{W_m}{\rho_m}\right)} \quad (5.15)$$



The void percentage of WCF/BPA epoxy resin composites in their natural state was 11.64 %. With the formation of ZnO NSs on the WCF surface, this dropped significantly. The void percentage began to drop as the development of ZnO NSs increased. Yahaya et al. [313] observed the 16.2 % void content in woven aramid/kenaf fiber/epoxy composites and found that composites with kenaf mat have a higher void percentage and poor interfacial adhesion. The interfacial relations among WCF and BPA epoxy resin were improved by ZnO NSs synthesized on WCF. Ionic bonds develop among the  $Zn^{2+}$  ion and the carboxylic acid groups present on WCF. The epoxide group of BPA epoxy resin also had a role in crosslinking bonding, leading in improved interfacial adhesion. As a result, the void content of WCF/ZnO/ BPA epoxy resin composites was significantly lower than that of neat WCF/BPA epoxy resin composites. The increase in density of ZnO NSs grown on WCF also reduces void content. The WCF/ZnO/BPA epoxy resin composite sample with 70mM ZnO molar concentration produced by 8 seeding cycles and 8 hours of growth time has the lowest void content.

## 5.5 Mechanical characterization of fabricated hybrid composites

The optimum growth of ZnO on WCF samples were used for the fabrication ZnO/WCF/BPA epoxy resin hybrid composites using vacuum bagging technique and after curing the composites panels were analyzed under mechanical loading conditions. Five categories of composite samples were considered for further study and three tests were performed on each category of samples to achieve the average value of the desired properties. The finalized categories of composite samples are illustrated in the Table 5.6.

Table 5.6: Fabricated ZnO/WCF/BPA epoxy composite samples for mechanical characterizations

S.no.	Sample name	Sample category
1	T-0	00 mM ZnO/WCF/BPA Epoxy resin hybrid composite
2	T-1	10 mM ZnO/WCF/BPA Epoxy resin hybrid composite
3	T-2	30 mM ZnO/WCF/BPA Epoxy resin hybrid composite
4	T-3	50 mM ZnO/WCF/BPA Epoxy resin hybrid composite
5	T-4	70 mM ZnO/WCF/BPA Epoxy resin hybrid composite

### 5.5.1 Drop weight impact test

Low-impact energy absorption makes CFRP composites vulnerable to impact damage. However, ZnO nanowires should be less susceptible to impact damage. The energy absorption owing to ZnO growth and failure behavior of the manufactured composite samples were investigated under impact loading. Increased surface area between ZnO nanowires, fibers, and a polymer matrix is thought to improve these qualities through improving chemical interaction and mechanical load-transfer capacity. It is due to the presence of functional groups (hydroxyl, carbonyl, and carboxyl) on the surface of carbon fibers. ZnO nanowires have a great affinity for these functional groups. The impact test was conducted using a drop-weight impact tester (Model: SPRANKTRONICS, Bangalore, India) fully computer controlled with data acquisition system in accordance with the ASTM D5628-10 standard to determine the energy absorption potential of composites subjected to impact force caused by vertically dropped weights. The impact energy scale ranges from 0-120 Joules, while the impactor's height ranges from 0.1 m to 1.0 m. The circular clamp with a 5 kg impactor was adjusted to a diameter of 45 mm at first. The impact velocity was 3.84 m/s and the drop height was 0.75 m in these experiments. Each sample has an average thickness of 1.8 mm. The drop weight impact tester, their impact data gathering system, and the produced composite samples are shown in Fig. 5.9. In the drop weight impact tester, data was collected between the initial impact contact point and the penetration point. The impact energy was calculated by adding the rebound and absorbed energies together. When the rebound energy was small, the resin and fibers absorbed all of the energy. For low velocity hits, the delamination and bending deformation energies were included in the absorbed energy. The brittle nature of the composites, on the other hand, resulted in moderate levels of absorption energy when the fibers broke. The remaining energy, which included shear-out, global deformation, and delamination energy, was absorbed by the impact energy of samples. The impact energy absorption findings of the plain WCF and WCF/ZnO/BPA epoxy resin composite specimens are shown in Fig. 5.10(a). The impact energy absorption of the bare WCF/BPA epoxy resin composite specimen was the lowest. With 10 mM ZnO growth on the WCF, the impact energy absorption increased by 41.33 %, and continued to increase with the growth of the ZnO NSs. The surface area of ZnO NSs grew in a linear relationship with their growth, improving the interaction of ZnO NSs with WCFs and the polymer matrix. These interactions resulted in a high level of entanglement within the composite, allowing it to absorb and transmit enough energy through the interfaces. Composites with 8 seeding cycles, an 8-hour growth time, and a growth solution concentration of 50 mM

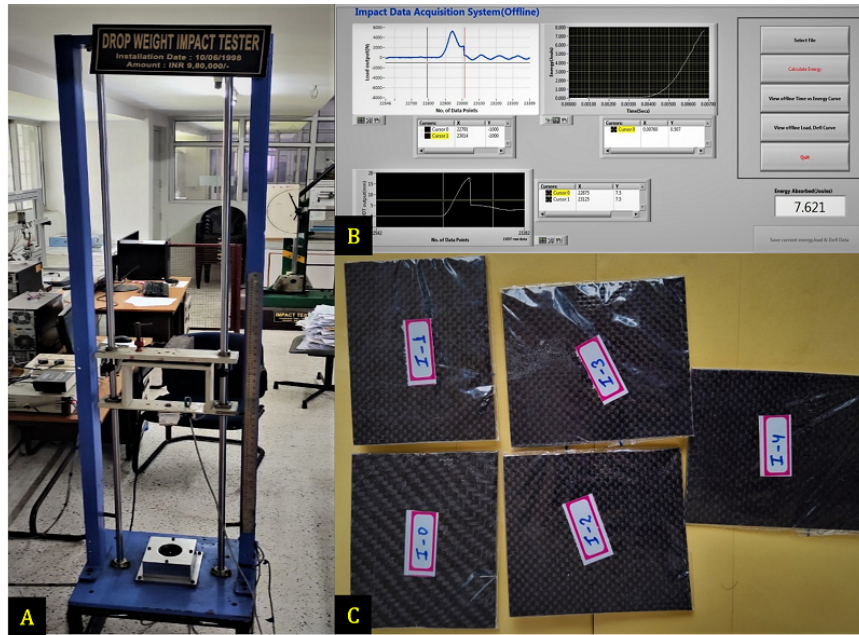


Figure 5.9: (a) Set up for drop weight impact tester, (b) Impact data acquisition system and (c) Fabricated impact test samples

and 70 mM had the highest growth of ZnO nanowires, as discussed above, and thus had the greatest effectiveness against impact energy, with a 62 % and 76 % increase over the bare WCF/BPA epoxy composite specimen, respectively. Furthermore, the affinities of the surface functional groups contained in the carbon fibers helped to improve the characteristics. Carbon fibers naturally have carboxyl, hydroxyl, and carbonyl groups on their surfaces. Strong ionic connections are formed when the hydroxyl and carboxyl groups contact with the  $Zn^{2+}$  ions in ZnO. The carbonyl group's extra-long pairs have a great affinity for ZnO nanowires as well. Furthermore, the functional groups of epoxy resin can react with the epoxy groups, generating strong connections. As a result of integrating these elements, WCF and BPA epoxy resin enhanced the overall impact absorption energy capacity of hybrid composites. The fractured surface and crack debris of ZnO/WCF/BPA epoxy resin hybrid composite samples are illustrated in Fig. 5.10(b). Fiber breakage, fiber pullout, crack debris, and other failure modes such as ZnO NSs pullout and ZnO NSs breakage are all examples of sample fracture mechanisms. The fracture point mainly offers fiber breaking information. The cracking interaction energy was estimated to be between the ZnO NSs and the surface of the WCFs up until the fracture point. Additionally, the WCFs absorbed delamination energy. Interactions between ZnO NSs and ZnO growing area zones

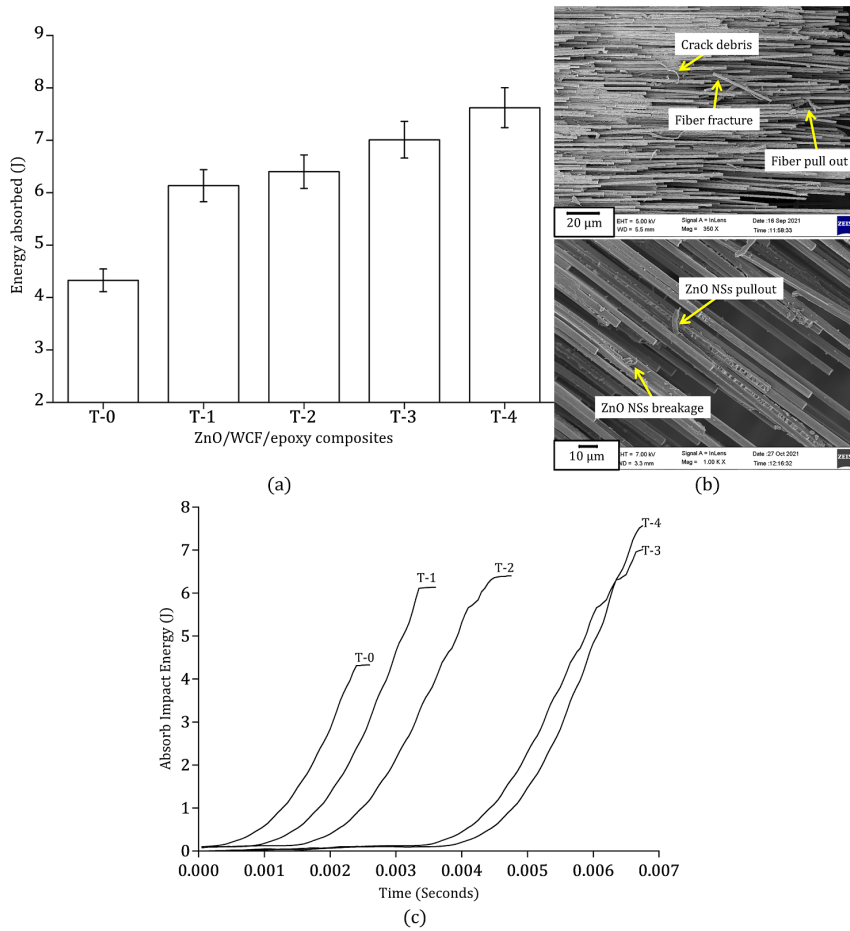


Figure 5.10: (a) Impact energy absorption, (b) fracture surface topography and (c) energy-time response of composite samples

on the surface of the WCFs resulted in variances in impact energy absorption. The cross-linking density was shown to increase with the molar density of ZnO. The following is the impact energy absorption relationship:

$$E_{total} = E_{rebound} + E_{absorbed} \quad (5.16)$$

The rebound energy of brittle composites is minimal. As a result, the resin and fibers absorbed nearly all of the total energy. The bending deformation energy and delamination energy are included in the absorbed energy in low-velocity impacts. Due to the composites' brittle nature, energy was absorbed mostly through fiber breakage, with the remaining energies (such as global deformation, delamination, and shear-out energy) absorbed by the impact. In all cases, the external area affected by the impact was nearly identical. The holes

in the composites formed at higher molar ZnO concentrations were arch-shaped, which was the most significant difference. The plain WCF/BPA epoxy composites were penetrated straight downward. The impact-damaged area of the composites formed at greater molar concentrations of ZnO, on the other hand, resembled an erupted volcano. The reason for this was that the surrounding ZnO NSs cross-linked the impact region. The bonding energy between the ZnO NSs and WCFs was stronger than the epoxy resin's deformation energy when the ZnO NSs extended up to the fractures. As a result, despite the fact that the damaged region was small, the ZnO NSs absorbed more energy. Higher the molar concentration of ZnO composites, the more impact energy is absorbed. The EDS graph with compositional details at the fractured portion has been illustrated in Fig. 5.11. The presence of Zn and O atoms have been seen at the interface of the fiber fracture which proves the interfacial enhancement of ZnO nanostructured CFRP composites.

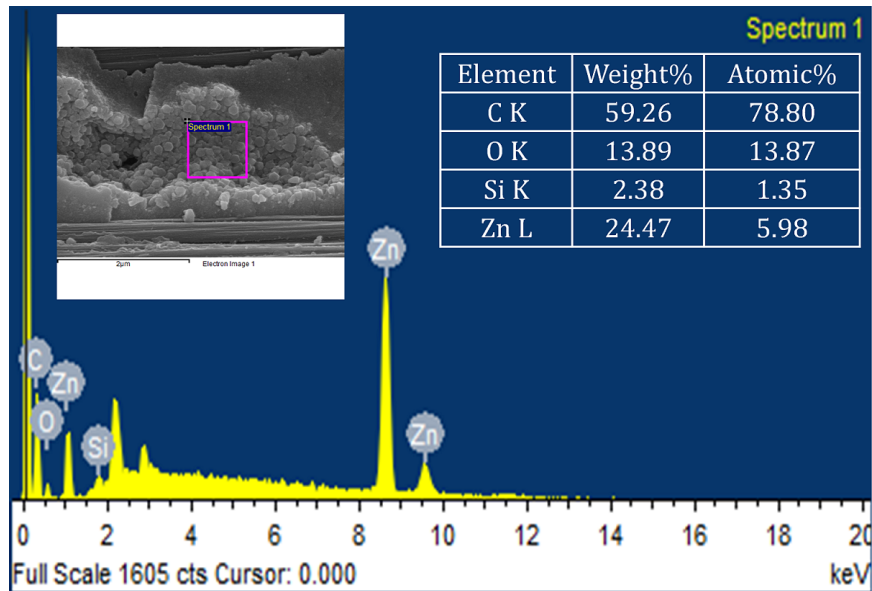


Figure 5.11: EDS graph with compositional details at the fracture regime

#### 5.5.1.1 Energy–time response

The impact energy is made up of both rebound and absorbed energies when samples are subjected to a low-velocity impact. When the striker did not pierce the composites, the rebound energy was low since the energy was completely absorbed by the resin and fibers. Bending deformation energy and delamination energy were among the absorbed energies. The absorbed impact energy of the WCF/BPA epoxy resin and WCF/ZnO/BPA epoxy resin

composites is graphed as a function of time in Fig. 5.10(c). After including ZnO NSs into WCF/BPA epoxy resin composites, an increase in the absorbed impact energy was found. When compared to WCF/BPA epoxy resin composites, the WCF/ZnO/BPA epoxy resin composites had higher absorbed impact energy. The impact absorption energy of plain WCF/BPA epoxy resin composites was the lowest, but this property improved as the number of ZnO NSs increased. For example, the sample with minimal ZnO growth (i.e., the sample treated with eight seed cycles, 10 mM concentration, and 8 hrs growth treatment) had a 41.73 % higher impact energy than the WCF/BPA epoxy resin composites, and the impact energy increased as the molar concentration of ZnO was increased. The greater surface area of the ZnO NSs resulted in a stronger interfacial interaction between the fibers and the epoxy resin, resulting in increased impact energy absorption. Surface carboxylic groups formed ionic bonds with  $Zn^{2+}$  ions, and these functional groups also interacted with the epoxide (oxirane) group of Bisphenol A (BPA) epoxy resin, resulting in further contacts between the fibers, ZnO NSs, and resin. Because energy is transferred more easily from the polymer to the fiber across the interface, the greater the interfacial interaction, the more energy is absorbed. The WCF/ZnO/BPA epoxy resin composite, which was made with 8 seeding cycles, 70 mM ZnO concentration, and 8 hrs of treatment, grew the most ZnO NSs and, as a result, absorbed the most impact energy, 76 % better than the plain WCF/BPA epoxy resin composite. The WCF/ZnO/BPA epoxy resin composites with 30 mM and 50 mM ZnO concentrations had 48 % and 62 % higher impact energy absorption capability than plain WCF/BPA epoxy composites.

### 5.5.2 Tensile and In-plane shear strength

In terms of ZnO concentration and morphologies, tensile strength measurements were used to determine the stiffness of WCF/BPA epoxy resin composites and WCF/ZnO/BPA epoxy resin composites. Instron 5982 universal testing equipment with a maximum load of 100kN was used to perform tensile tests on the specimens. According to the ASTM D3039 standard, five specimens were examined at a displacement rate of 1mm/min for each sample category. For further analysis, the average values of the tests are taken into account. Figure 5.12(a) illustrates stress-strain curves of the WCF/BPA epoxy resin composite and the WCF/ZnO/BPA epoxy resin composite. The increments represent the amount of interaction between the WCFs and the epoxy resin. These findings demonstrate the overall trend of rising strength and modulus values: more ZnO NSs development led to better results. Earlier studies have shown that external impact energy causes fiber breakage in brittle com-

posites [37]. Higher ZnO NS growth rates result in more effective load sharing between the NSs and fibers, resulting in higher energy requirements for fiber breakage. The tensile strength and elastic modulus results of all the composite samples are illustrated in Fig. 5.12(b and c). The plain WCF/BPA epoxy resin composite samples had the lowest strength and modulus values, probably because the fibers and epoxy had the least interfacial contacts. The surface area of the fibers rose as the ZnO NSs were embodied on the surface of WCFs. Composites containing ZnO nanowires produced with 8 seeding cycles and 8h of development time at a growth solution concentration of 70mM achieved the highest modulus (46.44%) and strength (48.63%). However, as previously mentioned, the surface functional groups of WCFs (e.g., hydroxyl, carboxyl, and carbonyl) interacted with the ZnO NSs and the epoxide groups of the BPA epoxy resin. The overall tensile strength of

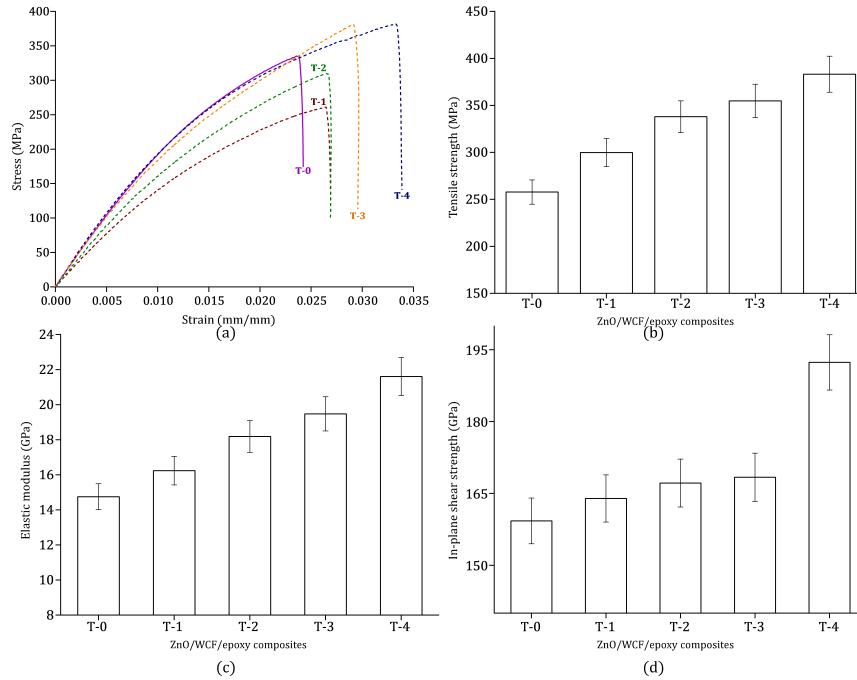


Figure 5.12: (a) Stress-strain characteristics and variation of (b) tensile strength, (c) elastic modulus and (d) in-plane shear strength of composite samples

the composite was greatly boosted as a result of the additional interfacial connections. The in-plane shear resistance of the as fabricated composite samples was also calculated, and it was discovered that while there is a small increase in in-plane shear strength for 10mM, 30mM, and 50mM molar concentrations of ZnO/WCF/BPA epoxy resin composite samples when compared to bare WCF/BPA epoxy composite samples, there is a large increase

in in-plane shear strength (20.79%) at higher molar concentration (70mM) as illustrated in Fig. 5.12(d). In addition, the hydrothermal growth process has been proven to improve the mechanical properties of large-scale composites. The tensile test findings indicate that a ZnO NSs network resulted in improved interfacial characteristics and enhanced interfacial shear strength. The ZnO NSs networking enhanced load transmission from the matrix to the WCFs.

## 5.6 Summary

Successful growth of ZnO NSs was developed on the surface of WCF using a low-temperature hydrothermal approach as a technique to improve the interfacial reinforcement of the plain WCF polymer composites. The carboxylic acid functional groups on the surface of the WCFs were developed by surface hydrolysis to promote the adherence of ZnO to the base fibers. It was found that the number of seeding cycles, hydrothermal treatment period, and molar concentration all influenced the growth of the ZnO NSs on WCF. Even at high concentrations and multiple seeding cycles, the NSs did not grow due to short treatment duration. The effective growths of ZnO were achieved at 8 seeding cycles and 8h growth duration. However, high density and uniform distribution of ZnO NSs were achieved at 8 seeding cycle, 8h growth duration and 70mM molar concentration. The improvement in thermal stability and % weight change were seen on ZnO-modified WCF samples due to fine growth of ZnO NSs. Drop weight impact testing and tensile testing were used to investigate the mechanical properties of ZnO/WCF/BPA epoxy resin hybrid composites. The cross-linked networks of ZnO-WCF-epoxy in hybrid composite diffuse the energy over the interface area which results into higher energy absorption. Furthermore ZnO NSs improve effective load transfer and interfacial strength of composites. The penetration limits of the hybrid composites were higher than those of the plain composites because of effective load transfer at interface, and it improved as the molar concentration increased. The impact energy absorbed by the ZnO-decorated composite with the maximum ZnO growth was 76% higher than the impact energy absorbed by the plain WCF polymer composites. The tensile strengths and elastic moduli of the hybrid composites were higher than those of the plain composites. In comparison to plain composites, the maximum ZnO molar concentration produced a 48.63% increase in tensile strength, 46.44% increase in inelastic modulus, and 20.79% increase in in-plane shear strength. The mechanical and thermal properties of the composites were improved as a result of improved interfacial contact between the surface-functionalized WCF, ZnO, and BPA epoxy resin. The zinc-oxide nanostructured



interphase was found more effective and achieved higher mechanical characteristics due to high effective surface area and crosslinking of ZnO NSs. Based on the findings of physical and mechanical characterizations, the hexagonal nanorods and nanoflakes type nanostructures have promising thermal and mechanical characteristics among the different nanostructures that include nanowires, hexagonal nanorods, nanoflakes, nanopallets, and nanoflowers. The hexagonal nanorods can make crosslinking of the nanorods with themselves and polymer matrix in the interfacial region which improves the interfacial strength and load transfer. Similarly, the nanoflakes can fill the voids and create graded interface of WCF in the CFRP composites which may increase interfacial interaction and effective load transfer. It has been reported that, the size and density of the grown nanostructures can be varied by choosing the appropriate synthesis parameters. Further, the strength of the nanostructured CFRP composites highly depends on their interfacial interaction which can be modified by growing different sized nanostructures. The finding of this chapter reveals that, the highest impact strength and tensile properties have been achieved for 70 mM samples which have thin flakes like structure having small thickness and large length/width. These nanoflakes can fill the voids and create graded interface in the CFRP composites which causes enhance interfacial interaction and effective load transfer. The evident correlations between these factors have not been deduced analytically. It can be developed by mathematical modeling or simulation of the current work in a future research. However, the proposed concept/theory has been verified with the required physical and mechanical characterizations of the developed ZnO nanostructured CFRP composites.



# 6

## Improvement of interfacial adhesion of CuO nanostructured carbon fiber reinforced polymer composites

This chapter deals with the development of CuO nanostructures on woven carbon fibers to produce a nanostructured interphase that increased the interfacial strength with an epoxy resin matrix. In this work, detailed analysis of structural, morphological, and mechanical properties of the pure WCF fabrics with CuO-coated WCF fabrics has been done. Further, the mechanical characteristics such as impact strength and tensile strength of CuO-coated WCF reinforced epoxy resin composite samples was assessed using drop-down impact test and universal material testing system. Moreover, this chapter concludes that the development of CuO nanostructures can lessen composite delamination and enhance composite performance because of the increase in interfacial surface area between the matrix and the fiber by CuO nanostructures which can potentially expand the spectrum of structural applications for these materials

## 6.1 Introduction

The development of value-added textiles with improved or innovative capabilities that can be used in a variety of applications is made possible by the use of nanotechnology in the fabric industry, such as the functionalization of fiber surfaces with nanostructures [227, 314]. The huge surface area unique to a given weight or volume of fabrics is the key factor causing the synergy between textiles and nanotechnology. In both civilian and military applications such as textiles, electronics, automobile, construction, chemical and aircraft industries, carbon fibers and composite materials are now frequently used [315, 316]. The rapid advancement of technology has made several scientists interested in advanced materials made up of carbon fibers. The composite may fail at the interface if the fiber matrix has inadequate adhesion, which could reduce the composite's performance. A graphite microcrystalline structure with a smooth shape and inert chemical characteristics makes up the surface of a carbon fiber [317]. In order to increase interface adhesion, it is crucial to surface treat the carbon fibers. Fibers are frequently subjected to physical and chemical changes to improve interactions and increase the compatibility of the fiber with the matrix [318, 319]. Figure 6.1 shows strategy of grafting CuO nanowires onto the surface of plain WCF to improve the interfacial interaction of composites. By grafting CNTs onto the surface of the fibers, Zhao et al. [320] enhanced the interfacial characteristics of carbon fiber/epoxy resin composites. Due to the strong chemical interaction between carbon

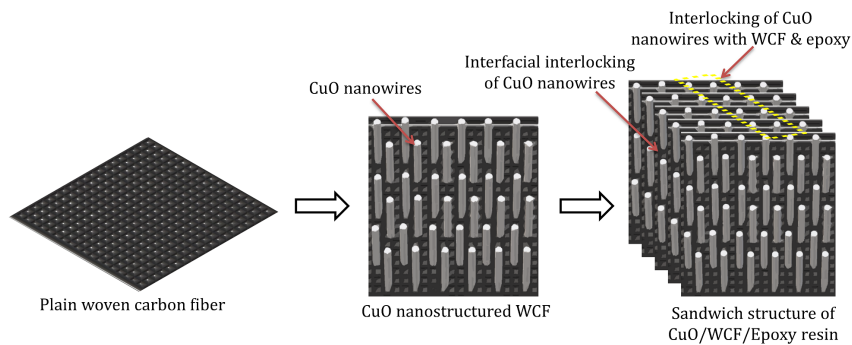


Figure 6.1: Surface modification of plain WCF by CuO nanowires

fibers and CNTs, the polarity, wettability, and roughness of carbon fibers are greatly increased, resulting in good interfacial properties and a better impact strength than untreated carbon fibers. To enhance the mechanical properties of carbon fiber composites, Zhang et al. [321] described a technique for directly grafting amino functionalized graphene oxide

(GO-NH<sub>2</sub>) onto the carbon fiber surface by covalent bonding. The mechanical characteristics and thermal conductivity of carbon fiber/phenolic resin matrix composites treated with HNO<sub>3</sub>/H<sub>2</sub>SO<sub>4</sub> were studied by Feng et al. [322]. The findings demonstrate that the fiber surface may be efficiently modified by oxidation to incorporate functional groups containing oxygen, enhance surface roughness and area, and greatly improve mechanical and thermal conduct of composites. Diverse methods to achieve desired non-structural functions in composite materials have been documented by a number of researchers. There are two ways to use nanostructures to change the surface of carbon fibers: either adding nanoparticles to the matrix or growing them directly on the fiber surfaces (whiskerization). Due to their huge interfacial surface area and low void content, growing nanostructures on fibers is the method with the most unexplored potential. Additionally, unlike when nanoparticles are mixed with a matrix, this method prevents nanoparticle agglomeration. Figure 6.2 shows the impact of growing CuO nanostructures on the surface of woven carbon fiber. A graded interface created by whiskerization which is a characteristic method for adjusting interfacial interactions lessens tension between the fiber and matrix phases. In composites, whiskerization improves the cohesiveness between the fiber and matrix by depositing a variety of whiskers onto the fiber. As a result of interlocking the matrix-fiber contact, the interphase characteristics are improved. Because of the cross-linked network acting as the increased load-bearing capacity due to the higher specific surface area of metal-oxide nanostructures, metal-oxides grafted on the surface of fiber have been reported to gain higher mechanical properties of composites [33]. This method of processing metal oxide nanomaterial has been used in novel sensor applications, including piezoelectric systems, chemical sensing, and photo-detection [61]. Due to their typical p-type semiconductor structure and 1.2 eV narrow band gap, CuO whiskers appear promising in this regard. Additionally, CuO whiskers have nonstructural properties that have been shown to be beneficial in a number of applications, such as solar energy transformers, lubricant additives, magnetic storage media, lithium-copper oxide electrochemical cells, gas sensors, and magnetic storage media [323, 324]. The mechanical properties of CuO nanostructures have been examined in any of the research conducted to yet be very limited because they have all concentrated on the chemical characterization of these nanostructures. CuO nanostructures have been described in a wide range of morphologies, including nanoparticles, nanowires, nanoribbons, nanoplates, microspheres, dandelion-like structures and many more [325, 165]. Sol-gel technique, vapor-liquid-solid synthesis, laser ablation, arc discharge, electron beam evaporation, template-assisted synthesis and template-free synthesis are only a few of the methods used to create these morphologies [326, 327, 328].

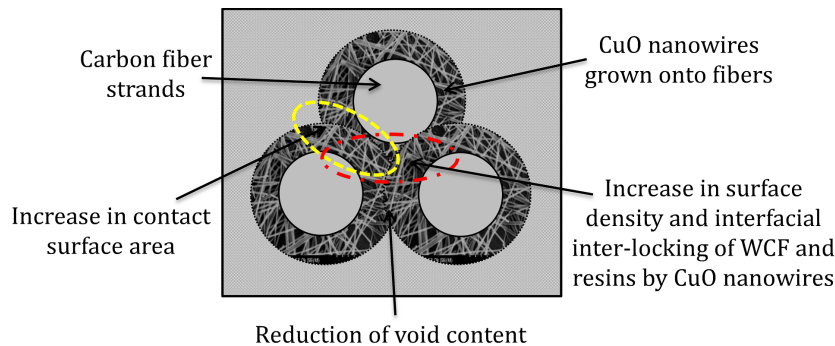


Figure 6.2: Surface whiskerization of carbon fiber using CuO nanostructures

However, the majority of the documented techniques call for extreme temperatures, inert environments, and high-tech optoelectronic devices. Furthermore, since the majority of stabilizers for functionalization are expensive and ineffective, achieving a uniform distribution of particles on fabrics without the use of expensive chemicals has remained a challenge. The procedures are typically time-consuming and complex. An economical hydrothermal approach that treats seeds is used to scale up production to overcome these issues. In general, templates and reagents for surface capping are used during the production of nanoparticles in liquid phase [329]. However, it is quite difficult to prepare, pick a suitable template, and clean up their impurities in the finished output. Therefore, in terms of cost and simplicity, template-free techniques are preferred [330]. The hydrothermal synthetic method, in contrast, is a flexible method for the creation of CuO nanostructures at relatively low temperatures, in high yields, and with controllable morphologies [331]. The impact of CuO nanowires on the enhancement of the mechanical characteristics of woven carbon fiber (WCF)-based polyester resin composite was studied by Deka et al. [36]. Following the formation of nanowires on the carbon fibers, the mechanical properties in terms of tensile strength, modulus, and impact resistance greatly enhanced. CuO nanostructures embedded in the surface of woven carbon fibers (WCFs) were grown using the hydrothermal technique with regulated chemical precursors as examined by Kong et al. [33] and they proposed that by regulating the thermal development temperature throughout the hydrothermal process during a growth time of 12 hours, CuO nanostructure morphologies ranging from petal-like to cuboid-like nanostructures can be created. The surfactant-aided hydrothermal method was utilized by Zhang et al. [332] to make shuttle-like CuO nanocrystals. CuO nanotubes and nanorods were also produced by Cao et al. [333] using a hydrothermal process. Teng et al. [334] used hydrothermal synthesis to cre-

ate flower-like CuO nanostructures without the use of a template. Furthermore by adopting a solution-phase synthesis at a relatively low temperature (100 °C) and without the use of a surfactant, Zhu et al. [335] created needle-shaped nanocrystals. The qualities of the individual major components and the interface, where load transfer from the matrix to the fiber takes place, both affect the performance of composite materials. Since the fiber to matrix surface-to-volume ratio is higher in composites with secondary reinforced nanomaterial formed on the surface of the fibers, therefore the interfacial interaction is stronger. In the presence of a strong adhesive interlocking activity between the fiber and the matrix, cracks propagate less before the composite is destroyed; the secondary reinforced nanomaterial operate as intermediary bridges. An attempt has been undertaken to create CuO embedded plain woven carbon fabric reinforced epoxy resin composites, taking inspiration from past works. Since transition-metal oxides like CuO have higher specific capacitance and energy density than materials like graphene or conductive polymers, they are widely used in a variety of industries [336]. The hydrothermal treatment of the woven carbon fabric to generate CuO nanostructures enhances the interfacial bonding with the matrix. Untreated and CuO-treated carbon fiber epoxy composites with various molar concentrations were characterized physically and mechanically. On the creation of well-aligned CuO grown as secondary nanostructures on a WCF substrate and their usage as a composite component, few investigations have been documented. The ability of CuO/WCF nanocomposites to absorb external impacts and how the shape of the CuO nanostructures affects crack propagation following an impact are of particular interest. To improve the interfacial adhesion of WCF/epoxy resin composites and preserve the tensile properties of the WCF, the present study is focused on the functionalization of carbon fibers by CuO via two-step seed-treated hydrothermal deposition. Therefore, the results of the mechanical tests show that, in comparison to the pristine WCFs, the CuO nanostructures on the surface of the WCFs significantly improve the apparent interfacial shear strength, impact strength, and tensile strength. Considering that there have only been a few papers on the coating of these multifunctional fibers by CuO hydrothermal deposition up to this point, the information from the current research offers fresh insights into constructing CuO nanostructured interphase on WCFs for diverse applications. Furthermore, because it uses readily available raw materials and affordable equipment, this functionalization strategy has a significant chance of scaling up.

## 6.2 Materials and methods

### 6.2.1 Materials

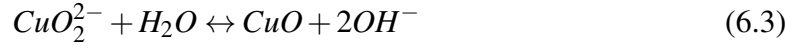
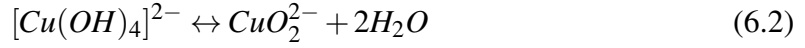
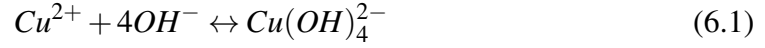
This experimental work made use of unsized bidirectional plain woven carbon fiber fabric (T300 grade, 3000 wires) that was provided by CF Composites (New Delhi). Without further purification, the experimental steps used analytical grade reagents from P.K. Enterprises (Dhanbad, Jharkhand) of copper acetate monohydrate ( $Cu(CH_3COO)_2 \cdot H_2O$ , 98 %), copper nitrate trihydrate ( $Cu(NO_3)_2 \cdot 3H_2O$ , 98 %), sodium hydroxide (NaOH, 98 %), hexamethylenetetramine (HMTA, 99 %) and absolute ethanol ( $C_2H_5OH$ , 99.9 %). Sakshi Dyes and Chemicals (New Delhi) provided the Bisphenol-A (BPA) epoxy resin ( $(CH_3)_2C(C_6H_4OH)_2$ ) and Dimethyl aniline ( $C_8H_{11}N$ ) hardener that was used to test the interfacial adhesion with modified carbon fiber yarns. It was combined in a recommended ratio of 2:1 by weight using overhead stirrer and desiccated to remove air bubbles. The curing procedure took place at ambient temperature for 24-48 hours.

### 6.2.2 Synthesis of reaction mixtures for hydrothermal treatment

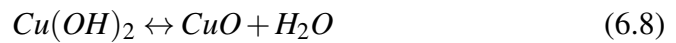
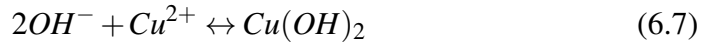
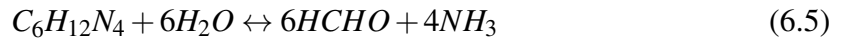
CuO nanoparticles on WCF yarns can be hydrothermally treated using one of the two different types of reaction mixtures, either seed solution or growth solution. In order to create these reaction combinations firstly, 400 mL of ethanol and 0.02 M copper acetate monohydrate were dissolved together at 65 °C. The mixture was then continuously stirred for 30 minutes. The second solution of 0.02 M NaOH in 80 ml ethanol was prepared by heating and stirring the mixture for 30 minutes at 65 °C. The obtained copper acetate monohydrate solution was then added to this ethanol solution. Furthermore 320 mL of ethanol was added to bring the overall amount to 800 mL. To ensure thorough and even mixing, the final solution was stirred for further 30 minutes at room temperature. To achieve efficient seeding, the seed solution's pH was monitored and kept in the range of 6 to 8. Over the course of an hour, the resulting light blue solution which contained a suspension of CuO particles was cooled to ambient temperature. The following chemical reactions took place



in the CuO seed solution:



Copper nitrate tetra hydrate and hexamethylenetetramine were mixed in a 1:1 molar ratio to create CuO growth solutions at the necessary concentration. 10 mM of HMTA was dissolved in 630 mL of distilled water over the course of 10 minutes to create 10 mM of the CuO growth solution. The addition of 10 mM copper nitrate tetra hydrate came next. For 30 minutes, the entire solution was stirred. The growing solution's pH was kept between 6 and 8. For the preparation of 15, 25, 35, 45, and 60 mM growth solutions, a similar process was used. On the WCFs that had been treated, CuO nanostructures were grown using these final solutions. The following chemical processes were engaged in the development of CuO and the production of CuO from  $OH^{-}$  and  $Cu^{2+}$ :



### 6.2.3 Preprocessing of carbon fiber fabric sample

Unaltered WCF samples were sliced into 150 X 150  $mm^2$  (length x breadth) pieces and washed in an acetone-ethanol solution to remove any organic contaminants. The samples were then dried in an oven at 90 °C for 20 minutes. The samples were then soaked for 30 minutes at room temperature in a 10 percent NaOH solution. Before the WCF samples were dried in the oven for an hour at 90 °C, they were repeatedly rinsed with deionized water. The functionalized WCF pieces were rinsed and oven-dried for an hour at 90 °C after being submerged in aqueous HCl (10 N) for 10 seconds. The specimens were submerged in aqueous HCl to remove extra metal ions that could have contaminated the growth solution. The hydrogen ions in the HCl solution caused carboxylic acid groups to form on the fiber surfaces through an ion-exchange reaction [297]. The creation of active groups, such as (-O-C-, -C=O, and -O-C=O), on the WCF surfaces as a result of surface treatment improved

the sample's total surface energy, polarity along with its wettability to interact with other components and the polymeric matrix [88] as seen in Fig. 6.3. The process parameters

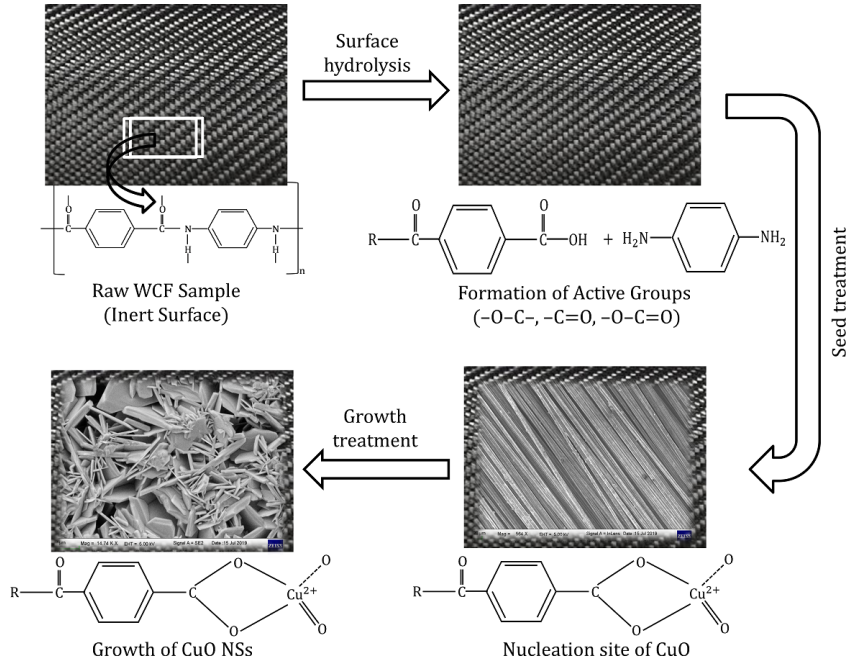


Figure 6.3: Surface treatment of woven carbon fiber by CuO nanostructure deposition

for hydrothermal synthesis of CuO NSs on WCF surface have been defined after detailed literature survey. However, the variations of selected process parameters have been defined after performing several some preliminary experiments. The variations of different factors affecting the growth of CuO NSs on WCF have been studied and illustrated in this chapter. Thus, the selection of process parameters for this work has been decided upon literature outcomes and our preliminary experimental findings.

### 6.2.4 Formation of CuO nanostructures on WCF

CuO nanostructures were created using a two-step hydrothermal process that included seeding and growth stages. CuO nanoparticles were deposited onto the WCFs during the seeding procedure. After that, the seeded WCFs were added to the growth solution in a beaker that was at a high temperature and atmospheric pressure. This two-step hydrothermal process was modified from that previously reported in that the metal-oxide, pH, concentration of precursor solution, development period, and temperature were different [88]. The CuO/WCF hybrid was completely rinsed with deionized water (DIW)

following the formation of the CuO nanostructures and allowed to air dry for a full day. Detailed description of steps involved in the growth of CuO nanostructures is discussed in this section. Using a prepared seed reaction mixture during seed treatment, the pre-processed WCF samples were then used for seeding of CuO nanoparticles. In order to improve adhesion between the substrate and nanoparticles, the surface-treated WCFs were next submerged in the seeding solution for 10 min. After that, they were annealed in a hot air furnace at 150 °C for 10 min. To guarantee that CuO nanoparticles were seeded completely across the WCFs, the soaking and annealing procedure was repeated many times. The prepared growth solution was added to the seeded WCFs, and then the entire mixture was moved into a glass beaker that was tightly sealed with aluminum foil and maintained in a hot air oven at the required growth temperature (120°C) for the development of CuO nanostructures on WCF. CuO nanostructure's morphology was investigated under a predetermined set of seeding cycles of 2, 4, 6, and 8 and variable molar concentrations of 10, 15, 25, 35, 45, and 60 mM, as well as under a separate set of growth durations of 3, 6, 9 and 12 hours at 120 °C. The CuO/WCF hybrid was rinsed with DIW after the hydrothermal processing to inhibit the formation of CuO nanostructures and dried at room temperature for 24 hours.

### **6.2.5 Fabrication of CuO/WCF/Epoxy hybrid composites**

The final composite materials were created from carbon fiber specimens that had CuO nanostructures produced on them using the vacuum bagging technique. The composite was made using a standard vacuum bagging procedure and flat glass plates with measurements of 500 × 500 × 5 mm. Acetone was used to clean the glass plates in order to get rid of debris, adhesives, and other contaminants. Using adhesive tape, a release fabric was connected, and a rubber gasket was used to seal the system all the way around the release fabric. One piece of silk fabric was employed as a peel ply above the samples, with the CuO-grown WCF sample being positioned just above this layer. A distribution medium that ensured an even spread of the resin followed this layer. To produce a vacuum, a plastic film was placed on top of these layers. To stop air or resin leaks, the film was firmly fastened to the rubber gasket. The intake was left open for the resin, and the outlet was attached to a vacuum pump. A 60 kPa vacuum pressure was applied to the system. The resin poured into the system when a vacuum at a pressure of 60 kPa was applied. The inlet and exit were shut when enough resin was poured into the mold. An illustration of the hydrothermal production of CuO nanostructured-WCF-epoxy hierarchical composites utilizing vacuum

bagging technique is shown in Fig. 6.4. This layer was followed by a distribution medium, which provided a uniform distribution of the resin. A plastic film was employed at the top of these layers to create a vacuum. The film was attached tightly to the rubber gasket so as to prevent leakage of the resin or air. The outlet was connected to a vacuum pump, and the inlet was opened for the resin. Vacuum pressure of 60 kPa was applied to the system. When the vacuum was applied at a pressure of 60 kPa, the resin flowed into the system. After sufficient resin had flowed into the mold, the inlet and the outlet were sealed. With each sample, an unsaturated Bisphenol-A (BPA) epoxy resin ( $((CH_3)_2C(C_6H_4OH)_2)$ ) was utilized as the matrix material. To improve the matrix's ability to cure, the BPA epoxy resin and dimethyl aniline ( $C_8H_{11}N$ ) hardener were combined in the prescribed 2:1 weight ratio. For 24-48 hours, the system was kept running to finish the curing process.

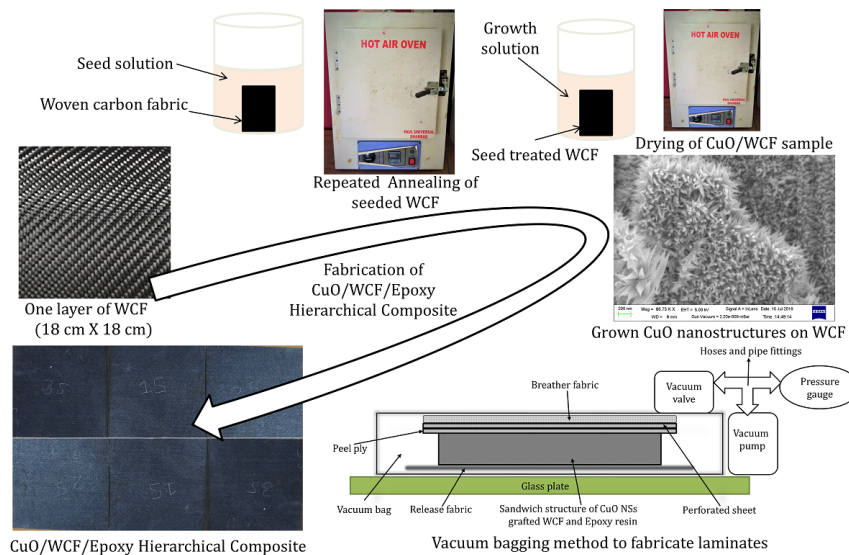


Figure 6.4: Hydrothermal approach for development of CuO nanostructured-WCF and their hierarchical composites by vacuum bagging method

## 6.2.6 Characterizations

FESEM model-Supra 55 was used to examine the shape of CuO nanostructures grafted on the WCF surface at varied CuO molar concentrations (10-60 mM) (make-Carl Zeiss, Germany). Utilizing an energy dispersive spectroscopy (EDS) instrument mounted with a FESEM model, the % atomic and % weight composition of CuO as formed on carbon fiber fabric was examined. The elemental mapping of each elements present on the surface of

CuO/WCF samples were also examined using EDS mapping technology. CuO nanostructures were grafted onto the surface of WCF, and their X-ray diffractograms were examined using a high resolution X-ray diffractometer (HRXRD) from Rigaku Smartlab that was automated with guidance software (SmartLab Studio II) and operated with a 40 kV, 200 mA operating voltage and current. Using a thermogravimetric analyzer (TGA, TA Instruments, USA), the formation of CuO nanostructures on woven carbon fiber was determined by examining the degradation pattern of the plain carbon fiber. The transmittance peaks of concomitant functional groups and CuO present on the bare WCF and carbon fiber with CuO nanostructures were examined by a Fourier Transform Infrared Spectrometer (FTIR, Thermo Fisher Scientific Instruments, USA) system. The surface chemistry, material composition, and presence of trace quantities of  $Cu^{3+}$  coexisting with  $Cu^{2+}$  in CuO were all examined using X-ray photoelectron spectroscopy (XPS) studies on CuO-modified WCF. The impact energy absorption of the CuO/WCF/epoxy composites was evaluated using an instrumented drop-down impact device (Spranktronics, Bangalore, India). The specimens prepared for drop-down impact test have a diameter of 45 mm. Data was gathered from the time of initial hit till penetration occurred using a photoelectric sensor. In accordance with ASTM D5628-10 standard, the impact test was performed using a drop-weight impact tester fully computer controlled with data acquisition system to assess the composite's ability to absorb energy from impacts caused by vertically dropped weights. The height of impactor varies from 0.1 to 1.0m, and the impact energy scale goes from 0-120J. The 5kg circular impactor clamp was first set to a 45mm diameter. In these studies, the drop height was 0.75m and the impact velocity was 3.84m/s. Each sample is approximately 2.0mm thick on average. A universal material testing equipment (Instron 8801, UK) with a load cell of around 100 kN was used to study in-plane shear response and uni-axial tensile properties. For applying strain in the sample, a constant displacement rate of 1 mm/min was used. The n-plane uniaxial tensile stress-strain response of a composite material reinforced by high-modulus continuous fibers or woven textiles is the basis for in-plane shear testing, which is based on the ASTM D3518/D3518M-13 standard test technique. Ultimate tensile strength and elastic modulus were assessed in accordance with ASTM D3039 for uni-axial tensile characteristics. The test has been conducted on five replicas of specimens in each sample category to estimate variability of the results. The average value was determined from the remaining three specimens after the top and lowest responses from five specimens were excluded because removal of outlying data provides more realistic average value. The average, standard deviation and coefficient of variance of each test results are reported in this work.

### 6.3 Results and discussion

Prior to the reaction sequences that led to the CuO growth pattern on the woven carbon fibers, a reliable experimental design was created. The number of seeding cycles (2, 4, 6, and 8) as well as the growth solution’s concentration (10, 15, 25, 35, 45, and 60 mM) and the duration of the seed-assisted hydrothermal treatment were the three variables that were taken into account during the experiment (3, 6, 9 and 12 h). Each seeding cycle for the samples lasts 20 minutes, which includes 10 minutes of soaking in the seed solution and 10 minutes of annealing in a hot air oven at 150°C. In all, 96 experiments were conducted to explore the growth phenomena of CuO nanostructures on carbon fiber fabric. A full-factorial experimental design was opted to develop optimal sequence of process parameters as illustrated in Table 6.1. The experimental parameters were chosen in accordance with the experiment design and each experiment was repeated three times to estimate their variability and increase in accuracy. The various combinations of parameters along with their outcome are listed in Table 6.2.

Table 6.1: Selected process parameters and their levels for full-factorial experimental design

Process parameters	Level-1	Level-2	Level-3	Level-4	Level-5	Level-6
Number of seeding cycle	2	4	6	8	-	-
Concentration (mM)	10	15	25	35	45	60
Duration of growth (hr)	3	6	9	12	-	-

#### 6.3.1 Morphological study and growth chemistry of CuO

Using a two-step seed-mediated hydrothermal process, the quantities of copper nitrate trihydrate and HMTA precursor chemicals between 10 and 60 mM were used to influence the morphologies of CuO nanostructures. Similar to nanostructures, CuO formations were developed mostly along the [0 1 0] direction. Increased  $L_{[010]}/L_{[100]}$  and  $L_{[100]}/L_{[001]}$  aspect ratios, which control self-aligned assembly into different microstructures, promoted growth in the [0 1 0] direction [337]. Thus, the  $NH_3$  molecules that passivate the surface have an impact on the growth mechanism of CuO. Then, aggregates and  $Cu^{2+}$  ions establish coordinate connections. CuO development is inhibited when HMTA is present at the right temperature and exposure period, which has been previously highlighted as being crucial for  $Cu^{2+}/OH^-$  ratio. The resulting  $OH^-$  ions from HMTA’s self-hydrolysis subsequently combine with copper nitrate to form  $Cu(OH)_2$  nuclei. Non-ionic cyclic tertiary

amines are functionalized by the pH buffer reactant HMTA, which on hydrolysis rapidly yields substantial amounts of  $OH^-$  ions. These ions then interact with the  $Cu^{2+}$  ions present in the growth mixture in a sealed beaker at the appropriate temperature. Because of the buffer conditions inside the sealed beaker, CuO self-aligns mostly along the [0 1 0] direction while preventing adhesion at the [1 0 0] and [0 1 0] directional planes. The only leftover result of the final chemical reaction is water. As a result,  $Cu^{2+}$  ions and WCF's carboxylic functional group create stable ionic connections. FESEM was used for the initial research into the formation of CuO nanostructures on WCF. However, independent of the growth solution concentration and the growth duration, our results showed that there was no growth of CuO nanostructures with 2 seeding cycles. The nanostructures did not grow despite the growth solution concentration and growth period being adequate because there were not enough seeding cycles. These findings demonstrated the significance of the seeding procedure as a growth process parameter. Even when the growth solution concentrations were 45 and 60 mM, CuO nanostructures did not grow in WCF samples with 2, 4, 6, or 8 seed cycles and 3 h of growth time. Even though the growth solution's concentration was rather high, the CuO nanostructure's quick development time was crucial since the seed nuclei did not have enough time to grow. Figure 6.5 depicts the impact of the seeding and growth phenomenon for the ultrafine growth of CuO nanostructures on WCF fabric. From Table 6.2, practically all seeding cycles  $\geq 6$  indicated considerable growth of nanostructures except the samples having modest growth periods (3 h). However the concentration of the growth solution varies slightly, such as when CuO is present in low density during the growth of CuO nanostructures, it cannot be regarded as a major parameter, whereas the duration of the seed-assisted hydrothermal treatment was crucial. CuO nanostructures were successfully formed under all growth solution concentrations between 10 mM and 60 mM for all growth times longer than 6 h. CuO nanostructures were most abundant after 8 seeding cycles for 9 hours, and 12 hours of development. Thus, seeding cycles and growing time played a major role in the growth process. With the exception of the samples with a 10 mM concentration that were only subjected to two seeding cycles, the CuO nanostructures grew in nearly all of the growth solution concentrations. According to planned experiments, the growth of CuO nanostructures on WCF yarns is divided into six categories: no growth, agglomerated growth, little growth, moderate growth, fine growth, and ultra-fine growth. Figure 6.6 shows FESEM images of WCF samples that have undergone seed-assisted hydrothermal processing for various treatment settings. These pictures show no growth, agglomerated growth, low growth, moderate growth and fine growth of CuO nanostructures under various process parameters that may have occurred due to low

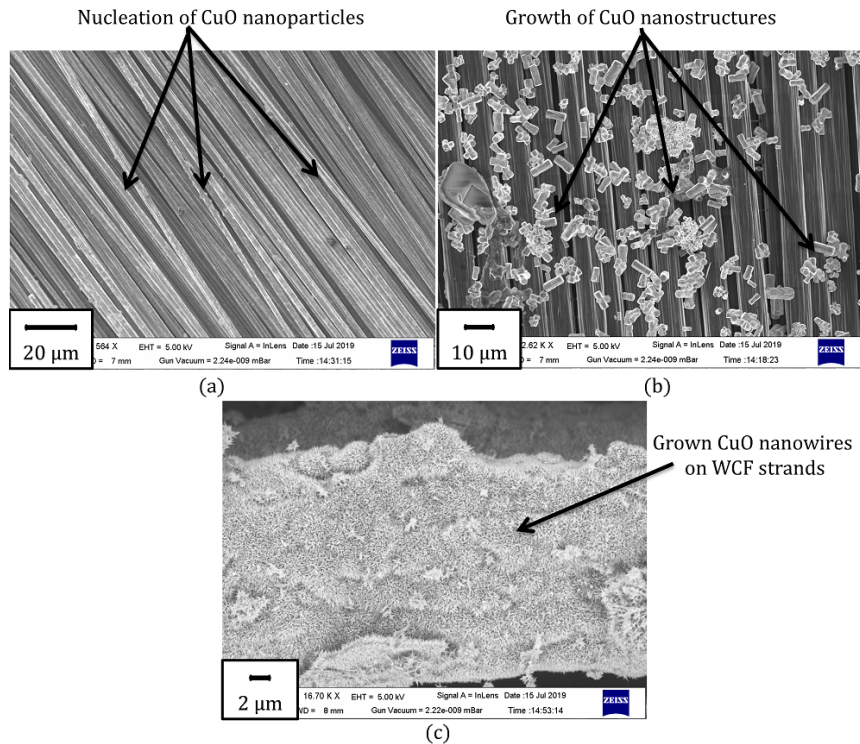


Figure 6.5: Effect of hydrothermal treatment on WCF in (a) seed solution only, (b) growth solution only and (c) seed-assisted growth treatment

seeding cycle and low growth duration. Low seeding is not capable to nucleate the CuO nuclei on WCF surface subsequently low growth duration does not have sufficient time to grow that nucleated CuO nanoparticles. Thus different set of experiments were performed to achieve optimum set of process parameters for ultrafine growth of CuO nanostructures. Figure 6.7 shows samples with ultrafine CuO nanostructure development on WCF strands under treatment settings corresponding to 8 number of seeding cycles and 12 h of growth treatment having different molar concentration. The developed CuO grown WCF samples have high density of CuO nanostructures and will be used for further study.

### 6.3.1.1 Structural and crystallographic analyses of CuO/WCF samples

X-ray diffractograms of CuO nanostructures produced on WCF samples are displayed in Fig. 6.8(a). These were obtained using a high resolution X-ray diffractometer (HRXRD) from Rigaku Smartlab that was automated with guidance software (SmartLab Studio II) and operated with crystal monochromated  $Cu - K\alpha$  radiation ( $\lambda = 1.5418 \text{ \AA}$ ) from  $20^\circ$  to



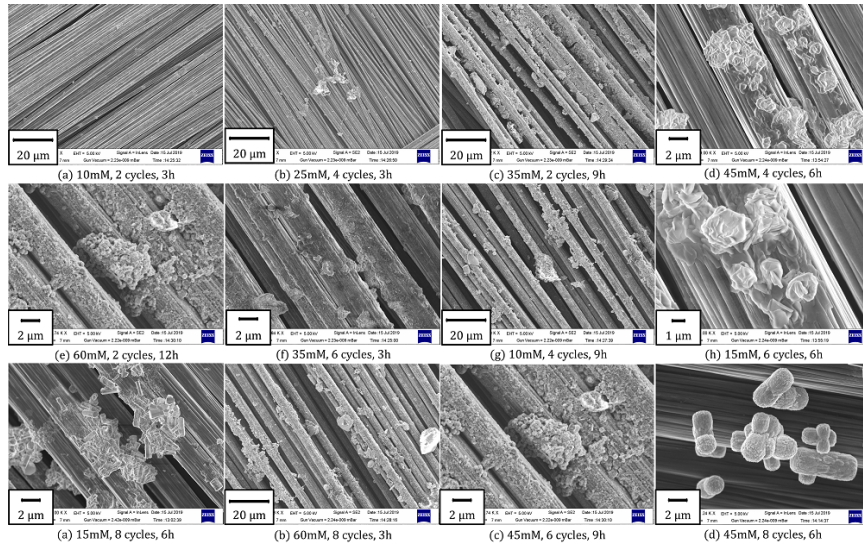


Figure 6.6: Unsuccessful growth of CuO nanostructures on woven carbon fibers showing no-growth, agglomerated-growth, little-growth, moderate-growth and fine-growth

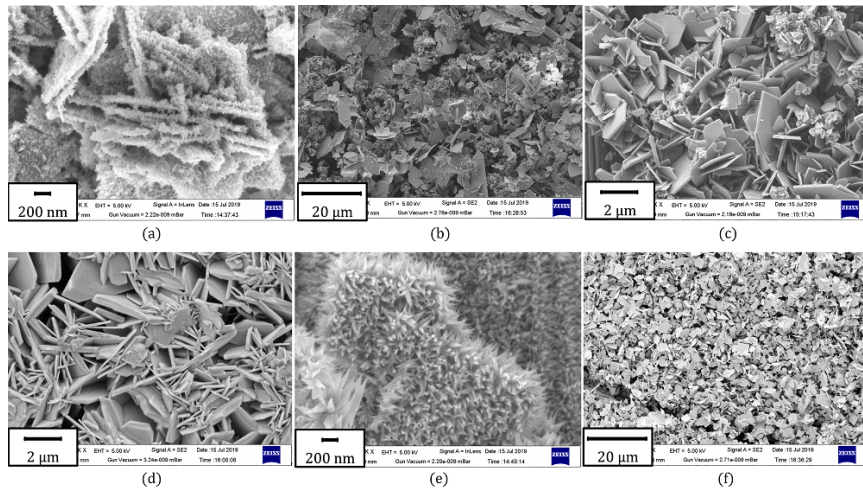


Figure 6.7: Ultrafine growth of CuO nanostructures on WCF corresponding to 8 number of seeding cycles and 12 h of growth treatment having different molar concentration of (a) 10 mM, (b) 15 mM, (c) 25 mM, (d) 35 mM, (e) 45 mM and (f) 60 mM

$80^\circ$  ( $2\theta$ ) at a scanning speed of  $5^\circ/\text{min}$ , 40 kV operating voltage, and 200 mA operating current. The lattice parameters  $a = 4.68 \text{ \AA}$ ,  $b = 3.43 \text{ \AA}$ ,  $c = 5.13 \text{ \AA}$  and  $\beta = 99.5^\circ$  converge to JCPDS database no. 05-0661, 1-0420 and were indexed to the monoclinic CuO crystal phase in all of the samples. Major peaks indexed as  $(\bar{1}11)$ - $(002)$  and  $(111)$ - $(200)$  planes, coupled with those of elemental Cu  $(111)$ , respectively, showed pure-phase mon-

oclinic CuO crystallites and concur with the outcomes of Kong et al. [338]. The carbon contained in the carbon fiber was responsible for the significant diffraction peak seen at  $25.8^\circ$  on (002) plane. Due to the development of CuO nanostructures on the WCF surface, additional diffraction peaks on the planes corresponding to (110), (111), ( $\bar{1}11$ ), (002), (111), (200), ( $\bar{2}02$ ), (020), (202), ( $\bar{1}13$ ), (311), (220), and (004) developed between  $30^\circ$  and  $80^\circ$ . With higher molar concentrations of CuO, the diffraction peaks intensities rose, indicating denser CuO nanostructures. The presence of CuO-specific peaks indicates the high crystallinity of the nanostructure. The samples with 8 seeding cycles, 40 mM growth solution concentration, and 8 h of growth time produced the second highest diffraction peak intensities after WCF with 8 seeding cycles, 60 mM growth solution concentration, and 8 h of growth time. These outcomes offered additional proof of the development of CuO nanostructures on the surface of WCF. The Debye Scherrer relation was used to calculate the crystallite sizes of the CuO nanostructures from the XRD peaks using the FWHM of the high intensity peak. Peak broadening of the XRD spectra caused by instrument errors and inhomogeneous strain was not taken into account in this procedure. According

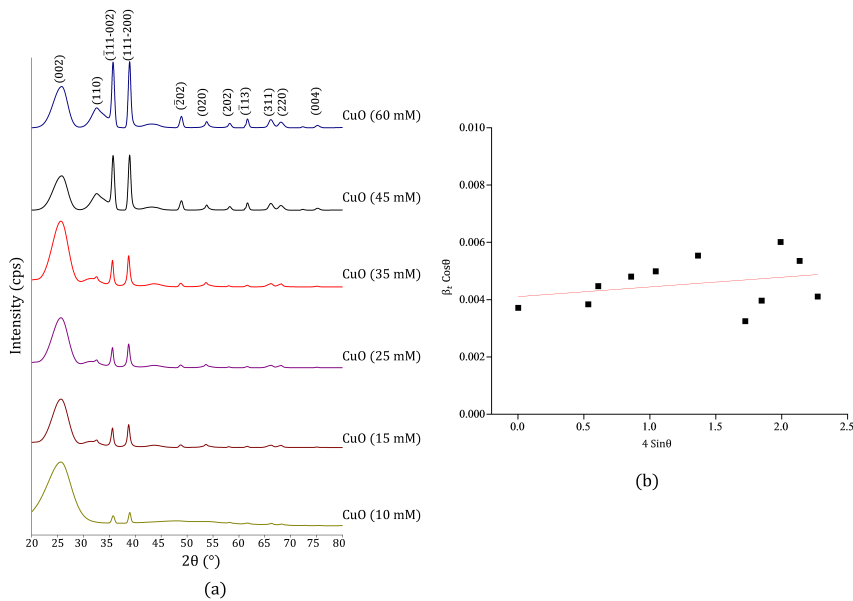


Figure 6.8: (a) XRD spectra and (b) Williamson Hall graph of as grown CuO nanostructures

to the Scherrer’s formula, the crystallite size for all CuO nanostructure XRD peaks that correspond to the sample’s high intensity peak (111) is found to be in the range of 36 nm. Williamson-Hall (W-H) plot technique was used to calculate FWHM in addition to the

crystallite size ( $D$ ) and strain ( $\epsilon$ ) of the produced CuO nanostructures on WCF. The sum of the broadening caused by strain and by crystallite size results in the overall broadening of XRD peaks [276]. That is;

$$\beta_t = \beta_D + \beta_\epsilon \quad (6.9)$$

And the Scherrer's relation is;

$$D = \frac{K\lambda}{\beta_D \cos\theta} \quad (6.10)$$

Where  $K$  (the shape factor) is equal to 0.9,  $\lambda$  is the X-ray source's wavelength (0.15406 nm),  $\theta$  (the peak location in radians), and  $D$  (the size of produced crystals) are other important parameters. The XRD peak's overall broadening can be expressed as follows:

$$\beta_t = \frac{K\lambda}{D \cos\theta} + 4\epsilon \tan\theta \quad (6.11)$$

Equation (6.11) can be written as,

$$\beta_t \cos\theta = \epsilon(4 \sin\theta) + \frac{K\lambda}{D} \quad (6.12)$$

Since the W-H graph in Fig. 6.8(b) is essentially a straight line drawn with  $(4 \sin\theta)$  on the x-axis and  $(\beta_t \cos\theta)$  on the y-axis, this expression (equation-11) is identical to a straight line equation ( $y=mx+c$ ). The amount of strain " $\epsilon$ " will be indicated by the line's slope, and the value of crystal size will be indicated by the line's y-intercept. The crystallite size is 33.81 nm, and the calculated strain is  $3.3933 \times 10^{-4}$ . For all XRD peaks of CuO nanostructures that correspond to the high intensity peak (111) of the sample, the measured value of the crystallite size using W-H plot and Scherrer's formula are found to be in the range of 33-36 nm.

### 6.3.2 Compositional analysis of as fabricated CuO nanostructures on WCF

The energy dispersive spectroscopy apparatus connected to the FESEM setup is used to analyze the composition of the CuO/WCF samples as they were developed. Figure 6.9 presents the findings of the Energy Dispersive Spectroscopy (EDS) examination. According to statistical analysis, Cu and O are present in a 1:1 stoichiometric ratio, and the EDS spectra clearly demonstrate the presence of Cu, O, and C components. It demonstrates the presence of copper and oxygen components on the surface of carbon fiber, supporting

nano-growth of CuO in the prepared precursor mixture by hydrothermal depositions. As illustrated in Fig. 6.9, the atomic percentage and weight percentage of each element are also determined using the EDS spectra. The inherent CuO often has a non-toxic p-type

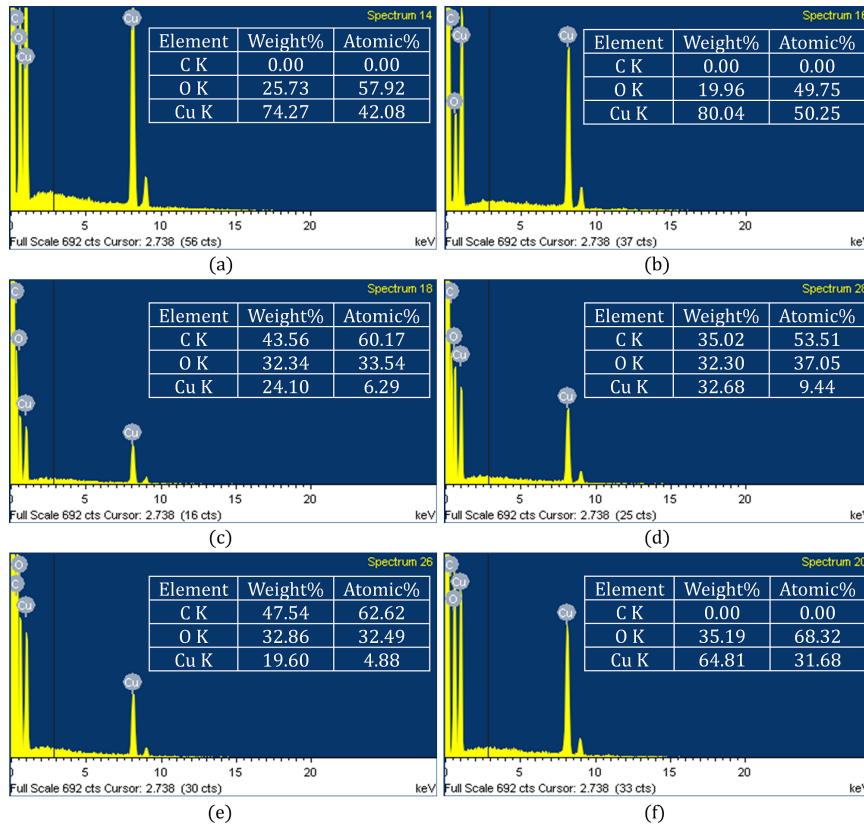


Figure 6.9: Elemental composition of CuO nanostructures

semiconductor property, which is supported by the fact that the created CuO nanostructures are frequently oxygen depleted. The spectrum does not contain any more undesirable elements. The CuO/WCF samples can be used to create hybrid composites employing BPA epoxy resin as a matrix for a number of applications after the EDS spectra showed the hydrothermal development of CuO nanostructures on carbon fiber surfaces. To explain the compositional variance, the elemental mapping of a synthesized CuO nanostructured WCF sample is shown in Fig. 6.10, coupled with an EDX analysis of the sample. The created sample includes the following elements such as carbon (C), oxygen (O), and copper (Cu) which are represented by the colors red, green, and blue respectively. This verifies the growth of CuO nanostructures on carbon fiber surface possesses high density and uniform growth distribution.

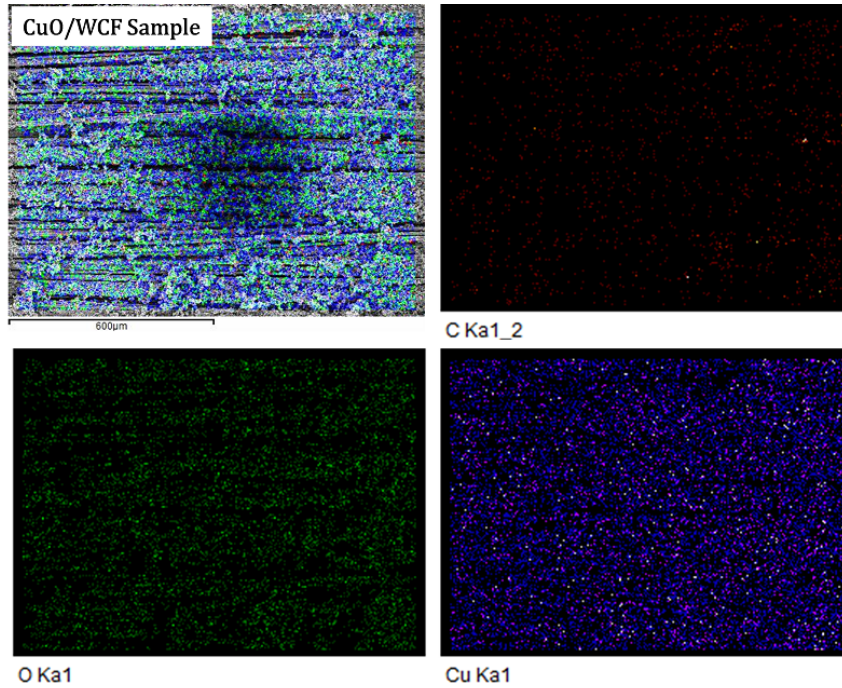


Figure 6.10: Elemental mapping of the CuO nanostructures grown on WCF strands

### 6.3.3 Impact of process parameters on dimensions of CuO nanostructures

Depending on the quantity of seeding cycles, the length of the growth process, and the molar concentration applied different geometric shapes of CuO nanostructures were produced by the seed-assisted hydrothermal growth technique. The nanoflakes, nanopellets, and nanowires have pointed tips and broader bases, as can be seen in Fig. 6.7. As measured from the base, all dimensions (height, width, and thickness) tended to decrease by adjusting the stated hydrothermal process parameters. The CuO nanostructures with the shapes of nanoflake, nanopellet, and nanowire ranged in height from 650 to 750 nm, 600 to 650 nm, and 200 to 300 nm, respectively. Similarly, CuO nanostructures with the shapes of nanoflake, nanopellet, and nanowire ranged in width from 200 to 250 nm, 150 to 200 nm, and 100 to 120 nm, respectively. The thickness of the generated CuO nanostructures with the shapes of nanoflake, nanopellet, and nanowire was calculated to be between 150 and 180 nm, 120 and 150 nm, and 80 and 100 nm, respectively. The dimensional fluctuation of CuO nanostructures as synthesized morphologies on WCF surface is shown in Fig. 6.11(a). Nanoflakes have higher dimensions (height, width, and thickness) than nanowires, which have smaller dimensions, but nanopellets have a moderate size fluctuation. These

major morphologies include nanoflakes, nanopellets, and nanowires. Figure 6.11(b) shows the relationship between the dimensional variation of produced CuO nanostructures and changes in molar concentration. It was clear that at low molar concentrations, the CuO nanostructure's surface exposure was higher. When the concentration of growth precursors grew, the base's width and thickness dropped but its height climbed. It makes sense that the bigger surface area of these CuO nanostructures and the higher density of CuO nanostructures per unit of WCF surface area could improve the performance of composites made with them.

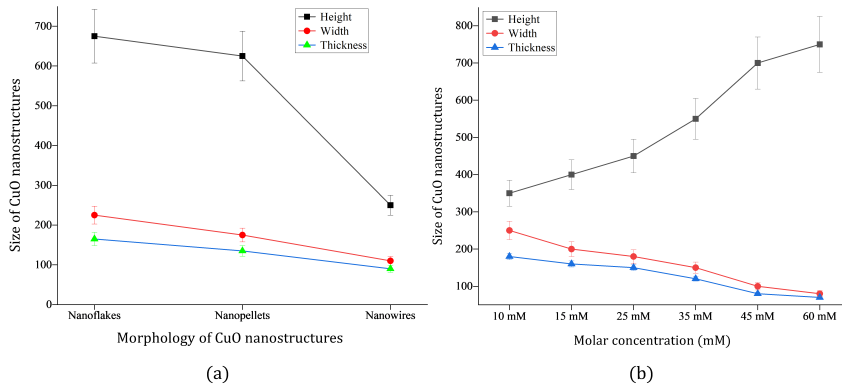


Figure 6.11: Dimensional variation of as grown CuO nanostructures (a) under varied morphologies and (b) under varied molar concentrations

### 6.3.4 Weight loss study of CuO by TGA thermograms

Using a Thermo Gravimetric Analyzer (TGA), the yield of the CuO synthesis and its effect on the thermal stability of the modified WCF were assessed (DTG-60, Shimadzu Co., Japan). The CuO/WCF sample was heated in a platinum crucible on the microbalance pan from room temperature to 1000 °C. Using nitrogen flow and a heating rate of 10 C/min<sup>-1</sup>, the experiment was conducted. Figure 6.12(a) depicts the TGA degradation trend of WCFs both before and after CuO nanostructure surface modification. The surface of the WCFs having developed CuO nanostructures exhibits improvement in the thermal stability. The sample's initial degradation temperature ( $T_i$ ), maximum pyrolysis temperature ( $T_m$ ), and residual weight all increased as compared to the unaltered WCF samples. A large amount of interfacial contact between the carbon fiber and the CuO was the cause of the increased thermal stability. Particularly with the carboxylic acid groups on the surface of the WCF, the  $Cu^{2+}$  ions formed strong ionic connections. The development of a densely networked

structure as a result of this interaction improved the thermal stability of the WCF samples by acting as a barrier to the transport of volatile breakdown products [307]. The amount

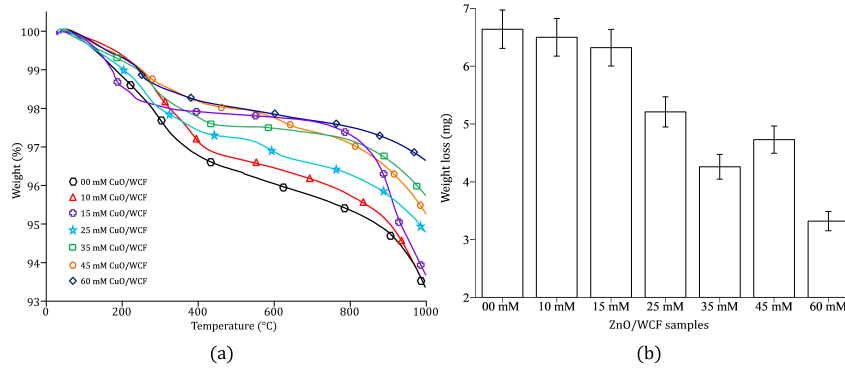


Figure 6.12: (a) Thermogravimetric degradation pattern and (b) weight loss evaluation of WCF before and after CuO growth

of CuO generated on the surface of the WCF was calculated using the difference in mass loss between the CuO-embedded WCF and the pure WCF. The weight loss of the WCF samples with and without CuO implanted is shown in Fig. 6.12(b) as a bar chart to show how the weight of the CuO/WCF samples varies in comparison to bare WCF. As compared to the plain WCF sample all of the CuO-embedded WCF samples produced by hydrothermal synthesis displayed a considerable weight change. The sample loses less weight as the concentration of CuO rises, but the weight loss for the 45 mM sample increases suddenly, which may be caused by a lack of crosslinking between the CuO nanostructures and the WCF surface. The samples with 60 mM CuO concentration, 8 seeding cycles, and 12 hours of treatment time show the least amount of weight loss when compared to the other samples. The sample that was subjected to 8 seed cycles, 60 mM, and a 12-hour hydrothermal condition produced the greatest growth of CuO on the WCF. In comparison to other aspects, the concentration of the growth solution has very little influence on the pattern of weight reduction. These findings demonstrate that the CuO nanostructures on the vertically oriented WCF pieces developed in this sample in the most controlled manner, and they can be used to establish the ideal growth conditions for subsequent research.

### 6.3.5 Fourier-transform infrared spectroscopy

The developed sample's functional groups and metal-oxide interactions were located utilizing the qualitative method of FT-IR spectroscopy. The FT-IR transmittance spectrum of

plain WCF and as produced CuO Nanostructures on WCF surfaces is given in Fig. 6.13 for the wavenumber range of 500 to 4000  $cm^{-1}$ . The presence of hydroxyl, carboxyl, and moisture on the surface of the carbon fiber was the primary cause of the tiny and broad absorption peak that was found between 3200 and 3500  $cm^{-1}$ . Peaks at 2921 and 2856  $cm^{-1}$  were caused by the methylene group's ( $-CH$ ) stretching. The WCF-CuO nanostructure's peaks at 3433, 2924, and 2851  $cm^{-1}$  were caused by the surface hydroxyl and methylene groups ( $-CH_2-$ ). Additionally, a peak at 3433  $cm^{-1}$  was used to assess the absorption of water molecules on the surface of the CuO nanostructures. The new peaks at 1632, 1427, 1361, and 1082  $cm^{-1}$  were caused by the stretching vibrations of C=C and C-O, which suggests the combination of carbon fibers and CuO [339]. The surface carbonyl group displayed a peak at 1722  $cm^{-1}$ . Cu-O was stretched in the  $[\bar{1}11]$  direction, producing the peaks at 617  $cm^{-1}$ . The Cu-O stretching along the [101] direction of the WCF-CuO nanostructures caused the peak at 531  $cm^{-1}$  to occur [36]. The Cu-O bond's characteristic

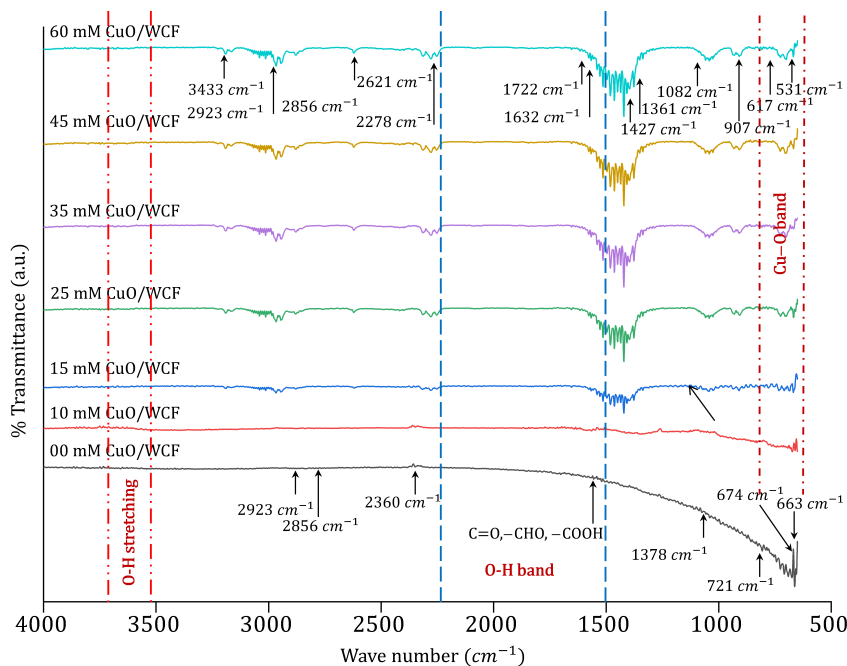


Figure 6.13: FT-IR spectroscopy spectra of plain WCF and CuO-modified WCF

stretching mode is attributed to a significant vibration band in the FTIR spectrum between 600  $cm^{-1}$  and 800  $cm^{-1}$ . Peaks at 1361 and 1427  $cm^{-1}$  were attributed to the bending vibrations of the  $-CH_3$  groups and  $-CH$  bonds, while peaks at 2852 and 2923  $cm^{-1}$  were assigned to the stretching vibrations of the  $-CH$  bonds. While the peaks at 3327 and 3428  $cm^{-1}$  were attributed to OH stretching vibrations, the peaks at 1626  $cm^{-1}$  were attributed



to  $C = C$  or  $C = N$  stretching vibrations. These results suggested the existence of certain polar groups on WCF surfaces. A cluster of water molecules in the process of crystallisation has a peak H–O–H vibration at  $2370\text{ cm}^{-1}$ . The peaks at 1652, 1520, 1082, and  $907\text{ cm}^{-1}$  correspond to the  $C = C$  stretching of an alkane group,  $C = C$  stretching in an aromatic ring and stretching in polyphenol ( $C = O$ ), C–H bending vibration of an alkane group, stretching of C–N, and bending vibration of C–H, respectively [306]. The small peak at  $664\text{ cm}^{-1}$  indicates that C-alkyl chloride and CuO hexagonal phase are present. Since the CuO-decorated WCF had a lower intensity of the peak at  $3327\text{ cm}^{-1}$ , the carboxylic acid must have played a role in the formation of the CuO bond. At  $617\text{ cm}^{-1}$ , and  $531\text{ cm}^{-1}$ , new peaks for the Cu/WCF/O stretching vibration appeared [36].

### 6.3.6 X-ray photoelectron spectroscopy (XPS) analysis

The physical behavior of CuO nanocomposites are significantly influenced by the concentration of oxygen vacancy and the existence of trace quantities of  $Cu^{3+}$  within CuO. It is well known that it is highly challenging to observe micro-quantities of  $Cu^{3+}$  through XRD examinations. The most effective method for identifying this minute amount of charge co-existing with  $Cu^{2+}$  in CuO is X-ray photoelectron spectroscopy (XPS). The surface chemistry and content of CuO-modified WCF and the same hybrid nanocomposite in laminated form were investigated using XPS measurements. Charge neutralizer was used throughout the analysis to remove the charging effect. With regard to quantification, Shirley's algorithm was used for background correction while data analysis and processing were carried out using vision processing software [340]. The collected spectra were deconvoluted, and a Gaussian fitting approach was used to fit them. C 1s at 284.6 eV was used to calibrate the binding energies. The survey scan spectra of CuO nanostructures as they have been formed, coupled with their atomic percentage, are shown in Fig. 6.14(a). The spectrum clearly identifies signals for Cu, O, and C, dispelling the possibility of additional element in the sample. High resolution Cu 2p spectra (Fig. 6.14(b)) show two prominent peaks at roughly 933.7 eV and 953.8 eV that correspond to the binding energies of Cu  $2p^{3/2}$  and Cu  $2p^{1/2}$ , respectively, with spin orbit splitting separation of 20 eV in accordance with published data [341]. These peaks represent typical Cu (II) state characteristics. CuO is also characterized by the presence of the shake-up satellite peak at 941–944 eV, which supports the occurrence of the CuO phase of synthetic CuO on WCFs. This further indicates the existence of an unfilled  $3d^9$  ground state, as opposed to the totally filled 3d states of  $Cu_2O$ , which make it impossible to have such a satellite peak [342]. CuO-modified car-

bon fiber's XPS O 1s spectra are shown in Fig. 6.14(c). The CuO lattice oxygen, which corresponds to the Cu-O bond, is indicated by the strong peak at 529.5 eV. There is no additional peak indicating surface adsorbed hydroxyl ions. As a calibration reference, the typical C 1s (284.6 eV) spectra depicted in Fig. 6.14(a) will be used. The XPS analysis of pure CuO/WCF confirms the existence of the CuO phase and is in line with the findings of XRD and EDS.

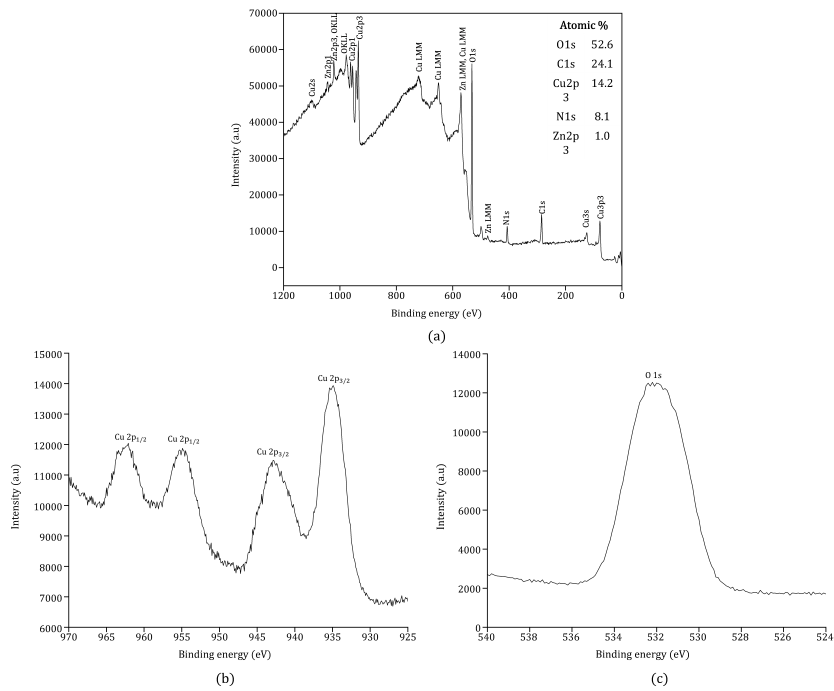


Figure 6.14: (a) XPS survey scan for the grown CuO nanostructures on WCF, high resolution XPS spectrum of as synthesized CuO-modified WCFs for (b) Cu 2p and (c) O 1s regions

Table 6.2: Findings of hydrothermal growth of CuO nanostructures on WCFs

S.no.	$S_c$	$C_g$	$T_g$	$O_e$	S. no.	$S_c$	$C_g$	$T_g$	$O_e$
1	2	10	3	$N_g$	49	6	10	3	$N_g$
2	2	10	6	$N_g$	50	6	10	6	$A_g$
3	2	10	9	$N_g$	51	6	10	9	$L_g$
4	2	10	12	$N_g$	52	6	10	12	$L_g$
5	2	15	3	$N_g$	53	6	15	3	$N_g$
6	2	15	6	$N_g$	54	6	15	6	$A_g$
7	2	15	9	$A_g$	55	6	15	9	$M_g$
8	2	15	12	$A_g$	56	6	15	12	$M_g$
9	2	25	3	$N_g$	57	6	25	3	$N_g$
10	2	25	6	$N_g$	58	6	25	6	$L_g$
11	2	25	9	$A_g$	59	6	25	9	$M_g$
12	2	25	12	$A_g$	60	6	25	12	$M_g$
13	2	35	3	$N_g$	61	6	35	3	$N_g$
14	2	35	6	$N_g$	62	6	35	6	$L_g$
15	2	35	9	$A_g$	63	6	35	9	$M_g$
16	2	35	12	$A_g$	64	6	35	12	$F_g$
17	2	45	3	$N_g$	65	6	45	3	$N_g$
18	2	45	6	$N_g$	66	6	45	6	$L_g$
19	2	45	9	$A_g$	67	6	45	9	$M_g$
20	2	45	12	$A_g$	68	6	45	12	$F_g$
21	2	60	3	$N_g$	69	6	60	3	$N_g$
22	2	60	6	$N_g$	70	6	60	6	$L_g$
23	2	60	9	$A_g$	71	6	60	9	$M_g$
24	2	60	12	$A_g$	72	6	60	12	$F_g$
25	4	10	3	$N_g$	73	8	10	3	$N_g$
26	4	10	6	$A_g$	74	8	10	6	$L_g$
27	4	10	9	$A_g$	75	8	10	9	$F_g$
28	4	10	12	$L_g$	76	8	10	12	$U_g$
29	4	15	3	$N_g$	77	8	15	3	$N_g$
30	4	15	6	$A_g$	78	8	15	6	$L_g$
31	4	15	9	$L_g$	79	8	15	9	$F_g$
32	4	15	12	$L_g$	80	8	15	12	$U_g$
33	4	25	3	$N_g$	81	8	25	3	$N_g$
34	4	25	6	$A_g$	82	8	25	6	$L_g$
35	4	25	9	$L_g$	83	8	25	9	$F_g$
36	4	25	12	$M_g$	84	8	25	12	$U_g$
37	4	35	3	$N_g$	85	8	35	3	$N_g$
38	4	35	6	$A_g$	86	8	35	6	$L_g$
39	4	35	9	$L_g$	87	8	35	9	$F_g$
40	4	35	12	$M_g$	88	8	35	12	$U_g$
41	4	45	3	$N_g$	89	8	45	3	$N_g$
42	4	45	6	$A_g$	90	8	45	6	$L_g$
43	4	45	9	$L_g$	91	8	45	9	$F_g$
44	4	45	12	$M_g$	92	8	45	12	$U_g$
45	4	60	3	$N_g$	93	8	60	3	$N_g$
46	4	60	6	$A_g$	94	8	60	6	$L_g$
47	4	60	9	$L_g$	95	8	60	9	$F_g$
48	4	60	12	$M_g$	96	8	60	12	$U_g$

## 6.4 Volume fraction and void analysis of the composites

The correct proportion of the fiber content should be determined because several studies have expressed that it is one of the most important factors in enhancing the mechanical properties of fiber reinforced composites [309]. The ASTM D2584 standard is typically used to calculate the fiber volume proportion as follows [312];

$$V_f = \left\{ \frac{\rho_m \cdot w_f}{\rho_m \cdot w_f + \rho_f \cdot w_m} \right\} \quad (6.13)$$

Where,  $V_f$  denotes the volume fraction of the fiber,  $\rho_f$  denotes fiber density,  $\rho_m$  denotes matrix density,  $w_f$  denotes weight of the fiber, and  $w_m$  denotes weight of the matrix. When it comes to textiles, the spacing between the yarns of the textile pattern determines the total fiber volume proportion. Yarns with different fiber volume proportions are designed and implemented within a certain framework. Because the polymeric matrix would occupy the threads, measuring the fiber content only on the space between yarns in a textile is insufficient. As a result, a reasoned mathematical expression may be used to determine the volume fraction of fiber as follows [312]:

$$V_f = \left\{ \frac{\rho_m \cdot w_y}{\rho_m \cdot w_y + \rho_y \cdot w_m} \right\} \quad (6.14)$$

Where,  $V_f$  stands for the fiber volume fraction,  $\rho_y$  for the fabric's yarn density,  $\rho_m$  for the matrix density,  $w_y$  for the yarn's weight, and  $w_m$  for the matrix's weight. With the composite density measured and the fiber and matrix densities known, the fiber volume proportion of the manufactured composites was determined using the aforementioned mathematical procedures. The estimated computed fiber volume proportions for the manufactured composites are shown in Table 6.3. The following equation was used to calculate the volume proportions of CuO nanostructures implanted in CuO/WCF/BPA epoxy resin hybrid composites:

$$V_{CuO} = \left\{ \frac{\left( \frac{W_{CuO}}{\rho_{CuO}} \right)}{\left( \frac{W_{CuO}}{\rho_{CuO}} \right) + \left( \frac{W_f}{\rho_f} \right) + \left( \frac{W_m}{\rho_m} \right)} \right\} \quad (6.15)$$

Where,  $\rho_{CuO}$  represents density of CuO Nanostructures,  $w_{CuO}$  represents the weight of CuO nanostructures,  $V_{CuO}$  represents the volume fraction of CuO nanostructures, and  $w_f$  and  $w_m$ , respectively indicate the weight of the fiber and matrix. The volume fraction measurements of the CuO nanostructures in the developed nanocomposite are shown in Table

6.3. The volume fraction of CuO nanostructures increases in specimens with 6 seeding cycles, and this trend continues as the number of seeding cycles and development time increase. The samples representing 8 seeding cycles and 12 hours of growth treatments with various molar concentrations were analyzed for volume fraction evaluation based on the CuO nanostructures growth that was the most effective. The volume fraction of CuO in the composite samples created with the most successful development of CuO on WCF and BPA epoxy resin similarly increases as the molar concentration of the growth solution increases, i.e., 10mM > 15mM > 25mM > 35mM > 45mM > 60mM. WCF's density and volume fraction both increased with the creation of CuO nanostructures. As the volume percentage and density increase, so does the quality of the created hybrid composites. Using 8 seeding cycles and a 12-hour growth period, the specimens made with a 60 mM solution appeared to have the highest volume fraction of CuO, indicating the highest growth of CuO nanostructures among the specimens. The interfacial contact between the CuO nanostructures, WCF, and BPA epoxy resin gets stronger as the CuO nanostructures growth progresses. These interactions enhance the net load transfer rate from the matrix material to the fibers. Therefore, composites with higher volume fractions of CuO function better [103]. Additionally, evaluations of void content are utilized to gauge a composite's qualities and possibilities for various operations. The majority of a composite's material properties are influenced by the void percentage. To calculate the densities of composites, ASTM D792 was employed. The specimen's weights were measured after they were submerged in distilled water at room temperature. According to ASTM D2734, the percent void proportions of the specimens were calculated using common mathematical methods derived from experimental and theoretical density as follows:

$$\text{Voidcontent} = \frac{(\rho_{\text{theoretical}} - \rho_{\text{experimental}})}{\rho_{\text{theoretical}}} \quad (6.16)$$

$$\rho_{\text{theoretical}} = \frac{1}{\left(\frac{W_{\text{CuO}}}{\rho_{\text{CuO}}}\right) + \left(\frac{W_f}{\rho_f}\right) + \left(\frac{W_m}{\rho_m}\right)} \quad (6.17)$$

In their natural form, WCF/BPA epoxy resin composites had a void rate of 11.64 %. This considerably decreased as CuO nanostructures began to develop on the WCF surface. As more CuO nanostructures were being developed, the void percentage started to decrease. In woven aramid/kenaf fiber/epoxy composites, Yahaya et al. [313] reported a 16.2 % void content and discovered that kenaf mat composites have a larger void percentage and poorer interfacial adhesion. Hazarika et al. [143] reported 16.24% of void content in the

fabrication of uncoated woven Kevlar fiber reinforced polyester composites using vacuum bagging technique and found reduction in void content on increase in coating of ZnO. However, the current work reported approximately 10.84% of void content for uncoated WCF reinforced polymer composites. The formation of high void content might have occurred during its fabrication because major cause of void formation is mechanical air entrapment during flow of resin and formation of gases due to chemical reactions. Further nucleation of dissolved gases in the resin can cause void formation. In this work, the fiber surface is treated under different chemical solutions during deposition of CuO nanostructures which may propagate creation of gases during curing of the samples. Furthermore, the fiber architecture changes due to chemical treatments which cause air entrapment resulting in non-uniform permeability of the fiber which may causes local variation in resin velocity. These are possible reasons of high void content which need to be explored for detailed information. CuO nanostructures generated on WCF increased the interfacial relationships between WCF and BPA epoxy resin. The  $Cu^{2+}$  ion forms ionic connections with the carboxylic acid groups on WCF. The BPA epoxy resin's epoxide group also contributed to the crosslinking and bonding that boosted interfacial adhesion. Therefore, compared to bare WCF/BPA epoxy resin composites, the void content of WCF/CuO/BPA epoxy resin composites is much reduced. CuO nanostructures formed on WCF have a higher density, which also has a lower void content. The WCF/CuO/BPA epoxy resin composite sample produced by 8 seeding cycles and 12 hours of development period exhibits the lowest void content at 60 mM CuO molar concentration.

Table 6.3: Study of CuO volume fraction and void content of fabricated composites

S.no.	Sample category	Fiber volume fraction (%)	CuO volume fraction (%)	Void content (%)	Tensile strength (MPa)	Elastic Modulus (GPa)	In-plane shear strength (MPa)
1	00 mM CuO/WCF/BPA Epoxy resin hybrid composite	≈ 48.76 ± 0.80	0.0	≈ 10.84	257.78	14.75	162
2	10 mM CuO/WCF/BPA Epoxy resin hybrid composite	≈ 48.76 ± 0.80	≈ 1.62	≈ 8.86	288.69	17.83	168
3	15 mM CuO/WCF/BPA Epoxy resin hybrid composite	≈ 48.76 ± 0.80	≈ 2.13	≈ 7.42	299.82	18.74	176.11
4	25 mM CuO/WCF/BPA Epoxy resin hybrid composite	≈ 48.76 ± 0.80	≈ 2.64	≈ 6.37	310.31	19.29	182.78
5	35 mM CuO/WCF/BPA Epoxy resin hybrid composite	≈ 48.76 ± 0.80	≈ 3.36	≈ 5.14	333.75	19.81	191.67
6	45 mM CuO/WCF/BPA Epoxy resin hybrid composite	≈ 48.76 ± 0.80	≈ 3.92	≈ 4.72	345.01	20.83	206.23
7	60 mM CuO/WCF/BPA Epoxy resin hybrid composite	≈ 48.76 ± 0.80	≈ 4.68	≈ 3.68	364.52	22.35	214

## 6.5 Mechanical characterization of fabricated hybrid composites

The CuO/WCF/BPA epoxy resin hybrid composites were made using the WCF samples with the highest CuO growth. The vacuum bagging technique was used to prepare the laminated composite samples and after curing, the samples were tested under mechanical loading. In order to determine the average value of the necessary attributes, seven categories of composite samples were considered for further study and five tests were run on

each category of composite samples. The average value was calculated from the remaining three responses after the top and lowest responses from five tests were excluded. Table 6.4 enlists the finalized categories of composite samples.

Table 6.4: Fabricated ZnO/WCF/BPA epoxy composite samples for mechanical characterizations

S.no.	Sample name	Sample category
1	S-1	00 mM CuO/WCF/BPA Epoxy resin hybrid composite
2	S-2	10 mM CuO/WCF/BPA Epoxy resin hybrid composite
3	S-3	15 mM CuO/WCF/BPA Epoxy resin hybrid composite
4	S-4	25 mM CuO/WCF/BPA Epoxy resin hybrid composite
5	S-5	35 mM CuO/WCF/BPA Epoxy resin hybrid composite
6	S-6	45 mM CuO/WCF/BPA Epoxy resin hybrid composite
7	S-7	60 mM CuO/WCF/BPA Epoxy resin hybrid composite

### 6.5.1 Drop weight impact test

CFRP composites are susceptible to impact damage due to their low impact energy absorption. However, carbon fiber coated with CuO nanostructures can improve resistance to failure under impact loading. In this section, the energy absorption caused by CuO growth and the failure behavior of the produced composite samples under drop down impact load were examined. The properties of fabricated hybrid composites are believed to be enhanced by increased surface area between CuO nanostructures, fibers, and a polymer matrix, which would enhance chemical interaction and mechanical load-transfer capacity. It results from the surface of carbon fibers having functional groups such as hydroxyl, carbonyl, and carboxyl. These functional groups have a strong affinity for CuO nanostructures and causes effective bonding site with polymeric matrix. In accordance with ASTM D5628-10 standard, the impact test was performed using a drop-weight impact tester (Model: SPRANKTRONICS, Bangalore, India) fully computer controlled with data acquisition system to assess the composites' ability to absorb energy from impacts caused by vertically dropped weights. The height of impactor varies from 0.1 to 1.0 meters, and the impact energy scale goes from 0-120 Joules. The 5 kg circular impactor clamp was first set to a 45 mm diameter. In these studies, the drop height was 0.75 m and the impact velocity was 3.84 m/s. Each sample is approximately 2.0 mm thick on average. Figure 6.15 illustrates the drop weight impact tester, their impact data collection system, and the fabricated composite samples. Data was gathered between the initial impact contact point and the penetration point. The rebound and absorbed energies were combined to determine



the impact energy. The resin and fibers absorbed all of the rebound energy while it was low. The delamination and bending deformation energies were incorporated into the absorbed energy for low velocity strikes. On the other hand, the composite's brittleness led to a moderate amount of absorption energy when the fibers broke. The impact energy of the samples absorbed the residual energy, which included shear-out, global deformation, and delamination energy.

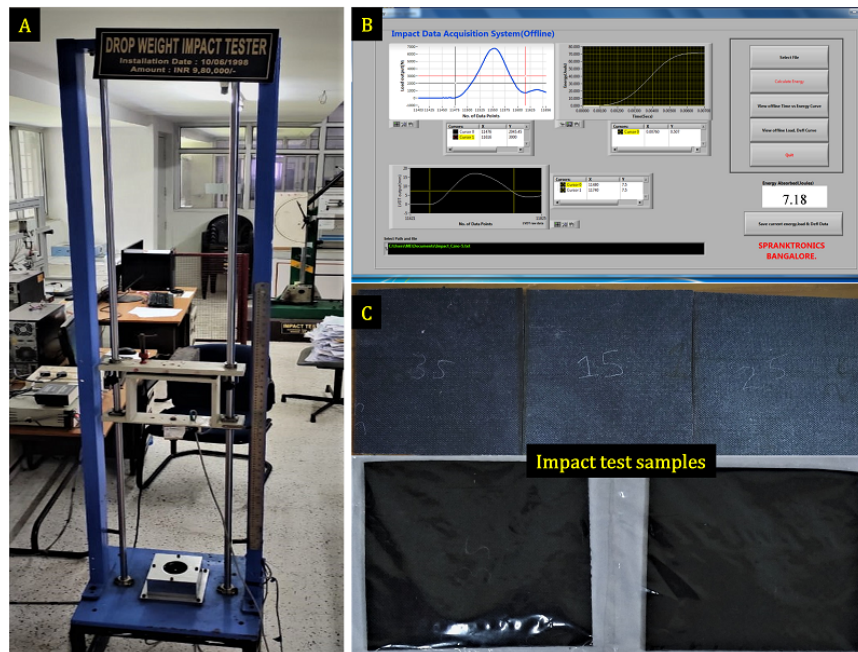


Figure 6.15: Drop weight impact tester along with data collection system and fabricated samples

#### 6.5.1.1 Impact energy absorption

Figure 6.16 displays the impact energy absorption results for the WCF/CuO/BPA epoxy resin composite specimens and the simple WCF specimens. The uncoated WCF/BPA epoxy resin composite specimen had the lowest impact energy absorption. The impact energy absorption rose by 48.34 % with 10 mM CuO growth on the WCF, and this increase persisted as the CuO nanostructures grew. CuO nanostructure's surface area increased linearly with their development, which improved their compatibility with WCF and the polymer matrix. Due to the high level of entanglement created by these interactions, the composite was able to efficiently absorb and transmit energy through its interfaces in comparison to plain CFRP composites [343] and microparticle embedded CFRP composites

[344]. As previously discussed, the highest growth of CuO nanostructures occurred in the composites with 8 seeding cycles, 12-hour growth times, and growth solution concentrations of 45 mM and 60 mM. As a result, these composites were the most effective at absorbing impact energy, with increases in energy absorption of 66.7 % and 74.8 % in comparison to bare WCF/BPA epoxy composite specimens, respectively. The features were also enhanced by the affinities of the surface functional groups present in the carbon fibers. Naturally carboxyl, hydroxyl, and carbonyl groups can be found on the surfaces of carbon fibers. When the hydroxyl and carboxyl groups come into touch with the  $Cu^{2+}$  ions in CuO, strong ionic bonds are created. Additionally, the long pairs of the carbonyl group exhibit a strong attraction for CuO nanostructures. Furthermore, the epoxy functional groups can interact to form strong linkages with the epoxide groups. WCF and BPA epoxy resin improved the overall impact absorption energy capacity of hybrid composites by merging these components. The average, standard deviation, and coefficient of variance of impact test results of each sample have been tabulated in the Table 6.5. It can be observed that, the coefficient of variance is around 5% which shows lower level of dispersion of the test results and good performance of the method applied.

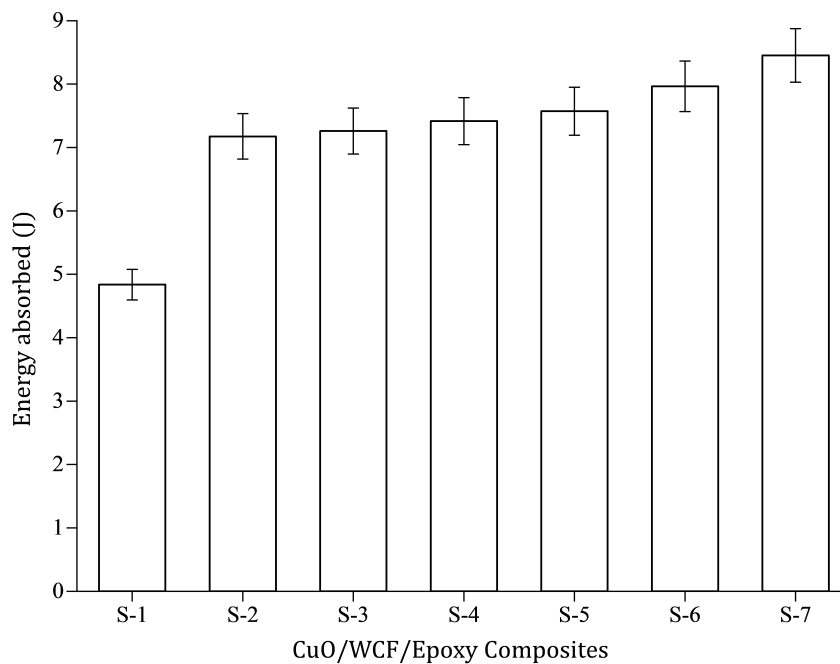


Figure 6.16: Absorbed impact energy of impact test samples

### 6.5.1.2 Energy Vs time response of impacted samples

When samples are subjected to a low-velocity impact, the impact energy is made up of both the rebound and the absorbed energies. The rebound energy was modest when the striker did not puncture the composites because the resin and fibers totally absorbed the energy. The energies that were absorbed included delamination and bending deformation energies. Figure 6.17 shows the variation in impact energy absorbed by the WCF/BPA epoxy resin and WCF/CuO/BPA epoxy resin composites as a function of time. CuO nanostructures were added, and it was discovered that the absorbed impact energy and time till failure increased in WCF/BPA epoxy resin composites. The impact absorption energy of plain WCF/BPA epoxy resin composites was the lowest and failed very rapidly, but this property improved as the quantity of CuO nanostructures increased. The impact energy increased as the molar concentration of CuO increased, for instance, the sample with minimal CuO growth (i.e., the sample treated with 8 seed cycles, 10 mM concentration, and 12 hrs growth treatment) had a 48.34 % higher impact energy and a 133 % increase in failure time than the plain WCF/BPA epoxy resin composites. The CuO nanostructure's larger surface area produced a stronger interfacial interaction between the fibers and the epoxy resin, increasing the absorption of impact energy. Surface carboxylic groups reacted with the epoxide

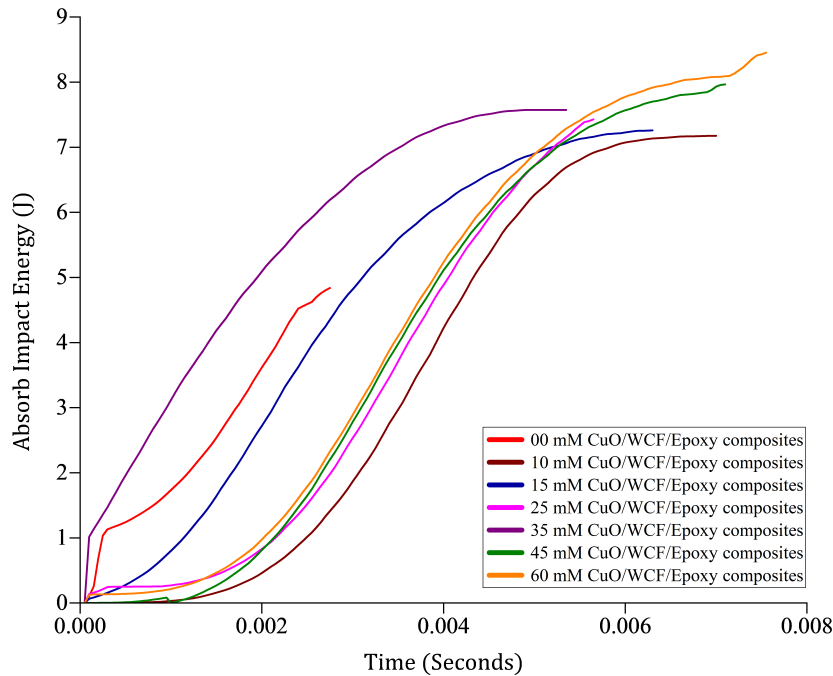


Figure 6.17: Variation of absorbed impact energy of samples as a function of time

(oxirane) group of the BPA epoxy resin to establish ionic interactions with  $Cu^{2+}$  ions, resulting in additional connections between the fibers, CuO nanostructures, and resin. The greater the interfacial interaction, the more energy is absorbed since energy can be transmitted from the polymer to the fiber across the interface more easily. The WCF/CuO/BPA epoxy resin composite, which was created with 8 seeding cycles, 60 mM CuO concentration, and 12 hours of treatment, grew the most CuO nanostructures and, as a result, absorbed the most impact energy, 74.8 % better than the bare WCF/BPA epoxy resin composite. Additionally, the time taken to failure was increased by 166 % in comparison to the bare WCF/BPA epoxy composites as shown in the Fig. 6.17. An investigation of load-deflection response of fabricated composites under impact loading is also performed and it was found that their variation is illustrated in the Fig. 6.18. It is evident that the fluctuation of load versus deflection graph of CuO treated composites is cubic in form, as opposed to sample-1 (plain WCF/BPA epoxy composites). The load supported by the samples increases initially as the deflection increases, then beyond a certain point the load decreases as the material reaches its ultimate point and moves toward the point of fracture, eventually tending to zero due to fracture of samples. Samples without CuO nanostructures sustained least value of load and it increases on increasing the growth of CuO nanostructures.

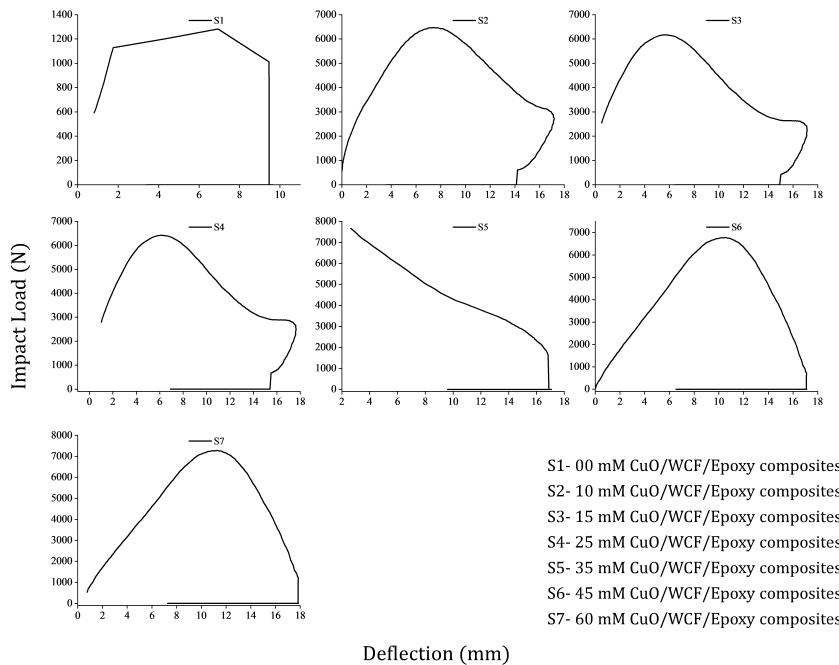


Figure 6.18: Investigation of load-deflection response of composites under impact loading

### 6.5.1.3 Fractured surface topography

As-fabricated CuO/WCF/BPA epoxy resin hybrid composite sample's fractured surface topography and crack debris are shown in Fig. 6.19. The all fracture mechanisms seen during the FESEM examination of tested samples has been reported in this section. Generally, the fracture mechanisms in case of plain CFRP such as sample-1 consist of fiber breakage, matrix cracking and delamination as shown in Fig. 6.19(a and b). However other failure modes such as fiber pullout, crack debris and de-bonding can be seen for hybrid composites such as sample having improved interfacial adhesion due to fiber modification as illustrated in Fig. 6.19(c-e). Further analysis of hybrid samples results into the information of other failure modes such as nanostructure pullout, nanostructure breakage, as well as nanostructure debonding due to presence of CuO nanostructures at the interface of CFRP as illustrated in Fig. 6.19(f-h). The fracture point primarily provides information on fiber breakage and delamination. Up until the fracture point was reached, the cracking interaction energy was thought to exist between the CuO nanostructure and the surface of the WCFs. The WCFs also absorbed delamination energy. Variations in impact energy absorption were caused by interactions between CuO nanostructure and CuO growth region zones on the surface of the WCFs. It has been demonstrated that the cross-linking density rises with the molar density of CuO. The impact energy absorption relationship is as follows:

$$E_{total} = E_{rebound} + E_{absorbed} \quad (6.18)$$

Brittle composites have very little rebound energy. As a result, almost all of the energy was absorbed by the resin and fibers. In low-velocity impacts, the absorbed energy also includes the bending deformation and delamination energy. Due to the brittle nature of the composite, the majority of energy was absorbed by fiber breakage, with the impact absorbing the remaining energies (such as global deformation, delamination, and shear-out energy). The impact's outward area in each case was essentially the same. The most notable difference was that the holes in the composites generated at higher molar CuO concentrations were shaped like arches. The straightforward WCF/BPA epoxy composites were straight down-penetrated. On the other hand, the impact-damaged region of the composites produced at higher molar concentrations of CuO resembled an erupted volcano. The impact zone was cross-linked by the nearby CuO nanostructures, which was the cause of this. When the CuO nanostructures reached up to the cracks, the bonding energy between the WCFs and CuO nanostructures was greater than the deformation energy of the epoxy resin. As a result, the CuO nanostructures absorbed more energy despite the modest size of the dam-

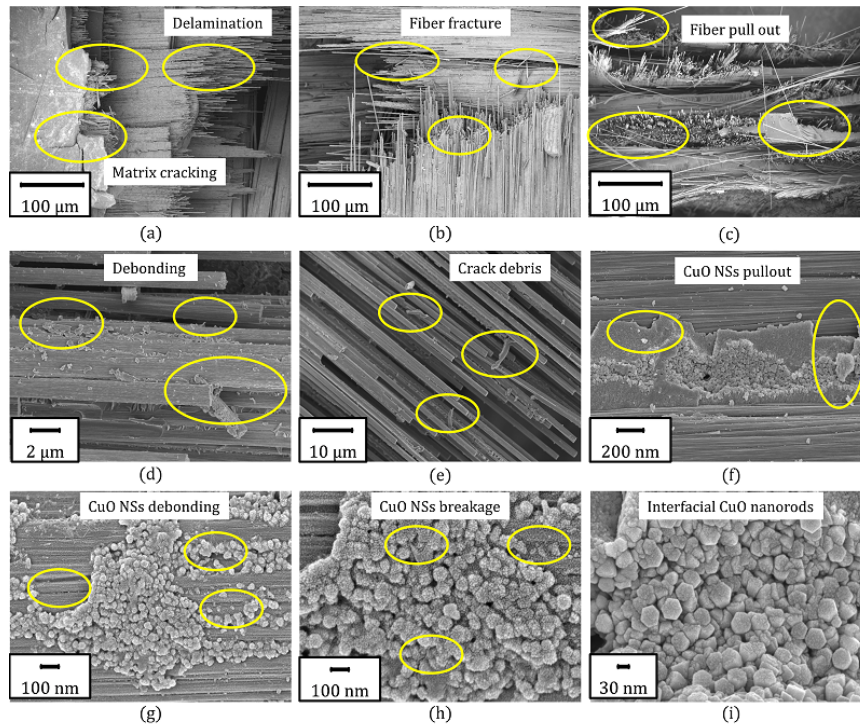


Figure 6.19: Fracture surface topography showing different fracture mechanism and interfacial interaction under impact loading

aged area. Impact energy is absorbed to a greater extent in CuO composites with larger molar concentrations. Different nanostructure failure mechanisms, such as debonding and breakage, were observed, confirming an improvement in the interfacial characteristics of the produced composites. The CuO nanostructure traces are seen as a result of the FESEM investigation of the damaged surface of the hybrid CFRP samples (S2-S7) as illustrated in Fig. 6.19(f-i) and the enlarged view of presence of CuO nanorods at the interface of the failure zone of hybrid composite sample is depicted in Fig. 6.19(i). It can be concluded that the presence of CuO nanostructures on the WCF and crosslinking of CuO at the interfacial area improved the mechanical properties of the fabricated hybrid composite samples.

### 6.5.2 Tensile and In-plane shear strength

Tensile strength measurements were performed to compare the stiffness of WCF/BPA epoxy resin composites with WCF/CuO/BPA epoxy resin composites based on CuO concentration and morphologies. Tensile tests were conducted on the specimens using Instron

5982 universal testing apparatus with a 100 kN maximum load. The pictorial representation of micro universal testing machine set up used for tensile testing is illustrated in Fig. 6.20(a). In this set up, a hydraulic wedge gripping has been used for effective gripping of the fabricated specimen as shown in Fig. 6.20(b). Further, a schematic representation of load direction, gauge length and location of clamped extensometer is illustrated in Fig. 6.20(c). The specimen showing fractured surface of CFRP under tensile loading is also depicted in Fig. 6.20(d). Five specimens from each sample category were tested and ana-

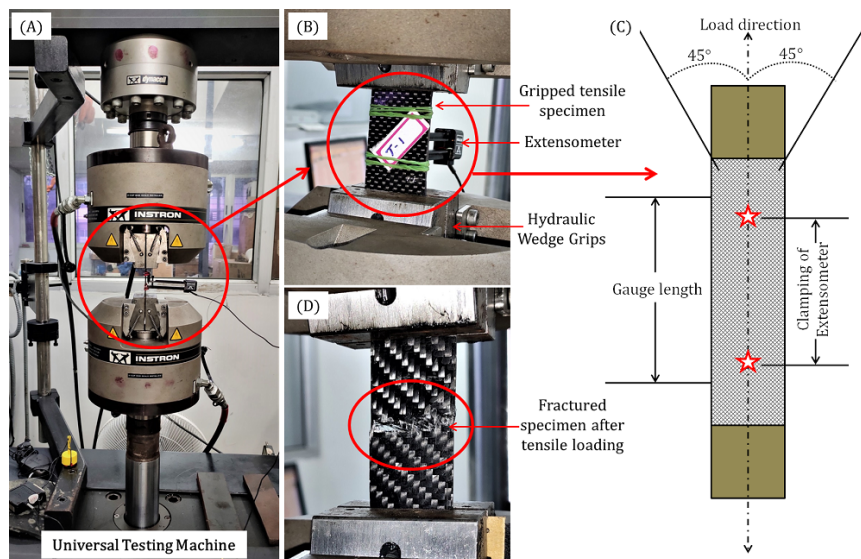


Figure 6.20: (a) Micro-universal testing machine set up used for tensile testing, (b) enlarged view of gripped specimen and location of extensometer, (c) schematic representation of load direction and gauge length and (d) fractured specimen after tensile loading

lyzed in accordance with ASTM D3039 standards at a displacement rate of 1 mm/min. The test average values are taken into consideration for further analysis. Figure 6.21 shows the average values for tensile strength, elastic modulus, and in-plane shear strength for all the manufactured composite samples in each category. Because the fibers and epoxy had less interfacial contacts, the plain WCF/BPA epoxy resin composite samples had the lowest tensile strength, elastic modulus, and in-plane shear strength values. As CuO nanostructures were embedded on the surface of WCFs, the surface area of the fibers increased. Figure 6.22 shows the tensile stress-strain curves for the WCF/BPA epoxy resin composite and the WCF/CuO/BPA epoxy resin composite. The increments show how much the WCF, CuO nanostructures, and epoxy resin interacts with one another. These results show the general upward trend in strength and modulus values and showed that greater CuO nanostructure

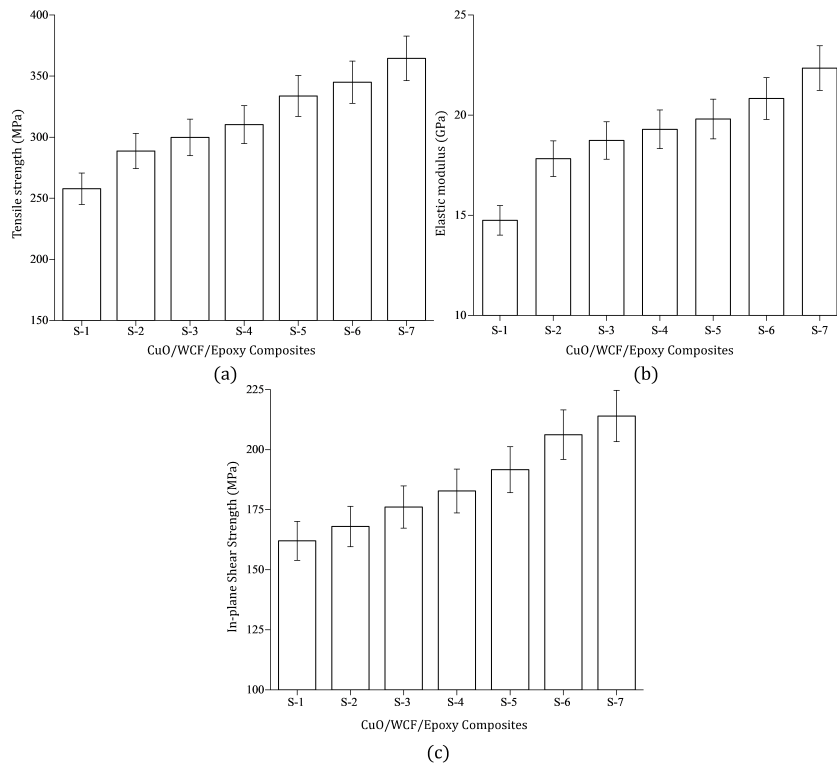


Figure 6.21: Variation of (a) Tensile strength, (b) Elastic modulus and (c) In-plane shear strength values of composite samples

growth produced superior outcomes. Previous research has demonstrated that in brittle composites, external impact energy leads to fiber breakage [37]. Increased load sharing between CuO nanostructures and fibers as a result of faster CuO nanostructure development rates raises the energy needed to break fibers. The maximum elastic modulus (52 %) and tensile strength (42 %) were attained by composites containing CuO nanostructures generated with 8 seeding cycles and 12 hours of development time at a growth solution concentration of 60 mM. The surface functional groups of WCFs, such as hydroxyl, carboxyl, and carbonyl, interacted with the CuO nanostructures and the epoxide groups of the BPA epoxy resin, enhancing the interfacial interaction, as was previously mentioned. The additional interfacial connections significantly increased the composite's overall tensile strength. When comparing the fabricated CuO/WCF/BPA epoxy resin composite samples to bare WCF/BPA epoxy composite samples, the in-plane shear resistance of the composite samples as fabricated was also calculated. It was found that the in-plane shear strength gradually increases on increasing the molar concentrations of CuO nanostructures. As seen in Fig. 6.21, the highest increase in in-plane shear strength of 32 % found at higher mo-



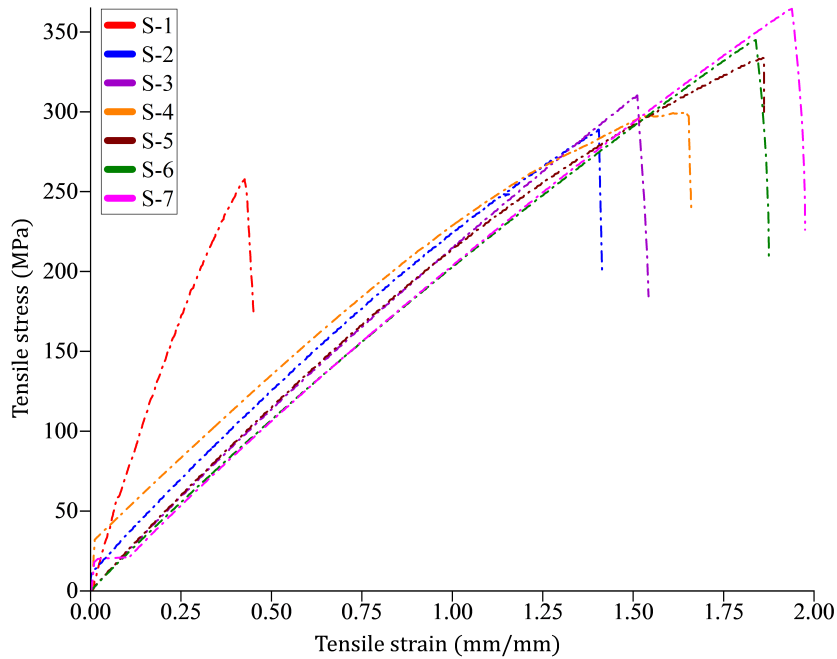


Figure 6.22: Stress-strain plot of the WCF/BPA and WCF/CuO/BPA epoxy resin composite

lar concentrations. Additionally, it has been demonstrated that the hydrothermal growth process enhances the mechanical characteristics of large-scale composites. The results of the tensile test show that the network of CuO nanostructures improved the interfacial properties and increased the interfacial shear strength because it improved load transmission from the matrix to the WCFs in comparison to plain CFRP composites modified by micro and nanofillers as reported in literatures [345, 346]. The average, standard deviation, and coefficient of variance of tensile test results such as tensile strength, elastic modulus and in-plane shear strength of each sample have been tabulated in the Table 6.5. The tabulated data reveals that, the coefficient of variance is around 5% which shows lower level of dispersion of the test results and good performance of the method applied. Hence the estimated values of the mechanical properties of as fabricated CFRP composites are more precise.

Table 6.5: Average, standard deviation, and coefficient of variance of each test results

Sample	Impact energy (J)			Tensile strength (MPa)			Elastic modulus (GPa)			In-plane shear strength (MPa)		
	$\mu$	$\sigma$	C.V (%)	$\mu$	$\sigma$	C.V (%)	$\mu$	$\sigma$	C.V (%)	$\mu$	$\sigma$	C.V (%)
S-1	4.84	0.25	5.16	257.78	12.89	5.01	14.75	0.74	5.01	162	8.1	5.00
S-2	7.18	0.36	5.1	288.69	14.43	4.98	17.83	0.89	5.00	168	8.4	5.01
S-3	7.26	0.37	5.09	299.82	15.01	5.00	18.74	0.94	4.99	176.11	8.82	5.01
S-4	7.42	0.37	4.98	310.31	15.52	4.99	19.29	0.96	5.00	182.78	9.14	4.99
S-5	7.57	0.38	5.02	333.75	16.69	5.01	19.81	0.99	5.01	191.67	9.58	4.98
S-6	7.96	0.40	5.02	345.01	17.25	4.98	20.83	1.04	4.98	206.22	10.31	4.99
S-7	8.45	0.42	4.97	364.52	18.23	5.00	22.35	1.12	5.01	214	10.7	5.00

## 6.6 Comparison on the effect of ZnO and CuO nanostructures

The comparison between grown CuO and ZnO nanostructures on thermal and mechanical properties of CFRP composites are included in this section. The effect of growth on CuO and ZnO nanostructures has great impact on the thermal and mechanical of the fabricated composites. The comparison on the effect of ZnO and CuO nanostructures is illustrated in the Table 6.6. From Table 6.6, it can be seen that each of the metal-oxide NSs has its own superiority in terms of properties. The elastic modulus, in-plane shear strength of CuO nanostructured CFRP composites are higher in comparison to ZnO nanostructured CFRP composites. Nevertheless, the percentage increase in impact energy absorption, tensile strength and TGA thermal degradation pattern (weight loss) of ZnO nanostructured CFRP composites are better than the CuO nanostructured CFRP composites. Hence, both the metal-oxide nanostructures can be used for the enhancement of mechanical and thermal properties of CFRP composites based on the requirement. However, the growth phenomenon and required process parameters for the CuO NSs have negative impacts in terms of large seeding cycles, high growth duration and high temperature. However, the occurrence of agglomeration in CuO NSs on WCF was higher, due to which the vertically aligned nanostructures were not grown. On analyzing each factors of both the nanostructured CFRP composites, the ZnO nanostructured CFRP composites are better in terms of ease of synthesis, less time consuming, high impact energy absorption capacity, high thermal stability, high tensile strength and moderate elastic modulus and in-plane shear strength.

Table 6.6: Properties of as fabricated ZnO and CuO nanostructured CFRP composites

S.no.	Concentration (mM)		Impact energy (J)		Tensile strength(MPa)		Elastic modulus(GPa)		In-plane shear strength(MPa)		Weight loss(%)	
	CuO	ZnO	CuO	ZnO	CuO	ZnO	CuO	ZnO	CuO	ZnO	CuO	ZnO
1	00	00	4.84	4.32	257.78	257.78	14.75	14.75	162	159.24	6.66	6.66
2	10	10	7.18	6.13	288.69	299.82	17.83	16.24	168	163.94	6.64	6.5
3	15	30	7.26	6.4	299.82	337.92	18.74	18.18	176.11	167.16	4.74	1.4
4	25	50	7.42	7.01	310.31	354.72	19.29	19.47	182.78	168.36	4.27	2.65
5	35	70	7.57	7.62	333.75	388.16	19.81	21.6	191.67	192.35	3.35	2.86
6	45		7.96		345.01		20.83		206.22		6.33	
7	60		8.45		364.52		22.35		214		5.22	

## 6.7 Summary

To enhance the interfacial adhesion of the basic WCF/BPA epoxy resin composites, CuO nanostructures were successfully produced on the surface of woven carbon fiber using a low-temperature hydrothermal method. The fabrication of WCF/CuO/BPA epoxy resin hierarchical composites was done using the vacuum bagging technique. Prior to creating the CuO nanostructures on the surface of the fibers, the WCF was subjected to surface hydrolysis and an ion-exchange technique to add carboxylic acid functional groups to the surface of the WCFs. The interactions of WCF and CuO nanostructure, surface hydrolysis of the WCF as well as the development of CuO nanostructures on the surface of the WCFs, were all examined using FT-IR. The XRD results showed the expected peaks for crystalline monoclinic CuO nanostructures, demonstrating that CuO had successfully grown on the surface of the WCF. The intensity of the crystalline CuO peaks increases as the CuO nanostructure develops further. The peak corresponding to the (101) crystal plane became stronger as more CuO nanostructures grew in the c-axis direction. A FESEM analysis revealed that the number of seeding cycles, the length of the hydrothermal treatment, and the CuO concentration all had an impact on the development of the CuO nanostructures. The CuO nanostructure did not spread even at high concentrations and numerous seeding cycles over small treatment durations. The CuO nanostructures successfully formed after 8 seeding cycles and a 12-hours treatment period. The high density of ultrafine CuO nanostructures growth took place when the treatment period was 12-hours long, the molar concentration was 60 mM, and there were 8 seeding cycles used. The heat behavior and weight change phenomenon of formed CuO nanostructures on the WCF were characterized using TGA analysis. The CuO-modified WCF samples have higher residual weight and better thermal stability than untreated WCF. The density of developed CuO on WCF is demonstrated by

elemental mapping of the sample, and the composition of CuO nanostructures formed on WCF samples is determined using EDS analysis. It is highly challenging to observe micro-quantities of  $Cu^{3+}$  through XRD examinations. The most effective method for identifying this minute amount of charge coexisting with  $Cu^{3+}$  in CuO is photoelectron spectroscopy. CuO-modified WCF's surface chemistry and composition were examined using XPS measurements. Analysis of the fiber volume fraction, CuO nanostructure fraction, and void content has been performed to evaluate the efficacy of the constructed composite samples. It was discovered that, at constant fiber volume fraction, the fraction of CuO nanostructures increases as the molar concentration of the growth precursor increases. Because of the low void content and improved interfacial characteristics, the quality of the produced composite increases at high concentrations of CuO nanostructures. The mechanical characteristics of CuO/WCF/BPA epoxy resin hybrid composites were studied using drop weight impact testing and tensile testing. The experiment results show that the produced CuO nanostructures boost energy absorption of the created hierarchical composite. The impact energy diffuses over the interfacial area due to cross-linked networks. CuO nanostructures were discovered to increase interfacial strength and improve load transmission. The WCF/CuO/BPA epoxy resin composite's impact energy absorptions from impact testing were used to calculate the perforation and penetration thresholds. The WCF/CuO/BPA epoxy resin composites had higher penetration limits than the WCF/BPA epoxy resin composites, and they got better as the CuO content increased. The impact energy absorbed by the composite with the most CuO growth (at 8 seeding cycles, 12 hours, and 60 mM) was 74.8 % higher than the impact energy absorbed by the composites made of plain WCF/BPA epoxy resin, and the time it took to fracture was reduced by 166 %. The WCF/CuO/BPA epoxy resin composites had greater tensile strengths and elastic moduli than the CuO-free composites. The CuO-modified WCF composite, developed at 8 seeding cycles, 12 h growth treatments, and 60 mM molar concentration, produced 42 % increase in tensile strength, 52 % increase in elastic modulus, and 32 % increase of In-plane shear strength when compared to bare WCF/BPA epoxy resin composite. Thus, it can be concluded that the improved interfacial contact between the surface-functionalized WCF, CuO, and BPA epoxy resin increased the mechanical and thermal properties of the composites, expanding their application in the automotive and aerospace industries.

# 7

## Conclusion and Future Scope

The present thesis work investigates the development of high performance carbon fiber reinforced polymer composites using metal oxide NSs as a secondary reinforcement. In this regard, the synthesis of metal-oxide NSs on WCF surface using solution phase synthesis and fabrication of their hybrid composites have been conducted. The controlled growth of NSs on carbon fiber fabric is achieved by tuning the hydrothermal process parameters such as pH, growth temperature, growth time, number of seeding cycles and molar concentration during synthesis of metal-oxide nanostructured fabrics. Extensive characterizations of WCF samples modified with metal-oxide NSs have been performed to study the formation of functional groups along with metal-oxides in order to enhance the mechanical performances of the composites. The influence of nanostructured interphase of hybrid CFRP composites on mechanical properties such as impact strength, tensile strength, elastic modulus and in-plane shear strength have been examined to assess the performance of composites for varied applications. The introduction of two prominent metal-oxides such as ZnO and CuO in the development of nanostructured CFRP has been found an effective strategy to develop enhanced mechanical attributes of CFRP. The mechanical properties such as impact strength and tensile strength of CFRP composites increase on increasing the molar concentration of the metal-oxide NSs. Out of both the nanostructured CFRP composites,

the ZnO-modified CFRP composites have better thermal and mechanical characteristics due to better interfacial interaction caused by morphological variation of ZnO NSs grown on WCF and their interaction with polymer matrix. However some properties are good in CuO- modified CFRP composites. Hence a holistic comparison between thermal and mechanical properties of CuO and ZnO nanostructured CFRP composites are tabulated in the Table 6.5 and on that basis it is concluded which one has more advantages.

## **7.1 The key conclusion of the thesis**

On the basis of theoretical and experimental analysis key conclusions of the thesis are as follows:

### **7.1.1 Hydrothermal Growth of ZnO nanostructures on woven carbon fiber and effect of synthesis parameters on morphology**

- Successful growth of ZnO NSs on woven carbon fiber fabrics were achieved through seed-assisted hydrothermal synthesis technique.
- The variation and control in size and shapes of the ZnO NSs can be done by varying synthesis conditions such as pH, molar concentration, time and temperature.
- Different NSs such as nanorods, nanowires, nanoflakes, nanoflowers and nanopallets were developed by varying the pH of precursor solution, molar concentration, growth duration and growth temperature.
- The pH commands the morphological structure of ZnO NSs and the nucleation density of ZnO NSs was directed by molar concentration of precursor solution.
- The aspect ratio of the grown ZnO NSs can be adjusted by varying the synthesis time and growth temperature but growth temperature also influences the morphology.
- The varied shapes and size of ZnO NSs can be grafted on woven carbon fibers by hydrothermal technique and their structures and morphologies can be directed simply by adjusting the above discussed parameters to achieve desired NSs for the potential applications.

### 7.1.2 One-step microwave-assisted hydrothermal synthesis of ZnO nanostructures on WCF and their characterization

- One step rapid growth of ZnO NSs on carbon fiber fabric using microwave-assisted chemical bath deposition technique has been successfully achieved which is quicker than the chemical bath deposition process.
- Rapid heating of growth solution consisting of  $[Zn(NH_3)_4]^{2+}$  nuclei under microwave irradiation causes production of ZnO NSs by forced hydrolysis.
- The impact of different microwave synthesis parameters such as salt concentration, microwave duration and microwave power have great influence on morphologies and growth rates of the ZnO nanorods.
- The distributions and orientations of NSs can be optimized by tuning these process parameters and their reaction with growth solution.
- The impact of different kind of growth solution for the well distributed and uniform growth of ZnO NSs on carbon fiber fabric provides a basis to effective functionalization of fabrics.
- The FESEM result shows that NSs are irregular in shape and size but have smooth surface and the size of generated ZnO NSs were around 300-2300 nm in longitudinal direction and 200-1100 nm in lateral direction.
- The preferred orientation of ZnO growth is in the [1 0 1] direction, which is highest for nanoflowers, according to XRD and texture coefficient results.
- The optical characteristics of the samples reveal that nanopetals have a big band gap and nanoflowers have a small band gap which indicates greater size crystals possess smaller band gaps.
- The findings of refractive index, extinction coefficient, dielectric constant, Urbach energy, and optical conductivity of grown ZnO NSs on WCF surface indicates that they have the potential to be employed in high performance nanocomposites for optoelectronics and photonics applications such as sensors, emitters, catalysts, active medium, and electrodes.

- The potential of developed ZnO NSs on WCF may be expanded in energy harvesting devices, bio-sensing, medicinal implementations, and environmental pollution sectors due to its outstanding morphological structure and enhanced surface to volume ratio.

### **7.1.3 Development of ZnO-modified WCF reinforced epoxy resin composites and their mechanical characterizations**

- The successful growth of ZnO NSs was realized on the surface of WCF using a low-temperature hydrothermal approach as a technique to improve the interfacial reinforcement of the plain WCF polymer composites.
- The carboxylic acid functional groups on the surface of the WCFs were developed by surface hydrolysis to promote the adherence of ZnO to the base fibers.
- The number of seeding cycles, hydrothermal treatment period, and molar concentration all influenced the growth of the ZnO NSs on WCF. Even at high concentrations and multiple seeding cycles, the NSs did not grow due to short treatment duration.
- The effective growth of ZnO NSs was achieved at 8 seeding cycles and 8h growth duration. However, high density and uniform distribution of ZnO NSs were achieved at 8 seeding cycle, 8h growth duration and 70mM molar concentration.
- The improvement in thermal stability and % weight change were seen on ZnO-modified WCF samples due to fine growth of ZnO NSs.
- The cross-linked networks of ZnO-WCF-epoxy in hybrid composite diffuse the energy over the interface area which results into higher energy absorption in drop weight impact testing.
- The penetration limits of the hybrid composites were higher than those of the plain composites because of effective load transfer at interface, and it improved as the ZnO molar concentration increased.
- The impact energy absorbed by the ZnO-decorated composite with the maximum ZnO growth was 76% higher than the impact energy absorbed by the plain WCF polymer composites.



- The tensile strength and elastic modulus of the hybrid composites were higher than those of the plain composites. In comparison to plain composites, the maximum ZnO molar concentration produced a 48.63% increase in tensile strength, 46.44% increase in elastic modulus, and 20.79% increase in in-plane shear strength.
- The mechanical and thermal properties of the composites were improved as a result of improved interfacial contact between the surface-functionalized WCF, ZnO, and BPA epoxy resin which provides basis for potential structural applications.

#### **7.1.4 Improvement of interfacial adhesion of CuO nanostructured carbon fiber reinforced polymer composites**

- To enhance the interfacial adhesion of the basic WCF/BPA epoxy resin composites, CuO NSs were successfully produced on the surface of woven carbon fiber using a low-temperature hydrothermal method.
- The number of seeding cycles, the length of the hydrothermal treatment, and the CuO concentration all had an impact on the development of the CuO NSs. However, the high density of ultrafine CuO NSs growth took place when the treatment period was 12-hours long, the molar concentration was 60 mM, and there were 8 seeding cycles used.
- The heat behavior and weight change phenomenon of formed CuO NSs on the WCF characterized by TGA analysis revealed that the CuO-modified WCF samples have higher residual weight and better thermal stability than untreated WCF.
- It was discovered that, at constant fiber volume fraction, the fraction of CuO NSs increases as the molar concentration of the growth precursor increases and due to low void content and improved interfacial characteristics, the quality of the produced composite increases at high concentrations of CuO NSs.
- The drop weight impact testing results showed that the produced CuO NSs boost energy absorption of the created hierarchical composite because the impact energy diffuses over the interfacial area due to cross-linked networks.
- The WCF/CuO/BPA epoxy resin composites have higher penetration limits than the WCF/BPA epoxy resin composites due to improved interfacial strength and load transmission, and it increases on increasing CuO content.

- The impact energy absorbed by the composite with the most CuO growth (at 8 seeding cycles, 12 hours, and 60 mM) was 74.8 % higher than the impact energy absorbed by the composites made of plain WCF/BPA epoxy resin, and the time it took to fracture was reduced by 166 %.
- The CuO-modified WCF composite developed at 8 seeding cycles, 12 h growth treatments, and 60 mM molar concentration achieved 42 % increase in tensile strength, 52 % increase in elastic modulus, and 32 % increase of in-plane shear strength when compared to bare WCF/BPA epoxy resin composite.
- It can be concluded that the improved interfacial contact between the surface-functionalized WCF, CuO, and BPA epoxy resin increased the mechanical and thermal properties of the composites, expanding their application in the automotive and aerospace industries.

## 7.2 Contribution

The main contributions from the presented thesis work are as follows:

- The functionalization of carbon fiber textiles by metal-oxide nanostructures deposition using seed-assisted hydrothermal synthesis and microwave-assisted hydrothermal techniques opens new insights into designing nanostructured interphase in order to develop high performance metal-oxide nanostructured carbon fiber reinforced polymer composites.
- The idea is that strengthening properties of CFRP composites can be controlled more when functionalized carbon fiber is used instead of plain carbon fiber for required applications.
- The CFRP composites made with functionalized carbon fiber have better interfacial interaction and load transfer mechanism which enhances their mechanical properties.
- Development of metal-oxide nanostructured carbon fiber fabrics is cost effective better substitute to the plain carbon fiber and their subsequent nanocomposites for advanced applications.
- The introduction of two prominent metal-oxides such as ZnO and CuO in the development of nanostructured CFRP has been found an effective strategy to develop enhanced mechanical attributes of CFRP.

- The mechanical properties such as impact strength and tensile strength of CFRP composites increase on increasing the molar concentration of the metal-oxide NSs. However the highest value has been achieved for ZnO-modified CFRP composite having 70 mM concentration.
- Out of both the nanostructured CFRP composites, the ZnO-modified CFRP composites have better mechanical characteristics due to better interfacial interaction caused by morphological variation of ZnO NSs grown on WCF and their interaction with polymer matrix.
- In addition, multifunctional structural materials with integrated damage detection capabilities can be envisaged by exploiting the piezoelectric properties of the ZnO NSs obtained by this scalable functionalization approach.
- The ZnO-modified carbon fiber fabrics have proven to increase surface functionalization which enhances crosslinking epoxides and their adherence capabilities with carbon fiber for strong interfacial bonding of WCF with polymer matrix.
- The thermal stability of metal-oxide nanostructured CFRP composites has been increased due to better interfacial strength and effective bonding of metal-oxides with WCF and polymer matrix. Hence the weight loss of the nanostructured CFRP composites is less and it decreases on increasing the molar concentration of metal-oxides.

Finally, it can be concluded that each of the metal-oxide NSs has its own superiority in terms of properties. The percentage increase in impact energy absorption, tensile strength and TGA thermal degradation pattern (weight loss) of ZnO nanostructured CFRP composites are better than the CuO nanostructured CFRP composites. Nevertheless, the elastic modulus and in-plane shear strength of CuO nanostructured CFRP composites are higher in comparison to ZnO nanostructured CFRP composites. Hence, both the metal-oxide nanostructures can be used for the enhancement of mechanical and thermal properties of CFRP composites based on the requirement. However, the growth phenomenon and required process parameters for the CuO NSs have negative impacts in terms of large seeding cycles, high growth duration and high temperature. However, the occurrence of agglomeration in CuO NSs on WCF was higher, due to which the vertically aligned nanostructures were not grown. On analyzing each factors of both the nanostructured CFRP composites, the ZnO nanostructured CFRP composites are better in terms of ease of synthesis, less time consuming, high impact energy absorption capacity, high thermal stability, high tensile strength and moderate elastic modulus and in-plane shear strength.

### 7.3 Future Work

As it can be clearly discovered, the prominent usages of nanocomposites are huge, consisting of evolution of advance materials and the quality advancement of regarded components like sensors, cells and depositions. Still there is least application of nanocomposites in industries but advancements of these material from research to industry is growing and in coming few years it is expected to be extensive. The following work can be explored for the further research on this topic:

- The advanced simulation techniques such as molecular dynamic simulation to study the surface chemistry and growth phenomenon involved in synthesis and size control of metal oxide NSs on carbon fiber fabrics can be conducted.
- Metal-oxide functionalized carbon fiber has genuinely shown to be a more effective alternative for secondary reinforcement in the plain carbon fiber polymer composites and can be investigated for other reinforcement and dopant materials.
- The investigation toward scaling up and economical feasibility about the production of metal oxide NSs for application on washable antimicrobial fabrics could be done.
- Mathematical modeling and multi-scale modeling for the failure analysis of nanostructured CFRP composites can be conducted to understand the mechanics of metal-oxide interactions at the interphase in mechanical strengthening of composite.
- The effect of metal-oxide functionalized carbon fiber is limited to strength enhancement and can be used for other applications areas.
- Development of hybrid nanocomposites by combination of metal-oxides with other transition metals for controlling properties such as band gap, ferromagnetism, electrical conductivity and others for advanced applications can be explored.
- The evident correlations between the factors affecting the performance of nanostructured CFRP composites such as size and density of the grown nanostructures and best suited morphology of ZnO NSs have not been deduced analytically. It can be developed by mathematical modeling or simulation of the current work in a future research.
- Investigation of machinability of developed metal-oxide nanostructured CFRP composites during high speed machining and cryogenic machining can be conducted.

## References

- [1] A. Janotti, C. G. Van de Walle, Fundamentals of zinc oxide as a semiconductor, Reports on progress in physics 72 (2009) 126501.
- [2] S. Brintha, M. Ajitha, Synthesis and characterization of zno nanoparticles via aqueous solution, sol-gel and hydrothermal methods, IOSR J Appl Chem 8 (2015) 66–72.
- [3] S. H. Ko, D. Lee, H. W. Kang, K. H. Nam, J. Y. Yeo, S. J. Hong, C. P. Grigoropoulos, H. J. Sung, Nanoforest of hydrothermally grown hierarchical zno nanowires for a high efficiency dye-sensitized solar cell, Nano letters 11 (2011) 666–671.
- [4] F. Wang, X. Qin, Z. Guo, Y. Meng, L. Yang, Y. Ming, Hydrothermal synthesis of dumbbell-shaped zno microstructures, Ceramics International 39 (2013) 8969–8973.
- [5] S. Liang, L. Zhu, G. Gai, Y. Yao, J. Huang, X. Ji, X. Zhou, D. Zhang, P. Zhang, Synthesis of morphology-controlled zno microstructures via a microwave-assisted hydrothermal method and their gas-sensing property, Ultrasonics sonochemistry 21 (2014) 1335–1342.
- [6] I. M. Daniel, O. Ishai, I. M. Daniel, I. Daniel, Engineering mechanics of composite materials, volume 1994, Oxford university press New York, 2006.

- [7] J. A. Brydson, *Plastics materials*, Elsevier, 1999.
- [8] O. Faruk, A. K. Bledzki, H.-P. Fink, M. Sain, Progress report on natural fiber reinforced composites, *Macromolecular Materials and Engineering* 299 (2014) 9–26.
- [9] Y. Lin, G. Ehlert, H. A. Sodano, Increased interface strength in carbon fiber composites through a zno nanowire interphase, *Advanced functional materials* 19 (2009) 2654–2660.
- [10] C. Kazmierski, Growth opportunities in global composites industry, 2012–2017, *Composites* (2012) 21–23.
- [11] P. K. Mallick, *Fiber-reinforced composites: materials, manufacturing, and design*, CRC press, 2007.
- [12] M. Kabir, H. Wang, K. Lau, F. Cardona, Chemical treatments on plant-based natural fibre reinforced polymer composites: An overview, *Composites Part B: Engineering* 43 (2012) 2883–2892.
- [13] T. Sathishkumar, P. Navaneethakrishnan, S. Shankar, R. Rajasekar, Mechanical properties and water absorption of short snake grass fiber reinforced isophthallic polyester composites, *Fibers and Polymers* 15 (2014) 1927–1934.
- [14] H. Lee, I. Ohsawa, J. Takahashi, Effect of plasma surface treatment of recycled carbon fiber on carbon fiber-reinforced plastics (cfrp) interfacial properties, *Applied Surface Science* 328 (2015) 241–246.
- [15] L. Yusriah, S. Sapuan, E. S. Zainudin, M. Mariatti, Characterization of physical, mechanical, thermal and morphological properties of agro-waste betel nut (areca catechu) husk fibre, *Journal of Cleaner Production* 72 (2014) 174–180.

- [16] M. Chandrasekar, M. Ishak, S. Sapuan, Z. Leman, M. Jawaid, A review on the characterisation of natural fibres and their composites after alkali treatment and water absorption, *Plastics, Rubber and Composites* 46 (2017) 119–136.
- [17] E.-s. Lee, C.-h. Lee, Y.-S. Chun, C.-j. Han, D.-S. Lim, Effect of hydrogen plasma-mediated surface modification of carbon fibers on the mechanical properties of carbon-fiber-reinforced polyetherimide composites, *Composites Part B: Engineering* 116 (2017) 451–458.
- [18] K. Mizukami, Y. Mizutani, A. Todoroki, Y. Suzuki, Detection of in-plane and out-of-plane fiber waviness in unidirectional carbon fiber reinforced composites using eddy current testing, *Composites Part B: Engineering* 86 (2016) 84–94.
- [19] C. Wu, Y. Gu, L. Luo, P. Xu, S. Wang, M. Li, Z. Zhang, Influences of in-plane and out-of-plane fiber waviness on mechanical properties of carbon fiber composite laminate, *Journal of reinforced plastics and composites* 37 (2018) 877–891.
- [20] S. Luo, W. J. Van Ooij, Surface modification of textile fibers for improvement of adhesion to polymeric matrices: a review, *Journal of adhesion science and technology* 16 (2002) 1715–1735.
- [21] A. Sayam, A. M. Rahman, M. S. Rahman, S. A. Smriti, F. Ahmed, M. F. Rabbi, M. Hossain, M. O. Faruque, A review on carbon fiber-reinforced hierarchical composites: Mechanical performance, manufacturing process, structural applications and allied challenges, *Carbon Letters* 32 (2022) 1173–1205.
- [22] P. K. Gangineni, S. Yandrapu, S. K. Ghosh, A. Anand, R. K. Prusty, B. C. Ray, Mechanical behavior of graphene decorated carbon fiber reinforced polymer composites: An assessment of the influence of functional groups, *Composites Part A: Applied Science and Manufacturing* 122 (2019) 36–44.

- [23] J.-K. Kim, M.-L. Sham, Impact and delamination failure of woven-fabric composites, *Composites Science and Technology* 60 (2000) 745–761.
- [24] B. Vieille, V. M. Casado, C. Bouvet, About the impact behavior of woven-ply carbon fiber-reinforced thermoplastic-and thermosetting-composites: a comparative study, *Composite structures* 101 (2013) 9–21.
- [25] B. A. Newcomb, Processing, structure, and properties of carbon fibers, *Composites Part A: Applied Science and Manufacturing* 91 (2016) 262–282.
- [26] R. Atif, I. Shyha, F. Inam, Mechanical, thermal, and electrical properties of graphene-epoxy nanocomposites—a review, *Polymers* 8 (2016) 281.
- [27] M. Siegfried, C. Tola, M. Claes, S. V. Lomov, I. Verpoest, L. Gorbatikh, Impact and residual after impact properties of carbon fiber/epoxy composites modified with carbon nanotubes, *Composite Structures* 111 (2014) 488–496.
- [28] B. K. Deka, M. Mandal, T. K. Maji, Effect of nanoparticles on flammability, uv resistance, biodegradability, and chemical resistance of wood polymer nanocomposite, *Industrial & engineering chemistry research* 51 (2012) 11881–11891.
- [29] D. C. Davis, J. W. Wilkerson, J. Zhu, D. O. Ayewah, Improvements in mechanical properties of a carbon fiber epoxy composite using nanotube science and technology, *Composite Structures* 92 (2010) 2653–2662.
- [30] B.-X. Yang, K. P. Pramoda, G. Q. Xu, S. H. Goh, Mechanical reinforcement of polyethylene using polyethylene-grafted multiwalled carbon nanotubes, *Advanced Functional Materials* 17 (2007) 2062–2069.
- [31] C. Dong, Review of natural fibre-reinforced hybrid composites, *Journal of Reinforced Plastics and Composites* 37 (2018) 331–348.



- [32] S. U. Khan, C. Y. Li, N. A. Siddiqui, J.-K. Kim, Vibration damping characteristics of carbon fiber-reinforced composites containing multi-walled carbon nanotubes, *Composites science and technology* 71 (2011) 1486–1494.
- [33] K. Kong, B. K. Deka, J. W. Seo, Y.-B. Park, H. W. Park, Effect of cuo nanostructure morphology on the mechanical properties of cuo/woven carbon fiber/vinyl ester composites, *Composites Part A: Applied Science and Manufacturing* 78 (2015) 48–59.
- [34] S. Sharma, S. Lakkad, Effect of cnts growth on carbon fibers on the tensile strength of cnts grown carbon fiber-reinforced polymer matrix composites, *Composites Part A: Applied Science and Manufacturing* 42 (2011) 8–15.
- [35] R. Mathur, S. Chatterjee, B. Singh, Growth of carbon nanotubes on carbon fibre substrates to produce hybrid/phenolic composites with improved mechanical properties, *Composites Science and Technology* 68 (2008) 1608–1615.
- [36] B. K. Deka, K. Kong, J. Seo, D. Kim, Y.-B. Park, H. W. Park, Controlled growth of cuo nanowires on woven carbon fibers and effects on the mechanical properties of woven carbon fiber/polyester composites, *Composites Part A: Applied Science and Manufacturing* 69 (2015) 56–63.
- [37] K. Kong, B. K. Deka, S. K. Kwak, A. Oh, H. Kim, Y.-B. Park, H. W. Park, Processing and mechanical characterization of zno/polyester woven carbon–fiber composites with different zno concentrations, *Composites Part A: Applied Science and Manufacturing* 55 (2013) 152–160.
- [38] D. Scida, Z. Aboura, M. Benzeggagh, E. Bocherens, A micromechanics model for 3d elasticity and failure of woven-fibre composite materials, *Composites Science and Technology* 59 (1999) 505–517.

- [39] X. Wang, L. Chen, J. Wang, X. Li, Z. Zhang, A novel multiaxial three-dimensional woven preform: process and structure, *Journal of Reinforced Plastics and Composites* 37 (2018) 247–266.
- [40] J. Aizenberg, J. C. Weaver, M. S. Thanawala, V. C. Sundar, D. E. Morse, P. Fratzl, Skeleton of euptectella sp.: structural hierarchy from the nanoscale to the macroscale, *Science* 309 (2005) 275–278.
- [41] M. Knaupp, F. Baudach, J. Franck, G. Scharr, Impact and post-impact properties of cfrp laminates reinforced with rectangular z-pins, *Composites science and technology* 87 (2013) 218–223.
- [42] O. Gohardani, M. C. Elola, C. Elizetxea, Potential and prospective implementation of carbon nanotubes on next generation aircraft and space vehicles: A review of current and expected applications in aerospace sciences, *Progress in Aerospace Sciences* 70 (2014) 42–68.
- [43] H. Qian, E. S. Greenhalgh, M. S. Shaffer, A. Bismarck, Carbon nanotube-based hierarchical composites: a review, *Journal of Materials Chemistry* 20 (2010) 4751–4762.
- [44] T. Ramanathan, H. Liu, L. Brinson, Functionalized swnt/polymer nanocomposites for dramatic property improvement, *Journal of Polymer Science Part B: Polymer Physics* 43 (2005) 2269–2279.
- [45] G. J. Ehlert, H. A. Sodano, Zinc oxide nanowire interphase for enhanced interfacial strength in lightweight polymer fiber composites, *ACS applied materials & interfaces* 1 (2009) 1827–1833.
- [46] L.-G. Tang, J. L. Kardos, A review of methods for improving the interfacial adhesion between carbon fiber and polymer matrix, *Polymer composites* 18 (1997) 100–113.

- [47] S. Tiwari, J. Bijwe, Surface treatment of carbon fibers-a review, *Procedia Technology* 14 (2014) 505–512.
- [48] M. Sharma, S. Gao, E. Mäder, H. Sharma, L. Y. Wei, J. Bijwe, Carbon fiber surfaces and composite interphases, *Composites Science and Technology* 102 (2014) 35–50.
- [49] M. Yoozbashizadeh, M. Chartosias, C. Victorino, D. Decker, Investigation on the effect of process parameters in atmospheric pressure plasma treatment on carbon fiber reinforced polymer surfaces for bonding, *Materials and Manufacturing Processes* 34 (2019) 660–669.
- [50] N. Li, G. Liu, Z. Wang, J. Liang, X. Zhang, Effect of surface treatment on surface characteristics of carbon fibers and interfacial bonding of epoxy resin composites, *Fibers and Polymers* 15 (2014) 2395–2403.
- [51] S. Erden, K. K. Ho, S. Lamoriniere, A. F. Lee, H. Yildiz, A. Bismarck, Continuous atmospheric plasma oxidation of carbon fibres: influence on the fibre surface and bulk properties and adhesion to polyamide 12, *Plasma Chemistry and Plasma Processing* 30 (2010) 471–487.
- [52] D.-K. Kim, K.-H. An, Y. H. Bang, L.-K. Kwac, S.-Y. Oh, B.-J. Kim, Effects of electrochemical oxidation of carbon fibers on interfacial shear strength using a micro-bond method, *Carbon letters* 19 (2016) 32–39.
- [53] L. Xing, L. Liu, Y. Huang, D. Jiang, B. Jiang, J. He, Enhanced interfacial properties of domestic aramid fiber-12 via high energy gamma ray irradiation, *Composites Part B: Engineering* 69 (2015) 50–57.
- [54] D. Aleksendrić, P. Carlone, Introduction to composite materials, *Soft Comput. Des. Manuf. Compos. Mater* 2015 (2015) 1–5.

- [55] A. Alipour Skandani, N. Masghouni, S. W. Case, D. Leo, M. Al-Haik, Enhanced vibration damping of carbon fibers-zno nanorods hybrid composites, *Applied Physics Letters* 101 (2012) 073111.
- [56] Z. Dai, F. Shi, B. Zhang, M. Li, Z. Zhang, Effect of sizing on carbon fiber surface properties and fibers/epoxy interfacial adhesion, *Applied Surface Science* 257 (2011) 6980–6985.
- [57] R. Sager, P. Klein, D. Lagoudas, Q. Zhang, J. Liu, L. Dai, J. Baur, Effect of carbon nanotubes on the interfacial shear strength of t650 carbon fiber in an epoxy matrix, *Composites Science and Technology* 69 (2009) 898–904.
- [58] S. A. Song, C. K. Lee, Y. H. Bang, S. S. Kim, A novel coating method using zinc oxide nanorods to improve the interfacial shear strength between carbon fiber and a thermoplastic matrix, *Composites Science and Technology* 134 (2016) 106–114.
- [59] K. B. Singh, N. Gautam, D. Upadhyay, G. Abbas, M. Rizvi, G. Pandey, Morphology controlled biogenic fabrication of metal/metal oxide nanostructures using plant extract and their application in organic transformations, *Inorganic Chemistry Communications* (2022) 109855.
- [60] M. Haruta, Size-and support-dependency in the catalysis of gold, *Catalysis today* 36 (1997) 153–166.
- [61] R. S. Rai, V. Bajpai, Recent advances in zno nanostructures and their future perspective, *Advances in nano research* 11 (2021) 37–54.
- [62] Y. Dai, X. Gao, Q. Wang, X. Wan, C. Zhou, Y. Yang, Recent progress in heterogeneous metal and metal oxide catalysts for direct dehydrogenation of ethane and propane, *Chemical Society Reviews* 50 (2021) 5590–5630.

- [63] S. M. Dizaj, F. Lotfipour, M. Barzegar-Jalali, M. H. Zarrintan, K. Adibkia, Antimicrobial activity of the metals and metal oxide nanoparticles, *Materials Science and Engineering: C* 44 (2014) 278–284.
- [64] Y.-B. Hahn, Zinc oxide nanostructures and their applications, *Korean Journal of Chemical Engineering* 28 (2011) 1797–1813.
- [65] Y.-F. Sun, S.-B. Liu, F.-L. Meng, J.-Y. Liu, Z. Jin, L.-T. Kong, J.-H. Liu, Metal oxide nanostructures and their gas sensing properties: a review, *Sensors* 12 (2012) 2610–2631.
- [66] W. Li, H. Xu, H. Yu, T. Zhai, Q. Xu, X. Yang, J. Wang, B. Cao, Different morphologies of zno and their triethylamine sensing properties, *Journal of Alloys and Compounds* 706 (2017) 461–469.
- [67] Ü. Özgür, Y. I. Alivov, C. Liu, A. Teke, M. Reshchikov, S. Doğan, V. Avrutin, S.-J. Cho, Morkoç, H, A comprehensive review of zno materials and devices, *Journal of applied physics* 98 (2005) 11.
- [68] B. Meyer, D. Marx, Density-functional study of the structure and stability of zno surfaces, *Physical Review B* 67 (2003) 035403.
- [69] A. Waris, M. Din, A. Ali, M. Ali, S. Afridi, A. Baset, A. U. Khan, A comprehensive review of green synthesis of copper oxide nanoparticles and their diverse biomedical applications, *Inorganic Chemistry Communications* 123 (2021) 108369.
- [70] S. Chaudhary, D. Rohilla, A. Umar, N. Kaur, A. Shanavas, Synthesis and characterizations of luminescent copper oxide nanoparticles: toxicological profiling and sensing applications, *Ceramics International* 45 (2019) 15025–15035.

- [71] S. Jadhav, S. Gaikwad, M. Nimse, A. Rajbhoj, Copper oxide nanoparticles: synthesis, characterization and their antibacterial activity, *Journal of cluster science* 22 (2011) 121–129.
- [72] Y. Cai, F. Yang, L. Wu, Y. Shu, G. Qu, A. Fakhri, V. K. Gupta, Hydrothermal-ultrasonic synthesis of cuo nanorods and cuwo<sub>4</sub> nanoparticles for catalytic reduction, photocatalysis activity, and antibacterial properties, *Materials Chemistry and Physics* 258 (2021) 123919.
- [73] M. Mansournia, L. Ghaderi, Cu@ zno core-shell nanocomposites: Novel hydrothermal synthesis and enhancement in photocatalytic property, *Journal of Alloys and Compounds* 691 (2017) 171–177.
- [74] C. Yang, X. Su, J. Wang, X. Cao, S. Wang, L. Zhang, Facile microwave-assisted hydrothermal synthesis of varied-shaped cuo nanoparticles and their gas sensing properties, *Sensors and Actuators B: Chemical* 185 (2013) 159–165.
- [75] S. Jung, S. k. Park, H.-d. Ghim, D. Y. Lee, S. H. Yoo, Synergetic effect of cross-linking and interfacial interaction in carbon fiber reinforced thermoplastic to enhance its tensile strength by electron-beam irradiation, *Carbon Letters* 30 (2020) 165–175.
- [76] H. Kishi, N. Nakao, S. Kuwashiro, S. Matsuda, Carbon fiber reinforced thermoplastic composites from acrylic polymer matrices: Interfacial adhesion and physical properties, *Express Polymer Letters* 11 (2017) 334.
- [77] A. K. Pathak, M. Borah, A. Gupta, T. Yokozeki, S. R. Dhakate, Improved mechanical properties of carbon fiber/graphene oxide-epoxy hybrid composites, *Composites Science and Technology* 135 (2016) 28–38.

- [78] J. Zhang, V. S. Chevali, H. Wang, C.-H. Wang, Current status of carbon fibre and carbon fibre composites recycling, *Composites Part B: Engineering* 193 (2020) 108053.
- [79] A. Badakhsh, K.-H. An, B.-J. Kim, Enhanced surface energetics of cnt-grafted carbon fibers for superior electrical and mechanical properties in cfrps, *Polymers* 12 (2020) 1432.
- [80] T. K. Das, P. Ghosh, N. C. Das, Preparation, development, outcomes, and application versatility of carbon fiber-based polymer composites: a review, *Advanced Composites and Hybrid Materials* 2 (2019) 214–233.
- [81] E. Y. Choi, M. H. Kim, C. Kim, Fabrication of carbon fiber grafted with acyl chloride functionalized multi-walled carbon nanotubes for mechanical reinforcement of nylon 6, 6, *Composites Science and Technology* 178 (2019) 33–40.
- [82] I. Raya, H. H. Kzar, Z. H. Mahmoud, A. Al Ayub Ahmed, A. Z. Ibatova, E. Kianfar, A review of gas sensors based on carbon nanomaterial, *Carbon Letters* (2021) 1–26.
- [83] R. Patton, C. Pittman Jr, L. Wang, J. Hill, Vapor grown carbon fiber composites with epoxy and poly (phenylene sulfide) matrices, *Composites Part A: Applied Science and Manufacturing* 30 (1999) 1081–1091.
- [84] S. Jabeen, A. Kausar, B. Muhammad, S. Gul, M. Farooq, A review on polymeric nanocomposites of nanodiamond, carbon nanotube, and nanobifiller: Structure, preparation and properties, *Polymer-Plastics Technology and Engineering* 54 (2015) 1379–1409.
- [85] A. M. Ismail, F. M. AL-Oqla, M. Risby, S. Sapuan, On the enhancement of the fatigue fracture performance of polymer matrix composites by reinforcement with carbon nanotubes: a systematic review, *Carbon Letters* 32 (2022) 727–740.

- [86] Y. Yi, B. Wang, X. Liu, C. Li, Flexible piezoresistive strain sensor based on cnts-polymer composites: A brief review, *Carbon Letters* 32 (2022) 713–726.
- [87] E. Serag, A. El-Maghraby, A. El Nemr, Recent developments in the application of carbon-based nanomaterials in implantable and wearable enzyme-biofuel cells, *Carbon Letters* 32 (2022) 395–412.
- [88] R. S. Rai, V. Bajpai, Hydrothermally grown zno nss on bi-directional woven carbon fiber and effect of synthesis parameters on morphology, *Ceramics International* 47 (2021) 8208–8217.
- [89] X. Li, X. Jia, J. Yang, Y. Li, S. Wang, H. Song, Interfacial modification and tribological properties of zno nanosheet carbon fiber reinforced poly (hexahydrotriazine) composites, *Tribology International* 165 (2022) 107310.
- [90] B. Pant, G. P. Ojha, Y.-S. Kuk, O. H. Kwon, Y. W. Park, M. Park, Synthesis and characterization of zno-tio<sub>2</sub>/carbon fiber composite with enhanced photocatalytic properties, *Nanomaterials* 10 (2020) 1960.
- [91] N. Yang, J. Zeng, J. Xue, L. Zeng, Y. Zhao, Strong absorption and wide-frequency microwave absorption properties of the nanostructure zinc oxide/zinc/carbon fiber multilayer composites, *Journal of Alloys and Compounds* 735 (2018) 2212–2218.
- [92] U. Galan, Y. Lin, G. J. Ehlert, H. A. Sodano, Effect of zno nanowire morphology on the interfacial strength of nanowire coated carbon fibers, *Composites Science and Technology* 71 (2011) 946–954.
- [93] M. Pirhashemi, A. Habibi-Yangjeh, S. R. Pouran, Review on the criteria anticipated for the fabrication of highly efficient zno-based visible-light-driven photocatalysts, *Journal of industrial and engineering chemistry* 62 (2018) 1–25.



- [94] S. Xu, Z. L. Wang, One-dimensional zno nanostructures: solution growth and functional properties, *Nano Research* 4 (2011) 1013–1098.
- [95] S. Baruah, J. Dutta, Hydrothermal growth of zno nanostructures, *Science and technology of advanced materials* (2009).
- [96] A. Król, P. Pomastowski, K. Rafińska, V. Railean-Plugaru, B. Buszewski, Zinc oxide nanoparticles: Synthesis, antiseptic activity and toxicity mechanism, *Advances in colloid and interface science* 249 (2017) 37–52.
- [97] S. G. Kumar, K. K. Rao, Zinc oxide based photocatalysis: tailoring surface-bulk structure and related interfacial charge carrier dynamics for better environmental applications, *Rsc Advances* 5 (2015) 3306–3351.
- [98] Y. Kozuka, A. Tsukazaki, M. Kawasaki, Challenges and opportunities of zno-related single crystalline heterostructures, *Applied Physics Reviews* 1 (2014) 011303.
- [99] C. Sun, J. Shi, X. Wang, Fundamental study of mechanical energy harvesting using piezoelectric nanostructures, *Journal of Applied Physics* 108 (2010) 034309.
- [100] R. Rai, Analysis of the urbach tails in absorption spectra of undoped zno thin films, *Journal of Applied Physics* 113 (2013) 153508.
- [101] X. Gu, C. Li, S. Yuan, M. Ma, Y. Qiang, J. Zhu, Zno based heterojunctions and their application in environmental photocatalysis, *Nanotechnology* 27 (2016) 402001.
- [102] Q. Chen, Y. Sun, Y. Wang, H. Cheng, Q.-M. Wang, Zno nanowires–polyimide nanocomposite piezoresistive strain sensor, *Sensors and Actuators A: Physical* 190 (2013) 161–167.
- [103] B. K. Deka, A. Hazarika, O. Kwon, D. Kim, Y.-B. Park, H. W. Park, Multifunctional enhancement of woven carbon fiber/zno nanotube-based structural supercapacitor

- and polyester resin-domain solid-polymer electrolytes, *Chemical Engineering Journal* 325 (2017) 672–680.
- [104] Z. L. Wang, Zinc oxide nanostructures: growth, properties and applications, *Journal of physics: condensed matter* 16 (2004) R829.
- [105] J. Hasnidawani, H. Azlina, H. Norita, N. Bonnia, S. Ratim, E. Ali, Synthesis of zno nanostructures using sol-gel method, *Procedia Chemistry* 19 (2016) 211–216.
- [106] A. Naveed Ul Haq, A. Nadhman, I. Ullah, G. Mustafa, M. Yasinzai, I. Khan, Synthesis approaches of zinc oxide nanoparticles: the dilemma of ecotoxicity, *Journal of Nanomaterials* 2017 (2017).
- [107] H. Fujisawa, C. Kobayashi, S. Nakashima, M. Shimizu, Two-step growth of zno nanorods by using mocvd and control of their diameters and surface densities, *Journal of the Korean Physical Society* 62 (2013) 1164–1168.
- [108] J. Wang, R. Chen, L. Xiang, S. Komarneni, Synthesis, properties and applications of zno nanomaterials with oxygen vacancies: a review, *Ceramics International* 44 (2018) 7357–7377.
- [109] Z. Liang, H. Cui, K. Wang, P. Yang, L. Zhang, W. Mai, C.-X. Wang, P. Liu, Morphology-controllable zno nanotubes and nanowires: synthesis, growth mechanism and hydrophobic property, *CrystEngComm* 14 (2012) 1723–1728.
- [110] M. Ahmad, J. Zhu, Zno based advanced functional nanostructures: synthesis, properties and applications, *Journal of Materials chemistry* 21 (2011) 599–614.
- [111] G. Elango, S. Mohana Roopan, N. Abdullah Al-Dhabi, M. V. Arasu, K. Irukatla Damodharan, K. Elumalai, Cocos nucifera coir-mediated green synthesis of pd nps and its investigation against larvae and agricultural pest, *Artificial Cells, Nanomedicine, and Biotechnology* 45 (2017) 1581–1587.

- [112] J. Singh, T. Dutta, K.-H. Kim, M. Rawat, P. Samddar, P. Kumar, 'green' synthesis of metals and their oxide nanoparticles: applications for environmental remediation, *Journal of nanobiotechnology* 16 (2018) 1–24.
- [113] S. M. Roopan, T. V. Surendra, G. Elango, S. H. S. Kumar, Biosynthetic trends and future aspects of bimetallic nanoparticles and its medicinal applications, *Applied microbiology and biotechnology* 98 (2014) 5289–5300.
- [114] Z. Abboud, S. Vivekanandhan, M. Misra, A. K. Mohanty, Leaf extract mediated biogenic process for the decoration of graphene with silver nanoparticles, *Materials Letters* 178 (2016) 115–119.
- [115] V. Kalpana, V. Devi Rajeswari, A review on green synthesis, biomedical applications, and toxicity studies of zno nps, *Bioinorganic chemistry and applications* 2018 (2018).
- [116] K. Parveen, V. Banse, L. Ledwani, Green synthesis of nanoparticles: their advantages and disadvantages, in: *AIP conference proceedings*, volume 1724, AIP Publishing LLC, p. 020048.
- [117] I. Hussain, N. Singh, A. Singh, H. Singh, S. Singh, Green synthesis of nanoparticles and its potential application, *Biotechnology letters* 38 (2016) 545–560.
- [118] S. Mishra, S. Daniele, Metal–organic derivatives with fluorinated ligands as precursors for inorganic nanomaterials, *Chemical Reviews* 115 (2015) 8379–8448.
- [119] I. Bretos, R. Jiménez, J. Ricote, M. L. Calzada, Low-temperature crystallization of solution-derived metal oxide thin films assisted by chemical processes, *Chemical Society Reviews* 47 (2018) 291–308.

- [120] C. Glynn, C. O'Dwyer, Solution processable metal oxide thin film deposition and material growth for electronic and photonic devices, *Advanced Materials Interfaces* 4 (2017) 1600610.
- [121] H. Haberland, M. Mall, M. Moseler, Y. Qiang, T. Reiners, Y. Thurner, Filling of micron-sized contact holes with copper by energetic cluster impact, *Journal of Vacuum Science & Technology A: Vacuum, Surfaces, and Films* 12 (1994) 2925–2930.
- [122] B. M. Smirnov, Processes involving clusters and small particles in a buffer gas, *Physics-Uspekhi* 54 (2011) 691.
- [123] V. Singh, P. Grammatikopoulos, C. Cassidy, M. Benelmekki, M. Bohra, Z. Hawash, K. W. Baughman, M. Sowwan, Assembly of tantalum porous films with graded oxidation profile from size-selected nanoparticles, *Journal of nanoparticle research* 16 (2014) 1–10.
- [124] P. Grammatikopoulos, S. Steinhauer, J. Vernieres, V. Singh, M. Sowwan, Nanoparticle design by gas-phase synthesis, *Advances in Physics: X* 1 (2016) 81–100.
- [125] V. N. Popok, O. Kylián, Gas-phase synthesis of functional nanomaterials, *Applied Nano* 1 (2020) 4.
- [126] Y. Huttel, *Gas-phase synthesis of nanoparticles*, John Wiley & Sons, 2017.
- [127] X. Zhao, M. Li, X. Lou, Sol–gel assisted hydrothermal synthesis of zno microstructures: morphology control and photocatalytic activity, *Advanced Powder Technology* 25 (2014) 372–378.
- [128] Y. Hou, A. M. Soleimanpour, A. H. Jayatissa, Low resistive aluminum doped nanocrystalline zinc oxide for reducing gas sensor application via sol–gel process, *Sensors and Actuators B: Chemical* 177 (2013) 761–769.

- [129] H. J. Jung, S. Lee, Y. Yu, S. M. Hong, H. C. Choi, M. Y. Choi, Low-temperature hydrothermal growth of zno nanorods on sol–gel prepared zno seed layers: Optimal growth conditions, *Thin Solid Films* 524 (2012) 144–150.
- [130] K. L. Foo, U. Hashim, K. Muhammad, C. H. Voon, Sol–gel synthesized zinc oxide nanorods and their structural and optical investigation for optoelectronic application, *Nanoscale research letters* 9 (2014) 1–10.
- [131] M. Hilgendorff, L. Spanhel, C. Rothenhäusler, G. Müller, From zno colloids to nanocrystalline highly conductive films, *Journal of the Electrochemical Society* 145 (1998) 3632.
- [132] M. Tokumoto, V. Briois, C. V. Santilli, S. H. Pulcinelli, Preparation of zno nanoparticles: structural study of the molecular precursor, *Journal of Sol-Gel Science and Technology* 26 (2003) 547–551.
- [133] H. Absalan, F. Ghodsi, Comparative study of zno thin films prepared by different sol-gel route., *Iranian Journal of Physics Research* 11 (2011).
- [134] L. Znaidi, Sol–gel-deposited zno thin films: A review, *Materials Science and Engineering: B* 174 (2010) 18–30.
- [135] M. Henry, J. P. Jolivet, J. Livage, Aqueous chemistry of metal cations: hydrolysis, condensation and complexation, *Chemistry, Spectroscopy and Applications of Sol-Gel Glasses* (1992) 153–206.
- [136] D. L. Golić, G. Branković, M. P. Nešić, K. Vojisavljević, A. Rečnik, N. Daneu, S. Bernik, M. Šćepanović, D. Poleti, Z. Branković, Structural characterization of self-assembled zno nanoparticles obtained by the sol–gel method from  $\text{zn}(\text{ch}_3\text{coo})_2 \cdot 2\text{h}_2\text{o}$ , *Nanotechnology* 22 (2011) 395603.

- [137] S.-H. Hong, M.-H. Kim, H.-W. Yun, T. Paik, H. Lee, Solution-processed fabrication of superhydrophobic hierarchical zinc oxide nanostructures via nanotransfer printing and hydrothermal growth, *Surface and Coatings Technology* 331 (2017) 189–195.
- [138] B. Baruwati, D. K. Kumar, S. V. Manorama, Hydrothermal synthesis of highly crystalline zno nanoparticles: a competitive sensor for lpg and etoh, *Sensors and Actuators B: Chemical* 119 (2006) 676–682.
- [139] P. Bhattacharyya, B. Agarwal, M. Goswami, D. Maiti, S. Baruah, P. Tribedi, Zinc oxide nanoparticle inhibits the biofilm formation of streptococcus pneumoniae, *Antonie Van Leeuwenhoek* 111 (2018) 89–99.
- [140] G. Das, B. K. Deka, S. H. Lee, Y.-B. Park, Y. S. Yoon, Poly (vinyl alcohol)/silica nanoparticles based anion-conducting nanocomposite membrane for fuel-cell applications, *Macromolecular Research* 23 (2015) 256–264.
- [141] A. Sayari, L. El Mir, Structural and optical characterization of ni and al co-doped zno nanopowders synthesized via the sol-gel process, *KONA Powder and Particle Journal* (2015) 2015003.
- [142] D. Ramimoghadam, M. Z. Bin Hussein, Y. H. Taufiq-Yap, Hydrothermal synthesis of zinc oxide nanoparticles using rice as soft biotemplate, *Chemistry Central Journal* 7 (2013) 1–10.
- [143] A. Hazarika, B. K. Deka, D. Kim, K. Kong, Y.-B. Park, H. W. Park, Growth of aligned zno nanorods on woven kevlar® fiber and its performance in woven kevlar® fiber/polyester composites, *Composites Part A: Applied Science and Manufacturing* 78 (2015) 284–293.

- [144] G. Amin, M. Asif, A. Zainelabdin, S. Zaman, O. Nur, M. Willander, Influence of pH, precursor concentration, growth time, and temperature on the morphology of ZnO nanostructures grown by the hydrothermal method, *Journal of Nanomaterials* 2011 (2011).
- [145] M. S. Al-Ruqeishi, T. Mohiuddin, B. Al-Habsi, F. Al-Ruqeishi, A. Al-Fahdi, A. Al-Khusaibi, Piezoelectric nanogenerator based on ZnO nanorods, *Arabian Journal of Chemistry* 12 (2019) 5173–5179.
- [146] N. A. Salahuddin, M. El-Kemary, E. M. Ibrahim, Synthesis and characterization of ZnO nanotubes by hydrothermal method, *Int J Sci Res Publ* 5 (2015) 3–6.
- [147] S. Ghasaban, M. Atai, M. Imani, Simple mass production of zinc oxide nanostructures via low-temperature hydrothermal synthesis, *Materials Research Express* 4 (2017) 035010.
- [148] A. K. Zak, W. A. Majid, M. E. Abrishami, R. Yousefi, X-ray analysis of ZnO nanoparticles by Williamson–Hall and size–strain plot methods, *Solid State Sciences* 13 (2011) 251–256.
- [149] A. Monshi, M. R. Foroughi, M. R. Monshi, Modified Scherrer equation to estimate more accurately nano-crystallite size using XRD, *World J Nano Sci Eng*, 2012, 2: 154–160 (2012).
- [150] M. Yilmaz, B. Bozkurt, C. Cirak, S. Aydogan, Hydrothermal growth of ZnO nanoparticles under different conditions, *Philosophical Magazine Letters* 96 (2016) 45–51.
- [151] M. Yilmaz, Investigation of characteristics of ZnO: Ga nanocrystalline thin films with varying dopant content, *Materials Science in Semiconductor Processing* 40 (2015) 99–106.

- [152] R. Yoo, S. Yoo, D. Lee, J. Kim, S. Cho, W. Lee, Highly selective detection of dimethyl methylphosphonate (dmmp) using cuo nanoparticles/zno flowers hetero-junction, *Sensors and Actuators B: Chemical* 240 (2017) 1099–1105.
- [153] C.-L. Xu, Y.-Z. Wang, Self-assembly of stearic acid into nano flowers induces the tunable surface wettability of polyimide film, *Materials & Design* 138 (2018) 30–38.
- [154] G. Kwak, M. Seol, Y. Tak, K. Yong, Superhydrophobic zno nanowire surface: chemical modification and effects of uv irradiation, *The Journal of Physical Chemistry C* 113 (2009) 12085–12089.
- [155] X. Guo, Q. Zhao, R. Li, H. Pan, X. Guo, A. Yin, W. Dai, Synthesis of zno nanoflowers and their wettabilities and photocatalytic properties, *Optics express* 18 (2010) 18401–18406.
- [156] M. Abdelfatah, A. El-Shaer, One step to fabricate vertical submicron zno rod arrays by hydrothermal method without seed layer for optoelectronic devices, *Materials Letters* 210 (2018) 366–369.
- [157] R. Sabry, O. AbdulAzeez, Hydrothermal growth of zno nano rods without catalysts in a single step, *Manufacturing Letters* 2 (2014) 69–73.
- [158] J. Fan, T. Li, H. Heng, Hydrothermal growth and optical properties of zno nanoflowers, *Materials Research Express* 1 (2014) 045024.
- [159] T. Venkatesha, Y. A. Nayaka, R. Viswanatha, C. Vidyasagar, B. Chethana, Electrochemical synthesis and photocatalytic behavior of flower shaped zno microstructures, *Powder technology* 225 (2012) 232–238.
- [160] L. Sun, R. Shao, Z. Chen, L. Tang, Y. Dai, J. Ding, Alkali-dependent synthesis of flower-like zno structures with enhanced photocatalytic activity via a facile hydrothermal method, *Applied Surface Science* 258 (2012) 5455–5461.



- [161] H. R. Pant, B. Pant, R. K. Sharma, A. Amarjargal, H. J. Kim, C. H. Park, L. D. Tijing, C. S. Kim, Antibacterial and photocatalytic properties of ag/tio<sub>2</sub>/zno nano-flowers prepared by facile one-pot hydrothermal process, *Ceramics International* 39 (2013) 1503–1510.
- [162] T. Liu, Y. Li, H. Zhang, M. Wang, X. Fei, S. Duo, Y. Chen, J. Pan, W. Wang, Tartaric acid assisted hydrothermal synthesis of different flower-like zno hierarchical architectures with tunable optical and oxygen vacancy-induced photocatalytic properties, *Applied Surface Science* 357 (2015) 516–529.
- [163] H. Guo, W. Zhang, Y. Sun, T. Zhou, Y. Qiu, K. Xu, B. Zhang, H. Yang, Double disks shaped zno microstructures synthesized by one-step ctab assisted hydrothermal methods, *Ceramics International* 41 (2015) 10461–10466.
- [164] Y. Sun, H. Guo, W. Zhang, T. Zhou, Y. Qiu, K. Xu, B. Zhang, H. Yang, Synthesis and characterization of twinned flower-like zno structures grown by hydrothermal methods, *Ceramics International* 42 (2016) 9648–9652.
- [165] D. Kumar, R. S. Rai, N. K. Singh, An innovative approach to deposit ultrathin zno nanoflakes (2d) through hydrothermal assisted electrochemical discharge deposition and growth method, *Ceramics International* 46 (2020) 26216–26220.
- [166] M. Hasanpoor, M. Aliofkhazraei, H. Delavari, Microwave-assisted synthesis of zinc oxide nanoparticles, *Procedia Materials Science* 11 (2015) 320–325.
- [167] A. Pimentel, A. Samouco, D. Nunes, A. Araújo, R. Martins, E. Fortunato, Ultra-fast microwave synthesis of zno nanorods on cellulose substrates for uv sensor applications, *Materials* 10 (2017) 1308.
- [168] K. Li, X. Zhou, Z. Zhao, C. Chen, C. Wang, B. Ren, L. Zhang, Synthesis of zirco-

- nium carbide whiskers by a combination of microwave hydrothermal and carbothermal reduction, *Journal of Solid State Chemistry* 258 (2018) 383–390.
- [169] M. Kang, H.-S. Kim, et al., Microwave-assisted facile and ultrafast growth of zno nanostructures and proposition of alternative microwave-assisted methods to address growth stoppage, *Scientific reports* 6 (2016) 1–13.
- [170] Z. Zhu, D. Yang, H. Liu, Microwave-assisted hydrothermal synthesis of zno rod-assembled microspheres and their photocatalytic performances, *Advanced Powder Technology* 22 (2011) 493–497.
- [171] R. Schmidt, J. Prado-Gonjal, E. Morán, Microwave assisted hydrothermal synthesis of nanoparticles, *arXiv preprint arXiv:2203.02394* (2022).
- [172] B. S. Witkowski, P. Dluzewski, J. Kaszewski, L. Wachnicki, S. Gieraltowska, B. Kurowska, M. Godlewski, Ultra-fast epitaxial growth of zno nano/microrods on a gan substrate, using the microwave-assisted hydrothermal method, *Materials Chemistry and Physics* 205 (2018) 16–22.
- [173] S. Duo, Y. Li, Z. Liu, R. Zhong, T. Liu, H. Xu, Preparation of zno from 2 d nanosheets to diverse 1 d nanorods and their structure, surface area, photocurrent, optical and photocatalytic properties by simple hydrothermal synthesis, *Journal of Alloys and Compounds* 695 (2017) 2563–2579.
- [174] G. Byzynski, A. P. Pereira, D. P. Volanti, C. Ribeiro, E. Longo, High-performance ultraviolet-visible driven zno morphologies photocatalyst obtained by microwave-assisted hydrothermal method, *Journal of Photochemistry and Photobiology A: Chemistry* 353 (2018) 358–367.
- [175] Y. Caglar, K. Gorgun, S. Aksoy, Effect of deposition parameters on the structural properties of zno nanopowders prepared by microwave-assisted hydrothermal syn-

- thesis, *Spectrochimica Acta Part A: Molecular and Biomolecular Spectroscopy* 138 (2015) 617–622.
- [176] G. Barreto, G. Morales, A. Cañizo, N. Eyler, Microwave assisted synthesis of zno tridimensional nanostructures, *Procedia Materials Science* 8 (2015) 535–540.
- [177] M. Ahmad, M. Ahmad, N. Nafarizal, C. Soon, A. Suriani, A. Mohamed, M. Mamat, Chemisorbed co<sub>2</sub> molecules on zno nanowires (100 nm) surface leading towards enhanced piezoelectric voltage, *Vacuum* 182 (2020) 109565.
- [178] W. Yu, J. Zhang, T. Peng, New insight into the enhanced photocatalytic activity of n-, c-and s-doped zno photocatalysts, *Applied Catalysis B: Environmental* 181 (2016) 220–227.
- [179] Y. Wu, P. Hermkens, B. Van De Loo, H. Knoops, S. Potts, M. Verheijen, F. Roozeboom, W. Kessels, Electrical transport and al doping efficiency in nanoscale zno films prepared by atomic layer deposition, *Journal of Applied Physics* 114 (2013) 024308.
- [180] B. Poornaprakash, U. Chalapathi, S. Babu, S.-H. Park, Structural, morphological, optical, and magnetic properties of gd-doped and (gd, mn) co-doped zno nanoparticles, *Physica E: Low-dimensional Systems and Nanostructures* 93 (2017) 111–115.
- [181] P. Zhu, X. Yin, X. Gao, G. Dong, J. Xu, C. Wang, Enhanced photocatalytic no removal and toxic no<sub>2</sub> production inhibition over zif-8-derived zno nanoparticles with controllable amount of oxygen vacancies, *Chinese Journal of Catalysis* 42 (2021) 175–183.
- [182] Y. Lv, Z. Zhang, J. Yan, W. Zhao, C. Zhai, Al doping influences on fabricating zno nanowire arrays: Enhanced field emission property, *Ceramics International* 44 (2018) 7454–7460.

- [183] L. Chow, O. Lupan, G. Chai, H. Khallaf, L. K. Ono, B. R. Cuenya, I. Tiginyanu, V. V. Ursaki, V. Sontea, A. Schulte, Synthesis and characterization of cu-doped zno one-dimensional structures for miniaturized sensor applications with faster response, *Sensors and Actuators A: Physical* 189 (2013) 399–408.
- [184] A. B. Lavand, Y. S. Malghe, Synthesis, characterization and visible light photocatalytic activity of nitrogen-doped zinc oxide nanospheres, *Journal of Asian Ceramic Societies* 3 (2015) 305–310.
- [185] M. Mittal, M. Sharma, O. Pandey, Uv–visible light induced photocatalytic studies of cu doped zno nanoparticles prepared by co-precipitation method, *Solar Energy* 110 (2014) 386–397.
- [186] S. Das, S. Das, S. Sutradhar, Effect of  $gd^{3+}$  and  $al^{3+}$  on optical and dielectric properties of zno nanoparticle prepared by two-step hydrothermal method, *Ceramics International* 43 (2017) 6932–6941.
- [187] S.-H. Hwang, K.-J. Moon, T. I. Lee, W. Lee, J.-M. Myoung, Controlling phosphorus doping concentration in zno nanorods by low temperature hydrothermal method, *Materials Chemistry and Physics* 143 (2014) 600–604.
- [188] F. Ajala, A. Hamrouni, A. Houas, H. Lachheb, B. Megna, L. Palmisano, F. Parrino, The influence of al doping on the photocatalytic activity of nanostructured zno: The role of adsorbed water, *Applied Surface Science* 445 (2018) 376–382.
- [189] J. R. Rangel-Mendez, J. Matos, L. F. Cházaro-Ruiz, A. C. González-Castillo, G. Barrios-Yáñez, Microwave-assisted synthesis of c-doped  $tio_2$  and zno hybrid nanostructured materials as quantum-dots sensitized solar cells, *Applied Surface Science* 434 (2018) 744–755.

- [190] J.-C. Sin, S.-M. Lam, Hydrothermal synthesis of europium-doped flower-like zno hierarchical structures with enhanced sunlight photocatalytic degradation of phenol, *Materials Letters* 182 (2016) 223–226.
- [191] M. Sathya, K. Pushpanathan, Synthesis and optical properties of pb doped zno nanoparticles, *Applied Surface Science* 449 (2018) 346–357.
- [192] Y. Wei, X. Wang, G. Yi, L. Zhou, J. Cao, G. Sun, Z. Chen, H. Bala, Z. Zhang, Hydrothermal synthesis of ag modified zno nanorods and their enhanced ethanol-sensing properties, *Materials Science in Semiconductor Processing* 75 (2018) 327–333.
- [193] J. M. Byun, H. R. Choi, Y. Do Kim, T. Sekino, S. H. Kim, Photocatalytic activity under uv/visible light range of nb-doped titanate nanostructures synthesized with nb oxide, *Applied Surface Science* 415 (2017) 126–131.
- [194] M. Bernardo, P. G. Villanueva, T. Jardiel, D. G. Calatayud, M. Peiteado, A. Caballero, Ga-doped zno self-assembled nanostructures obtained by microwave-assisted hydrothermal synthesis: Effect on morphology and optical properties, *Journal of Alloys and Compounds* 722 (2017) 920–927.
- [195] S. Das, A. Bandyopadhyay, S. Das, D. Das, S. Sutradhar, Defect induced room-temperature ferromagnetism and enhanced dielectric property in nanocrystalline zno co-doped with tb and co, *Journal of Alloys and Compounds* 731 (2018) 591–599.
- [196] H. Chen, S. Ma, H. Jiao, G. Yang, X. Xu, T. Wang, X. Jiang, Z. Zhang, The effect microstructure on the gas properties of ag doped zinc oxide sensors: spheres and sea-urchin-like nanostructures, *Journal of Alloys and Compounds* 687 (2016) 342–351.

- [197] G. Poongodi, P. Anandan, R. M. Kumar, R. Jayavel, Studies on visible light photocatalytic and antibacterial activities of nanostructured cobalt doped zno thin films prepared by sol–gel spin coating method, *Spectrochimica Acta Part A: Molecular and Biomolecular Spectroscopy* 148 (2015) 237–243.
- [198] M. Wang, F. Ren, J. Zhou, G. Cai, L. Cai, Y. Hu, D. Wang, Y. Liu, L. Guo, S. Shen, N doping to zno nanorods for photoelectrochemical water splitting under visible light: engineered impurity distribution and terraced band structure, *Scientific reports* 5 (2015) 1–13.
- [199] C. V. Manzano, D. Alegre, O. Caballero-Calero, B. Alén, M. Martín-González, Synthesis and luminescence properties of electrodeposited zno films, *Journal of Applied Physics* 110 (2011) 043538.
- [200] D. Panda, T.-Y. Tseng, One-dimensional zno nanostructures: fabrication, optoelectronic properties, and device applications, *Journal of Materials Science* 48 (2013) 6849–6877.
- [201] K. Qi, B. Cheng, J. Yu, W. Ho, Review on the improvement of the photocatalytic and antibacterial activities of zno, *Journal of Alloys and Compounds* 727 (2017) 792–820.
- [202] G. K. Weldegebrical, Synthesis method, antibacterial and photocatalytic activity of zno nanoparticles for azo dyes in wastewater treatment: A review, *Inorganic Chemistry Communications* 120 (2020) 108140.
- [203] M. Samadi, M. Zirak, A. Naseri, E. Khorashadizade, A. Z. Moshfegh, Recent progress on doped zno nanostructures for visible-light photocatalysis, *Thin Solid Films* 605 (2016) 2–19.

- [204] S. Goktas, A. Goktas, A comparative study on recent progress in efficient zno based nanocomposite and heterojunction photocatalysts: A review, *Journal of Alloys and Compounds* 863 (2021) 158734.
- [205] S. Wang, P. Kuang, B. Cheng, J. Yu, C. Jiang, Zno hierarchical microsphere for enhanced photocatalytic activity, *Journal of Alloys and Compounds* 741 (2018) 622–632.
- [206] S. Cheng, F. A. Hill, E. V. Heubel, L. F. Velásquez-García, Low-bremsstrahlung x-ray source using a low-voltage high-current-density nanostructured field emission cathode and a transmission anode for markerless soft tissue imaging, *Journal of Microelectromechanical Systems* 24 (2014) 373–383.
- [207] R.-Z. Wang, W. Zhao, H. Yan, Generalized mechanism of field emission from nanostructured semiconductor film cathodes, *Scientific Reports* 7 (2017) 1–8.
- [208] A. Umar, H. Algarni, S. Kim, M. Al-Assiri, Time dependent growth of zno nanoflowers with enhanced field emission properties, *Ceramics International* 42 (2016) 13215–13222.
- [209] M. O. da Silva Dantas, D. Criado, A. Zúñiga, W. Silva, E. Galeazzo, H. Peres, M. Kopelovski, Zno nanowire-based field emission devices through a microelectronic compatible route, *Journal of Integrated Circuits and Systems* 15 (2020) 1–6.
- [210] S. Kumar, P. Sahare, S. Kumar, Optimization of the cvd parameters for zno nanorods growth: Its photoluminescence and field emission properties, *Materials Research Bulletin* 105 (2018) 237–245.
- [211] N. M. Noah, Design and synthesis of nanostructured materials for sensor applications, *Journal of Nanomaterials* 2020 (2020).

- [212] N. P. Shetti, S. D. Bukkitgar, K. R. Reddy, C. V. Reddy, T. M. Aminabhavi, ZnO-based nanostructured electrodes for electrochemical sensors and biosensors in biomedical applications, *Biosensors and Bioelectronics* 141 (2019) 111417.
- [213] M. Ekrami, G. Magna, Z. Emam-Djomeh, M. Saeed Yarmand, R. Paolesse, C. Di Natale, Porphyrin-functionalized zinc oxide nanostructures for sensor applications, *Sensors* 18 (2018) 2279.
- [214] Q. Ren, Y.-Q. Cao, D. Arulraj, C. Liu, D. Wu, W.-M. Li, A.-D. Li, Resistive-type hydrogen sensors based on zinc oxide nanostructures, *Journal of The Electrochemical Society* 167 (2020) 067528.
- [215] G. Li, Y. Wu, Y. Hong, X. Zhao, P. I. Reyes, Y. Lu, Magnesium zinc oxide nanostructure-modified multifunctional sensors for full-scale dynamic monitoring of pseudomonas aeruginosa biofilm formation, *ECS Journal of Solid State Science and Technology* 9 (2020) 115026.
- [216] J. Theerthagiri, S. Salla, R. Senthil, P. Nithyadharseni, A. Madankumar, P. Arunachalam, T. Maiyalagan, H.-S. Kim, A review on zno nanostructured materials: energy, environmental and biological applications, *Nanotechnology* 30 (2019) 392001.
- [217] M. Laurenti, N. Garino, S. Porro, M. Fontana, C. Gerbaldi, Zinc oxide nanostructures by chemical vapour deposition as anodes for li-ion batteries, *Journal of Alloys and Compounds* 640 (2015) 321–326.
- [218] L. Xiao, E. Li, J. Yi, W. Meng, S. Wang, B. Deng, J. Liu, Enhancing the performance of nanostructured zno as an anode material for lithium-ion batteries by polydopamine-derived carbon coating and confined crystallization, *Journal of Alloys and Compounds* 764 (2018) 545–554.



- [219] J. Liu, J. Wu, C. Zhou, P. Zhang, S. Guo, S. Li, Y. Yang, K. Li, L. Chen, M. Wang, Single-phase  $\text{ZnCO}_3$  derived ZnO-coo mesoporous microspheres encapsulated by nitrogen-doped carbon shell as anode for high-performance lithium-ion batteries, *Journal of Alloys and Compounds* 825 (2020) 153951.
- [220] G. Yuan, J. Xiang, H. Jin, L. Wu, Y. Jin, Y. Zhao, Anchoring ZnO nanoparticles in nitrogen-doped graphene sheets as a high-performance anode material for lithium-ion batteries, *Materials* 11 (2018) 96.
- [221] Y. Wang, J. Feng, H. Wang, M. Zhang, X. Yang, R. Yuan, Y. Chai, Fabricating porous ZnO/ $\text{Co}_3\text{O}_4$  microspheres coated with n-doped carbon by a simple method as high capacity anode, *Journal of Electroanalytical Chemistry* 873 (2020) 114479.
- [222] A. Sirelkhatim, S. Mahmud, A. Seeni, N. H. M. Kaus, L. C. Ann, S. K. M. Bakhori, H. Hasan, D. Mohamad, Review on zinc oxide nanoparticles: antibacterial activity and toxicity mechanism, *Nano-micro letters* 7 (2015) 219–242.
- [223] N. A. A. Yusof, N. M. Zain, N. Pauzi, Synthesis of ZnO nanoparticles with chitosan as stabilizing agent and their antibacterial properties against gram-positive and gram-negative bacteria, *International journal of biological macromolecules* 124 (2019) 1132–1136.
- [224] S. Jiang, K. Lin, M. Cai, ZnO nanomaterials: current advancements in antibacterial mechanisms and applications, *Frontiers in Chemistry* 8 (2020) 580.
- [225] E. Samuel, B. Joshi, M.-W. Kim, Y.-I. Kim, M. T. Swihart, S. S. Yoon, Hierarchical zeolitic imidazolate framework-derived manganese-doped zinc oxide decorated carbon nanofiber electrodes for high performance flexible supercapacitors, *Chemical Engineering Journal* 371 (2019) 657–665.

- [226] V. O. Fávero, D. A. Oliveira, J. L. Lutkenhaus, J. R. Siqueira, Layer-by-layer nanostructured supercapacitor electrodes consisting of zno nanoparticles and multi-walled carbon nanotubes, *Journal of materials science* 53 (2018) 6719–6728.
- [227] H. Yun, X. Zhou, H. Zhu, M. Zhang, One-dimensional zinc-manganate oxide hollow nanostructures with enhanced supercapacitor performance, *Journal of Colloid and Interface Science* 585 (2021) 138–147.
- [228] A. Guerra, A. Achour, S. Vizireanu, G. Dinescu, S. Messaci, T. Hadjersi, R. Boukherroub, Y. Coffinier, J.-J. Pireaux, ZnO/carbon nanowalls shell/core nanostructures as electrodes for supercapacitors, *Applied Surface Science* 481 (2019) 926–932.
- [229] X. Wang, M. Ahmad, H. Sun, Three-dimensional zno hierarchical nanostructures: Solution phase synthesis and applications, *Materials* 10 (2017) 1304.
- [230] N. Zheng, Y. Huang, W. Sun, X. Du, H.-Y. Liu, S. Moody, J. Gao, Y.-W. Mai, In-situ pull-off of zno nanowire from carbon fiber and improvement of interlaminar toughness of hierarchical zno nanowire/carbon fiber hybrid composite laminates, *Carbon* 110 (2016) 69–78.
- [231] G. J. Ehlert, U. Galan, H. A. Sodano, Role of surface chemistry in adhesion between zno nanowires and carbon fibers in hybrid composites, *ACS applied materials & interfaces* 5 (2013) 635–645.
- [232] H. Moussa, E. Girot, K. Mozet, H. Alem, G. Medjahdi, R. Schneider, ZnO rods/reduced graphene oxide composites prepared via a solvothermal reaction for efficient sunlight-driven photocatalysis, *Applied Catalysis B: Environmental* 185 (2016) 11–21.

- [233] T. Velayutham, W. H. Abd Majid, W. Gan, A. Khorsand Zak, S. Gan, Theoretical and experimental approach on dielectric properties of zno nanoparticles and polyurethane/zno nanocomposites, *Journal of Applied Physics* 112 (2012) 054106.
- [234] Y. Chen, Y. Wang, J. Fang, B. Dai, J. Kou, C. Lu, Y. Zhao, Design of a zno/poly (vinylidene fluoride) inverse opal film for photon localization-assisted full solar spectrum photocatalysis, *Chinese Journal of Catalysis* 42 (2021) 184–192.
- [235] H. Deng, F. Xu, B. Cheng, J. Yu, W. Ho, Photocatalytic co<sub>2</sub> reduction of c/zno nanofibers enhanced by an ni-nis cocatalyst, *Nanoscale* 12 (2020) 7206–7213.
- [236] S.-J. Young, C.-C. Yang, L.-T. Lai, growth of al-, ga-, and in-doped zno nanostructures via a low-temperature process and their application to field emission devices and ultraviolet photosensors, *Journal of The Electrochemical Society* 164 (2016) B3013.
- [237] A. Kushwaha, M. Aslam, Zns shielded zno nanowire photoanodes for efficient water splitting, *Electrochimica Acta* 130 (2014) 222–231.
- [238] N. Abraham, R. R. Krishnakumar, C. Unni, D. Philip, Simulation studies on the responses of zno-cuo/cnt nanocomposite based saw sensor to various volatile organic chemicals, *Journal of Science: Advanced Materials and Devices* 4 (2019) 125–131.
- [239] W. Li, G. Wang, Y. Feng, Z. Li, Efficient photocatalytic performance enhancement in co-doped zno nanowires coupled with cus nanoparticles, *Applied Surface Science* 428 (2018) 154–164.
- [240] C. Ye, X. Fang, Y. Hao, X. Teng, L. Zhang, Zinc oxide nanostructures: morphology derivation and evolution, *The Journal of Physical Chemistry B* 109 (2005) 19758–19765.

- [241] Q. L. Ma, R. Xiong, B.-g. Zhai, Y. M. Huang, Ultrasonic synthesis of fern-like zno nanoleaves and their enhanced photocatalytic activity, *Applied Surface Science* 324 (2015) 842–848.
- [242] D. Wei, Y. Qi, S. Lv, G. Shi, Y. Dai, Y. Qi, Facile synthesis of thin coating c/zno composites with strong electromagnetic wave absorption, *Ceramics International* 45 (2019) 4448–4454.
- [243] Y. Tao, M. Fu, A. Zhao, D. He, Y. Wang, The effect of seed layer on morphology of zno nanorod arrays grown by hydrothermal method, *Journal of alloys and Compounds* 489 (2010) 99–102.
- [244] A. Moulahi, F. Sediri, Zno nanoswords and nanopills: Hydrothermal synthesis, characterization and optical properties, *Ceramics International* 40 (2014) 943–950.
- [245] D.-Y. Son, K.-H. Bae, H.-S. Kim, N.-G. Park, Effects of seed layer on growth of zno nanorod and performance of perovskite solar cell, *The Journal of Physical Chemistry C* 119 (2015) 10321–10328.
- [246] D. Upadhaya, D. D. Purkayastha, Enhanced wettability and photocatalytic activity of seed layer assisted one dimensional zno nanorods synthesized by hydrothermal method, *Ceramics International* 46 (2020) 15831–15839.
- [247] M. Podlogar, A. Rečnik, G. Yilmazoglu, I. Ö. Özer, M. Mazaj, E. Suvaci, S. Bernik, The role of hydrothermal pathways in the evolution of the morphology of zno crystals, *Ceramics International* 42 (2016) 15358–15366.
- [248] D. Polsongkram, P. Chamninok, S. Pukird, L. Chow, O. Lupan, G. Chai, H. Khallaf, S. Park, A. Schulte, Effect of synthesis conditions on the growth of zno nanorods via hydrothermal method, *Physica B: Condensed Matter* 403 (2008) 3713–3717.

- [249] I. Y. Bu, Rapid synthesis of zno nanostructures through microwave heating process, *Ceramics International* 39 (2013) 1189–1194.
- [250] R. Wahab, S. Ansari, Y. S. Kim, M. Song, H.-S. Shin, The role of ph variation on the growth of zinc oxide nanostructures, *Applied Surface Science* 255 (2009) 4891–4896.
- [251] S. Baruah, J. Dutta, ph-dependent growth of zinc oxide nanorods, *Journal of Crystal Growth* 311 (2009) 2549–2554.
- [252] L. Vayssieres, K. Keis, A. Hagfeldt, S.-E. Lindquist, Three-dimensional array of highly oriented crystalline zno microtubes, *Chemistry of Materials* 13 (2001) 4395–4398.
- [253] T. Jiang, Y. Wang, D. Meng, X. Wu, J. Wang, J. Chen, Controllable fabrication of cuo nanostructure by hydrothermal method and its properties, *Applied Surface Science* 311 (2014) 602–608.
- [254] Q. Chen, Y. Wang, M. Zheng, H. Fang, X. Meng, Nanostructures confined self-assembled in biomimetic nanochannels for enhancing the sensitivity of biological molecules response, *Journal of Materials Science: Materials in Electronics* 29 (2018) 19757–19767.
- [255] Y. Wang, T. Jiang, D. Meng, J. Yang, Y. Li, Q. Ma, J. Han, Fabrication of nanostructured cuo films by electrodeposition and their photocatalytic properties, *Applied surface science* 317 (2014) 414–421.
- [256] W. Guo, M. Fu, C. Zhai, Z. Wang, Hydrothermal synthesis and gas-sensing properties of ultrathin hexagonal zno nanosheets, *Ceramics International* 40 (2014) 2295–2298.

- [257] I. D. Tunç, M. Erol, F. Güneş, M. Sütçü, Growth of zno nanowires on carbon fibers for photocatalytic degradation of methylene blue aqueous solutions: an investigation on the optimization of processing parameters through response surface methodology/central composite design, *Ceramics International* 46 (2020) 7459–7474.
- [258] N. Kiomarsipour, R. S. Razavi, Hydrothermal synthesis and optical property of scale-and spindle-like zno, *Ceramics International* 39 (2013) 813–818.
- [259] Y. Zhu, D. Fan, W. Shen, A general chemical conversion route to synthesize various zno-based core/shell structures, *The Journal of Physical Chemistry C* 112 (2008) 10402–10406.
- [260] J. Wang, B. Weng, P. Larson, Y. Liu, Synthesis and characterization of self-assembled zno nanoarrays on hybrid structural fibers, *Surfaces and Interfaces* 16 (2019) 188–193.
- [261] V. Gerbreders, M. Krasovska, E. Sledevskis, A. Gerbreders, I. Mihailova, E. Tamaniš, A. Ogurcovs, Hydrothermal synthesis of zno nanostructures with controllable morphology change, *CrystEngComm* 22 (2020) 1346–1358.
- [262] E. Goh, X. Xu, P. McCormick, Effect of particle size on the uv absorbance of zinc oxide nanoparticles, *Scripta Materialia* 78 (2014) 49–52.
- [263] W. Muhammad, N. Ullah, M. Haroon, B. H. Abbasi, Optical, morphological and biological analysis of zinc oxide nanoparticles (zno nps) using papaver somniferum l., *RSC advances* 9 (2019) 29541–29548.
- [264] T. Feng, N. Liu, S. Wang, C. Qin, S. Shi, X. Zeng, G. Liu, Research on the dispersion of carbon nanotubes and their application in solution-processed polymeric matrix composites: A review, *Advances in nano research* 10 (2021) 559–576.

- [265] A. G. Arani, A. Farazin, M. Mohammadimehr, The effect of nanoparticles on enhancement of the specific mechanical properties of the composite structures: A review research, *Adv. Nano Res* 10 (2021) 327–337.
- [266] S. Mallakpour, F. Sirous, C. M. Hussain, A journey to the world of fascinating zno nanocomposites made of chitosan, starch, cellulose, and other biopolymers: Progress in recent achievements in eco-friendly food packaging, biomedical, and water remediation technologies, *International Journal of Biological Macromolecules* 170 (2021) 701–716.
- [267] S. Baizae, M. Arabi, A. Bahador, A simple, one-pot, low temperature and pressure route for the synthesis of rgo/zno nanocomposite and investigating its photocatalytic activity, *Materials Science in Semiconductor Processing* 82 (2018) 135–142.
- [268] C. A. Marin-Flores, O. Rodríguez-Nava, M. García-Hernández, R. Ruiz-Guerrero, F. Juárez-López, A. de Jesús Morales-Ramírez, Free-radical scavenging activity properties of zno sub-micron particles: Size effect and kinetics, *Journal of Materials Research and Technology* 13 (2021) 1665–1675.
- [269] C. Chankaew, W. Tapala, K. Grudpan, A. Rujiwatra, Microwave synthesis of zno nanoparticles using longan seeds biowaste and their efficiencies in photocatalytic decolorization of organic dyes, *Environmental Science and Pollution Research* 26 (2019) 17548–17554.
- [270] H. A. Alshamarti, A. H. O. Alkhayatt, Enhancement characterization of the msm detector based on mn doped-zno nrs synthesized by microwave assisted chemical bath deposition, *Materials Science in Semiconductor Processing* 114 (2020) 105068.
- [271] L. A. Gusmão, D. A. Peixoto, J. Z. Marinho, F. C. Romeiro, R. F. Gonçalves, E. Longo, C. A. de Oliveira, R. C. Lima, Alkali influence on zno and ag-doped

- zno nanostructures formation using the microwave-assisted hydrothermal method for fungicidal inhibition, *Journal of Physics and Chemistry of Solids* 158 (2021) 110234.
- [272] N. A. Neto, K. Matsui, C. Paskocimas, M. Bomio, F. Motta, Study of the photocatalysis and increase of antimicrobial properties of  $Fe^{3+}$  and  $Pb^{2+}$  co-doped zno nanoparticles obtained by microwave-assisted hydrothermal method, *Materials Science in Semiconductor Processing* 93 (2019) 123–133.
- [273] F. Ahmed, N. Arshi, M. Anwar, R. Danish, B. H. Koo, Morphological evolution of zno nanostructures and their aspect ratio-induced enhancement in photocatalytic properties, *RSC advances* 4 (2014) 29249–29263.
- [274] J. Radhakrishnan, M. Kumara, et al., Growth of zno nanostructures: Cones, rods and hallow-rods, by microwave assisted wet chemical growth and their characterization, *Ceramics International* 47 (2021) 5300–5310.
- [275] S. El-Nahas, M. Abd El-sadek, H. M. Salman, M. M. Elkady, Controlled morphological and physical properties of zno nanostructures synthesized by domestic microwave route, *Materials Chemistry and Physics* 258 (2021) 123885.
- [276] M. Caglar, S. Ilican, Y. Caglar, F. Yakuphanoglu, Electrical conductivity and optical properties of zno nanostructured thin film, *Applied surface science* 255 (2009) 4491–4496.
- [277] A. Kothari, T. K. Chaudhuri, One-minute microwave-assisted chemical bath deposition of nanostructured zno rod-arrays, *Materials Letters* 65 (2011) 847–849.
- [278] R. Al-Gaashani, S. Radiman, A. Daud, N. Tabet, Y. Al-Douri, Xps and optical studies of different morphologies of zno nanostructures prepared by microwave methods, *Ceramics International* 39 (2013) 2283–2292.



- [279] M. Piccardo, C.-K. Li, Y.-R. Wu, J. S. Speck, B. Bonef, R. M. Farrell, M. Filoche, L. Martinelli, J. Peretti, C. Weisbuch, Localization landscape theory of disorder in semiconductors. ii. urbach tails of disordered quantum well layers, *Physical Review B* 95 (2017) 144205.
- [280] T. S. Moss, G. J. Burrell, B. Ellis, *Semiconductor opto-electronics*, Butterworth-Heinemann, 2013.
- [281] Z. Liu, L. Li, X. Yuan, P. Yang, Study on photoelectric properties of si supported zno, *Journal of Alloys and Compounds* 843 (2020) 155909.
- [282] K.-B. Sim, D. Baek, J.-H. Shin, G.-S. Shim, S.-W. Jang, H.-J. Kim, J.-W. Hwang, J. U. Roh, Enhanced surface properties of carbon fiber reinforced plastic by epoxy modified primer with plasma for automotive applications, *Polymers* 12 (2020) 556.
- [283] Z. Hu, Q. Ma, T. Xu, High-temperature stability of carbon fiber reinforced polymer-derived sialoc composites under different environment, *Ceramics International* 45 (2019) 1434–1438.
- [284] M. Caminero, J. Chacón, I. García-Moreno, G. Rodríguez, Impact damage resistance of 3d printed continuous fibre reinforced thermoplastic composites using fused deposition modelling, *Composites Part B: Engineering* 148 (2018) 93–103.
- [285] R. M. A. Khan, I. E. Tabrizi, H. Q. Ali, E. Demir, M. Yildiz, Investigation on interlaminar delamination tendency of multidirectional carbon fiber composites, *Polymer Testing* 90 (2020) 106653.
- [286] Z. Cherif, C. Poilâne, A. Vivet, B. B. Doudou, J. Chen, About optimal architecture of plant fibre textile composite for mechanical and sorption properties, *Composite Structures* 140 (2016) 240–251.

- [287] M. Bhattacharya, Polymer nanocomposites—a comparison between carbon nanotubes, graphene, and clay as nanofillers, *Materials* 9 (2016) 262.
- [288] V. Kumar, M. N. Alam, A. Manikkavel, M. Song, D.-J. Lee, S.-S. Park, Silicone rubber composites reinforced by carbon nanofillers and their hybrids for various applications: A review, *Polymers* 13 (2021) 2322.
- [289] K. Gong, K. Zhou, X. Qian, C. Shi, B. Yu, Mxene as emerging nanofillers for high-performance polymer composites: A review, *Composites Part B: Engineering* (2021) 108867.
- [290] M. Šupová, G. S. Martynková, K. Barabaszová, Effect of nanofillers dispersion in polymer matrices: a review, *Science of advanced materials* 3 (2011) 1–25.
- [291] B. K. Deka, A. Hazarika, J. Kim, Y.-B. Park, H. W. Park, Recent development and challenges of multifunctional structural supercapacitors for automotive industries, *International Journal of Energy Research* 41 (2017) 1397–1411.
- [292] E. Albiter, A. S. Merlano, E. Rojas, J. M. Barrera-Andrade, Á. Salazar, M. A. Valenzuela, Synthesis, characterization, and photocatalytic performance of zno–graphene nanocomposites: A review, *Journal of Composites Science* 5 (2021) 4.
- [293] D. Kumar, R. S. Rai, V. Bajpai, N. K. Singh, Mass fabrication of 2d nanostructure (zno) in chemical growth solution using tip induced lithography, *Materials and Manufacturing Processes* (2021) 1–9.
- [294] P.-y. Hung, K.-t. Lau, L.-k. Cheng, J. Leng, D. Hui, Impact response of hybrid carbon/glass fibre reinforced polymer composites designed for engineering applications, *Composites Part B: Engineering* 133 (2018) 86–90.

- [295] J.-I. Kim, Y.-T. Hwang, K.-H. Choi, H.-J. Kim, H.-S. Kim, Prediction of the vacuum assisted resin transfer molding (vartm) process considering the directional permeability of sheared woven fabric, *Composite Structures* 211 (2019) 236–243.
- [296] M. R. Abusrea, S.-W. Han, K. Arakawa, N.-S. Choi, Bending strength of cfrp laminated adhesive joints fabricated by vacuum-assisted resin transfer molding, *Composites Part B: Engineering* 156 (2019) 8–16.
- [297] B.-J. Kim, S.-H. Cha, G.-H. Kang, K. Kong, W. Ji, H. W. Park, Y.-B. Park, Interfacial control through zno nanorod growth on plasma-treated carbon fiber for multiscale reinforcement of carbon fiber/polyamide 6 composites, *Materials Today Communications* 17 (2018) 438–449.
- [298] H. Zhang, S. Li, X. Ma, D. Yang, Controllable growth of dendrite-like cuo nanostructures by ethylene glycol assisted hydrothermal process, *Materials Research Bulletin* 43 (2008) 1291–1296.
- [299] Y. Sun, G. M. Fuge, N. A. Fox, D. J. Riley, M. N. Ashfold, Synthesis of aligned arrays of ultrathin zno nanotubes on a si wafer coated with a thin zno film, *Advanced materials* 17 (2005) 2477–2481.
- [300] Z. Hu, G. Oskam, P. C. Searson, Influence of solvent on the growth of zno nanoparticles, *Journal of colloid and interface science* 263 (2003) 454–460.
- [301] L. E. Greene, M. Law, D. H. Tan, M. Montano, J. Goldberger, G. Somorjai, P. Yang, General route to vertical zno nanowire arrays using textured zno seeds, *Nano letters* 5 (2005) 1231–1236.
- [302] Z. H. Ibupoto, K. Khun, M. Eriksson, M. AlSalhi, M. Atif, A. Ansari, M. Willander, Hydrothermal growth of vertically aligned zno nanorods using a biocomposite seed layer of zno nanoparticles, *Materials* 6 (2013) 3584–3597.

- [303] K. Kong, B. K. Deka, M. Kim, A. Oh, H. Kim, Y.-B. Park, H. W. Park, Interlaminar resistive heating behavior of woven carbon fiber composite laminates modified with zno nanorods, *Composites science and technology* 100 (2014) 83–91.
- [304] U. Holzwarth, N. Gibson, The scherrer equation versus the 'debye-scherrer equation', *Nature nanotechnology* 6 (2011) 534–534.
- [305] W. L. de Almeida, N. S. Ferreira, F. S. Rodembusch, V. C. de Sousa, Study of structural and optical properties of zno nanoparticles synthesized by an eco-friendly tapioca-assisted route, *Materials Chemistry and Physics* 258 (2021) 123926.
- [306] J. Santhoshkumar, S. V. Kumar, S. Rajeshkumar, Synthesis of zinc oxide nanoparticles using plant leaf extract against urinary tract infection pathogen, *Resource-Efficient Technologies* 3 (2017) 459–465.
- [307] M. Dastpaki, H. A. Khonakdar, Thermal, thermomechanical, and morphological characterization of poly (vinyl chloride)(pvc)/zno nanocomposites: Pvc molecular weight effect, *Journal of Vinyl and Additive Technology* 25 (2019) E63–E71.
- [308] Y. Zhao, X. Song, Q. Song, Z. Yin, A facile route to the synthesis copper oxide/reduced graphene oxide nanocomposites and electrochemical detection of catechol organic pollutant, *CrystEngComm* 14 (2012) 6710–6719.
- [309] M. Mohsin, L. Iannucci, E. Greenhalgh, Fibre-volume-fraction measurement of carbon fibre reinforced thermoplastic composites using thermogravimetric analysis, *Heliyon* 5 (2019) e01132.
- [310] D.-Y. Yoo, S. Kim, G.-J. Park, J.-J. Park, S.-W. Kim, Effects of fiber shape, aspect ratio, and volume fraction on flexural behavior of ultra-high-performance fiber-reinforced cement composites, *Composite Structures* 174 (2017) 375–388.

- [311] S. Keck, M. Fulland, Effect of fibre volume fraction and fibre direction on crack paths in flax fibre-reinforced composites, *Engineering Fracture Mechanics* 167 (2016) 201–209.
- [312] M. El Messiry, Theoretical analysis of natural fiber volume fraction of reinforced composites, *Alexandria Engineering Journal* 52 (2013) 301–306.
- [313] R. Yahaya, S. Sapuan, M. Jawaid, Z. Leman, E. Zainudin, Effects of kenaf contents and fiber orientation on physical, mechanical, and morphological properties of hybrid laminated composites for vehicle spall liners, *Polymer composites* 36 (2015) 1469–1476.
- [314] M. H. A. Elella, E. S. Goda, K. R. Yoon, S. E. Hong, M. S. Morsy, R. A. Sadak, H. Gamal, Novel vapor polymerization for integrating flame retardant textile with multifunctional properties, *Composites Communications* 24 (2021) 100614.
- [315] N. Preda, A. Costas, M. Lilli, F. Sbardella, C. Scheffler, J. Tirillò, F. Sarasini, Functionalization of basalt fibers with zno nanostructures by electroless deposition for improving the interfacial adhesion of basalt fibers/epoxy resin composites, *Composites Part A: Applied Science and Manufacturing* 149 (2021) 106488.
- [316] C. Fragassa, A. Pavlovic, G. Minak, On the structural behaviour of a cfrp safety cage in a solar powered electric vehicle, *Composite Structures* 252 (2020) 112698.
- [317] G. Yang, M. Park, S.-J. Park, Recent progresses of fabrication and characterization of fibers-reinforced composites: A review, *Composites Communications* 14 (2019) 34–42.
- [318] Y. Zheng, X. Wang, G. Wu, Chemical modification of carbon fiber with diethylenetriaminepentaacetic acid/halloysite nanotube as a multifunctional interfacial rein-

- forcement for silicone resin composites, *Polymers for Advanced Technologies* 31 (2020) 527–535.
- [319] R. S. Rai, V. Bajpai, Synthesis of zno nanostructures on woven kevlar fabric and impact of hydrothermal conditions on growth of nanorods, in: *Industry 4.0 and Advanced Manufacturing*, Springer, 2023, pp. 219–229.
- [320] M. Zhao, L. Meng, L. Ma, L. Ma, X. Yang, Y. Huang, J. E. Ryu, A. Shankar, T. Li, C. Yan, et al., Layer-by-layer grafting cnts onto carbon fibers surface for enhancing the interfacial properties of epoxy resin composites, *Composites Science and Technology* 154 (2018) 28–36.
- [321] R. Zhang, B. Gao, Q. Ma, J. Zhang, H. Cui, L. Liu, Directly grafting graphene oxide onto carbon fiber and the effect on the mechanical properties of carbon fiber composites, *Materials & Design* 93 (2016) 364–369.
- [322] A. Feng, G. Wu, C. Pan, Y. Wang, The behavior of acid treating carbon fiber and the mechanical properties and thermal conductivity of phenolic resin matrix composites, *Journal of Nanoscience and Nanotechnology* 17 (2017) 3786–3791.
- [323] Y. Lv, J. Liu, Z. Zhang, W. Zhang, A. Wang, F. Tian, W. Zhao, J. Yan, Green synthesis of cuo nanoparticles-loaded zno nanowires arrays with enhanced photocatalytic activity, *Materials Chemistry and Physics* 267 (2021) 124703.
- [324] S. H. Kim, A. Umar, S.-W. Hwang, Rose-like cuo nanostructures for highly sensitive glucose chemical sensor application, *Ceramics International* 41 (2015) 9468–9475.
- [325] A. Umar, A. A. Ibrahim, U. T. Nakate, H. Albargi, M. A. Alsaiari, F. Ahmed, F. A. Alharthi, A. A. Alghamdi, N. Al-Zaqri, Fabrication and characterization of cuo nanoplates based sensor device for ethanol gas sensing application, *Chemical Physics Letters* 763 (2021) 138204.

- [326] S. Tharchanaa, K. Priyanka, K. Preethi, G. Shanmugavelayutham, Facile synthesis of Cu and CuO nanoparticles from copper scrap using plasma arc discharge method and evaluation of antibacterial activity, *Materials Technology* 36 (2021) 97–104.
- [327] R. S. Rai, V. Bajpai, Rapid synthesis of ZnO nanostructures on woven carbon fiber using microwave treated chemical bath deposition and their characterization, *Materials Today: Proceedings* 57 (2022) 84–89.
- [328] D. Kumar, R. S. Rai, V. Bajpai, N. K. Singh, Mass fabrication of 2D nanostructure (ZnO) in chemical growth solution using tip induced lithography, *Materials and Manufacturing Processes* 37 (2022) 177–185.
- [329] C. Lu, L. Qi, J. Yang, D. Zhang, N. Wu, J. Ma, Simple template-free solution route for the controlled synthesis of Cu(OH)<sub>2</sub> and CuO nanostructures, *The Journal of Physical Chemistry B* 108 (2004) 17825–17831.
- [330] Z. Komeily-Nia, M. Montazer, B. Nasri-Nasrabadi, et al., A practical approach to load CuO/MnO<sub>2</sub> core/shell nanostructures on textiles through in situ wet chemical synthesis, *Colloids and Surfaces A: Physicochemical and Engineering Aspects* 583 (2019) 123998.
- [331] B. K. Deka, A. Hazarika, K. Kong, D. Kim, Y.-B. Park, H. W. Park, Interfacial resistive heating and mechanical properties of graphene oxide assisted CuO nanoparticles in woven carbon fiber/polyester composite, *Composites Part A: Applied Science and Manufacturing* 80 (2016) 159–170.
- [332] Y. Zhang, S. Wang, X. Li, L. Chen, Y. Qian, Z. Zhang, CuO shuttle-like nanocrystals synthesized by oriented attachment, *Journal of Crystal Growth* 291 (2006) 196–201.
- [333] M. Cao, C. Hu, Y. Wang, Y. Guo, C. Guo, E. Wang, A controllable synthetic route

- to Cu, Cu<sub>2</sub>O, and CuO nanotubes and nanorods, *Chemical Communications* (2003) 1884–1885.
- [334] F. Teng, W. Yao, Y. Zheng, Y. Ma, Y. Teng, T. Xu, S. Liang, Y. Zhu, Synthesis of flower-like CuO nanostructures as a sensitive sensor for catalysis, *Sensors and Actuators B: Chemical* 134 (2008) 761–768.
- [335] J. Zhu, H. Bi, Y. Wang, X. Wang, X. Yang, L. Lu, CuO nanocrystals with controllable shapes grown from solution without any surfactants, *Materials Chemistry and Physics* 109 (2008) 34–38.
- [336] C. Xu, K. V. Manukyan, R. A. Adams, V. G. Pol, P. Chen, A. Varma, One-step solution combustion synthesis of CuO/Cu<sub>2</sub>O/C anode for long cycle life Li-ion batteries, *Carbon* 142 (2019) 51–59.
- [337] X. Xu, H. Yang, Y. Liu, Self-assembled structures of CuO primary crystals synthesized from Cu(CH<sub>3</sub>COO)<sub>2</sub>-NaOH aqueous systems, *CrystEngComm* 14 (2012) 5289–5298.
- [338] K. Kong, R. K. Cheedarala, M. Kim, H.-D. Roh, Y.-B. Park, H. W. Park, Electrical thermal heating and piezoresistive characteristics of hybrid CuO-woven carbon fiber/vinyl ester composite laminates, *Composites Part A: Applied Science and Manufacturing* 85 (2016) 103–112.
- [339] B. Zhao, P. Liu, H. Zhuang, Z. Jiao, T. Fang, W. Xu, B. Lu, Y. Jiang, Hierarchical self-assembly of microscale leaf-like CuO on graphene sheets for high-performance electrochemical capacitors, *Journal of Materials Chemistry A* 1 (2013) 367–373.
- [340] L. Martin, H. Martinez, D. Poinot, B. Pecquenard, F. Le Cras, Comprehensive x-ray photoelectron spectroscopy study of the conversion reaction mechanism of CuO



- in lithiated thin film electrodes, *The Journal of Physical Chemistry C* 117 (2013) 4421–4430.
- [341] S. Zhu, M. Wu, M.-H. Ge, H. Zhang, S.-K. Li, C.-H. Li, Design and construction of three-dimensional cuo/polyaniline/rgo ternary hierarchical architectures for high performance supercapacitors, *Journal of Power Sources* 306 (2016) 593–601.
- [342] W. Chen, H. Zhang, Z. Ma, B. Yang, Z. Li, High electrochemical performance and lithiation–delithiation phase evolution in cuo thin films for li-ion storage, *Journal of Materials Chemistry A* 3 (2015) 14202–14209.
- [343] D. Karagiozova, P. B. Ataabadi, M. Alves, Finite element modeling of cfrp composite tubes under low velocity axial impact, *Polymer Composites* 42 (2021) 1543–1564.
- [344] M. M. Rehman, K. Shaker, Y. Nawab, Effect of poly ether ether ketone particles on v-notched shear and drop weight impact behavior of carbon/epoxy composite, *Polymer Composites* 43 (2022) 3219–3227.
- [345] M. V. Burkov, A. V. Eremin, Mechanical properties of carbon-fiber-reinforced epoxy composites modified by carbon micro-and nanofillers, *Polymer Composites* 42 (2021) 4265–4276.
- [346] V. Jain, S. Jaiswal, K. Dasgupta, D. Lahiri, Influence of carbon nanotube on interfacial and mechanical behavior of carbon fiber reinforced epoxy laminated composites, *Polymer Composites* 43 (2022) 6344–6354.



# List of Publications

## Published Articles

1. **Ravi Shankar Rai**, Vivek Bajpai, “Hydrothermally grown ZnO NSs on Bi-Directional woven carbon fiber and effect of synthesis parameters on morphology”, *Ceramics International* 47(2021) 8208–8217. <https://doi.org/10.1016/j.ceramint.2020.11.180>. (SCI, Q1, I.F.-5.532)
2. **Ravi Shankar Rai**, Vivek Bajpai, “Recent advances in ZnO nanostructures and their future perspective”, *Advances in Nano Research*, 11(2021), 37-54. <https://doi.org/10.12989/anr.2021.11.1.037>. (SCI, Q1, I.F.-13.052)
3. **Ravi Shankar Rai**, Vivek Bajpai, “One-step microwave synthesis of surface functionalized carbon fiber fabric by ZnO nanostructures”, *Advances in Nano Research*, (2022). [Accepted] (SCI, Q1, I.F.-13.052)
4. **Ravi Shankar Rai**, Vivek Bajpai, “Improvement of interfacial adhesion of CuO nanostructured carbon fiber reinforced polymer composites”, *Polymer Composites*, (2022). <https://doi.org/10.1002/pc.27205>. (SCI, Q2, I.F.-3.531)
5. **Ravi Shankar Rai**, Girish J.P, Vivek Bajpai, Muhammad Imran Khan, Noured-

dine Elboughdiri, Abdallah Shanableh, Rafael Luque, “An eco-friendly approach on green synthesis, bio-engineering applications, and future outlook of ZnO nano-material: A critical review”, *Environmental Research*, 221(2023), 114807. <https://doi.org/10.1016/j.envres.2022.114807>. (SCI, Q1, I.F.-8.431)

6. **Ravi Shankar Rai**, Vivek Bajpai, “Growth of CuO nanoparticles using one step chemical bath deposition under microwave heating and their characterizations”, *International Journal of Materials Research*, (2023). [Accepted] (SCI, Q4, I.F.-0.678)

## Communicated Articles

1. **Ravi Shankar Rai**, Vivek Bajpai, “Surface functionalization by hydrothermally synthesized ZnO nanostructures for improved impact strength of ZnO/carbon-fiber/epoxy-resin hybrid nanocomposites”, *Materials today chemistry*, (2022). (SCI, Q1, I.F.-7.613).
2. **Ravi Shankar Rai**, Vivek Bajpai, “Carbon fiber fabrics functionalized with monoclinic CuO nanostructures using seed-assisted hydrothermal growth treatment”, *Advanced Engineering Materials*, (2022). (SCI, Q2, I.F.-4.122).
3. **Ravi Shankar Rai**, Vivek Bajpai, “A practical approach to functionalize carbon fiber textiles by hydrothermal deposition of ZnO nanorods for enhanced hydrophilicity and tribological performance”, *Surfaces and Interfaces*, (2022). (SCI, Q1, I.F.-6.137).

## International Conference

1. **Ravi Shankar Rai**, Chandra Prakash Singh, Vivek Bajpai, “Impact Behaviour of Hydrothermally Synthesized ZnO/Polyester Woven Carbon Fibre Hybrid Compos-

- ites” Proceedings of the Third World congress on Micro and Nano Manufacturing, WCMNM 2019 Raleigh, NC, USA.
2. **Ravi Shankar Rai**, Vivek Bajpai, “Fabrication of ZnO nanostructures on woven carbon fiber via hydrothermal route and effect of synthesis conditions on morphology” Proceedings of the International Conference on Precision, Meso, Micro and Nano Engineering, COPEN 2019 IIT Indore, India.
  3. **Ravi Shankar Rai**, Vivek Bajpai, “Fabrication and characterization of CuO/epoxy/woven carbon fiber hybrid composites with different CuO concentrations” Proceedings of the International Conference on Frontiers in Materials Processing Applications Research and Technology, FIMPART 2019 Ahmedabad, India.
  4. **Ravi Shankar Rai**, Vivek Bajpai, “Microwave assisted wet chemical synthesis and characterizations of ZnO nanoflowers for optoelectronic applications” Proceedings of the Fourth World congress on Micro and Nano Manufacturing, WCMNM 2021 IIT Bombay, India.
  5. **Ravi Shankar Rai**, Vivek Bajpai, “Rapid synthesis of ZnO nanostructures on woven carbon fiber using microwave treated chemical bath deposition and their characterization” International Symposium on Materials of the Millennium: Emerging Trends and Future Prospects, 2021 Pandit Deendayal Energy University, Gujarat India. Materials Today: Proceedings, Elsevier. <https://doi.org/10.1016/j.matpr.2022.01.356>.
  6. **Ravi Shankar Rai**, Vivek Bajpai, “Development of CuO nanostructures using one step chemical bath deposition under microwave heating and their characterizations” Proceedings of the International Conference on Processing and Characterization of Materials, ICPCM 2021 NIT Rourkela, India.
  7. **Ravi Shankar Rai**, Vivek Bajpai, “Enhancement of impact strength of hybrid CFRP

- by surface modification of carbon fiber with controlled growth of CuO nanostructures” Proceedings of the International Conference on Advancements and Futuristic Trends in Mechanical and Materials Engineering, AFTMME 2021 IIT Ropar, India.
8. **Ravi Shankar Rai**, Vivek Bajpai, “Synthesis of ZnO Nanostructures on Woven Kevlar Fabric and Impact of Hydrothermal Conditions on Growth of Nanorods”, International Conference on Industry 4.0 and Advanced Manufacturing, I4AM 2022 Indian Institute of Science, Bangalore, India. Proceedings of the Lecture Notes in Mechanical Engineering. Springer, Singapore. [https://doi.org/10.1007/978-981-19-0561-2\\_20](https://doi.org/10.1007/978-981-19-0561-2_20).
  9. **Ravi Shankar Rai**, Vivek Bajpai, “Solvothermal growth of ZnO nanorods on woven carbon fabric for enhanced impact energy absorption capacity of laminated composite” Proceedings of the Fifth World congress on Micro and Nano Manufacturing, WCMNM 2022 KU Leuven, Belgium.
  10. **Ravi Shankar Rai**, Vivek Bajpai, “Development of metal-oxide nanostructured interphase in basalt fiber reinforced polymer composites for structural applications” Proceedings of the International Conference on Frontiers in Materials Engineering, ICFME 2022 IIT Indore, India.
  11. **Ravi Shankar Rai**, Vivek Bajpai, “Improvement of impact strength of CuO nanostructured carbon fiber reinforced hybrid polymer composites” Proceedings of the Industrial Problems on Machines and Mechanisms, IPRoMM 2022 IIT(ISM) Dhanbad, India.